Design and Synthesis of Novel High Temperature Materials

A
Dissertation
Presented to
the faculty of the School of Engineering and Applied Science
University of Virginia

---

in partial fulfillment
of the requirements for the degree

Doctor of Philosophy

by

Christopher T. Kassner

May 2022

APPROVAL SHEET

This
Dissertation
is submitted in partial fulfillment of the requirements
for the degree of
Doctor of Philosophy

Author: Christopher T. Kassner

This Dissertation has been read and approved by the examining committee:

Advisor: Haydn N.G. Wadley

Committee Member: Elizabeth J. Opila

Committee Member: Sean R. Agnew

Committee Member: Prasanna Balachandran

Committee Member: James Fitz-Gerald

Committee Member: Chloe Dedic

Committee Member:

Accepted for the School of Engineering and Applied Science:

Jennifer L. West, School of Engineering and Applied Science

May 2022

Table of Contents

List of Figures

List of Tables

Abstract

Ongoing efforts to create more efficient gas turbine engines able to operate at temperatures above those feasible today have stimulated an interest in new high temperature materials and methods for making them. This dissertation investigates the synthesis of two candidates. The first is a silicon carbide foam with submicron pores made from a preceramic polymer via a space holder method. The second is a class of materials called refractory complex concentrated metal alloys (RCCA) with potential maximum use temperatures significantly above those of superalloys, but whose optimal compositions remain to be discovered. The dissertation describes the exploration of a combinatorial approach intended to accelerate their discovery.

A method was developed for making silicon carbide foams with an average pore diameter of 650 nm and 150 nm wide interpore ligaments using spherical polymethylmethacrylate (PMMA) particle templating of a β-SiC nanoparticle loaded polycarbosilane (PCS) preceramic polymer. Differential scanning calorimetry and thermogravimetric analysis were used to investigate the effects of PMMA decomposition and the presence of β-SiC nanoparticles upon PCS cure, pyrolysis, and partial crystallization mechanisms. Incomplete thermal decomposition and evaporation of the PMMA in the presence of the PCS resulted in retention of excess carbon in the amorphous pyrolyzed foam and the appearance of small PMMA remnant particles in each foam pore. During the highest temperature crystallization treatments, these remnant particles began to decompose along with the solid foam ligaments. The foam's Young's modulus and compressive strength at first increased with maximum processing temperature, reaching a maximum after

processing at 1300 ˚C. Further increases in temperature resulted in a rapid fall both in elastic modulus and compressive strength. Well established micromechanical foam models were combined with metallographically determined relative density to estimate the foam's solid ligament Young's modulus and modulus of rupture. These results indicated that changes to the solid (inter-pore ligament) material properties were primarily responsible for the observed trends in nanofoam mechanical properties rather than changes of foam density.

While much work is underway to develop SiC composites for use in load supporting applications in engines, an alternative superalloy replacement strategy is to develop a refractory alloy whose maximum use temperature meets or exceeds the needs of future engines (i.e. an alloy that functions at temperatures T >1300 °C). Complex Concentrated Alloys (CCAs) have emerged as a promising new class of advanced metallic material for high temperature applications. CCAs utilize four or more principal elements in non-dilute concentration to achieve high strength, toughness, and fatigue endurance, as well as reduced thermal and electrical conductivity. When made from combinations of three, four or more high melting temperature refractory metals (tungsten, tantalum, molybdenum, niobium together with hafnium, vanadium, chromium, zirconium and titanium) these properties could potentially be achieved in alloys with exceptionally high melting temperatures. However, gaps in the fundamental understanding of the mechanistic origins of many of the properties of CCAs has impeded alloy design and development. This is amplified by the lack of experimental tools for the rapid exploration of the extraordinarily large compositional design space; especially tools suitable for the difficult to process refractory metal alloys. While refractory CCAs (RCCAs) promise high strength, in combination with high melting temperature, the tendency for brittle fracture at low temperatures, the difficult processing paths, the extreme sensitivity to interstitial impurities (C, N, O), their susceptibility to oxidation in general, and particularly to volatile oxide formation, and the combinatorial complexity of the compositional space, make the discovery of new compositions via experimental approaches challenging. The goal of this aspect of the dissertation was to explore the application of an electron beam evaporation-based combinatorial synthesis tool to refractory, body centered cubic (BCC) CCAs based upon mixtures of W, Ta, Mo, Nb, Hf, V, Cr, and Ti. By using inert gas jet-controlled intermixing of the vapor plumes from two, three or four laterally separated metal sources, combinatorial libraries with concentration gradients up to 12 at% across 50 mm wide combinatorial libraries have been achieved using an electron beam directed vapor deposition (EB-DVD) approach. It is shown that the region of library concentration space could be adjusted by varying the electron beam power applied to each source. The high electron beam power (10 kW) available enabled high rates of evaporation from the sources and the growth of thick (greater than 10 μm thickness) coatings on 50 mm x 50 mm molybdenum substrates. This enabled the synthesis of Ta-Cr-Nb-Ti and Ta-Hf-Nb-Ti libraries that permitted x-ray diffraction assessments of the composition - phase space relationships for libraries formed at 1200 °C. These films were sufficiently thick that they permitted application of nano-indentation methods for assessments of their ambient temperature elastic modulus and hardness.

Chapter 1: Introduction

1.1 High Temperature Materials

High use temperature materials, including high melting temperature metallic alloys, ceramics, and composites are critical enablers of numerous technological applications including gas turbine engines (1–3), nuclear (fission and future fusion) reactors (4), and the leading edges of hypersonic vehicles (5). Many efforts are being made to increase the operating temperatures of these technologies by developing new materials with higher use temperatures but without sacrificing other key properties such as a low relative density, high strength, high toughness, and environmental resistance.

Superalloys based upon nickel, cobalt, and iron have been widely used to advance the performance of gas turbine engines. The creep governed strength of superalloys are limited to typical operating temperatures less than 1150˚C (6,7). In order to achieve better fuel burn efficiency, efforts continue to increase the temperature at which engines operate. The drive for materials that can operate at higher temperature lead to an extensive amount of research on ceramic matrix composites (CMCs) (7–10). CMCs offer a higher temperature, higher specific strength and lower density alternative to metallic super-alloys.

The gas turbine engine is comprised of four primary stages; air intake, compression, combustion and exhaust stages, Figure 1(a). The intake region of the engine takes in large volumes of air and directs it into the compression region. The compression region causes the air to increase in pressure, and therefore increase in temperature. When the compressed air enters the combustion region, hydrocarbon fuel is injected, combustion ensues and the reacting hydrocarbon fuel and air and the combustion reaction products increase to an engine maximum temperature while maintaining a constant pressure (isobaric). The combustion gas then flows through a high-pressure turbine where it systematically is expanded and finally exits the exhaust to reach the local atmospheric pressure. The momentum of this exhaust gas provides the propulsive momentum to accelerate the engine in the opposite direction. The efficiency of this process is dependent on avoiding gas pressure losses via the gap between the turbine blade tips and the interior engine wall, or shroud (11,12). An abradable shroud on the interior surface of the pressure containment system is typically used to reduce gas leakage between the blade tip and the engine shroud. It was realized that large improvements in thermodynamic efficiency are possible if the combustion process operates at higher temperatures. It was also found that the use of a fraction of the compressed air that by-passes the combustion process entirely and exits the engine at high speeds increases the momentum of the propulsion process and thus increases the propulsive efficiency as the by-pass ratio (BPR) increases. Figure 1(b) shows an example of a recently introduced engine that that has significantly increased both the thermodynamic and propulsive efficiency and thus the overall efficiency (the product of these two efficiencies) of gas turbine engines.

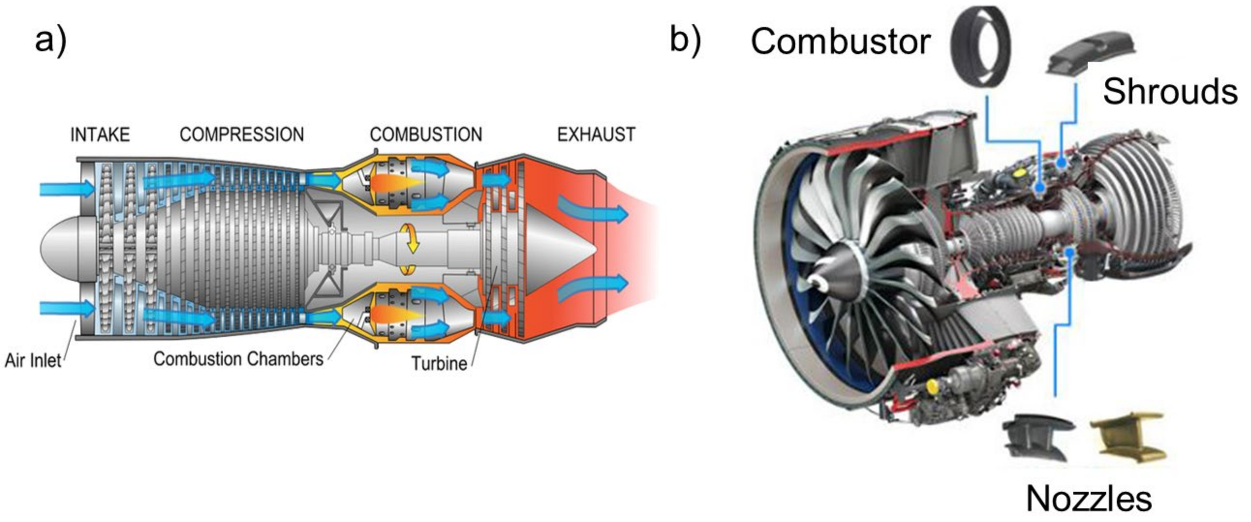

Figure 1. (a) Schematics of a gas turbine engine (FAA Handbook) and (b) GE9X engine schematic showing current and future locations of SiC/SiC CMC components (13)

GE Aviation has aggressively implemented CMC materials in their GE9X engine with CMC inner and outer combustor liners, High Pressure Temperature (HPT) Stage 1 shrouds and nozzles and HPT Stage 2 nozzles shown schematically in Figure 1b. The use of CMCs offers a lower density alternative to the metallic alloys traditional used; however, the density can be further reduced with the use of porous ceramics; particularly in applications where strength is not required such as abradable shrouds.

An Ashby plot for high temperature materials used in aerospace applications is shown in Figure 2 and identifies material specific strengths and use temperatures (2). It is evident that SiC/SiC (fiber/matrix) CMCs extend both the specific strength and operation temperature capabilities. Although carbon-carbon (C-C) composites extend to slightly higher temperatures, they cannot be used in oxidizing environments due to their high reactivity with oxygen and water vapor resulting in vapor phase oxides (CO, CO_2). Though oxygen and other oxidizing gas permeation barrier coatings have been proposed, the risk of a single pin hole in the coating providing access of oxidants with the carbon, and subsequent loss of the component within its coating, have precluded their use in gas turbine engines. Currently, there is no useful strategy to mitigate this issue. Even though the carbon of SiC composites is also volatilized by similar reactions with oxidants, a passivating silica layer develops, and in a dry oxygen environment this provides good protection from linear oxidation. However, in the presence of water vapor, silica is volatilized and so environmental barrier coating systems are used to slow this process and provide a long operational life. While environmental barrier coatings (EBCs) have proven useful to mitigate environmental issues for SiC/SiC CMCs (1), further increases of the operation temperature of combustion engines remains of interest. Refractory metal alloys show promise in increasing the operation temperatures of gas turbine engines. While environmental issues still remain, refractory metal alloys show promise to extend operation temperatures by >200 °C.

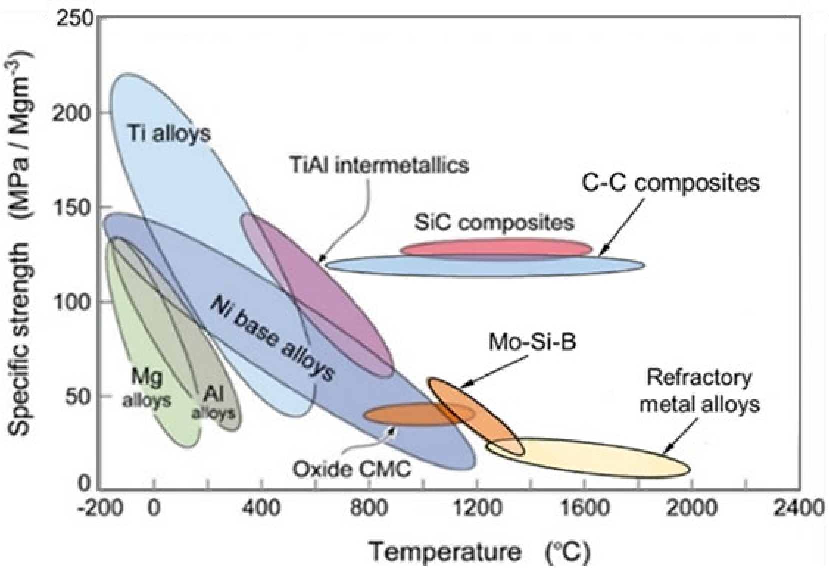

Figure 2. Specific strength vs temperature for commonly used materials in aerospace engines. (2)

1.2 Current High Temperature Material Needs

While both ceramics and refractory metals have relatively high modulus and strengths, the ability to reduce the density of these materials while maintaining superior mechanical properties offers a new range of material applications for lightweight, strong, low density, and high temperature materials.

1.2.1 Light Weight Ceramic Foams

One area where new materials promise improvements is for the shrouds used in gas turbine engines. Improvements is could be realized through the use of SiC foams which have an innately high melting temperature (2,730 °C), a low density determined by the degree of porosity (3,210 kg/m^3 for fully dense SiC), shapeability via preceramic polymer processing approaches, low thermal conductivity enhanced by porosity, sufficient stiffness and strength to resist compression by high pressure, and availability of existing EBC systems for SiC CMC to delay oxidation. While efforts to increase the shrouds temperature capabilities have been investigated using SiC CMC materials (>1300 °C), opportunities to reduce the weight of the shroud remain. This dissertation investigates a SiC foam that offers promise as low density, sufficiently strong (>100 MPa) and stiff (modulus >15 GPa), as a shroud material that is usable above 1300 °C. Furthermore, the proposed synthesis method is near net shapeable, making the fabrication process relatively low cost.

1.2.2 Refractory Metal Alloys

Refractory metal alloys whose constituents have melting temperatures above 2,000 °C also provide potential solutions to many other high temperature applications; especially those where their high density is less of a design constraint. Refractory elements, highlighted in purple and red within the d-orbitals portion of the periodic table provided below (Figure 3) (14). However, due to cost, elements such as Te, Ru, Rh, Re, Os, and Ir are not being considered at this time.

Recently, it was proposed that the near equiatomic combinations of 4-6 (or more) refractory metal elements into an alloy can increase strength while also increasing the operating temperatures (15–18). These refractory complex concentrated alloys (CCAs) may offer an opportunity to extend the temperature limits of conventional high temperature material design. For these reasons, refractory metal alloys have attracted interest as possible candidates to continue to push the engine operation temperature even higher.

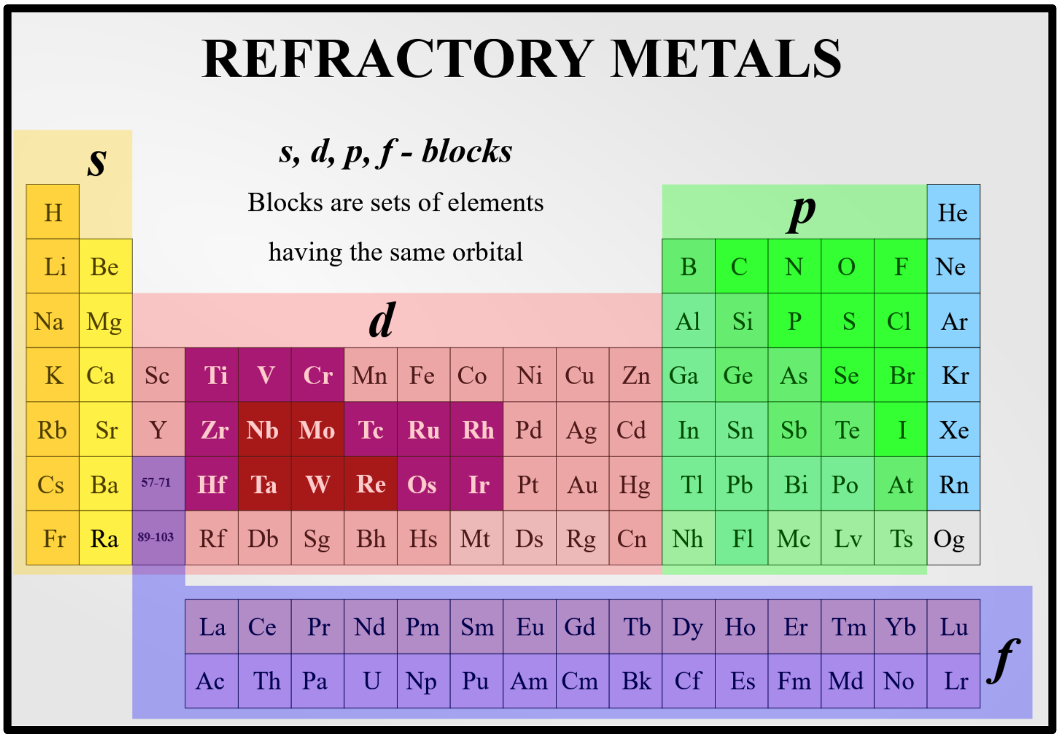

Figure 3. Periodic table showing the refractory metals highlighted in purple and red.

1.3 Dissertation Goals

While environmental resistance remains a challenge for SiC based ceramics and refractory metals that will need to be addressed by environmental barrier coating systems (1,10), this dissertation explores two new material solutions for gas turbine engine applications. The first seeks to reduce the density of commonly used SiC, by investigating a method for making a SiC foam and the resulting microstructure, mechanical properties, and processing temperature relations are examined. A novel processing method for porous SiC has been developed resulting in a SiC foam with an average pore diameter of 650 nm and 150 nm wide interpore ligaments using spherical polymethylmethacrylate (PMMA) particle templating of a β-SiC nanoparticle loaded polycarbosilane (PCS) preceramic polymer. With this method, shroud materials could be shaped and produced as a continuous component, and environmental protection provided with existing environmental barrier coatings (such as the Si-$Yb_2Si_2O_7$) developed for silicon carbide-based composites (1).

The second material system explores complex concentrated metal alloys based upon combinations of the refractory metals identified in Figure 3 whose optimal compositions remain to be discovered. The dissertation describes a combinatorial approach intended to accelerate the discovery process. Refractory metals offer excellent high temperature capabilities; however, they too suffer from environmental effects. More recently, refractory complex concentrated alloys (RCCAs) have quickly gained interest as they were shown to retain high strength at temperatures exceeding 1000°C and even approaching 1600°C (6,17,19). Refractory alloys offer a secondary approach to high temperature material capabilities other than using CMCs, Figure 2 (20). Refractory metals have a higher density than CMCs; however, they have higher toughness and strength making them of interest for more robust high temperature applications. The primary goal of this aspect of the dissertation is the development of a combinatorial synthesis tool to explore, and understanding of the properties of refractory, body centered cubic (BCC) CCAs based upon mixtures of Ta, Mo, Nb, Hf, V, Cr, and Ti.

1.3.1 Dissertation Outline

The dissertation presented focuses on two topics: the synthesis and investigation of SiC foams and the use of a vapor deposition approach to produce refractory metal alloy libraries for high-throughput investigation.

Chapter 2 provides a background of ceramic foam materials, outlines the empirically determined mechanical models for compressive strength and Young's modulus of brittle foams, and presents the opportunities and challenges for ceramic foams. Chapter 3 discusses a novel synthesis approach for bulk processing of submicron porous SiC foams utilizing a preceramic polymer approach. Chapter 4 investigates the mechanical properties of the SiC foams produced and determines the effect of the final processing temperature on the compressive strength and Young's modulus of the produced foams.

Chapter 5 reviews the state of RCCA discovery and presents the challenges and opportunities within the area. Chapter 6 explores the use of an electron beam directed vapor deposition (EB-

DVD) to deposit refractory film libraries. Chapter 7 of this dissertation then outlines and implements the necessary upgrades to the legacy EB-DVD system to improve the quality of the deposited films. Lastly, Chapter 8 shows the ability to deposit four refractory elements with atomic concentrations varied radially around a near equiatomic center of the sample, investigates the microstructure and crystal structure, and illuminates the need for further studies to improve film quality.

Chapter 2: Cellular Ceramics

The desire to reduce the density and manipulate the mechanical, thermal, and other functional properties of materials to meet novel design requirements has led to the study and development of cellular solids, which include foams with a random topologies and lattice materials whose topology can be described by a unit cell that can be translated in two and three dimensions to create a macroscopic solid (21). The term 'cellular solid' is derived from the Latin, *cella,* meaning an enclosed space and the Roman, *cellarium*, which translates to a cluster of cells (21). Cellular materials are three dimensional structures consisting of an interconnected network of solid material that typically occupies 2-50% of the volume. Cells constructed of struts contain interconnected voids and are referred to as open-celled foams, Figure 4 (a). Conversely, foams whose voids are bounded by solid material walls (webs or membranes) such that the void space is enclosed by solid material are referred to as closed-celled foams, Figure 4 (b).

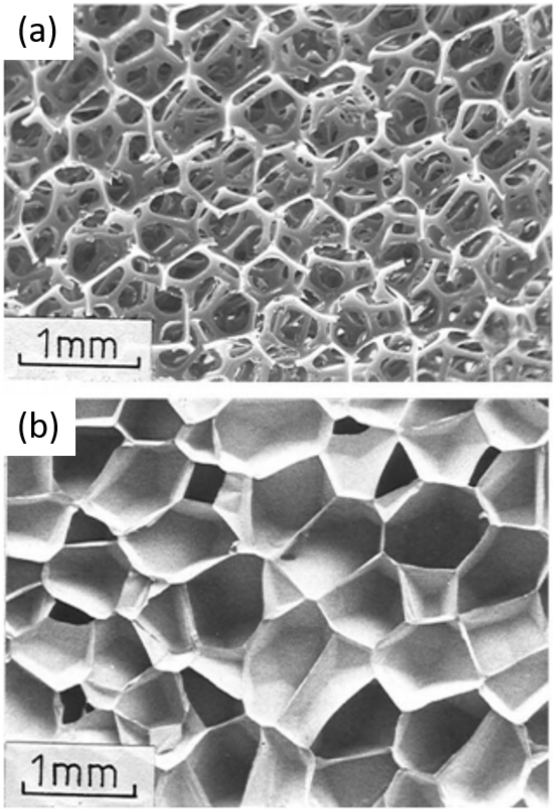

Figure 4. Engineering cellular solids (a) open-cell polyurethane foam and (b) closed-cell polyethylene foam. Figure originally from Gibson and Ashby (21)

Examples of natural cellular materials include the honeycombs made by bees, with a hexagonal unit cell translated in two dimensions and foams such as wood, coral, and bones. Engineered cellular solids are widely used in efficient light weight sandwich panels (22–25), for impulse load mitigation (23), as bone replacements (26), for heat exchange (27,28), for the support of catalysts (29), and for filtration (30). Those made from ceramics can be used for liquid metal filtration (31–33), are being considered for hydrogen storage (34), and high temperature thermal management (35,36). The ceramic foams described in this dissertation are of interest as potential shroud materials in the hot section of gas turbine engines where component weight can be reduced while maintaining a relatively high strength and modulus at temperatures approaching 1300 °C.

2.1 Brittle Foam Mechanical Models

The broader use of ceramic foams is limited by their typically low stiffness resulting from the low nodal connectivity of the foam topology (37), and modest compressive strength (11) resulting from their inefficient bend-dominated load support and presence of defects in ligaments and webs. Micromechanical models (21) have successfully linked the modulus and compressive strength of micro-architected materials to cell topology, pore volume fraction and the modulus or strength of the ligaments or webs themselves. As the web or ligament width is decreased, the probability of defects in them falls, and the micro-architected material strength has been predicted to increase (12, 13), stimulating interest in the development of nanofoams and lattices with ligament widths of less than a micron.

Gibson and Ashby have analyzed the compressive response of representative unit cells of both open and closed cell foams (21,39,40). The analysis assumes a rigid open or closed-cell structure, shown in Figure 5, and applies linear elastic, visco-elastic/plastic, elastic-plastic or elastic brittle responses depending on what system/property is being modeled. (20, 40).

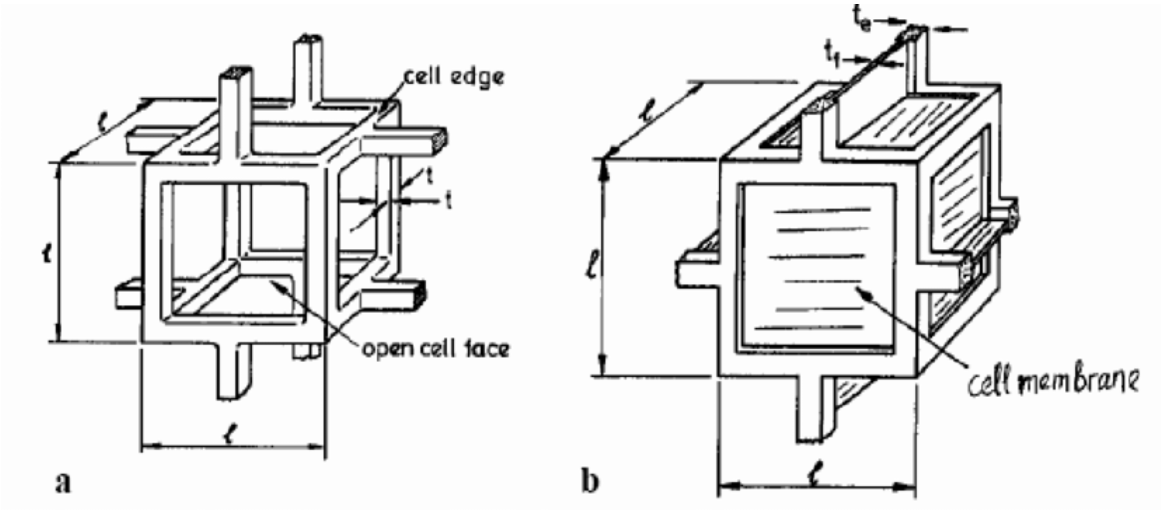

Figure 5. Cubic models of a) open-cell foam and b) closed-cell foam. The foams show edge length, l, while the edge thickness for the open-cell is t and the closed cell t_e with a membrane thickness t_f (Figure taken from Gibson and Ashby 1997 (21)).

The foams of interest to this dissertation are brittle foams. Gibson and Ashby (21,39,40) proposed general relationships between the Young's modulus, E and compressive strength, σ of a brittle foam, their solid material properties and foam relative density, $\frac{\rho}{\rho_s}$ (where ρ is the density of the foam and ρ_s that of the solid from which it is made). They showed that for open cell systems:

$$\frac{E}{E_s} = C_1 \left(\frac{\rho}{\rho_s}\right)^2 \qquad (1)$$

$$\frac{\sigma}{\sigma_s} = C_2 \left(\frac{\rho}{\rho_s}\right)^{\frac{3}{2}} \tag{2}$$

While for closed cell systems:

$$\frac{E}{E_s} = C_3 \varphi^2 \left(\frac{\rho}{\rho_s}\right)^2 + C_3'(1-\varphi)\left(\frac{\rho}{\rho_s}\right) \tag{3}$$

$$\frac{\sigma}{\sigma_s} = C_4 \left(\varphi \frac{\rho}{\rho_s}\right)^{\frac{3}{2}} + C'_4(1-\varphi)\left(\frac{\rho}{\rho_s}\right) \tag{4}$$

In these equations φ is the fraction of solid in the cell walls for closed cell foams, E_s, and σ_s, are the modulus, and modulus of rupture of the solid material from which the foam is made, and C_1, C_2, C_3, C_3', C_4 and C'_4 are dimensionless constants determined by the foam topology. C_2 and C_4 were found to have a value of 0.2 while the other coefficients have values close to unity. The second terms in the relationships for closed cell geometries (Equations 3 and 4) accounted for the contribution of the cell wall membrane stress to modulus and strength of the foam. However, the effective exponents then depend upon the fraction of mass in the cell walls. Chapter 4 of this dissertation will apply these models to the foams of interest and outline the assumptions needed to adequately determine solid ligament properties of the synthesized foams.

It has been empirically determined by Colombo et al. (40) that brittle foams Young's modulus and compressive strength can be adequately modeled using a general power law relationship of the form:

$$\frac{E}{E_s} = k\left(\frac{\rho}{\rho_s}\right)^n \tag{5}$$

$$\frac{\sigma}{\sigma_s} = c\left(\frac{\rho}{\rho_s}\right)^m \tag{6}$$

where k and c had values close to unity and the exponents $n=3$ and $m=2$ (21,40,42–44). In the case for foams with solid fractions less than 0.6, the accuracy of the applied models is dependent on the foam microstructure; however, the proposed general relationships are within reasonable agreement to Colombo's general power law relationships (45).

2.2 Opportunities and Challenges in Ceramic Foams

A wide variety of 3D printing approaches have emerged that seek to create stretch-dominated (high nodal connectivity) microarchitectured lattice topologies with interconnected void spaces that are more efficient at supporting stress than random, open cell foams (46,47). Some are capable of creating lattices with strut diameters approaching the small-scale regime resulting in lattices with very high reported specific strengths (48–52). However, many of the processes used to make these materials are costly to implement, and restricted in sample volume and therefore unable to make the large scale structures needed for most applications (53). In contrast, polymeric, and metal foams can be inexpensively made at large scale by the use of gas releasing (54–56), or other temporary space holding solids (40,55,57). While recent 3D printing approaches are seeking to address this challenge (58), here we investigate the application of a templated preceramic polymer-based approach for synthesis of bulk silicon carbide ceramic foams.

This ceramic foam synthesis approach exploits polymer derived ceramics (PDCs) for the synthesis of silicon carbide (SiC) ceramic components via traditional polymer processing techniques such as resin transfer molding followed by cure, pyrolysis and crystallization heat treatments in inert environments (57,59–64). Their use has been investigated for over 40 years as an alternative to the fabrication of ceramic parts by powder based methods (65). The PDC processing route has been extended to SiC/SiC fiber fabrication (66,67), ceramic powder consolidation (65,68), and ceramic matrix composite synthesis (69–71). Previous studies of ceramic foam synthesis using PDCs have utilized a powder space holder (PSH) method to fabricate large porous SiC samples (55). This method utilizes a sacrificial powder template such as polymethylmethacrylate (PMMA) that results in a highly porous material. Thermal decomposition is used to remove the space holding powder, leaving behind an array of pores throughout the host structure (42,55). However, reduction of the spherical pore diameter into the submicron regime where the width of the ligaments between pores enters the nanoscale regime has proven to be challenging (38,50,51). Furthermore, there is a lack of understanding of the effects PMMA inclusions on the cure, pyrolysis, crystallization and consequently the mechanical properties of foams synthesized using preceramic polymers. The dissertation investigates a synthesis technique which allows for bulk processing of submicron pore-size SiC foams for the first time. The resulting samples are sufficiently large that they can be used to establish the relationships between the foam’s Young’s modulus and compressive strength and those of the constituent materials.

Chapter 3: SiC Foam Synthesis: Templating of pre-ceramic polymers, shrinkage control and reaction kinetics.

3.1 Introduction

Organosilicon polymers with a Si-C backbone such as a polycarbosilane (PCS) can be cured, pyrolyzed and crystallized during high temperature processing to form SiC containing some level of oxygen derived from the starting polymer and contamination from the processing environment (72). Since typically only a fraction of the pre-ceramic polymer (PCP) mass is retained after thermal decomposition, the conversion of liquid polycarbosilanes to a solid ceramic component involves not only large changes in composition and profound molecular structure reorganization, but also significant gas release and substantial reductions in mass and volume. The development of allylhydridopolycarbosilane (AHPCS; $[Si(CH_2CH = CH_2)_2CH_2]_{0.1}[SiH_2CH_2]_{0.9}$), a now widely available pre-ceramic polymer, has increased the volumetric ceramic yield to nearly 30 vol% and a mass yield approaching 70 wt% (69,73–76). AHPCS, has the molecular arrangement shown schematically in Figure 6(a). It consists of a −Si-C− backbone with an attached allyl ($H_2C{=}CH{-}CH_2{-}$) group composed of a vinyl ($-CH{=}CH_2$) group attached to the −SiC-C− backbone via $-CH_2-$ methylene bridge. While the still very large volume shrinkage, and gas evolution associated with vinyl side group and methylene bridge scission and hydrogen loss during conversion to amorphous or β-SiC remains an issue for the production of large, crack free parts (55,57,59), unconstrained shapes with small cross-sectional areas (such as fibers and particles), can be nearly crack free after processing (66,67). This is enabled by short mass transport distances and fast reaction product diffusion which together avoid internal bubble formation, and by self-similar shrinkage when shrinkage displacements are unconstrained (61,77–79).

It was discussed in the previous chapter that a PSH method can be used to introduce porosity into pyrolyzed AHPCS using PMMA. Polymethylmethacrylate (PMMA), Figure 6(b), consists of a [CH_3-C] backbone with a methyl (CH_3) branch, and a branch consisting of a carbonyl (C=O) connected to a methyl (CH_3) via an oxygen bond. The decomposition of these powder space holders allows for spherical pore formation within the pyrolyzed AHPCS. Further discussion on the decomposition can be found in section 3.3 of this chapter.

Initial attempts at fabricating submicron porous SiC using PCS and PMMA powder space holders resulted in an uneven distribution of pores (55). Furthermore, the shrinkage cracking and gas bubble formation due to the rapid gas release accompanying cure and pyrolysis of polycarbosilanes also proved problematic. It has been reported that preloading the preceramic polymer with SiC particles reduces the fractional mass loss, increases the overall SiC content and helps maintain the overall shape of the sample after pyrolysis (80). This also decreases the overall volume reduction and gas release during curing, pyrolysis and crystallization. However, neither the properties of SiC foams after high temperature (T > 1200 °C) crystallization of SiC in the presence of decomposed PMMA and filler SiC powders nor the effects of these constituents upon the pyrolysis and crystallization processes of PCSs have been reported.

(a) Allylhydridopolycarbosilane (AHPCS)

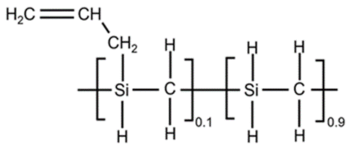

(b) Polymethyl methacrylate (PMMA)

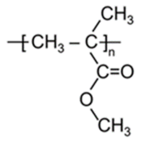

(c) n-hexane

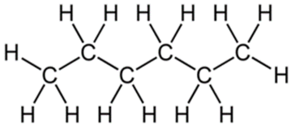

Figure 6. Molecular structures of (a) SMP-10 showing the CH_2=CH-CH_2 allyl group attachment to the -Si-C- backbone, (b) PMMA and (c) n-hexane used as a solvent for AHPCS.

The ability to mix the three constituent materials (PCS, PMMA, and β-SiC powder) requires a method that allows for uniform mixing and constituent distribution. PCS can be dispersed in solvents such as hexanes, tetrahydrofuran, and toluene (81). Mehr et al (68) showed the possibility of diluting SMP-10 in n-hexane, Figure 6c, as a method for coating ceramic powders. N-hexane is a solvent organic compound with an alkane straight-chain of six carbon atoms and has a molecular formula of C_6H_{14}. Furthermore, mesoporous membranes formed using SMP-10 and α-SiC powder suspended in n-hexane have been synthesized by König et al. (82). This method allows for even distribution of material and resolves the mixing issue with fine particles presented by Kotani et al (55). To overcome the issue of volume shrinkage, nano sized β-SiC seed particles can be used as a filler material. This method replaces a volume of SMP-10 with already crystalline SiC leading to less volume shrinkage. To the best of the author's knowledge, the mixing of SMP-10 in n-hexane method has not been used with spherical pore formers.

This study investigates application of the space holder approach for the synthesis of SiC foams with 100-300 nm width ligaments using sub-micron PMMA space holding particles in combination with an allylhydridopolycarbosilane SiC source preloaded with nanoscale β–SiC particles. The study uses differential scanning calorimetry (DSC) and thermogravimetric analysis (TGA) to investigate the high temperature interactions of the pre-ceramic polymer, β-SiC nanoparticle, and PMMA particle system.

3.2 Experimental Methods

Ceramic foams were made by mixing a preceramic polymer with sub-micron diameter, space-holding PMMA spheres, followed by preceramic polymer cure, pyrolysis and crystallization through progressive heating in argon.

A summary of the materials used to synthesize the SiC foams is provided in Table 1. The preceramic polymer was based upon AHPCS and is commercially available as StarPCS^{TM} SMP-10 (Starfire Systems, Inc., Schenectady, NY). The AHPCS was stored in a chemical storage freezer at -10 °C to reduce ambient environment polymer crosslinking (83). PMMA particles (Chemisnow grade MX-80H3wT) were procured from Soken Chem. & Eng. Co., LTD (Tokyo, Japan). The PMMA particles are highly cross-linked spherical particles with an average particle diameter of 800 nm ± 100 nm. To reduce shrinkage during processing, nano sized β-SiC filler particles were used to replace some of the preceramic polymer with crystalline SiC. Nearly spherical β-SiC particles of greater than 99+% purity, and diameter of 45-65 nm were purchased from US Research Nanomaterials, Inc. (Houston, Texas) for this purpose.

Table 1. Particles and preceramic polymer used for fabricating SiC foams

Material, Supplier (grade)	Use	Diameter (nm)	Density (kg•m^{-3})	Volume Fraction	Mass Fraction
Allylhydridopolycarbosilane Starfire Systems (StarPCS^{TM} SMP-10)	Preceramic Polymer Binder/Sintering Aid	--------	990	0.40	1.2
PMMA Particles Soken Chem. & Eng. Co., LTD. (Chemisnow MX-80H3wT)	Sacrificial Space Holder	0.793 ± 0.34	1,180	0.50	2
β-SiC Particles US Research Nanomaterials, Inc (SiC, Beta, 99+ %)	Seed Particles	20-60	3,210	0.10	1

3.2.1 Sample Preparation

Preliminary pyrolysis trials with the high viscosity SMP-10, β-SiC, and PMMA material system resulted in cracked components resulting from a non-uniform distribution of pores indicative of insufficient mixing of the constituents. To address this, a series of trials were conducted with samples of the preceramic polymer that were diluted with n-hexane to reduce its viscosity, and a recipe was eventually found which resulted in crack-free specimens. This consisted of a mixture of 2 parts by weight PMMA to 1-part β-SiC to 1.2-parts preceramic polymer to 3-parts n-hexane. The masses of these materials were then weighed to an accuracy of ± 0.01% using a Mettler Toledo Excellence XSE205DU Analytical Balance. The mixtures were blended for 90 minutes using a SPEX high-speed ball mill, and the n-hexane solvent then removed by evaporation at ambient temperature for 12 hours. This resulted in dry powder mixture with a uniform, random distribution of space holding particles. A schematic of the intended structure can be seen in Figure 7, where PMMA spheres are surrounded by β-SiC impregnated SMP-10.

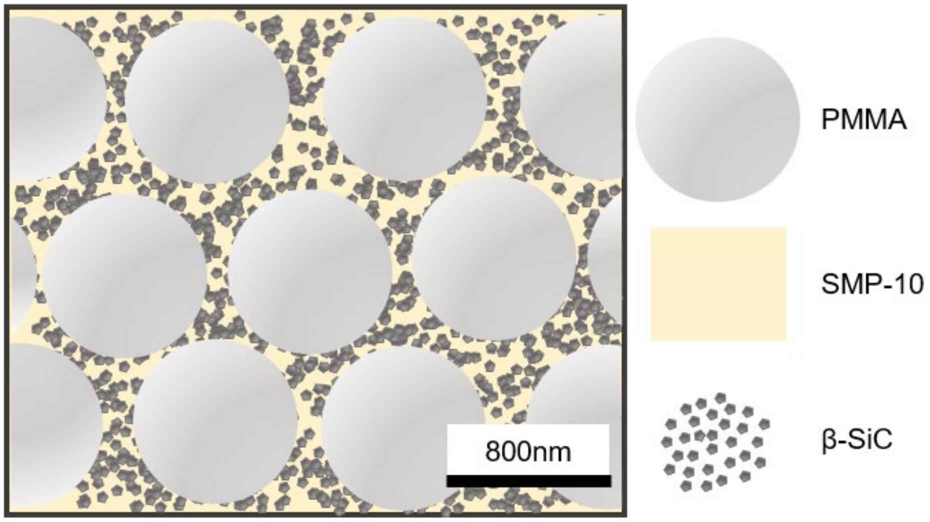

Figure 7. Illustration of the constituent materials used to synthesize SiC foams prior to pyrolysis and densification.

3.2.2 Differential Scanning Calorimetry and Thermogravimetric Analysis

As-received SMP-10, SMP-10 after ball milling, PMMA, SMP-10 + PMMA, SMP-10 + β-SiC, and SMP-10 + PMMA + β-SiC were characterized. All samples, aside from the as received SMP-10, were diluted in n-hexane, ball milled for 90 minutes, and the n-hexane removed by evaporation at ambient temperature. The material mixture ratios for each sample (i.e., SMP-10 was used in 1.2-parts to 2-parts PMMA and/or 1-part β-SiC) remained constant. The as-received SMP-

10 sample was not diluted in n-hexane in order to determine if n-hexane altered its cure or pyrolysis. The samples which were diluted in n-hexane were allowed to evaporate overnight in a fume hood. Approximately 50-150 mg portions of each "dried" sample were compressed to a pressure of 10 MPa into a 6.35 mm diameter pellet in a cylindrical steel die. The cold pressed samples were then placed in a 6.8 mm diameter (85µl, 99.7% purity) Al_2O_3 pan crucible with perforated lid to allow gasses, but not condensed material, to escape. The sample and crucible were then set in a model STA 449 F1 Jupiter DSC/TGA (Netzsch, Selb, Germany) for analysis. Samples were evaluated using a heating rate of 10 °C/min from room temperature to 1500°C under a constant argon flow. Scans were first performed with an empty crucible prior to each run, and the recorded background subtracted from the sample scan. DSC/TGA experiments were performed at least twice to ensure reproducibility and accuracy (2% uncertainty) of the collected curves.

3.2.3 Characterization

The internal structure of the specimens was examined with a Quanta 650 FEI-SEM scanning electron microscope (Thermo Scientific, Hillsboro, OR) operating in the secondary electron (SE) mode under high vacuum conditions. The average diameter of the PMMA powders was determined using ImageJ processing package, Fiji (84), on SEM images. A total of 150 individual powder particles were measured to determine the average diameter and the standard deviation.

The crystal structures of the SiC foam and its constituents were determined as a function of maximum processing temperature by X-ray diffraction using a PANalytical Empyrean (Malvern

PANalytical, Westborough, MA) instrument. The instrument was used in powder X-ray diffraction (XRD) mode using a Cu-K_α source and Bragg-Brentano optics combined with a reflection/transmission-spinner stage set-up for reflectance measurements. Data were collected at diffraction angles (2θ) of 20 to 95 ° at a rate of 0.12 °/s. Samples were spun at a rate of 0.25 rev/s to ensure an adequate sampling of grain orientation. XRD data were collected for high temperature processed pure SMP-10, SMP-10 and PMMA, SMP-10 and β-SiC, and SiC foams processed at 1200 ˚C, 1350 ˚C, and 1500 ˚C.

3.3 Results and Discussion

While the cure, pyrolysis and crystallizations reactions of SMP-10 have been reported (71,83), the influence of n-hexane mixing, and PMMA and β-SiC nanoscopic powder additions on the cure, pyrolysis, and crystallization behavior of SMP-10 have not been reported and are addressed here. The effect of crystallization temperature upon the foam topology and pore volume fraction are then investigated together with their effect upon the SiC foams mechanical properties in Chapter 4.

Samples of as received SMP-10, n-hexane diluted SMP-10, PMMA, SMP-10 + PMMA particles, SMP-10 + β-SiC particles and a complete SiC foam composition consisting of n-hexane diluted SMP-10 + β-SiC + PMMA particles have been examined. Table 1 lists the mass and volume fraction of SMP-10, PMMA, and β-SiC used for analysis.

The PMMA spheres used for templating porosity are shown in Figure 8. Using ImageJ analysis, 150 individual PMMA spheres were measured and their diameters were determined to be 0.793 nm ± 0.34 nm, as reported in Table 1. A transmission electron image and average diameter measurements for SiC nanoparticles were collected via ImageJ and analyzed at the Air Force Research Lab (85) and are presented in Figure 9. The average particle size was reported to be 47.9 nm; however, the mode was reported to be 25.5 nm. Particles in the 100-300 nm range were also reported, however, the majority of powders fell within the 20-60 nm range.

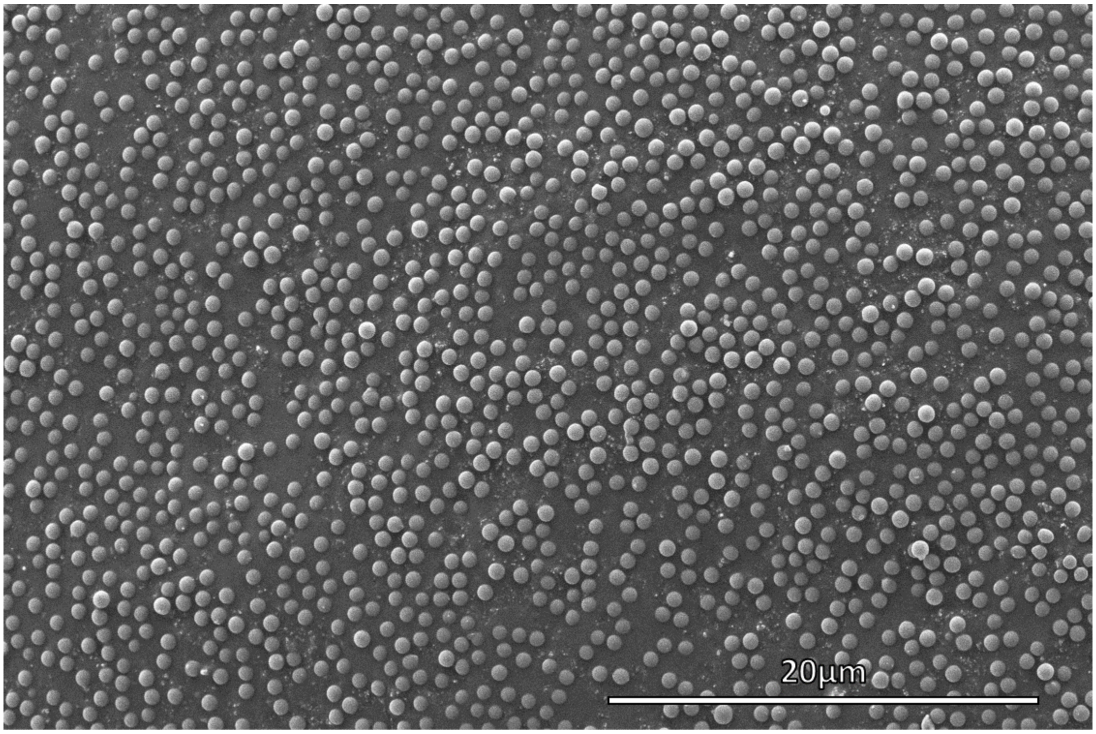

Figure 8. PMMA spheres used for sacrificial templating

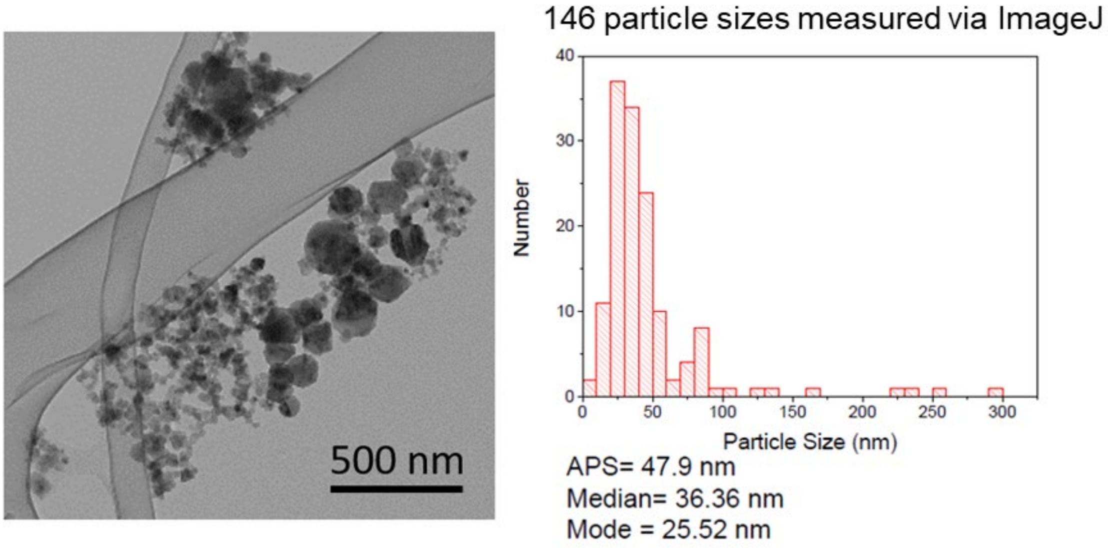

Figure 9. TEM images and ImageJ analysis of SiC nanoparticles collected by the Air Force Research Laboratory (85)

The internal structure after all three constituent materials had been mixed together using the n-hexane diluted ball mill approach, and then heated in an argon atmosphere to 1200°C, is shown in Figure 10. Figure 10 reveals a network of spherical pores where the ligament structure shows both granular and featureless regions; which are attributed to a high density of β-SiC powders and amorphous SiC formed during the pyrolysis of SMP-10, respectively. The presence of the PMMA remnants in each pore shown in the micrograph indicates an incomplete PMMA sphere decomposition had occurred. A TEM analysis of the PMMA remnants is presented later in this section. Further details on the heating schedule to form compression test specimens, a description of the bulk and internal structure, and the final processing temperature's effect on the mechanical performance of SiC synthesized foams are presented and discussed in Chapter 4.

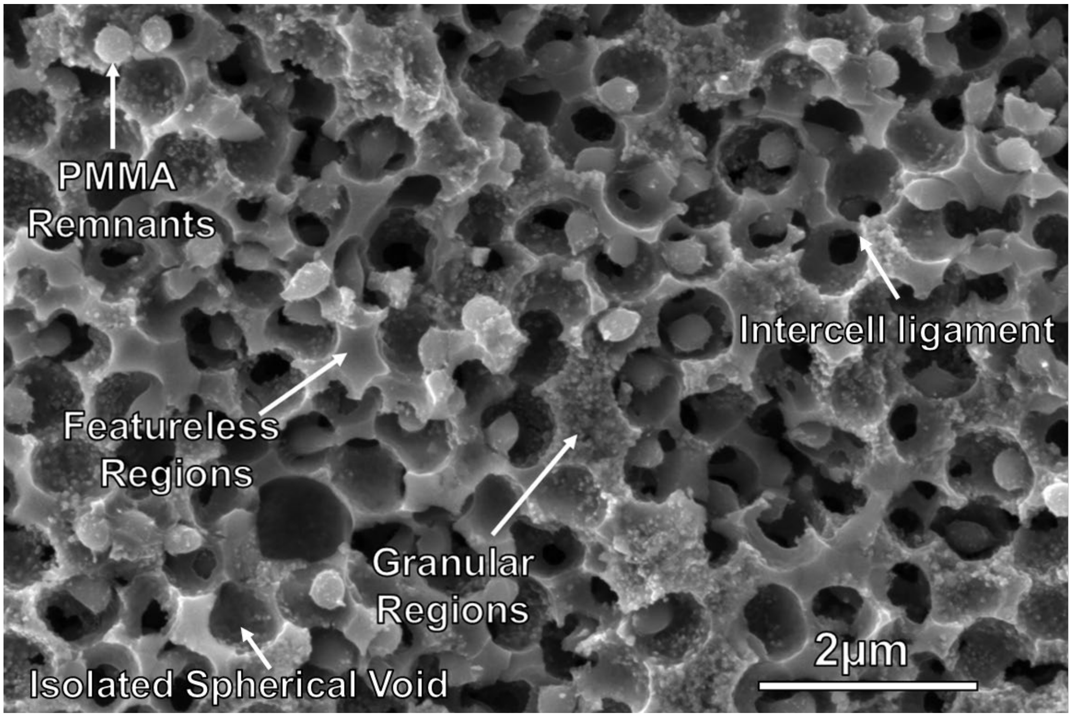

Figure 10. SEM image of SiC foams fabricated using SMP-10, PMMA, and β-SiC particles processed at 1200 °C.

3.3.1 Constituent Material Interactions

To investigate potential interactions between constituents during the synthesis of the SiC foam, the temperature derivative of weight loss and heat release are shown as a function of temperature during constant rate heating (at 10 °C/min) to 1500 °C in Figure 11 for (a) the as received SMP-

10, (b) SMP-10 ball milled in n-hexane, (c) the PMMA spheres, (d) a mixture of 2 parts (by mass) PMMA spheres immersed in 1.2 parts SMP-10, (e) 1 part β-SiC immersed in 1.2 parts (by mass) SMP-10 and (f) the complete material system used to synthesize the SiC foam consisting of 2 parts PMMA, 1 part β-SiC, and 1.2 parts SMP-10 (all by mass).

Figure 12 shows the measured mass loss verses temperature for each of the system components to identify changes to the processing response of the system as each component material was added to the n-hexane modified SMP-10. To identify potential interactions between the components during cure, pyrolysis and crystallization, Figure 12 also compares the measured mass loss with that predicted from a rule of mixtures (ROM) prediction of the component material weight losses using the mass fractions identified in Table 1.

SMP-10 and effect of n-hexane treatment: As the as-received SMP-10 preceramic polymer was cured, underwent pyrolysis, and then crystallized, a weight loss of approximately 34 wt% was observed after heating to a temperature of 1500 °C, Figure 12 (a). The loss of mass began at approximately 140 °C, consistent with previous reports of SMP-10 cure (86). Mass loss continued at a high, approximately constant rate to a temperature of 235 °C, whereupon the rate of mass loss slowed upon further heating to ~400 °C, Figure 11 (a). A second smaller mass loss rate peak was observed at 450 °C, consistent with the literature (87), while thereafter the rate of mass continued to decrease as the temperature was increased to approximately 1000 °C. Further heating to 1500 °C resulted in almost no additional mass loss (the change of mass was <1 wt%), Figure 12 (a). The observed mass loss for the as-received SMP-10 is very similar to that previously reported for the this PCP (55,69,71,86–90). By comparing the TGA results in Figure 11 (a) and (b) and those for the as received SMP-10 and n-hexane treated SMP-10 in Figure 12 (a), it is evident that dispersing SMP-10 in n-hexane followed by ball milling and n-hexane removal had no detectable effect upon the mass change behavior of SMP-10.

The DSC data collected during the heating of the as-received SMP-10, Figure 11 (a), indicated the presence of three heat release peaks at temperatures of approximately 235 °C, 450 °C and 1,050 °C labeled [1], [2] and [3] respectively. Comparing Figure 11 (a) and (b) it is evident that both samples behave similarly to previously reported results for SMP-10 (86,87,91). It is therefore concluded that dispersing SMP-10 in n-hexane followed by ball milling and then removal of the n-hexane by evaporation had no effect upon the subsequent thermal decomposition processes transforming SMP-10 to SiC.

PMMA decomposition: Thermal decomposition of PMMA is believed to proceed by the thermally activated release of the methyl methacrylate (MMA) monomer (92). The PMMA microsphere TGA data, Figure 12 (a), indicates that this grade of PMMA began to decompose at a temperature of approximately 200 °C for the heating rate of 10 °C/min used here. Once the temperature had risen to approximately 450 °C, mass loss ceased since the PMMA had almost fully decomposed leaving approximately 1 wt% carbon residue. This PMMA residue was progressively lost during further heating to 1500 °C. The mass loss rate data in Figure 11 (c) shows that the rate of decomposition for this grade of PMMA exhibited two temperature peaks with the first at 275 °C, followed by a small drop-in mass loss rate before attainment of a maximum weight loss rate at 350 °C.

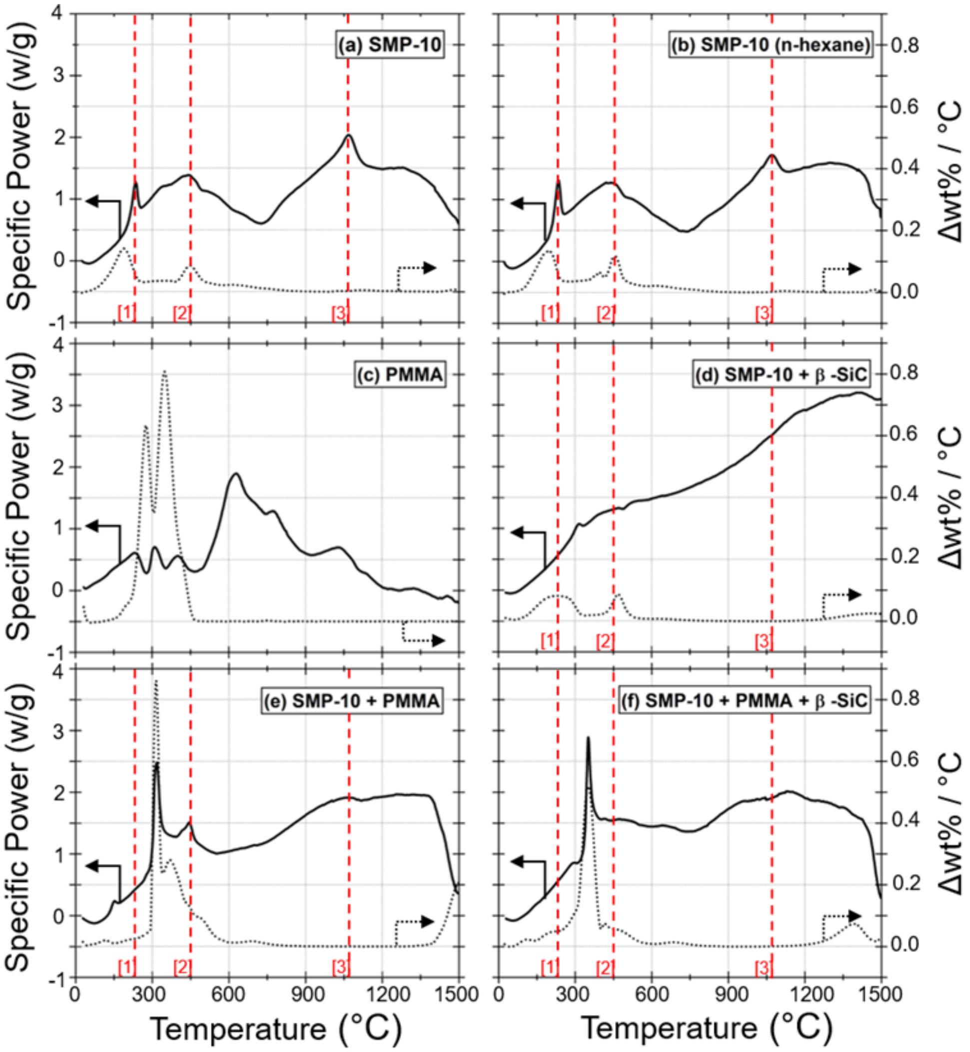

Figure 11. First derivative of weight loss and thermal power emitted versus temperature during heating of (a) as received SMP-10, (b) SMP-10 ball milled in n-hexane, (c) PMMA microspheres, (d) ball milled SMP-10 + PMMA, (e) ball milled SMP-10 + β-SiC, and (f) ball milled SMP-10 + PMMA + β-SiC. Positive values for specific power indicate exothermic behavior. The red dotted lines in (a) (b), (d), and (f) correspond to the rise in heat release due to [1] hydrosilylation, [2] hyperbranched polymer formation, and [3] atomic reordering.

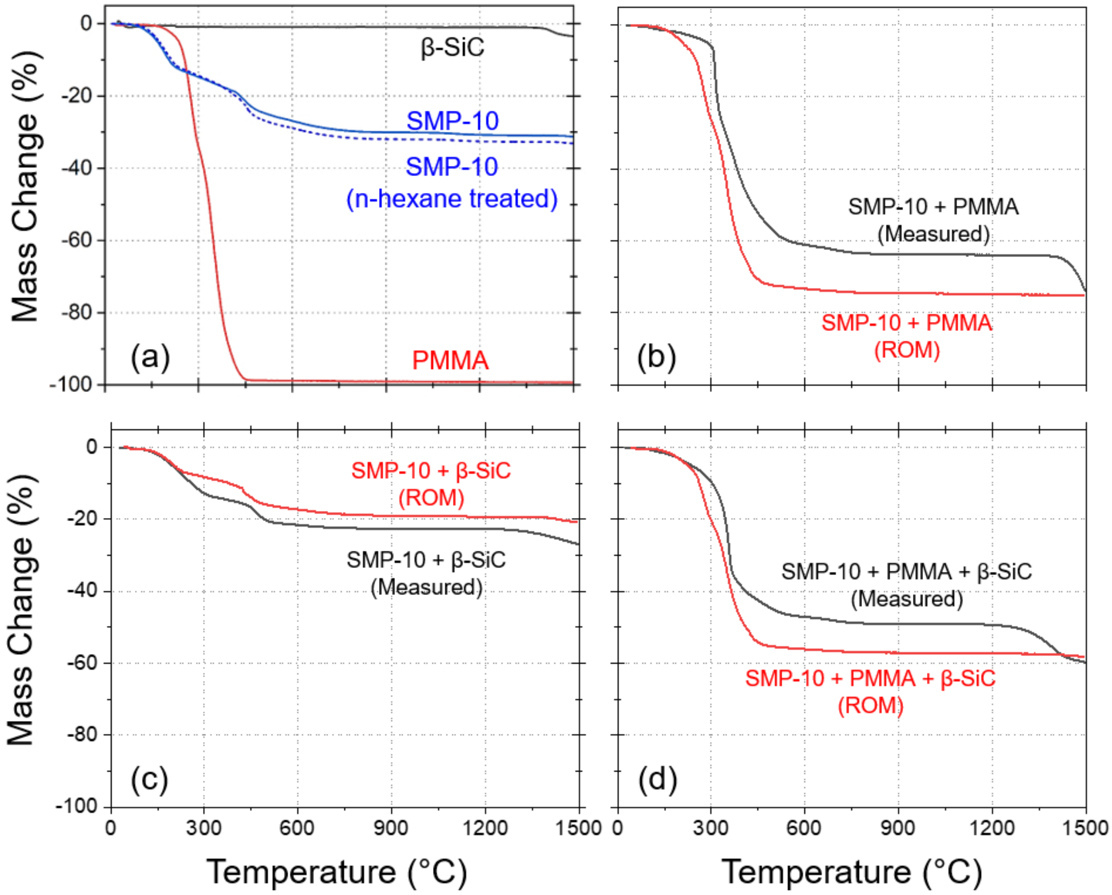

Figure 12. Measured TGA curves of individual constituents. b) Comparison of deduced TGA curves for SMP-10 + PMMA (black) with measured values (red). c) Comparison of deduced TGA curves for SMP-10 + β-SiC (black) with measured values (red). d) Comparison of deduce

The DSC data for PMMA decomposition shown in Figure 11 (c) reveal the presence of three weak exothermic peaks at temperatures in the regime of maximum mass loss. Decomposition of PMMA occurs by depolymerization and thermal decrosslinking (or unzipping) which are both endothermic in nature (93–95), therefore these peaks are attributed to oxidation reactions since the

PMMA particles were not pre-dried. A larger exothermic peak was observed during PMMA heating between 460 °C and 1200 °C, and is tentatively assigned to re-arrangement of the carbon residue atomic structure, and its reaction with trace levels of oxygen in the furnace environment to form CO (g) (95). These observations indicate PMMA to be a promising space holding powder since the onset of its decomposition (~200 °C) occurs after the start of SMP-10 cure (83,87), allowing the SMP-10 to stiffen and retain the PMMA defined pore shape as the system is converted to a solid.

SMP-10 plus PMMA: Figure 11 (e) shows the weight loss rate and DSC results for the decomposition of a mixture of SMP-10 and PMMA with mass fractions given in Table 1. Figure 12 (a) compares the mass loss for PMMA and SMP-10 when decomposed separately while Figure 12 (b) shows the mass loss of the mixture predicted by rule of mixtures behavior. Figure 12 (b) compares the expected mass loss with that measured result, and reveals an upward shift in the temperature for onset of rapid PMMA decomposition from approximately 200 °C to 300 °C, and a significantly delayed weight loss until the temperature exceeded 1350 °C. These observations are indicative of an interaction between the decomposition products of PMMA and SMP-10 beginning at a temperature of about 400 °C and only ending after heating 1500 °C. The total weight loss after heating the mixture to 600 °C was approximately 62 wt% compared to the ROM prediction of ~70%. Further heating to 1350 °C resulted in little additional mass loss, consistent with the behavior of the two-component materials Figure 12 (a). However, heating to 1350 °C initiated further loss of mass from ~62 wt% to 72 wt% as the temperature increased to 1500 °C.

This response was not evident in the response of either the SMP-10 or the PMMA. The total mass loss after heating to 1500 °C was approximately equal to the ROM estimate, Figure 12 (b).

Figure 11 (e) shows the DSC data for SMP-10 plus PMMA mixture, and by comparing it with that of the SMP-10 alone, Figure 11 (a), it indicated a shift in the first exothermic peak (at position [1]) from a temperature of 235 °C to approximately 315 °C. This shift in the first SMP-10 decomposition peak can be clearly seen by comparing Figure 11 (a) and (e). The exothermic peak [2] seen at 450 °C and attributed to the crosslinking of SMP-10 was also present in the SMP-10 plus PMMA system, but the decline in power following the peak was reduced in the presence of PMMA. The thermal power of the mixture also remained higher than in the SMP-10 as the temperature was increased to 1350 °C consistent with an interaction between the decomposition products of the two components. Figure 11 (e) also shows that mass loss above 1350 °C and corresponding reduction in exothermic power of the mixture compared to SMP-10 was observed indicative of endothermic decomposition processes.

SMP-10 plus SiC particles: Figure 12 (d) shows the response of SMP-10 containing β-SiC nanoparticles. After heating to a temperature of 1200 °C, SMP-10 containing β-SiC had undergone a weight loss of approximately 22%. The TGA data for β-SiC nanoparticles, Figure 12 (a), indicates a 1% weight loss up to a temperature of approximately 200 °C with no further mass loss until the temperature reached approximately 1350 °C. When the TGA data of the SMP-10 + β-SiC system was compared with that of the ROM prediction, Figure 12 (c), the mass losses were within the experimental uncertainty of the measurements. The rate of mass loss of SMP-10 and SMP-10 with β-SiC was almost identical other than a small increase in mass loss rate above 1250 °C for the mixture, Figure 12 (d).

Figure 11 (d) shows that the DSC data for the SiC particle loaded SMP-10 differed substantially from that of SMP-10 alone, Figure 11 (a). The exothermic peak [1] was shifted in temperature from 235 °C to approximately 315 °C. The reduction of power thereafter observed between 350 and 750 °C (i.e., between peak [2] at 450 °C and peak [3] at 1050 °C) for as-received SMP-10 was not observed in the presence of SiC particles. Indeed, when SiC particles were added, Figure 11 (d), a progressive increase in the exothermic power was observed during heating to approximately 1350 °C, consistent with SiC particle surface induced increase of the amorphous to crystalline SiC transition rate in the SiC particle loaded system. The plateau and slight decrease in heat release above 1350 °C coincided with an increase in mass loss rate and is likely a result of the carbothermal reduction of silica that was expected to be present as the native oxide on the β-SiC particles (96).

Full system response: The DSC/TGA analysis of the SMP-10, PMMA and β-SiC nanoparticles system used to make the SiC foams is shown in Figure 11 (f) and Figure 12 (d), and was similar to that of the SMP-10 plus PMMA system, Figure 11 (d). The onset of weight loss began at approximately 150 °C and reached a maximum weight loss rate at 360 °C, Figure 11 (f), resulting from a combination of PMMA decomposition and SMP-10 cure and pyrolysis. There is a large retention of mass in the measured sample between 300 °C and 1200 °C of approximately 10%, Figure 12 (d). The PMMA remnants, the cause of the lower mass loss, are shown in Figure

10. The majority of mass loss occurred during heating to 600 °C, at which point the mass had decreased by 48%. No further mass loss occurred until the temperature reached 1300 °C, whereupon an additional mass loss of 11% was observed. The addition of the SiC particles to the SMP-10 and PMMA mixture reduced the mass loss from 72% for SMP-10 plus PMMA, Figure 12 (b) to 61% because of the reduced mass fraction of PMMA and SMP-10 in the system, Figure 12 (d). Figure 12 (d) shows that once again, the measured loss of mass during decomposition and crystallization below 1350 °C was slightly less than the ROM prediction; consistent with an interaction between PMMA and SMP-10 decomposition products.

The DSC response of the full system, Figure 11 (f), was similar to that of SMP-10 with PMMA, Figure 11 (e). The higher exothermic reaction rate of the full system below 900 °C compared to that of SMP-10 and PMMA is attributed to β-SiC particle surface induced reaction. The reduction in specific power above 1400 °C was again evident with the full system and coincided with loss of the mass associated with the SMP-10 – PMMA interaction, consistent with the carbothermal reduction of silica introduced into the system by water vapor and the native oxide of the SiC particles (97).

TEM images, Figure 13, were collected and analyzed via EDS on a sample processed at 1250 °C to investigate the Si, O, and C amounts in parts of the sample, including 1) areas where β-SiC particles were present, 2) the remnant region of PMMA and 3) the crystallized SMP-10 matrix. It should be noted that the amount of Si-O-C in the sample revealed by EDS is qualitative and high levels of carbon are expected from TEM and FIB contamination (98,99). When comparing relative amounts of Si-O-C it is seen that the lowest amount of Si and highest amount of C is found on the PMMA remnant while the highest amount of Si and lowest amount of C is found on the β-SiC particle inclusions. It should be noted that the O and Si amounts in the PMMA remnants are about the same; therefore, the marker for O overlaps with that of the Si. Although this is a qualitative measurement, it is expected that the regions where PMMA had occupied would have carbon or char after decomposition and is confirmed by the 1 wt% yield shown by the TGA in Figure 12 (a). Furthermore, the presence of Si in the PMMA remnant implies an interaction between PMMA and SMP-10 during the decomposition process leaving behind a non-loadbearing Si-O-C particle.

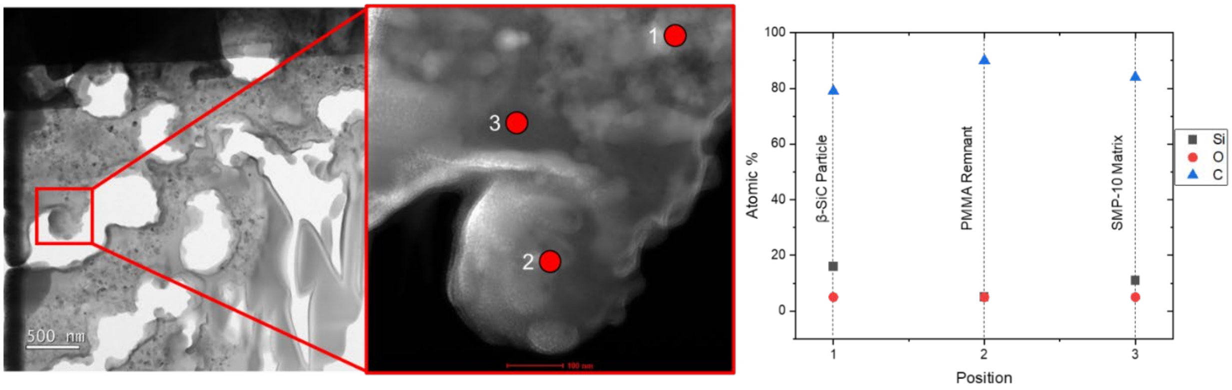

Figure 13. TEM images and EDS data on a sample processed to 1250 °C showing 1) β-SiC particle, 2) PMMA remnant, and 3) SMP-10 matrix. (Data collected by Eric Hogland, UVA).

3.3.2 Crystal Structure Changes

XRD patterns for the as-received SMP-10, SMP-10 with PMMA, SMP-10 with β-SiC and the SiC foams as a function of maximum processing temperature are shown in Figure 14 for maximum processing temperatures of 1200 °C, 1350 °C, and 1500 °C. Each scan is normalized by the height of the most intense peak and the background has been subtracted. The raw XRD data and normalized data (with background included) for the as received SMP-10, SMP-10 with PMMA, and the SiC foams are shown in Figure 15 for maximum processing temperatures of 1200 °C, 1350 °C, and 1500 °C. The XRD patterns for SMP-10 are consistent with recent observations of Poerschke et al. (71) who conducted similar studies of SMP-10. Following heating to 1200 °C, the XRD pattern for SMP-10 showed three broad peaks, Figure 14 (a), consistent with the (111), (220) and (311) reflections of β-SiC. Furthermore, XRD patterns for all three temperatures show an amorphous onset peak before 30°, revealing a degree of crystalline and amorphous material present at all temperatures, Figure 15 (a) and (d). After heating to 1350 °C, the onset of a β-SiC (200) peak can be seen. Following heating to 1500 °C, the β-SiC (111), (220), and (311) peaks had all sharpened considerably. The sharpening of the β-SiC peaks as the temperature was increased is consistent with the Poerschke et. al. (71) observation of the SiC crystallite size doubling (from ~3nm to 6 nm) as SMP-10 was heated from 1200 to 1500 °C.

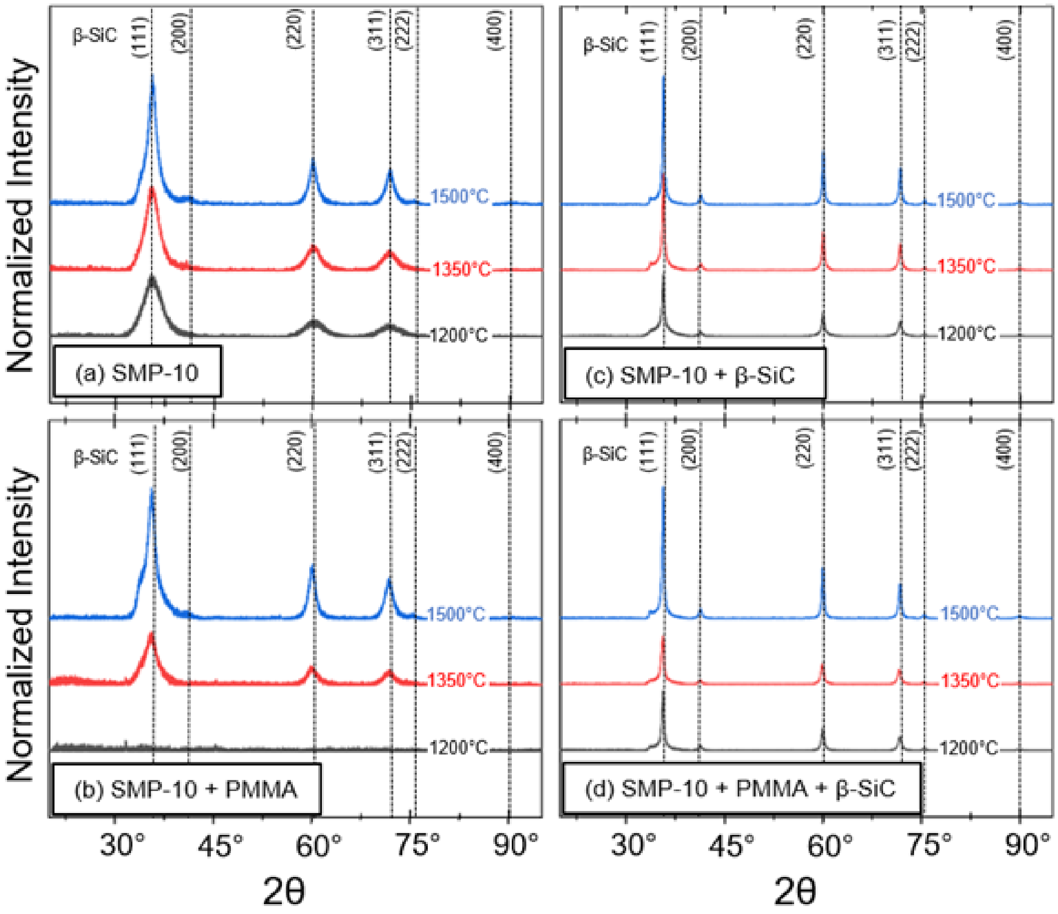

Figure 14. Normalized XRD patterns with background subtracted for (a) SMP-10 and (b) SMP-10 + PMMA, (c) SMP-10 + β-SiC, and (d) SMP-10 + PMMA + β-SiC after processing at crystallization temperatures of 1200°, 1350° and 1500°C. The β-SiC XRD peak position are also indicated.

Comparison of Figure 14 (a) and (b) shows that the addition of PMMA to SMP-10 had a substantial effect on crystallization behavior at 1200 °C. The XRD pattern of the SMP-10 + PMMA showed no evidence of crystalline β-SiC while the SMP-10 alone, heated to the same temperature, Figure 14 (a), showed β-SiC formation. Similarly, in Figure 15 (b) and (e) it is shown that at 1200 °C, there are no crystalline peaks observed, however this is a large amorphous background observed. This amorphous peak is commonly observed for both amorphous SiO_2 and amorphous carbon. It was shown that there are remnant PMMA (carbon containing) particles within the foam structure and likely have had their decomposition products react with SMP-10 suppressing the formation of SiC, a known interaction of free carbon and preceramic polymers (100–102). The SMP-10 + PMMA system only began to crystallize as the processing temperature was raised above 1200 °C, providing additional evidence of an interaction between the decomposition products of these two materials. Figure 14 (b) shows that only after increasing the processing temperature to 1350 °C, did the emergence of the β-SiC (111), (220), and (311) peaks found in the pure SMP-10 system begin to appear; although their signal was weak as shown in Figure 15 (b) and (e). When the SMP-10 + PMMA system was heated to a final temperature of 1500 °C, the β-phase SiC (111), (220), and (311) peaks sharpened considerably, and the amorphous contribution to the scattering had disappeared. The XRD pattern was then almost identical to that of the SMP-10, Figure 14 (a), containing strong β-SiC (200) and (222) peaks.

The addition of β-SiC nanoparticle to SMP-10 and to the SMP-10 + PMMA mixture resulted in XRD peaks dominated by the crystalline β-SiC at all temperatures, Figure 14 (c) and (d). As the processing temperature was increased, the width of the peaks decreased, consistent with crystallization of pyrolyzed SMP-10. The broad peaks seen in the SMP-10 system, Figure 14 (a), associated with gradual formation of β-SiC from an amorphous matrix were not observed because of the high intensity of the β-SiC nanoparticle x-ray scattering. It is shown that the signal of the amorphous peaks Figure 15, are considerably less intense than that of the β-SiC nanoparticles and can be determined to be buried beneath the signal.

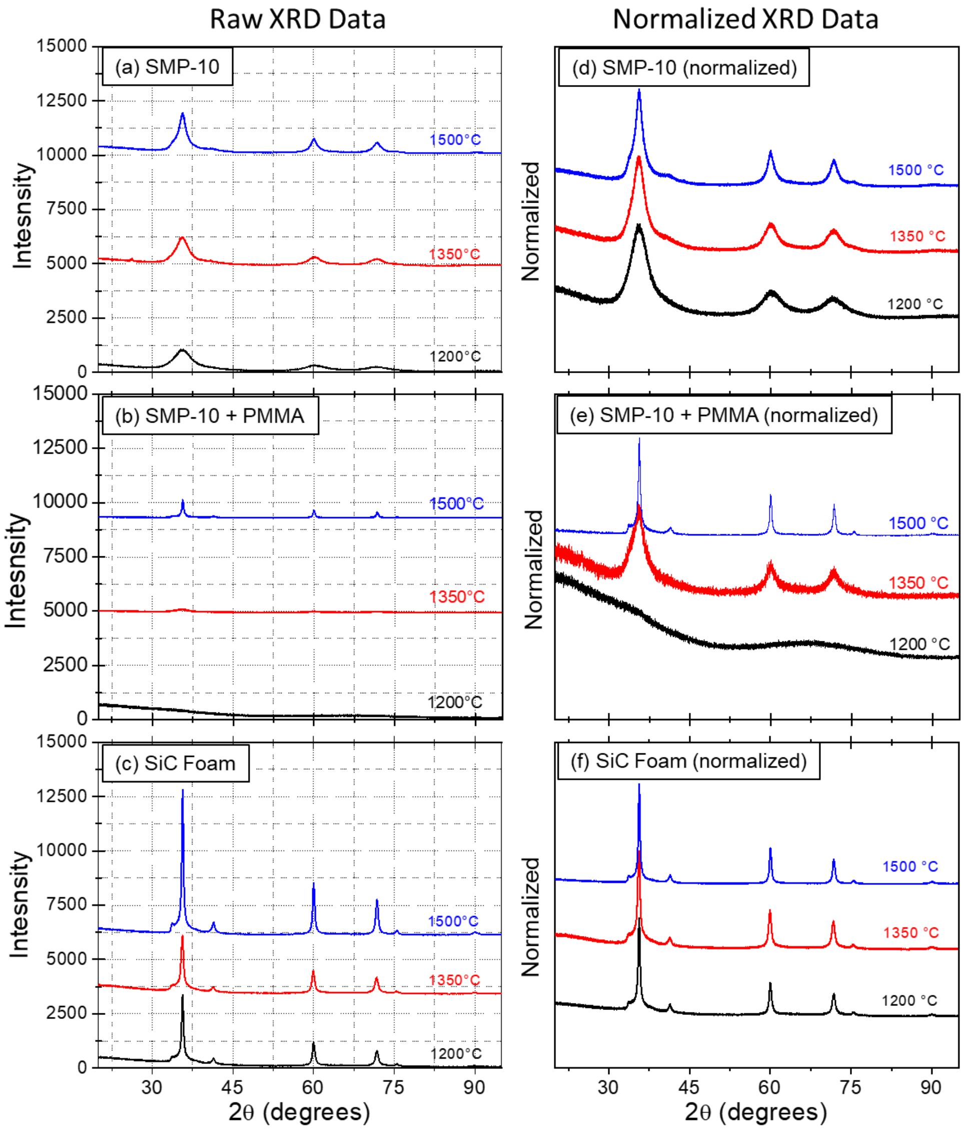

Figure 15. As collected XRD spectra for (a) SMP-10, (b) SMP-10 + PMMA, and (c) SiC foam with the respective normalized XRD shown in (d), (e), and (f). Background subtraction was not conducted.

3.3.3 Synopsis of decomposition process

Silicon carbide (SiC) foams suitable for mechanical property assessments with an average pore diameter of 700 nm and 150 nm wide ligaments have been synthesized using spherical PMMA particle templating of a β-SiC nanoparticle loaded pre-ceramic polymer (StarPCS^{TM} SMP-10). This was achieved by dispersing the constituent materials in n-hexane which reduced the viscosity of the mixture enabling a more uniform distribution of PMMA, β-SiC, and SMP-10 than achieved in the past (55). The effects of this processing approach upon the cure, pyrolysis and crystallization of the mixture was investigated and compared to the well-established processes responsible for conversion of SMP-10 to SiC (83,87,90).

PMMA appears well suited for use as a pore forming agent for SiC foams since it thermally decomposed in SMP-10 to form monomer vapor. This decomposition occurs at temperatures of between 300 and 450 °C which was above that for the onset SMP-10 cure (150-200 °C) but below the temperature at which the systems rigidity inhibited pore formation. Thus, as the mixture was heated, pores were formed by the increase in monomer vapor pressure simultaneously with the stiffening of the interpore webs and ligaments by SMP-10 cross linking. However, while the decomposition of PMMA alone resulted in almost complete mass loss by monomer evaporation below 400 °C, the inclusion of 800 nm diameter PMMA particles in β-SiC loaded SMP-10 resulted in retention of PMMA remnants with an average diameter of about 300 nm after processing to a temperature of 1200 °C, Figure 10 (b), and thus the retention of a significant non-load bearing mass. The presence of these remnant particles is consistent with the reaction of silicon containing

SMP-10 decomposition species with the decomposing PMMA particles resulting in the retention of a carbon rich particle.

Upon heating above ~1300 °C, the carbon-rich particles began to disappear, Figure 16, and the mass of the foam approached that expected using a rule of mixtures estimate of the mass all components, Figure 12 (b). Heating from 1200 °C was also accompanied by a delay in crystallization of a PMMA plus SMP-10 mixture, Figure 14 (b) compared to SMP-10 alone, Figure 14 (a). As PMMA decomposes and AHPCS undergoes pyrolysis, excess carbon is likely to have remained. This carbon is then available to interact with the small quantity of SiO_2 present in the system from the native oxide on SiC particles and reactions with residual oxygen during processing. These carbo-thermal reactions reduce silica to SiC and CO gas (103,104):

$$SiO_{2(s)} + 3C \rightarrow SiC_{(s)} + 2CO_{(g)} \tag{7}$$

The CO gas created in this reaction can then reduce residual SiO_2 to form SiC and CO_2 gas (103):

$$SiO_{2(s)} + 4CO_{(g)} \rightarrow SiC_{(s)} + 3CO_{2(g)} \tag{8}$$

Free carbon is also able to reduce silica by forming gas phase reaction products (103):

$$SiO_2 + C \rightarrow SiO_{(g)} + CO_{(g)} \tag{9}$$

The consequence of these endothermic reactions was evident Figure 11 (d) as a decrease in the exothermic power coincident with the observed weight loss as the maximum processing temperature was increased towards 1500 °C.

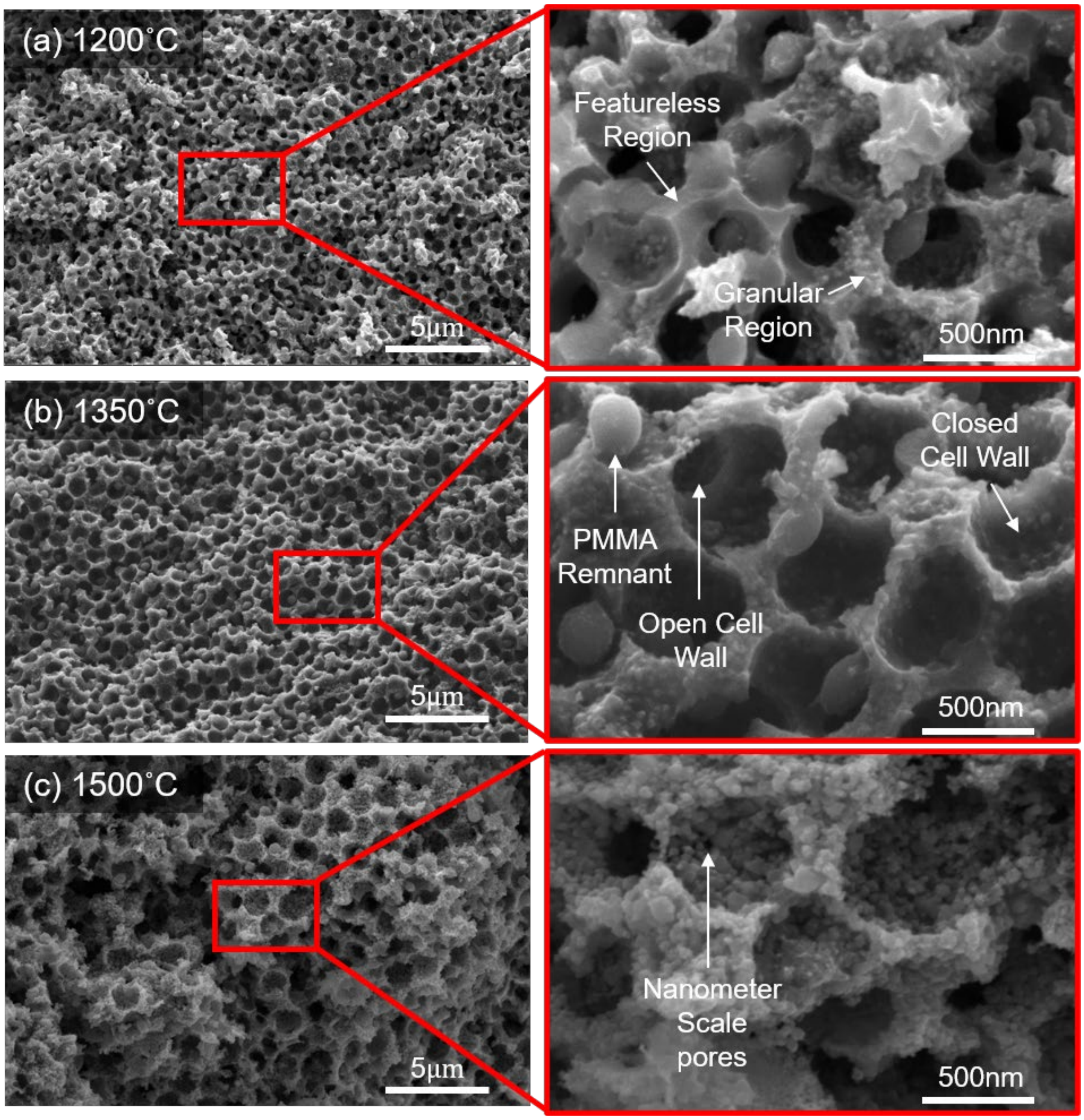

Figure 16. Secondary electron SEM images of SiC foam fractured surfaces crystallized at (a) 1200 ˚C, (b) 1350 ˚C and (c) 1500 ˚C

3.4 Conclusions

The presented study developed a deeper understanding of the synthesis of SiC foams made from PMMA sacrificial templating of PCS (SMP-10) with β-SiC nanopowder fillers. A new method for SiC foam synthesis has been developed utilizing n-hexane to dilute PCS prior to mixing with PMMA space holder powders and β-SiC nanoparticles.

1. Bulk SiC foams have been synthesized utilizing n-hexane diluted PCS mixed with PMMA space holder powders and β-SiC nanoparticles. The dilution method allows for evenly distributed submicron space holder powders, which was previously not achieved due to the increase of the mixture's viscosity for high surface to volume ratio of the PMMA spheres.
2. Crack free SiC foams were synthesized with pore fractions ranging from 0.5-0.6. By using 800 nm diameter PMMA particles, foams with regions of open and closed porosity were obtained with a cell diameter of 650 nm and interpore web thicknesses ranging from 50-300 nm.
3. TGA and DSC studies of the pure components used to make the foams indicated thermal decomposition of PMMA by methyl methacrylate monomer evaporation was completed before completion of the cure reactions of the SMP-10. However, when the two materials were combined, the PMMA decomposition process interacted with SMP-10 resulting in retention of excess carbon in the foam. Heating SiC foams containing excess carbon to temperatures above 1300 °C resulted in a gradual loss of mass consistent with carbothermal reductions of silica from passivation layers on the SiC nanoparticles and residual oxygen introduced during mixing of the system.
4. The inclusion of β-SiC nanoparticles leads to the weight loss at temperatures above 1200 °C due to reduction of the native oxide on the β-SiC nanoparticles. When the

crystal structure is investigated for various processing temperatures, the β-SiC XRD pattern dominates the signal due to the inclusion of β-SiC nanoparticles. Therefore, the observation of the pyrolyzed SMP-10 and SMP-10 + PMMA spectra is buried beneath the strong β-SiC signal.

The mass loss and identification of high temperature reactions in this chapter informed an appropriate heating schedule to mitigate rapid outgassing and therefore, reduce the effect of cracking during curing and pyrolysis. Chapter 4 investigates the effects of the final processing temperature ranging from 1200°C – 1500°C on the microstructure and mechanical properties. It is currently unknown what the consequence of these reactions are on the microstructure of the system as well as the mechanical performance.

Chapter 4: Mechanical Properties of SiC Foams

4.1 Introduction

The SiC foam synthesis method developed in Chapter 3 offers a promising novel approach for fabricating ceramic foams with submicron ligaments and, therefore, a possibility to increase the mechanical performance of ceramic foams. The results in Chapter 3 indicate that the final processing temperature significantly influenced the structure of the SiC foam. The influence of the high temperature crystallization process temperature upon the porous structure and its compressive elastic modulus and compressive strength are investigated here. The influence of the high temperature crystallization process temperature upon the foam structure and its mechanical properties are then investigated. To identify contributions to the foam modulus and strength by the foam density versus interpore ligament properties, micromechanical models for cellular foams (21,39) are fitted to the measured mechanical properties and used to indirectly infer the effect of the crystallization temperature upon the elastic modulus and strength of the SiC foams solid ligaments of the ceramic foams made via this approach.

4.2 Materials and Methods

The cellular foam samples intended for compressive testing were prepared by the mixing of 2-parts by weight PMMA to 1-part β-SiC to 1.2-parts preceramic polymer to 3-parts n-hexane. The mixtures were blended for 90 minutes using a SPEX high-speed ball mill, and the n-hexane solvent was then removed by evaporation at ambient temperature for 12 hours. This resulted in dry powder mixture with a uniform, random distribution of space holding particles. The dry powder was then placed in a cylindrical, 1 cm diameter stainless steel die and cold pressed to a pressure of 30 MPa resulting in a cylindrical sample with an approximate height of 2 cm, Figure 17. Chapter 3 developed an understanding of the temperatures at which reactions, and consequently, rapid mass loss occurs. This information was used to develop a heating schedule to produce bulk specimens for compression testing. Batches of these samples were subjected to the same initial cure and pyrolysis heating schedule, Figure 18. The cold pressed samples were placed in Al_2O_3 crucibles and loaded into a Verder Scientific Inc Carbolite LHGT 200-300/30-1G high temperature graphite furnace, Figure 19, equipped with an afterburner exhaust system. The chamber was initially evacuated to a pressure of 10^{-2} Pa, and then backfilled to a pressure of 0.1MPa with high purity argon (99.999% purity from PRAXAIR Danbury, CT). Once this pressure was achieved, a continuous flow of argon at a flow rate of 200 l/hour was established. Specimens were produced in which the final 2-hour high temperature region of the synthesis cycle (where crystallization occurs) was systematically varied from 1200˚C to 1500˚C in 50°C increments. The resulting SiC foam densities were calculated from their measured weight and dimensions with the uncertainty calculated as the standard deviation from the average density for each sample batch. An example of the SiC cylinders formed after heat treatment to 1200°C can be seen in Figure 17. The resulting cylinders are approximately 1 cm in diameter and 2 cm tall.

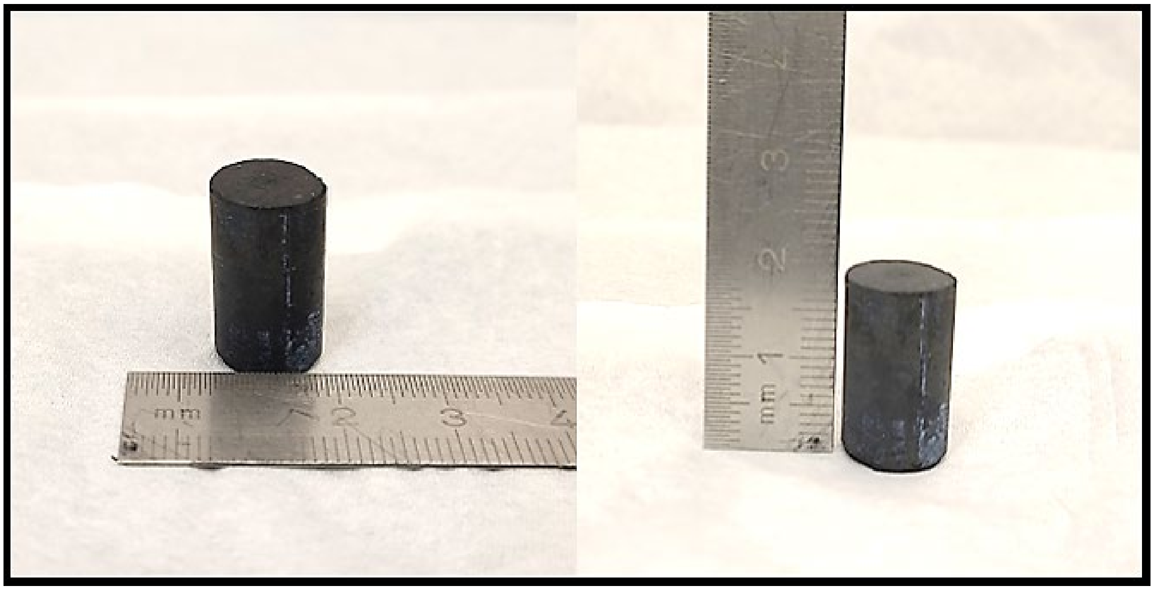

Figure 17. Bulk SiC specimens after final processing to 1200°C. The specimens have a diameter of approximately 1 cm and a height of approximately 2 cm.

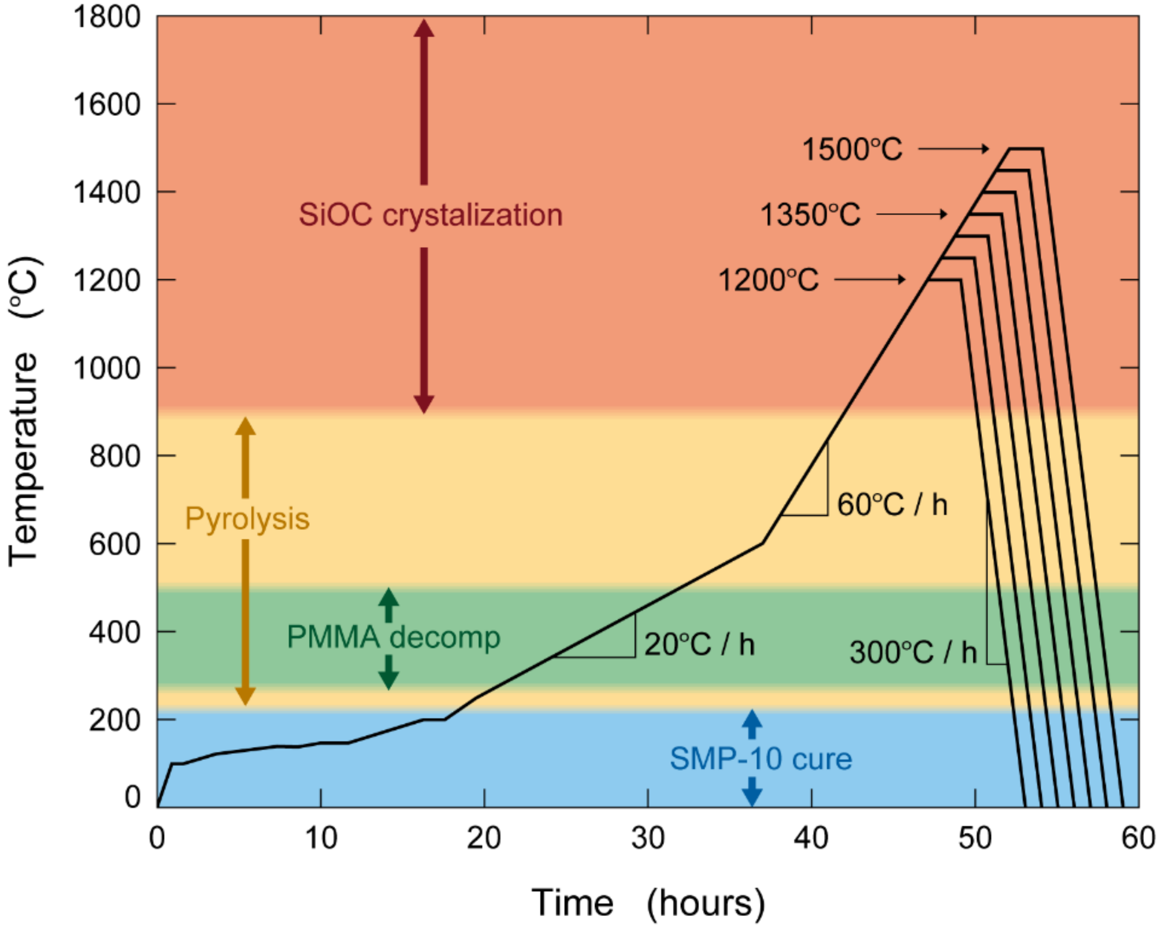

Figure 18. Thermal profiles used for SMP-10 curing, PMMA decomposition, pyrolysis, and crystallization of submicron pore diameter SiC foam. The samples were held for 2 hours at their highest processing temperature before cooling.

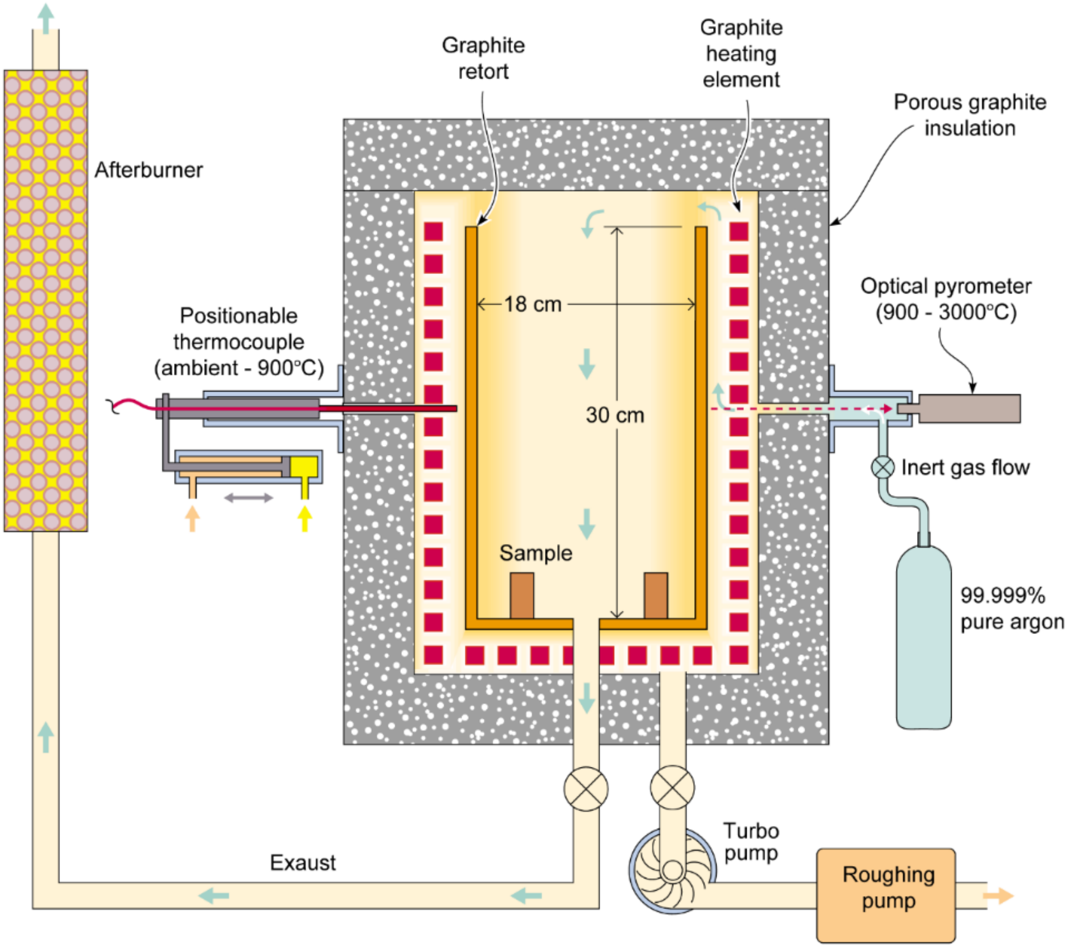

Figure 19. The high temperature graphite furnace used for PMMA burnout and pre-ceramic polymer cure, pyrolysis and crystallization

Quasi-static compression tests were conducted at room temperature (~26°C) on 4 - 6 specimens for each processing condition using an Instron model 5500R screw driven testing machine. The samples were positioned between two stainless steel blocks, Figure 20, compressed at a strain rate of 0.00667 /min and the load monitored using a 50kN load cell as the samples were compressed to failure. A LE model laser extensometer (EIR, Irwin, PA) was used to measure the axial displacement of the sample during compressive loading. Load/unloading cycles were used during the nominally elastic loading stage of the tests to obtain a reliable estimate for the Young's modulus. The uncertainty in compressive strength and Young's modulus was characterized by the standard deviation from the average value for each sample batch.

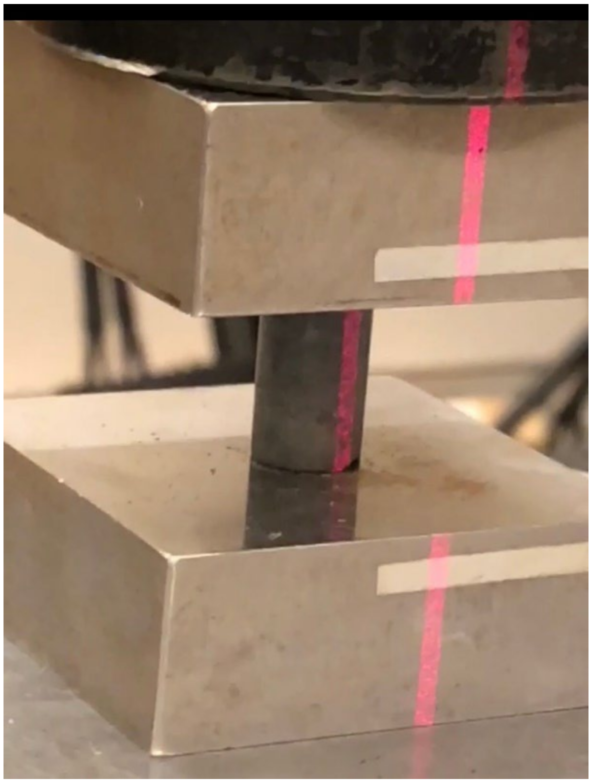

Figure 20. Experimental set up of quasistatic compression tests on bulk SiC foam specimens.

The pore volume fraction (ϕ) was determined from SEM images of samples that were diamond wafer blade sectioned and diamond grit polishing ending with a 0.05 µm diamond diameter particle suspension. Using ImageJ Fiji software package, twenty micrographs per sample, from 1200 °C to 1350 °C, were analyzed to deduce pore fractions, pore diameters, and their standard deviations. Pore volume fraction increased with temperature from 1200 °C to 1350 °C. Values for 1400 °C and 1450 °C were not collected due to the difficulty in polishing the brittle ligaments. The sectioned plane does not always cross the center of a pore and it is assumed that nearly spherical pores were sectioned between the pore equator and a latitude of approximately 45°. Therefore, 100 pores for each sample temperature were measured for statistical relevance and pore diameters remain within 650 ± 55 nm for the evaluated temperature range

The internal structure of the specimens was examined with a Quanta 650 FEI-SEM scanning electron microscope (Thermo Scientific, Hillsboro, OR) operating in the secondary electron (SE) mode under high vacuum conditions. Since the solid material density normally used to compute a cellular materials relative density was unknown, an ImageJ processing package, Fiji (84) was used to deduce the pore volume fraction (and thus relative density) from the pore area of SEM images using a minimum resolution of 8.4 nm per pixel.

4.3 Results

4.3.1 Density and Pore Topology Development

The density of the SiC foams as a function of processing temperature is summarized in Table 2, and is seen to have generally decreased with increase in processing temperature. After processing to 1200˚C, a density of 1,180 ± 30 kg·m^{-3} was measured and this decreased to 910 ± 10 kg·m-3 as the temperature was increased to 1450°C. The change in density with maximum processing temperature is graphically shown in Figure 21 (a). Between 1250 and 1300 °C a small increase in density was observed. This is attributed to the decrease in specimen volume (i.e. sintering (105)) prior to the acceleration of the high temperature weight loss observed in Figure 11 (e), which exceeded the rate of volume reduction (90).

Table 2. Processing temperature, sample diameter, density, and mechanical properties of SiC foams

Sample	Processing Temperature (°C)	Sample Diameter (mm)	Density (kg•m^{-3})	Young's Modulus (GPa)	Compressive Strength (MPa)
1	1200	10.95 ± .04	1,180 ± 30	13 ± 0.7	82 ± 12
2	1250	10.90 ± .02	1,100 ± 10	14 ± 0.8	99 ± 7
3	1300	10.84 ± .02	1,140 ± 10	15 ± 1.3	96 ± 11
4	1350	10.81 ± .03	1,050 ± 20	10 ± 2.2	52 ± 11
5	1400	10.80 ± .03	1,010 ± 20	8 ± 1.7	34 ± 5
6	1450	10.77 ± .02	910 ± 10	5 ± 0.8	26 ± 4

The pore structure can be seen in the fractured surface of a sample processed to 1200 °C, Figure 10. The surface is characteristic of a foam with spherical pores but in this case with interpore ligaments containing both featureless and granular regions. Small remnants of the PMMA particles were also present in many of the pores of SiC foams synthesized at temperatures of 1200 °C to 1350 °C, Figure 22. These micrographs reveal a relatively uniform distribution of porosity and regions of both closed, Figure 22 (a) and open (interconnected) pores, Figure 22 (b).

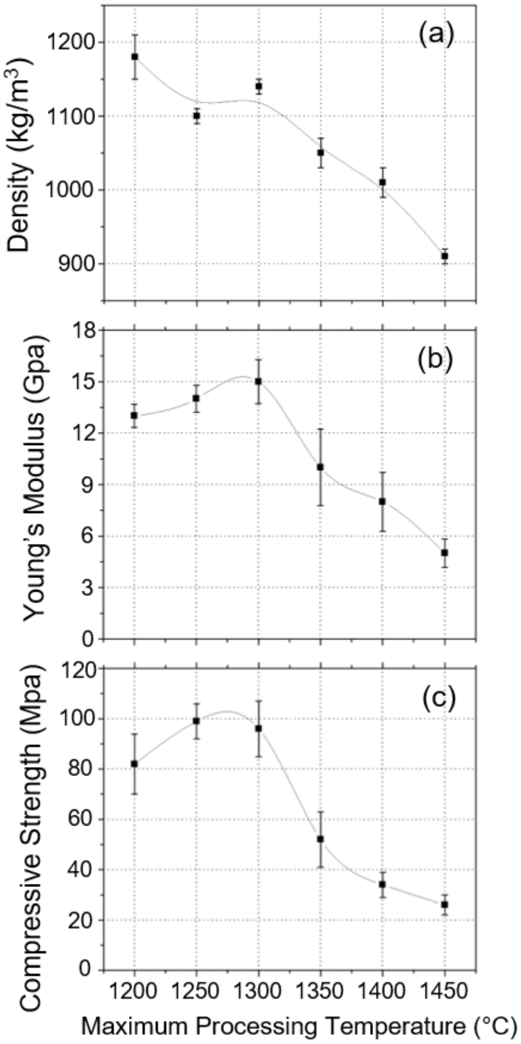

Figure 21. The effects of maximum processing temperature upon (a) the density, (b) Young's Modulus and (c) the compressive strength.

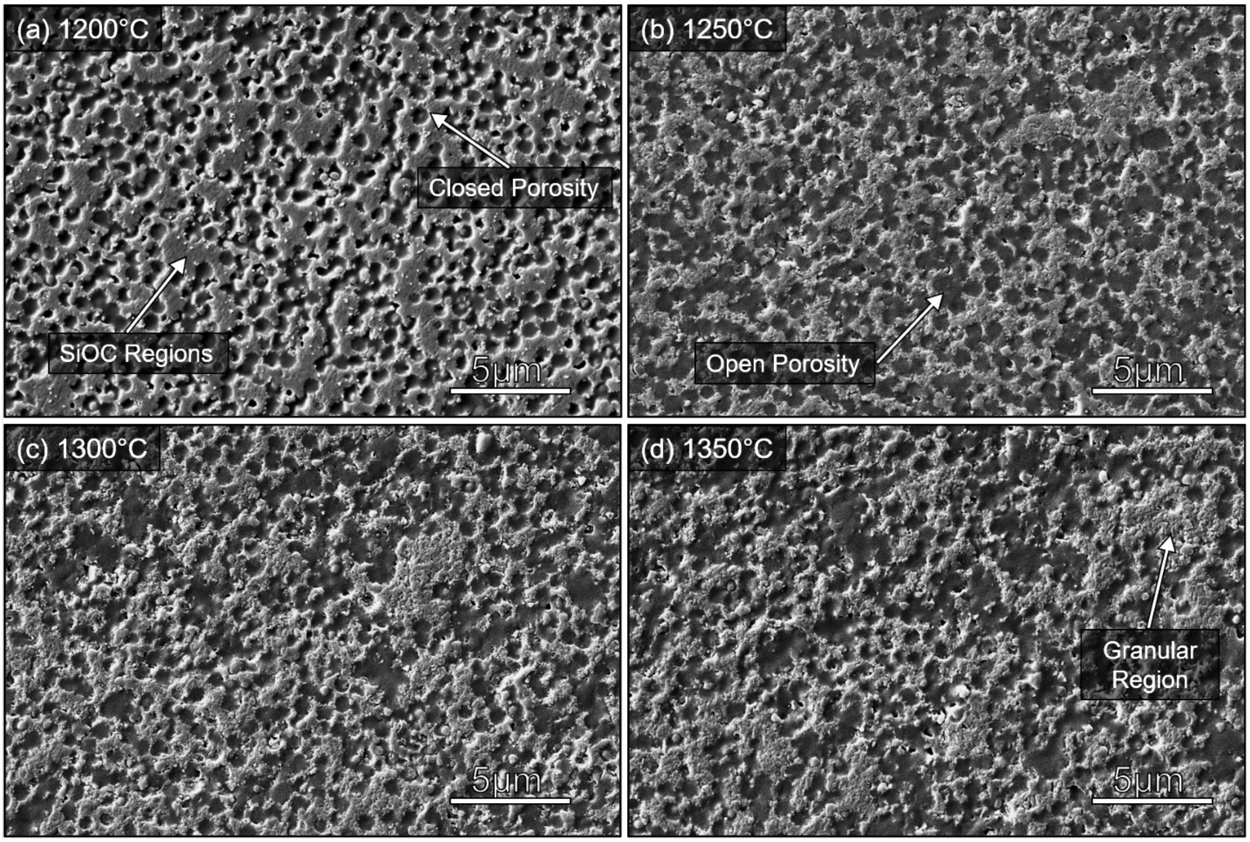

Figure 22. Cross-sectional image of SiC foam processed at (a) 1200°C, (b) 1250°C, (c) 1300°C and (d) 1350°C. As temperature is increased, SiC regions, shown in 17(a), transition to granular regions, shown in 17(d).

Figure 16 shows the fracture surface of samples heated to 1200, 1350 and 1500 °C. The higher magnification inset of Figure 16 (a) again shows that samples processed at 1200 °C, has interpore ligaments composed of both granular and featureless regions. The grain size of the granular features was less than 100 nm and is attributed to SMP-10 bonded β-SiC nanoparticles, while the featureless regions are consistent with amorphous SiC resulting from SMP-10 pyrolysis. As the processing temperature was raised first to 1350 °C, Figure 16 (b), and then 1500 °C, Figure 16 (c), the featureless regions gradually disappeared and were completely absent after processing at 1500 °C. This evolution was accompanied by the formation of nanometer scale pores between granular features within the ligaments and a reduction in the number of pores containing PMMA remnants. Measured pore fraction values obtained from Figure 22 are shown as a function of temperature and are tabulated in Table 3.

Table 3. Pore fractions and calculated solid material properties as a function of crystallization temperature.

	1200°C	1250°C	1300°C	1350°C
ϕ	0.50 ± 0.034	0.55 ± .024	0.55 ± 0.015	0.56 ± 0.026
Pore Diameter (nm)	647 ± 58	652 ± 52	648 ± 49	649 ± 48
ρ_s **(kg/m^3)**	2,370 ± 130	2,400 ± 100	2,520 ± 70	2,400 ± 120
E_s **(GPa)**	110 ± 20	150 ± 20	160 ± 10	120 ± 20
σ_s **(MPa)**	330 ± 40	470 ± 40	470 ± 30	270 ± 30

4.3.2 Mechanical Properties

Representative stress-strain curves can be seen for samples processed at maximum temperatures of 1200 °C, 1300 °C and 1400 °C in Figure 23. Initial load-up contains possible crushing of irregularities in the sample surface due to the interaction of the platens and the surface of the sample. The Young's modulus was measured after softening response and first unloading cycle to determine the elastic response upon loading, shown in Figure 24 for a sample processed at a max temperature of 1250 °C (highlighted in blue).The dependence of both Young's modulus and the compressive strength of the foams with the maximum processing temperature is shown in Figure 21 (b) and (c). The Young's modulus initially increased with increase in processing temperature to 1300 °C, but then decreased rapidly as the temperature was further increased to 1450 °C. The maximum Young's Modulus achieved after processing at 1300 °C was 15 GPa. The compressive strength followed a similar trend to that of the modulus with crystallization temperature, with a maximum strength of about 100 MPa observed after processing between 1250 °C and 1300 °C. As the processing temperature increased, the compressive strength decreased rapidly to less than 25 MPa after processing at 1450 °C. This trend of decreasing failure strength continued since attempts to measure the mechanical properties of samples crystallized at a temperature of 1500 °C were unsuccessful because the samples crumbled upon removal from the Al_2O_3 crucibles. Specimens processed at this temperature show cracking along the direction of compression, Figure 25.

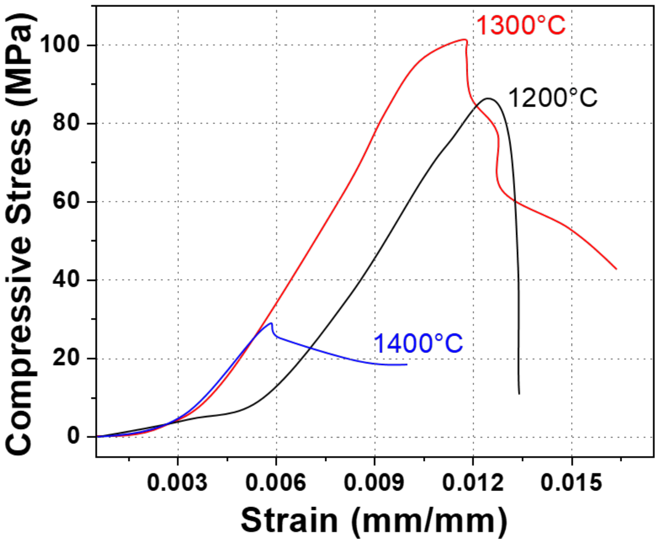

Figure 23. Representative stress-strain curves for samples processed at a maximum temperature of 1200 °C, 1300 °C, and 1400 °C.

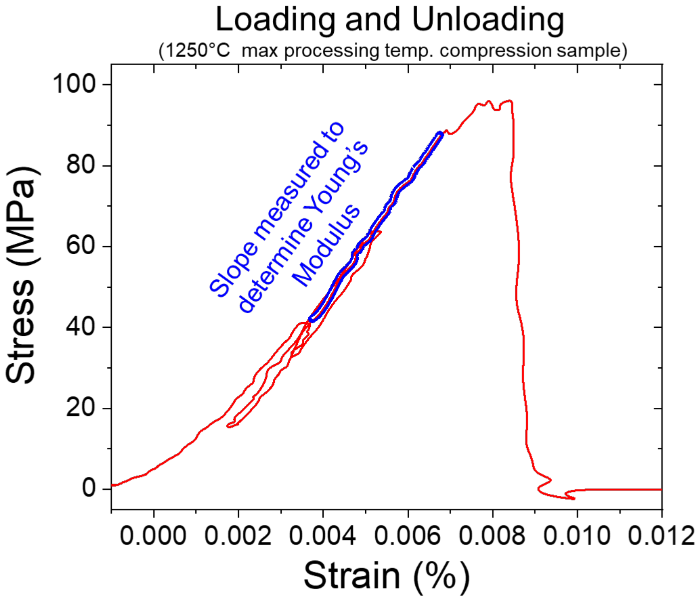

Figure 24. Representative loading and unloading curve for a sample processed at 1250 °C. The highlighted blue region shows where upon reload the slope was measured and thus Young's modulus was determined

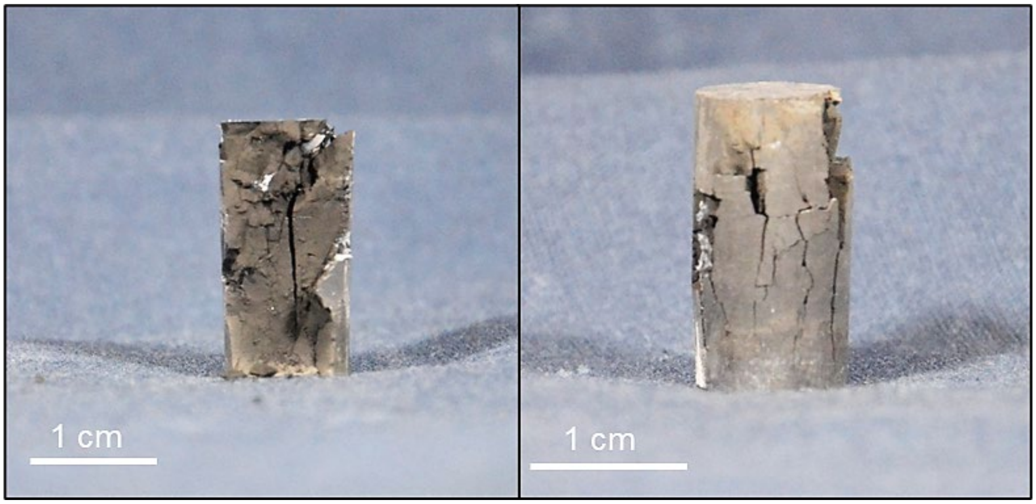

Figure 25. Test specimens (processed at a temperature of 1300 °C) after compressive failure.

4.4 Discussion

4.4.1 Foam Topology and Solid Ligament Properties

The results shown in Figure 21 indicate the existence of a complex relationship between the Young's modulus and compressive strength of the SiC foams, their density and the maximum temperature to which they were heated following pyrolysis of the pre-ceramic polymer. Figure 26 (a) and (b) plot the Young's modulus and compressive strength of the foams against their measured density, and reveals the presence of a peak in the modulus and strength versus density relationship after processing to a temperature of ~1300 °C. Micromechanical models (21,106) have been widely used to relate the elastic moduli and compressive strength of open and closed cell foams to cell topology, relative density, and to the properties of the solid material from which they are made (42). None predict the existence of a peak in modulus and strength as their density increases.

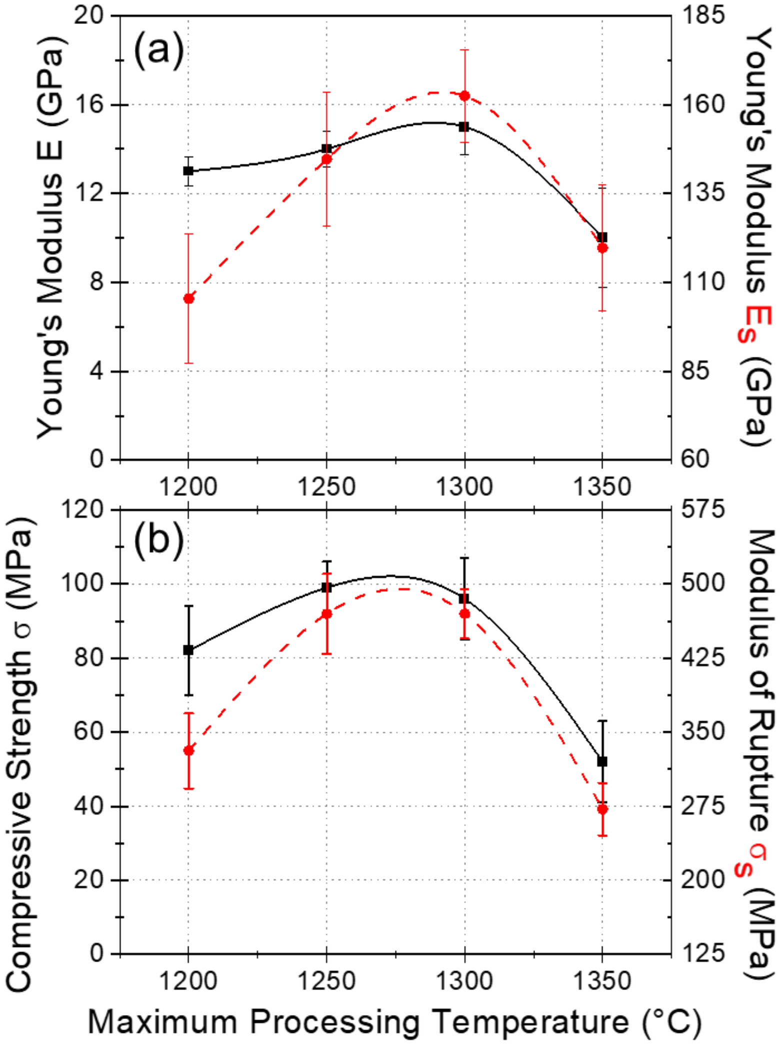

Figure 26. The calculated effect of maximum processing temperature on (a) the solid material Young's modulus (E_s) and (b) the solids compressive strength (σ_s) based foam models are also shown (red). The black lines in (a) and (b) compares these results with the trend for the measured values of the foam modulus and compression strength (Figure 21). Tabulated results are shown in Table 3.

Examination of the micrographs, Figure 22, indicted φ to be substantial but difficult to quantify, and so the membrane stress contributions are significant for foams made by the space holding approach used here, and thus the effective exponents in Equations 3 and 4 are reduced. However, direct comparisons between these micromechanical predictions and the measured foam properties are not possible since the solid moduli and moduli of rupture of the solid are unknown. Examination of Figure 10, Figure 16, and Figure 22 indicates that the SiC foams made via the PMMA templating approach had a random, near-uniform spherical porosity distribution with a mixture of open porosity and closed pores. The density, ρ of the foams is given by:

$$\rho = (1 - \phi)\rho_s \tag{10}$$

where ϕ is the pore volume fraction. The data in Table 3 indicate that the foam pore volume fraction varied weakly with maximum processing temperature ranging from 0.5 at 1200 °C to 0.58 at 1400 °C. Since ϕ is known, and the foam density, ρ has been measured, the density of the ligament or cell wall material can be determined from Equation 10, and is summarized in Table 3. It indicates that the cell wall density increased with processing temperature from 2,370 kg/m^3 after processing at 1200 °C, reached a maximum of 2,520 kg/m^3 after heating to a temperature of 1300 °C and then declined sharply with further increase of temperature to 1400 °C. Using the phase fraction data of Poerschke et al. (71), and sample mixing ratios of 1 β-SiC : 0.84 SMP-10 (based upon an initial mass fraction of 1.2 and mass yield of 70%), and assuming densities of 3,210 kg/m^3 for β-SiC and 2,550 kg/m^3 for Si(O)C (107), the expected solid density ρ_s would be in the range of 3,000 – 3,100 kg/m^3 over the processing temperature range explored here. The difference between the experimentally deduced and expected densities is consistent with the presence of porosity in the inter-pore ligaments, Figure 16 (c), and excess carbon from the PMMA particle decomposition contributing to the reduction in experimentally deduced density.

Colombo et al. (40,42) experimentally investigated the mechanical properties of SiC foams with similar topologies to those studied here i.e. foams consisting of regions of both open and closed porosity that were synthesized using the preceramic polymer -space holder approach. They empirically showed that the Young's moduli and compressive strengths of SiC foams made by the space holder approach were well fitted by Equations (5) and (6). Assuming the foams made here were similar to those studied by Colombo et al (40), Equations (5) and (6) can be used to obtain estimates for the Young's modulus, E_s and the modulus of rupture, σ_s of the solid SiC with the later determined by the defect population of the cell walls. The resulting values for solid material properties as a function of maximum processing temperature are summarized in Table 3.

Solid ligament material Young's moduli, E_s, and compressive strengths, σ_S were deduced by using a combination of Equations (10) with Equations (5) and (6). Since the foam modulus, *E,* strength, σ and pore fraction, ϕ are known, the Young's modulus, E_s and modulus of rupture, σ_S of the solid ligaments can be deduced from these values by using the following equations:

$$E_S = \frac{\mathrm{E}}{\left(\frac{\rho}{\rho - \phi}\right)^n} = E\left(\frac{1}{1-\phi}\right)^{-n} \tag{11}$$

$$\sigma_S = \frac{\sigma}{\left(\frac{\rho}{\rho - \phi}\right)^m} = \sigma\left(\frac{1}{1-\phi}\right)^{-m} \qquad (12)$$

where $n=3$ and $m=2$ (21,42,108). The uncertainty in measured pore fraction (ϕ) was used to calculate an uncertainty for the Young's modulus, E_s and modulus of rupture, σ_S of the solid ligaments. This as an inferred measurement of the solid ligament properties deduced by comparing the foam properties to the model, and is only as good as the model's applicability to the foam. It is used only as a means to estimate the Young's modulus and modulus of rupture trends for the solid ligaments as a function of maximum processing temperature.

Figure 26 plots the measured Young's modulus, E and strength, σ of the foams as a function of maximum processing temperature together with the deduced solid ligament modulus, E_s and modulus of rupture, σ_s inferred via Equations 11 and 12. The solid ligament Young's modulus varied from 87-160 GPa with processing temperature, Figure 26 (a) while the modulus of rupture lay between 275-470 MPa. In both cases the maximum values were obtained after processing at 1300 °C; similar to a trend previously reported for SMP-10 derived materials (75,76). However, both E_s and σ_s decreased rapidly with process temperature as the maximum processing temperature was increased beyond 1300°C.

Since the primary pore volume fraction varied weakly with processing temperature, two competing temperature dependent phenomena appear to have been responsible for the existence of the peak in mechanical properties. As the processing temperature increased towards 1300 °C, the solid ligament density increased due to crystallization of the SMP-10 (90), and resulted in an increase ligament modulus and strength. However, as the processing temperature was increased beyond 1300 °C, further crystallization of Si(O)C on the β-SiC particles, as observed in Figure 16 (c), occurred. This was accompanied by a reduction in polymer derived ceramic volume, resulting in a change in pore topology which results in an increased pore fraction due to the surface area of the pore increased, shown schematically in Figure 27. Although, crystallization continued as the maximum processing temperature increased, the reduction in ligament mechanical properties associated with the degradation of the microstructure appears to have dominated, and was responsible for the reduction of foam density, Figure 21 (a), stiffness, Figure 26 (a), and compressive strength, Figure 26 (b).

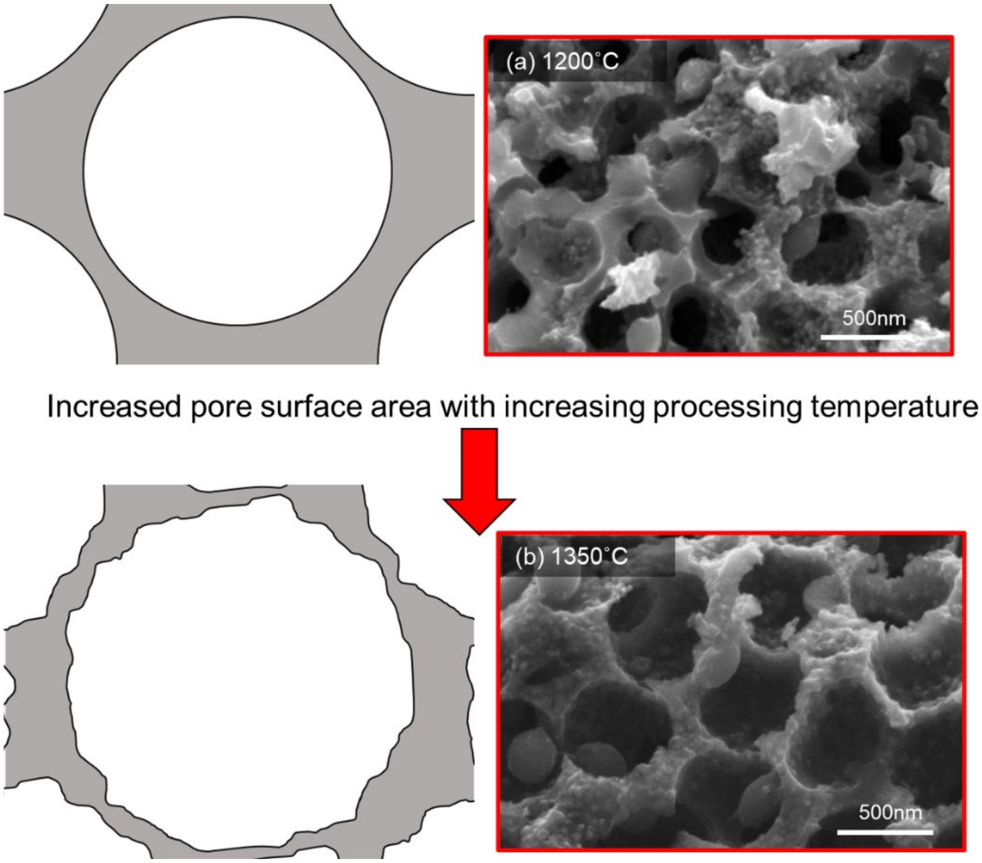

Figure 27. Schematic showing pore topology evolution as a function of processing temperature. As temperature increases, the pore surface area increases resulting in an increase in pore fraction (ϕ).

4.4.3 Comparisons with Ceramic Foams and Lattices

Maps showing the Young's modulus and compressive strength versus density data collected in this study are shown (in red) in Figure 28 together with data from reference (109), and other studies of Si(O)C foams formed using preceramic polymer approaches (110–114). Data for mullite foams (115), syntactic alumina foams (116), alumina 3D printed lattices (50,117), Si(O)C 3D printed lattices (61), as well as glassy carbon lattices (118), and coated silica inverse opals (119) are also included on the maps. The modulus of the SiC nano foams made here were less than those reported by other approaches (110) while their compressive strengths were comparable or exceeded those of other Si(O)C preceramic foam approaches (110–114). The compressive strengths of nanofoams made here also appear to be similar to those reported for 3D printed Si(O)C lattices. The reduction of fabrication time, cost, and the ability to scale the PMMA space holder manufacturing therefore shows promise for development of a scalable route to the bulk synthesize of SiC nanofoams.

It is noted that the choice of ligament material and its topology significantly influence the modulus of ceramic foams. Figure 28 shows that both silica inverse opals coated with titania and glassy carbon lattices attain very high moduli and compressive strengths. However, concerns about the scalability of the glassy carbon method and restriction of its use temperature in oxidizing environments remain significant issues.

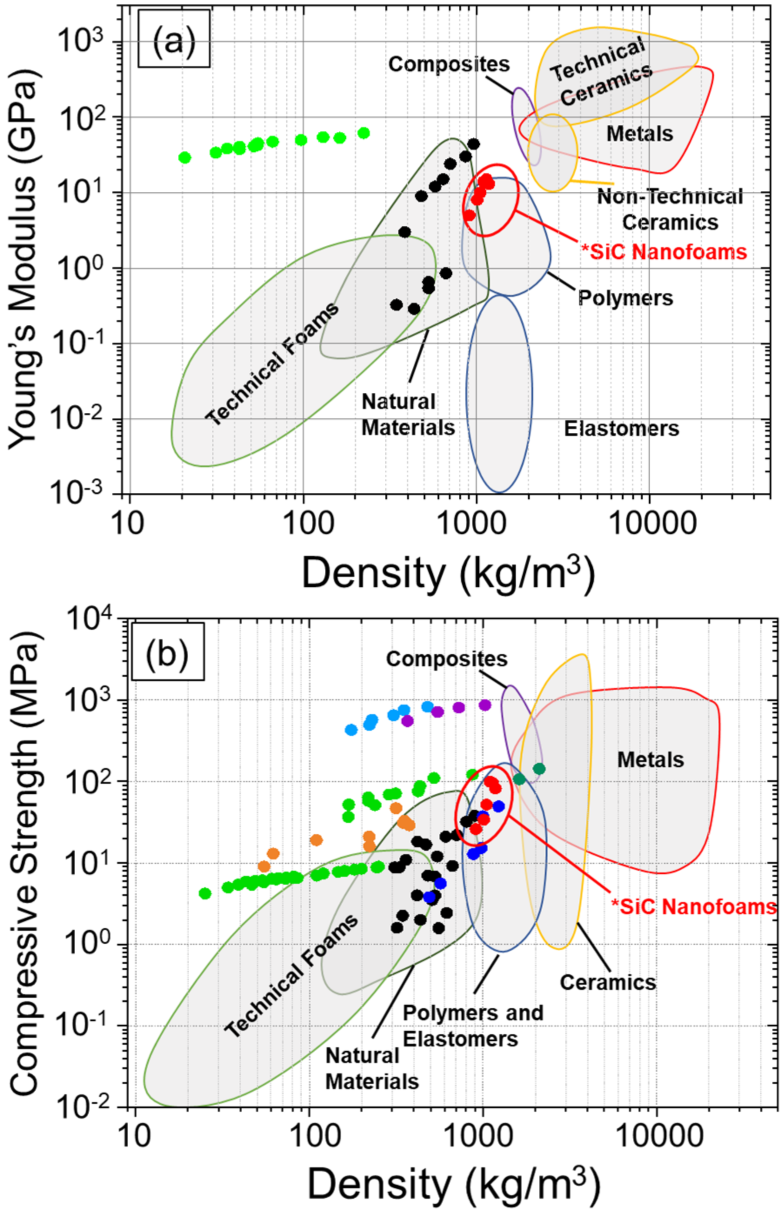

Figure 28. Ashby plots for Young's Modulus and compressive strength of synthesized SiC foams shown in red. Data were collected from the literature on Si(O)C foams formed using preceramic polymer approaches (110–114) (black), mullite foams (115) (blue), syntactic alumina foams (116) (teal), alumina 3D printed lattices (50,117) (light green), Si(O)C 3D printed lattices (61) (orange), glassy carbon lattices (118) (light blue), and coated silica inverse opals (119) (purple)

4.5 Conclusions

The study described here provided an understanding of the synthesis and mechanical properties of SiC foams made via PMMA sacrificial templating and a β-SiC nano-powder loading of a preceramic polymer. The effect of the final processing temperature on the foams structure and mechanical properties was investigated. The study revealed that:

1. The Young's modulus and compressive strength of the foams varied strongly with the crystallization temperature used to convert the SMP-10 preceramic polymer to SiC. A peak in foam modulus E = 15 GPa, and compressive strength σ = 100 MPa, was found to occur after heating to 1300 °C.
2. By accounting for changes in modulus and strength due to variations in pore volume fraction, the study found that the peak in both foam modulus and strength resulted from a peak in the Young's modulus and modulus of rupture of the 50-300 nm width interpore webs.
3. The peak in interpore web modulus and strength after processing at 1300 °C is consistent with a competition between the formation of a crystalline (high modulus and strength) -Si-C- network between the nano β-SiC particles and the development of nanoporosity between the nano β-SiC particles with the latter increasingly dominate as the processing temperature was increased to 1400 °C and above.
4. While the modulus of the foams made using this processing route are similar to those reported by others for similar materials and foam topologies, the compressive strengths were substantially higher consistent with the high modulus of rupture of the nanoscale interpore webs and absence of large-scale flaws in the foams.

The results of this study can be used to determine the necessary processing conditions that will result in a foam with a low relative density and high relative strength. Future studies can be done to determine the degree of crystallization and verify E_s, σ_s, and ρ_s as a function of processing temperature. Furthermore, dispersion methods must be further improved to achieve an even pore distribution.

4.5.1 Novel Contributions and Broader Impact

A novel method for synthesizing bulk sub-micron porous SiC foams has been developed in which a preceramic polymer (SMP-10), PMMA spheres and β-SiC nanoparticles (~50 nm) were diluted in n-hexane, ball-milled, dried overnight, compressed, and then thermally treated. The concept is based on a sacrificial template composed of PMMA spheres (800 nm) that is thermally decomposed during the pyrolysis of the preceramic polymer leaving behind a foam network. β-SiC nanoparticles (~50 nm) were successfully used to reduce mud cracking during SMP-10 curing and pyrolysis. The n-hexane approach allows for even distribution of the three constituent materials ***which has not previously been achieved for preceramic polymer approaches using sub-micron spherical PMMA space holders.***

The interactions of spherical pore forming additives as well as solid SiC loading of templated preceramic polymers has not been previously explored and therefore was not well understood. *For the first time, the constituent material's (PMMA, β-SiC, and hexane) effect on the cure, pyrolysis, crystallization and mechanical properties as a function of final processing temperature has been explored and understood.*

4.5.2 Future Work

The dissertation presented here illuminates the role of excess carbon and oxygen in the high temperature processing of SiC foams. It is critical for future work to mitigate the char retention of PMMA during its decomposition process. Therefore, the chemistry of the polymer particle used to form pores is critical to mitigate high-temperature (>1250 °C) decomposition of foam ligaments processed using a polycarbosilane ceramic precursor. Furthermore, removal of native oxide and moisture from the surfaces of SiC nano powders is also necessary to mitigate high temperature degradation of the foam ligaments. Another processing route to mitigate this issue would be to partially pyrolyzed SMP-10, ball mill it to form a powder, then use the SMP-10 as a seed material to help reduce volume shrinkage.

Future work could also explore methods for a more even distribution and higher level of porosity. Large-scale fabrication of inverse opal SiC foams fabricated using the powder space holder method with preceramic polymers is of high interest to increase the mechanical performance of the foam material. Increasing porosity, allowing for even distribution of pores, and forming an inverse opal will allow for an open cell, low density foam with superior mechanical properties to that of a random distribution of pores.

Chapter 5: Review of RCCA Alloy Design/Discovery

5.1 Complex Concentrated Alloys

Complex Concentrated Alloys (CCAs) have emerged as a promising new class of advanced metallic materials. CCAs utilize four, five or more elements in non-dilute concentration to achieve high strength, toughness, and fatigue endurance, as well as reduced thermal and electrical conductivity at exceptionally high temperatures. Their study was intensified after Cantor et al. (120) reported that a 3d transition metal alloy containing equiatomic concentrations of five to six metals formed a single solid solution phase as opposed to multiphase intermetallic compounds that would have been expected. In the Cantor study, single phase solid solutions of FeCrMnNiCo with non-dilute additions of Nb, Ge, Cu, Ti and V were formed. Subsequently, there has been a great effort in studying metals with four or more principal elements (15,121). The formation of a single solid solution phase was attributed to the entropy stabilization due to intrinsically high configurational entropy and, the alloys were later designated as high entropy alloys (HEAs) (121). Subsequent discoveries of equiatomic metallic alloys with four or more principle elements with multiple phases (6,16,17,19) as well as ceramic counterparts (122,123), have challenged this simple idea, and the definitions and terms used to describe these material systems have evolved in the literature. High entropy alloys (HEAs), multi-principal element alloys (MPEAs), complex concentrated alloys (CCAs) and multicomponent alloys are all now used to describe material systems consisting of five or more elements, and the scientific community, has yet to agree on the terminology to describe these alloy systems (124).

Terminology based upon either a composition-based vs. entropy-based perspective can be considered. The composition-based definition, that leads to MPEA terminology, encompasses any alloy that "consists of five or more principal elements with the concentration of each element lying between 5 and 35 at.%" (121). The entropy-based definition categorizes an alloy by its calculated configurational entropy, or the amount of the system's entropy that is determined by the discrete positions elements can occupy within a crystal structure. The Gibbs Free Energy (ΔG) of mixing of a system can be calculated using the general expression:

$$\Delta G_{mix} = \Delta H_{mix} - T\Delta S_{mix} \tag{13}$$

where ΔH_{mix} is the change in enthalpy of mixing, T is the temperature, and ΔS_{mix} is the change in entropy of mixing. When ΔH_{mix} is relatively small, the $T\Delta S_{mix}$ term of a solid solution can exceed the enthalpic contribution to mixing and the Gibbs free energy of mixing is minimized for solid solution formation. Assuming the entropy is dominated by configurational entropy, Boltzmann's equation for configurational entropy can be used to determine the ΔS_{mix}:

$$\Delta S_{mix} = -R \sum_{i=1}^{N} c_i ln(c_i) \tag{14}$$

where R is the ideal gas constant, N is the number of components, and c_i is the atomic fraction of component i. For a five component system, the lower limit of the entropy of mixing to offset the enthalpy of mixing and ensure the formation of the solid solution (SS) is given by $\Delta S_{mix} > 1.61R$, where R is the gas constant (125). When this criterion is satisfied, the system is considered to be "high entropy". However, as T in Equation (13) rapidly decreases (due to cooling of the alloy), the entropy term ceases to be sufficient to favor the formation of a solid solution and the formation of a solid solution becomes unfavorable. Although the formation of the SS phase is unfavorable at lower T, the system is kinetically constrained from forming intermetallic compounds. Subsequent research has shown that many HEA alloys are multi-phase when given sufficient opportunity for equilibration (124). Indeed, the opportunity for decomposition of metastable solid solution phases to form multiple phase microstructures, gives new opportunity to manipulate the properties of HEAs.

In view of this, the term CCA has increasingly grown to encompasses HEAs and MPEAs, while also considering alloys with multiple phases present i.e. analogues to conventional Ni, Co, or Fe-base superalloys with a disordered FCC, BCC, and ordered phases such as the B2 structure (16,124). From an exploratory perspective, this broader definition encourages investigations of material systems without being defined by only entropy considerations or presence of a single phase.

5.1.1 Refractory Metal Complex Concentrated Alloys

The first report of a CCA composed of BCC refractory complex concentrated alloys (RCCAs) appeared in 2010 (18). RCCAs quickly gained interest as they were discovered to retain high strength at temperatures exceeding 1000°C and even retained strength as temperatures approached 1600°C (6,17,19). Such refractory alloys might therefore offer an alternative to SiC based CMCs for some high temperature applications since CMC's lose strength rapidly as the temperatures rises above the fiber creep temperature, (>1400 °C for SiC/SiC) (20), provided the higher density of these refractory metals were not an issue. Their high toughness in addition to strength might also make them attractive candidates for some high temperature applications. If they could be made via inexpensive processing routes they might compete with CMCs on the basis of cost since CMCs remain expensive to manufacture with multiple processing steps including fiber synthesis, fiber weaving, fiber coating and matrix infiltration (126), and require an environmental protection coating when used in oxidizing environments.

The four primary refractory metal elements of interest for RCCAs are W, Ta, Mo, and Nb. This can be extended to the broader definition of refractory elements that includes all metals whose melting temperature is above 1650 °C (6). This includes Hf, V, Cr, Zr, and Ti. Guidance on the potential solubility of these metals in each other can be provided by the Hume-Rothery rules (127). These indicate high solubility is favored when the atomic radius of the solutes and solvent differ by less than 15%, when the solvent and solute crystal structures are similar, and when they have similar valence and electronegativity. Indeed, as electronegativity differences increase, so does the propensity for intermetallic compound formation.

Couziné et al recently published a comprehensive data compilation of 122 RCCAs made to date and their mechanical properties (17). A summary of the yield strength as a function of temperature for RCCAs vs conventional high temperature alloys Inconel 718 and Haynes 230 can be seen in Figure 29. It is immediately evident that there is great promise for exceptional high temperature mechanical properties with RCCAs. However, the vast combinations of elements in varying amounts limits the current research to a fraction of the available alloys. Recently, it was shown that the near equiatomic combination of 4-6 (or more) of refractory metal elements in an alloy can increase strength while also increasing the operating temperatures (15–18). The MoNbTaW and MoNbTaVW alloys have both been shown to have strengths exceeding 400MPa at temperatures as high as 1600°C (128,129). These refractory complex concentrated alloys may offer an opportunity to extend the temperature limits of conventional high temperature material design.

While refractory CCAs (RCCAs) promise high yield and creep strength, at very high temperature, the tendency for brittle fracture at low temperature, the difficult processing paths, extreme sensitivity to interstitial impurities (C, N, O), susceptibility to volatile oxide formation and the breadth of the unexplored compositional space, has slowed the discovery of new, commercially significant compositions.

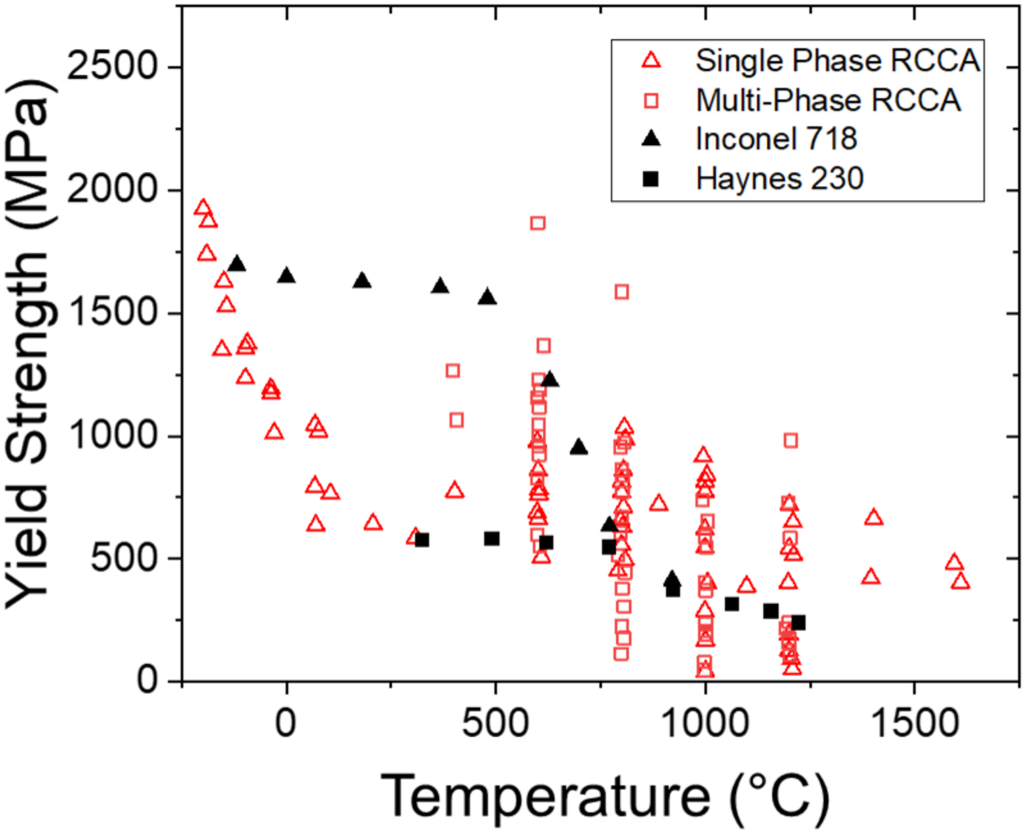

Figure 29. A review of yield strength of RCCAs as a function of temperature between 2010 and 2018 by Couzinié et al. and a data compilation of high temperature metallic alloys. (6, 16)

5.1.2 RCCA Opportunities and Challenges

The processing of RCCAs has proven to be challenging due to the high melting temperatures (1855˚C for Zr to 3422˚C for W), wide range of electronegativities (1.30 for Hf to 2.36 for W) and vast differences in atomic radii (0.130 nm for Cr and 0.216 nm for Hf) all of which have an influence on the expected phases, microstructure, and properties of the resulting alloys. The differences in these values for refractory metals can be seen in Figure 30. Most RCCAs are processed using liquid phase mixing methods, such as arc melting (130), induction melting (131), electron beam melting (132), or laser melting (6). The significantly different melting temperatures for the refractory elements of interest (see Figure 30) increases the difficulty of these traditional melting approaches and can lead to phase segregation or evaporation of a constituent element. Vapor methods are also used, and offer opportunities for a reduction of micro-segregation and refined grain sizes due to the rapid condensation rates (128,129). Powder metallurgy methods are often used as well (133–135). Pure or alloyed powders can be mechanically mixed and consolidated, using techniques such as spark plasma sintering, to form RCCAs. However, this method can result in much contamination from native oxides on the powder surfaces, ball-mill media, consolidation dies, and O and N reactions with the environment in which the material is processed (136,137).

While conventional alloys based upon a single principal element have been historically developed via Edisonian approaches (17,138), the design of CCAs containing four or more principal elements is much more difficult due to vast compositional space that can be explored. It is quickly realized that making and testing each individual alloy would require so much time as to be infeasible (15,139). The development of combinatorial library approaches combined with computational and high-throughput investigations provides a potential route to accelerate alloy discovery in such systems.

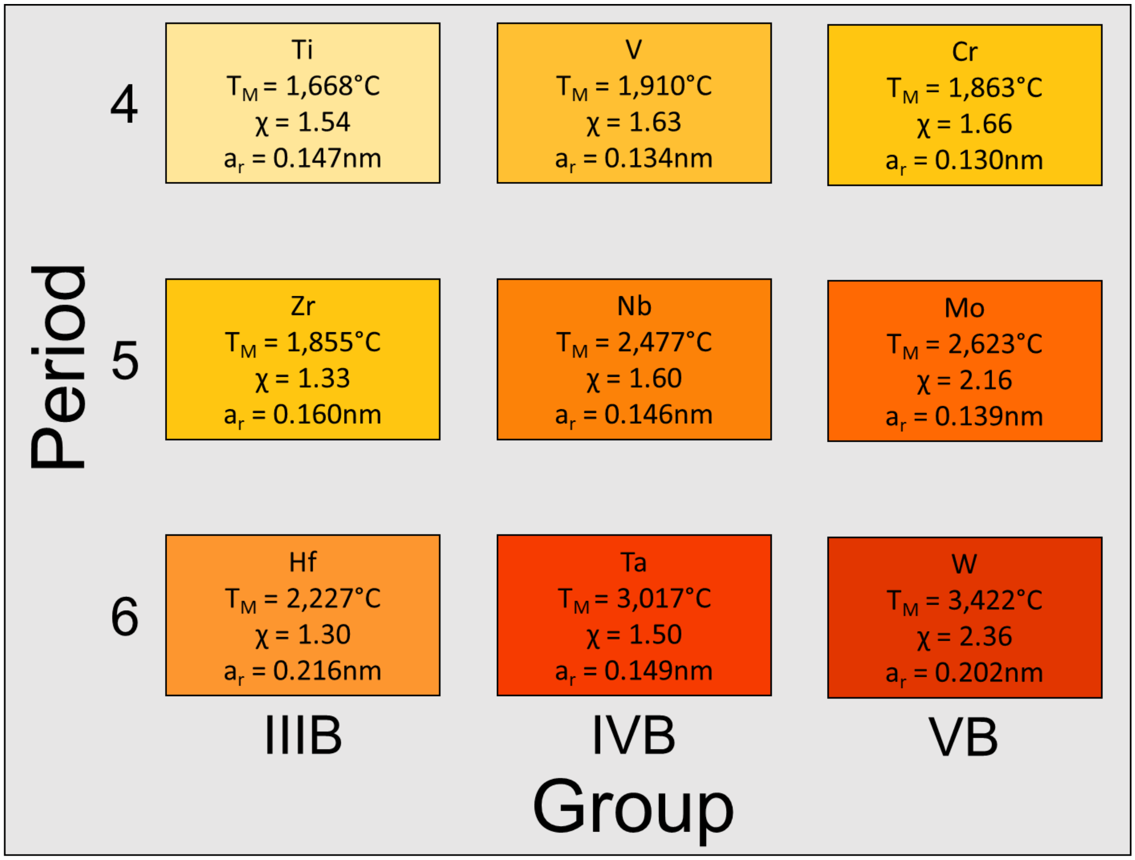

Period	IIIB	IVB	VB
4	Ti T_M = 1,668°C χ = 1.54 a_r = 0.147nm	V T_M = 1,910°C χ = 1.63 a_r = 0.134nm	Cr T_M = 1,863°C χ = 1.66 a_r = 0.130nm
5	Zr T_M = 1,855°C χ = 1.33 a_r = 0.160nm	Nb T_M = 2,477°C χ = 1.60 a_r = 0.146nm	Mo T_M = 2,623°C χ = 2.16 a_r = 0.139nm
6	Hf T_M = 2,227°C χ = 1.30 a_r = 0.216nm	Ta T_M = 3,017°C χ = 1.50 a_r = 0.149nm	W T_M = 3,422°C χ = 2.36 a_r = 0.202nm

Figure 30. Periodic table of refractory elements showing their respective melting temperatures, electronegativities and atomic radii.

5.2 Combinatorial Library Exploration and Material Discovery

Combinatorial synthesis tools have been developed for many fields of research, ranging from biomaterials to electronic materials, as a means to sample many chemical compositions within a single alloy (133,140–152). Several approaches have been proposed for the synthesis of alloy combinatorial libraries in which the composition is varied as a function of position. In order to perform in-depth studies of the composition-phase-microstructure effects on the mechanical properties, it is paramount to use a synthesis technique that produces specimens of sufficient thickness and density for crystal structure and mechanical properties investigation (>20 μm) (153) while also being able to arbitrarily vary compositions while maintaining low interstitials or oxides.

Laser additive manufacturing has been used with varying constituent powder feed rate to achieve varied compositions throughout a build (133–135). By varying the volume fraction of each metal powder component, and accounting for the differences in their melting temperatures and vapor pressures, combinatorial libraries can be made that are amenable to microscale mechanical testing. For the refractory metal combinatorial libraries made using a laser melting technique, ensuring chemical homogeneity, avoiding high oxygen levels inherited from adsorbates on powder particles surfaces and from the laser melting environment has proven to be challenging (135,152). Furthermore, not all alloy elements of interest exist in an appropriate powder form.

Many other approaches are based upon sputter deposition, and enable the deposition of films (<10 μm) using plasma-assisted deposition to obtain pore free coatings (142,147,148). These methods use various targets, pure and alloyed, to create composition libraries. An example of this, seen in Figure 31, shows a method of using four individual sources to sputter deposit an array of compositionally unique sections to screen for antibacterial films (142). The sputtered flux scales with flux of ions that induce sputtering which is dictated by the sputter system power. From this library, high-throughput antibacterial tests can be done on each individual point and a systematic study can be done on the antibacterial properties as a function of composition.

Typical sputtering systems have power levels that enable the deposition of thin refractory alloy films using plasma-assisted deposition to obtain to obtain pore free coatings (148,154). However, the deposition rate of this approach is relatively low, and it is therefore challenging to make refractory films of sufficient thickness for evaluation of material properties such as elastic modulus, strength and ductility (148,154). Without sufficiently thick, dense films, it is not feasible to use characterization techniques such as nanoindentation and X-ray diffraction. Nanoindentation requires a film thickness of approximately 10x the depth of the indentation being made (153). Therefore, for a 1-3µm deep indent, a minimum film thickness needed is approximately 10-30µm minimum. For XRD measurements, a thicker film avoids large substrate interferences with the spectra being collected. Therefore, a combinatorial approach in which thicker films can be produce could prove to be advantageous.

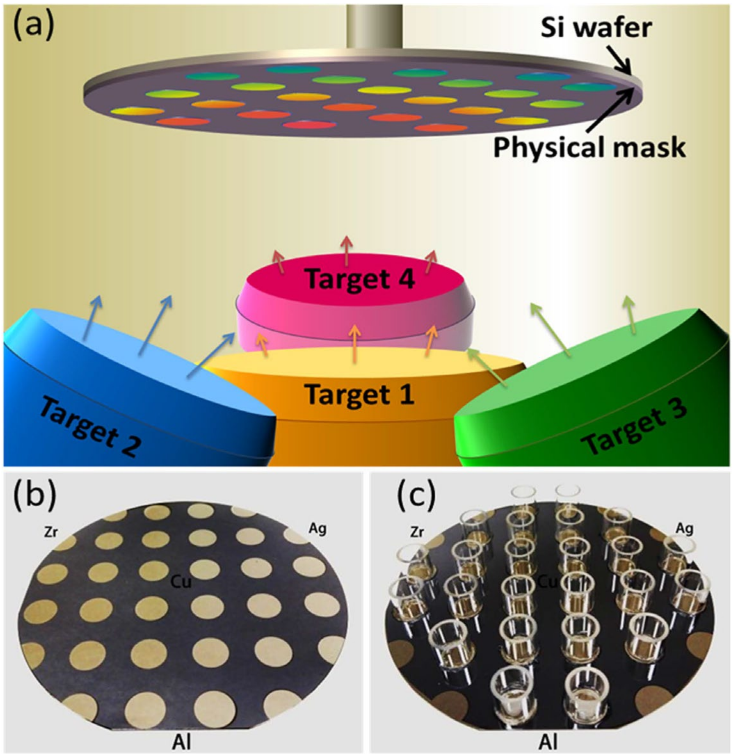

Figure 31. Schematic diagram showing the co-sputtering deposition of Zr-Cu-Al-Ag to create combinatorial library (Liu et al. 2016)

A more recent implementation of metallic CrFeMnNi libraries has been conducted using Directed Energy Deposition in a Laser Engineered Net Shaping system at the University of Wisconsin (155). This deposition set up allows for an array of 5 x 5 sampling regions that are cubes with dimensions of approximately 6 x 6 x 3 mm. This allows for sample with sufficient thicknesses (> 10 µm) for material property investigation as well as environmental testing. However, this method relies on the ability to process powders of interest for RCCA libraries, which can be problematic for some of the materials of interest. Furthermore, oxygen interstitials and oxide formation remain an issue.

5.3 Objectives of the dissertation

The core motivation for this research has been the need for a better combinatorial library approach for refractory alloys that is efficient and has the ability to produce specimens with sufficient thickness and density (>20 µm), a large and systematically controllable compositional variation (>15 at%), and with little contamination. EB-DVD has the capability to meet all of these requirements where other methods fall short. There are critical knowledge gaps in the understanding of the deposition of refractory metals using the EB-DVD method. The following work therefore aims to develop the necessary processing conditions for achieving dense, thick, low oxygen refractory allows with compositional gradients exceeding 10 at% and identify opportunities for equipment and experimental manipulation for optimized RCCA films. The first objective of this part of the dissertation is to demonstrate the application of an electron beam evaporation approach for the combinatorial synthesis of refractory, body centered cubic (BCC)

CCAs based upon mixtures of Ti, Zr, Hf, V, Nb, Ta, Cr, Mo, and W (17). This synthesis tool had been used successfully to synthesize combinatorial libraries for the Ni-Al-Pt system (156). The second objective is to evaluate RCCA films synthesized by the electron beam evaporation approach for composition, phase, microstructure and suitability for screening mechanical properties.

Chapters 6 and 7 describe development of a method for depositing films with a thickness that exceeds that of sputtering and does not suffer from the limitations of the powder melting approaches. The goal was the development of a process for making combinatorial libraries with thicknesses of 10 to more than 100μm. It begins (Chapter 6) with an overview of the electron-beam directed vapor deposition (EB-DVD) technique and evaluates the feasibility of depositing RCCA libraries. Chapter 6 describes the implementation of a four-source deposition approach and shows the potential for high-throughput investigation of RCCA films deposited using the EB-DVD method. The study is completed (Chapter 7) by an assessment of the combinatorial synthesis approach, and suggested potential improvements to it.

Chapter 6: Electron Beam Directed Vapor Deposition of Combinatorial Libraries

6.1 Introduction

The ability to synthesize materials using solid and liquid phase methods has been implemented and developed over thousands of years. However, it wasn't until 1852 when Grove observed metal deposits sputtered from a glow discharge (157) and then five years later as Faraday experimented with metal wire explosions in an inert atmosphere (158), that the precursors of modern day vapor phase synthesis emerged. From a historical perspective, vapor phase synthesis has been implemented for a significantly shorter time than both solid and liquid phase material synthesis. Following rapid vacuum technology improvements in the 1940s, scientists and engineers have improved vapor phase synthesis processes to meet the design requirements of many products for applications ranging from environmentally resistant coatings (159,160) to semiconducting and optical materials (159,161). Furthermore, vapor processing approaches allow for unique properties and microstructures not found in traditional bulk processing approaches (e.g. giant magnetoresistive (GMR) multilayers (162), thermal barrier coatings (TBC) (163), infrared transmission window coatings (164,165) and functionally graded materials (FGM) (166–168)).

Since the implementation of vapor phase materials synthesis, various methods to deposit thin films have been developed such as chemical vapor deposition (169), and a host of physical vapor deposition approaches including electron beam evaporation (170), reactive and activated evaporation (171,172), magnetron sputtering (169), radio frequency diode sputtering (173), ion plating (174), cathodic arch deposition (175), and ion-beam assisted deposition (176). Although these technologies are readily implemented and widely explored by manufacturers, the need for further development of materials continues to push some vapor phase synthesis techniques past their current limitations. To overcome obstacles and synthesis shortcomings, materials scientists and engineers must continue to expand upon and develop vapor phase synthesis techniques.

6.2 Electron beam deposition

An electron beam method that uses a helium gas jet to direct the vapor (Electron beam directed vapor deposition: EB-DVD) developed by the Wadley group at UVa has been previously used to coat complex geometries and create novel coatings for applications ranging from thin film batteries to high temperature thermal barrier coatings (177–181). It is well established that the EB-DVD method has the potential for generating homogeneous deposits by co-deposition from two to four sources. A schematic of the EB-DVD chamber used during the studies performed for this dissertation is shown in Figure 32. The quality of a RCCA library film produced using the EB-DVD method is determined by three main controllable parameters of the system: source evaporation, vapor transport to the substrate, and vapor-substrate interaction.

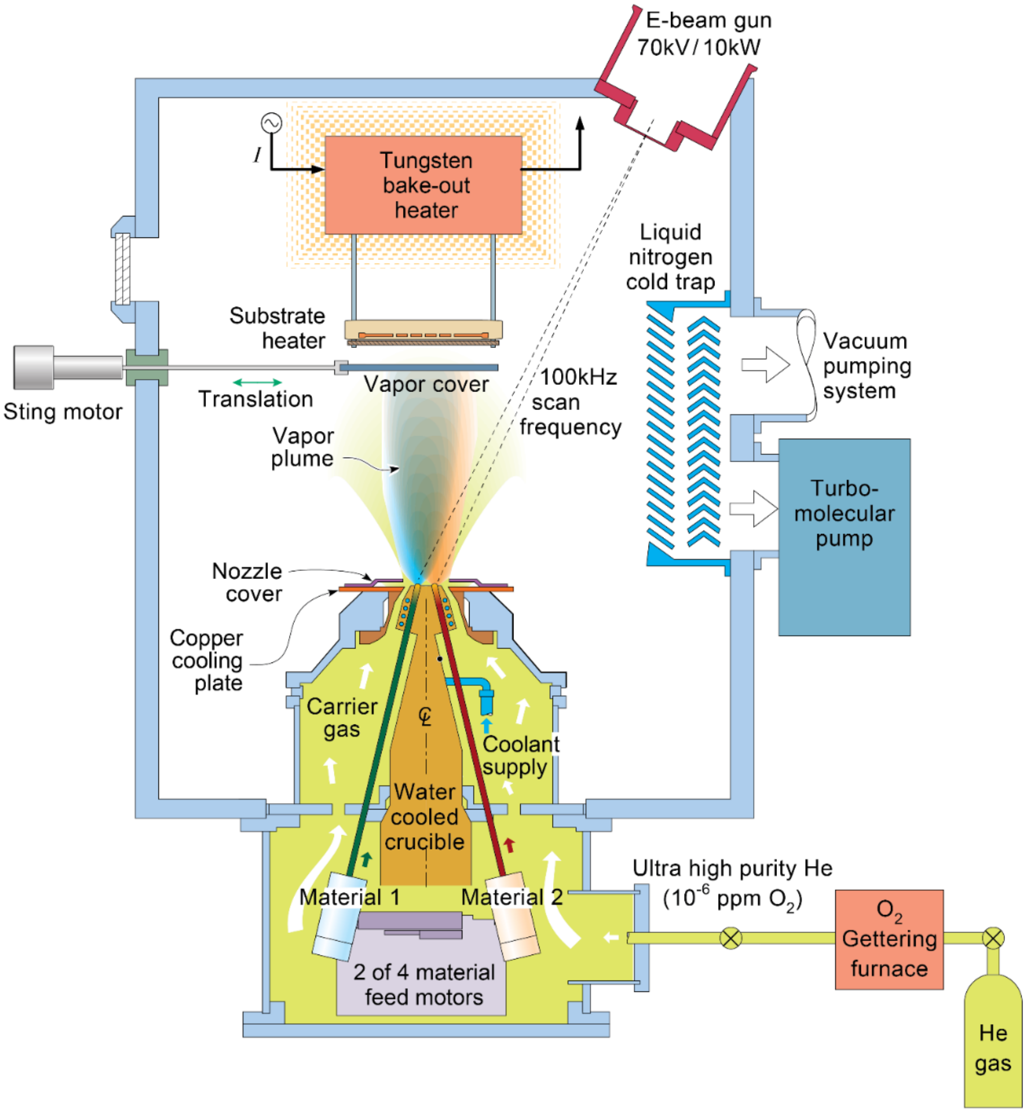

Figure 32. Schematic of EB-DVD including the system bake-out heater, oxygen gettering furnace, and improved substrate heater.

Source evaporation is enabled by the use of an electromagnetically focused 10kW (70kV) electron gun with very high frequency scanning capability so it can sustain molten pools and evaporation from multiple adjacent sources. Previous research has shown the possibility of co-depositing or sequentially evaporating up to four different sources in the gas jet forming nozzle region enabaling creation of complex chemistry alloys or multilayer coatings (140,182). However, as the melting temperature of a source material increases, the ability to simultaneously melt four refractory sources becomes challenging. Evaporation mechanisms and fluxes as a function of vapor source melting temperature are overviewed in section 6.2.1. In multi-source electron beam evaporation, the beam is scanned over several adjacent sources approximately 1-5 times per millisecond. The fraction of the duty cycle applied to each source is adjusted to achieve a surface temperature that results in the desired vapor flux from each source.

In the EB-DVD process, the evaporant is produced within the throat of an inert gas jet-forming nozzle; therefore, momentum transfer from the accelerated gas jet atoms redirects the vapor atoms from a roughly omni directional $\cos^n(\theta)$ angular distribution (where n is ~2) to a collimated flux with a vapor flux cross section comparable to the width of the sample (183). The gap between the crucible and nozzle ring in the EB-DVD chamber is 1.5 cm, leading to a converging-diverging nozzle. The velocity of the coaxial, high velocity rarified inert gas flow directing the vapor toward a substrate controls the intermixing of the vapor species from the different sources which gives rise to the ability to use this process to produce films with complex chemistries across the sample surface (140,183). In the EB-DVD process, vapor speeds can greatly exceed 300 m/s due to the nozzle geometry (140). While the high accelerating voltage aids EB propagation in the low vacuum deposition chamber (the scattering cross section decreases with electron energy), much lower pressures are needed within the electron column gun. This is achieved by using a small EB aperture and differential pumping of the electron gun column using a turbomolecular pump. Within this configuration, the electron beam evaporation and rarified helium gas jet assisted deposition function synergistically. The vapor transport via coaxial, high velocity rarified inert gas flow is overviewed in section 6.2.2.

The microstructure of a film deposited using the EB-DVD technique is dependent on the deposition conditions such as substrate temperatue, chamber pressure, and gas jet speed (167,177,178,180,181,184). Film morphology has been emperically determined by many researchers showing the substrate temperature and background pressure effect (185–188). The vapor-substrate interactions in the EB-DVD process are outlined in section 6.2.3.

6.2.1 Evaporation Mechanisms

The rate of evaporation from a heated liquid surface has been difficult to predict, even with the use of molecular dynamic simulations due to the long range of vapor attraction (189–192). Langmuir predicted the rate of evaporation from a heated vapor source surface in a vacuum from the Clausius – Clapeyron equation (193). The evaporation flux, *J*, is given by:

$$J(gcm^{-2}s^{-1}) = (5.83 \times 10^{-2})P(m/T)^{1/2} \tag{15}$$

Here, P (Pa) is the saturation vapor pressure of the evaporants, *m* is the vapor molecular weight, and *T* the absolute temperature of the evaporating surface. The composition at any point within the combinatorial library is governed by the evaporation fluxes (mass evaporated per unit area per unit time) from each of the heated source surfaces and their rates of lateral spreading during transport to the substrate. In a high vacuum environment, the evaporated flux *J* (in units of mass per unit area per second) from a source is determined by the surface evaporation flux (J_{evp}) leaving the source material and the re-condensation flux and is given by the Schrage relationship (189,194) as equation (16):

$$J_{evp} = \alpha \sqrt{\frac{k_B}{2\pi m}} \left[\rho_{sat}(T_L) \cdot \sqrt{T_L} - \Gamma(v_R) \cdot \rho_v \cdot \sqrt{T_v}\,\right] \tag{16}$$

where $\propto$ is the mass accommodation coefficient, *m* is the molecular weight of the fluid, k_B is Boltzmann's constant, T_L and T_V are the temperatures of the liquid and vapor at the surface-vapor interface, $\rho_{sat}(T_L)$ is the saturated vapor density at T_L, ρ_v is the density of the vapor, and v_R is ratio of the macroscopic speed of the vapor ($v_{v,0}$) to the most probable thermal velocity of vapor molecules given by:

$$v_R = \frac{v_{v,0}}{\sqrt{2k_B T_v/_m}} \tag{17}$$

The term $\Gamma(v_R)$ is given by:

$$\Gamma(v_R) = e^{-v_R^2} - v_R\sqrt{\pi}[1 - \mathrm{erf}(v_R)] \tag{18}$$

At high relative vapor velocities present within the EB-DVD process (140,195), the contribution of the recondensation of the Schrage relationship $\left(\Gamma(v_R)\rho_v\sqrt{T_v}\right)$ approaches zero due to the

$\Gamma(v_R)$ term and can be neglected. The reduced equation for relatively high vapor velocities is given as:

$$J_{evp} = \alpha\sqrt{\frac{k_B}{2\pi m}}\left[\rho_{sat}(T_L)\cdot\sqrt{T_L}\right] \tag{19}$$

The mass accommodation constant is the probability for a vapor molecule to condense on the surface of a solid or liquid interface and, in the case of metals, tends to approach unity (196).

The effective rate of evaporation is highly temperature dependent because the saturation vapor pressure that appears in the Schrage relations for metals is itself a very strong function of their surface temperatures and can be described by an expression of the form:

$$P_{sat} = \exp\left[A + \frac{B}{T} + Cln(T) + DT^{E}\right] \tag{20}$$

where P_{sat} is the saturation vapor pressure, T is the temperature of the liquid surface, the coefficients (A-E) are fitting parameters (197). Figure 33 shows examples of the vapor pressure-temperature relations for a number of metals including those of interest for refractory metal alloy development (198). The rate of evaporation is a sensitive function of the surface temperature, as well as the evaporants molecular weight, and scales with the area from which evaporation occurs. Under static environments, the net evaporation is also a function of the background pressure under which evaporation occurs. For evaporation to be successful, the saturation vapor pressure should exceed that of the background. Figure 33 shows that for the saturation vapor pressure above a heated source material to exceed that within a stagnant deposition chamber (say 1Pa), the surface temperature of Al must exceed about 1100 °C. The vapor pressure rises rapidly with temperature above this threshold (from 1Pa at 1100 °C to 5Pa at 1300 °C). The temperature, needed to achieve the threshold vapor pressure of 1 Pa increases to ~1250 °C for Cr, Sc, Pd, Au and Ge, to ~1500 °C for Si and Ti, to 2300 °C for Mo and can exceed ~2700 °C for W, Nb, Ta and Re. This information is vital for understanding the vapor flux of evaporated source material and thus determining the expected concentration of a particular element. Since the Stephan-Boltzmann relationship indicates that as the source temperatures rises, an increasing a fraction of the energy deposited into a surface is radiatively re-emitted, the evaporation of refractory metals requires a high electron beam power to achieve the necessary evaporation conditions.

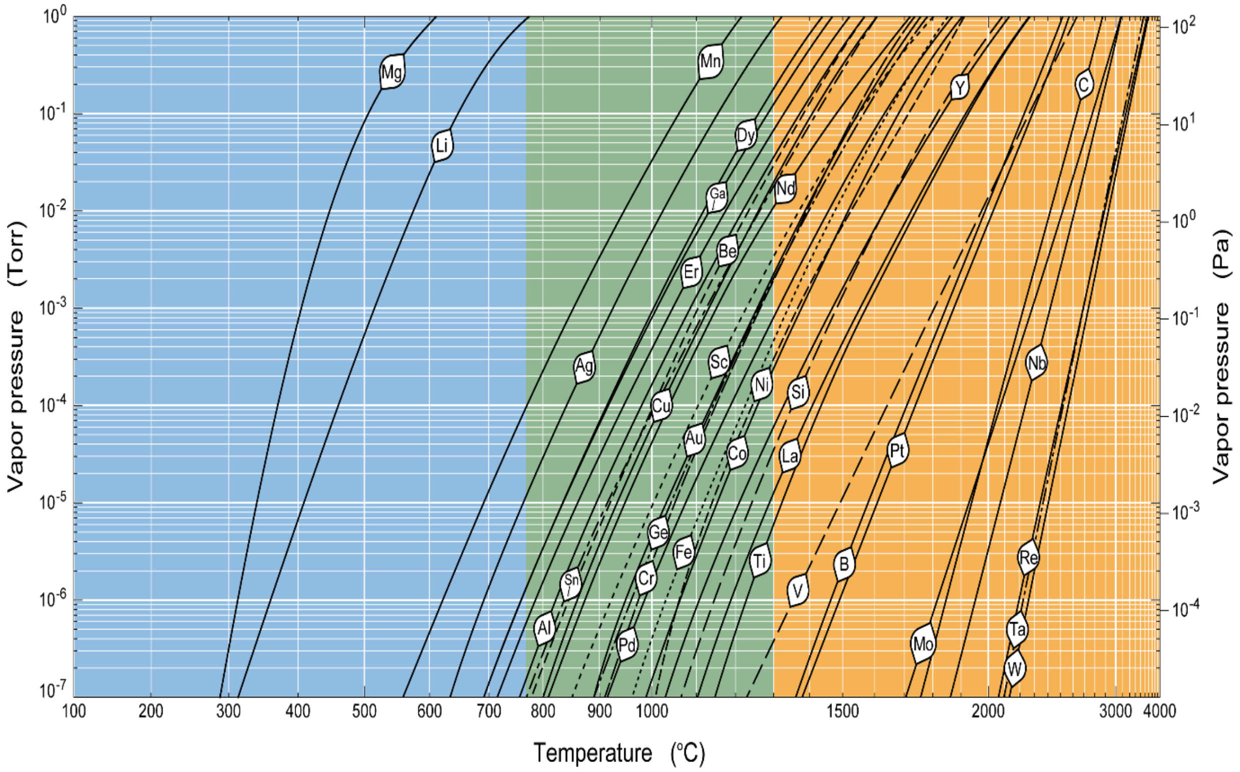

Figure 33. The saturation vapor pressure versus temperature of elements (198).

6.2.2 Vapor Transport

The EB-DVD approach utilizes a rarified inert gas flow coupled with a converging diverging nozzle design to create a rarefied transonic inert gas jet flow that entrains the vapor emitted from an electron beam heated surface within the nozzle to enable the normally near omni directional vapor emission angle distribution to be collimated along the axis of the jet and transported to a substrate (188). This is achieved by binary collisions between the gas jet atoms and the vapor. These transfer momentum from the jet atoms to the vapor, removing it rapidly from the vicinity of the source surface while also focusing the vapor into a plume that propagates toward a substrate (in the direction of the jet). Previous studies (140) have shown that vapor plumes of four sources each spread laterally by gas phase diffusion, and begin to overlap resulting in a compositional gradient over the substrate surface, Figure 34. As the vapor from adjacent sources is transported by the helium jet towards a substrate, it diffuses in all direction leading to lateral spreading and overlap of the plumes as schematically illustrated in Figure 34 for a plane above four sources (A, B, C and D) in this case spaced 50 mm apart.

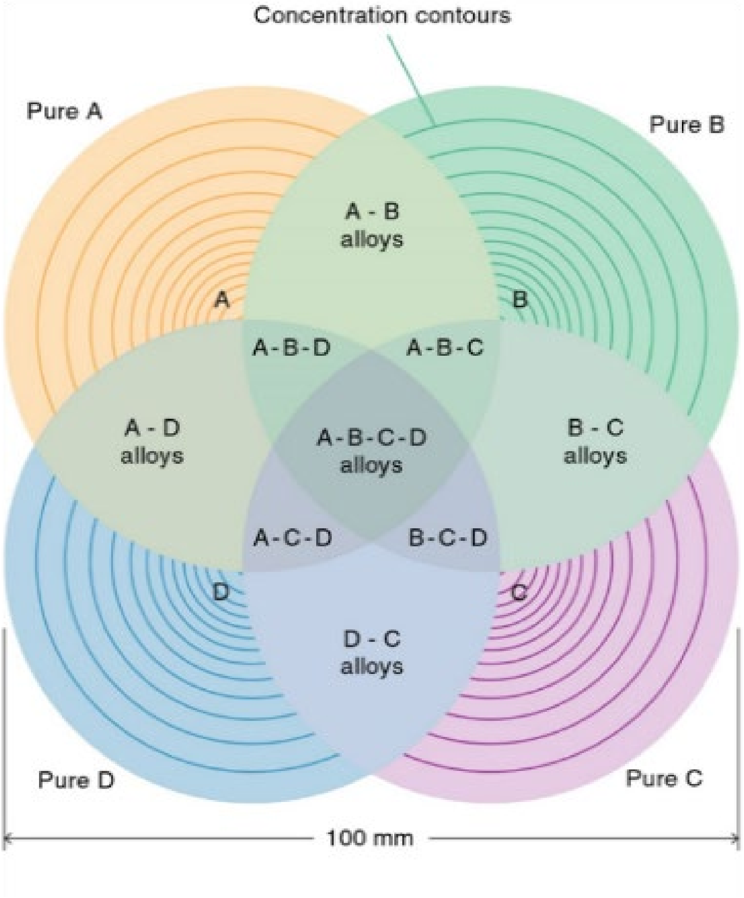

Figure 34. The use of the EB-DVD process for synthesis of combinatorial libraries.

The flow field created by a converging-diverging (CD) nozzle can be seen in Figure 35 (195). It should be noted that the Mach number (M) of the carrier gas is largest in the immediate region near the nozzle opening. Rapid expansion of the gas occurs in this region. The nozzle geometry and background pressure may generate a Mach disk shock; secondary shock disks may also form depending on the CD nozzle conditions. The flow dynamics are also affected by the substrate resulting in a wall jet, or buildup of pressure, near the surface of the substrate (184,195). It is therefore essential that vapor atoms acquire sufficient momentum to penetrate this region and impact the substrate. The Mach number, M depends upon the ratio of the upstream pressure and that in the chamber:

$$\frac{P_o}{P_d} = \left[1 + \frac{\gamma - 1}{2} M^2\right]^{\frac{\gamma}{(\gamma-1)}} \tag{21}$$

where P_o is the upstream pressure (Pa), P_d is the downstream (chamber) pressure, γ is the ratio of specific heat (5/3 for He and Ar (200)). When rearranged to calculate the Mach number, it can be seen that *M* scales with P_o/P_d:

$$M = \sqrt{\left(\frac{P_o}{P_d}\right)^{\frac{\gamma}{1}+\gamma} - 1 \Big/ 1 - \gamma} \tag{22}$$

In order to achieve a $M=1$ for a He or Ar flow, a pressure ratio of $P_o/P_d \approx 2.05$ must be achieved ($\gamma = \frac{5}{3}\ for\ He\ and\ Ar$). When $M=1$, the vapor speeds of He and Ar are 927 m/s and 319 m/s, respectively.

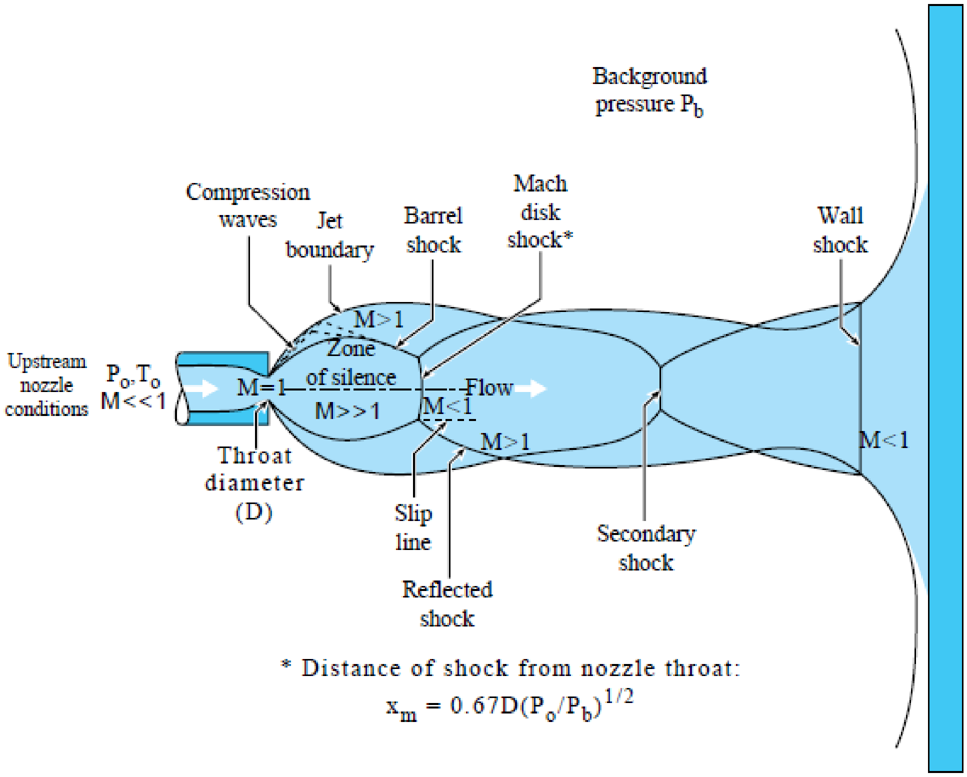

Figure 35. Structure of a continuum free-jet (195).

The gas jet pressure and its temperature, the source to substrate distance, *h* and average jet speed, *v* determine the distance, *x* of lateral vapor diffusion, and therefore the degree of intermixing (alloying) of the vapor, and resulting gradient in composition across a substrate. If the time taken for vapor to travel from the source to substrate (a distance, *h*) is *h/v*, the diffusion distance is approximately:

$$x \approx \sqrt{2hD/v} \tag{23}$$

Here, the gas phase diffusion coefficient, *D* (201). In gases, the diffusion coefficient is both temperature and pressure dependent, and depends upon the masses of the background gas and the diffusing species and their scattering cross section. For gases, D is typically calculated using Chapman-Enskog (202) theory which gives an expression for the diffusion coefficient of the form:

$$D = \frac{CT^{3/2}\sqrt{1/M_1 + 1/M_2}}{P\sigma^2 \Omega} \qquad (24)$$

where *T* is the temperature (K), *P* the pressure, M_1 and M_2 are the masses of the evaporating and background gas species, σ is a characteristic collision diameter, *C* is a constant and Ω a collision integral (201).

Atom tracking simulations by Hass et al. (140), show the that the ability to control the background pressure by flowing He at different rates can lead to intermixed vapor or vapor that remains columated as it reaches the substrate surface, given by the Chapman-Enksog equation, Figure 36. The ability to control the lateral diffusion of gas species from adjacent sources is possible by adjusting the He velocity exiting the gas nozzle. It is immediately evident that controlling the gas flow determines the lateral diffusion thus illuminating the capability to create vapor plumes with lateral compositional variance. The gas jet density and speed can be altered such that lateral diffusion of evaporated materials from adjacent sources can be controlled to create vapor plumes whose composition varies sharply with lateral position. Therefore, the background pressure, vapor speed, and pressure ratio can be finely tuned while controlling the vapor flux, J_{evp}, and result in a lateral diffusion scenario as shown in Figure 34.

(a) P_o = 8 Pa, Pressure Ratio = 4.0

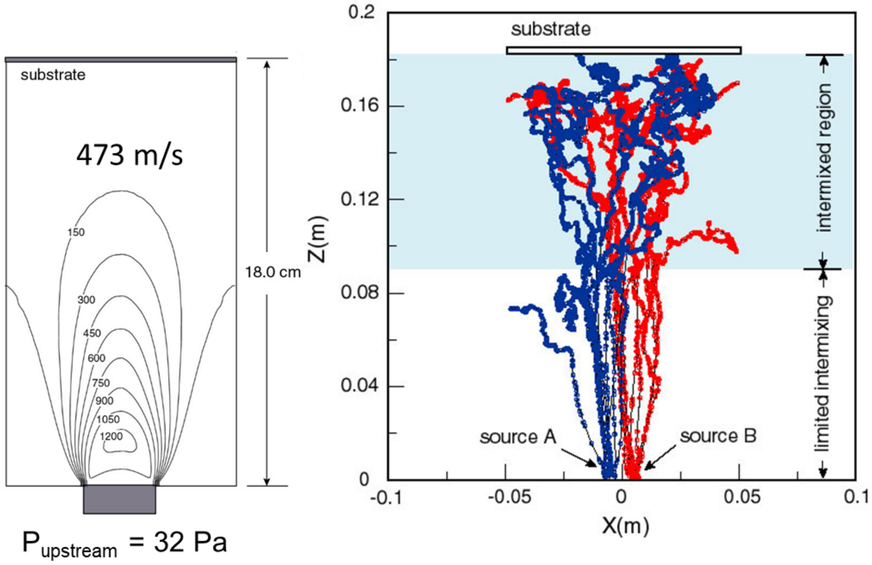

(b) P_o = 27 Pa, Pressure Ratio = 4.0

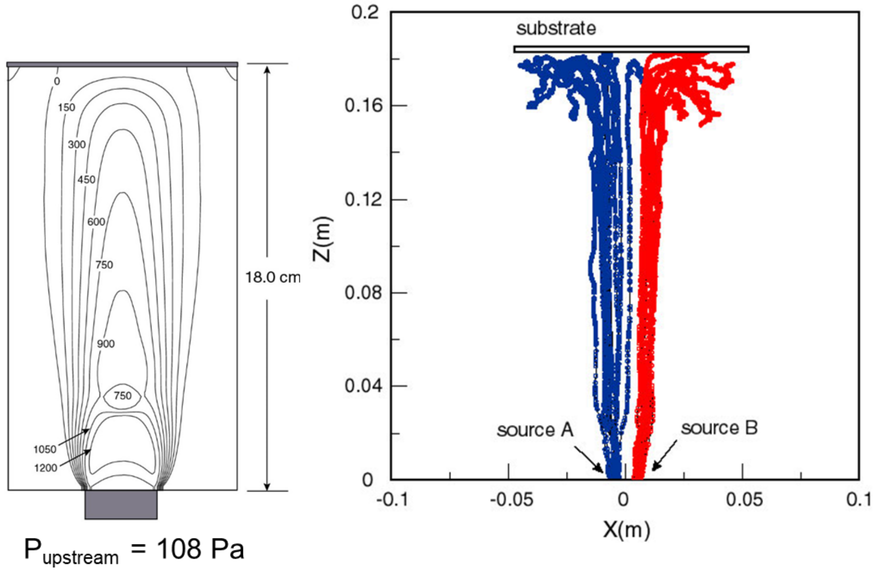

Figure 36. Co-evaporation from two vapor sources placed within the throat of a gas jet forming nozzle showing the lateral diffusion of the vapor from each source to form an alloy vapor plume with a strong composition gradient (140). The diffusivity of each metal vapor in a helium background predicted by the Chapman-Enskog theory at (a) a background pressure of 8 Pa and pressure ratio of 4.0 versus (b) a background pressure of 27 Pa and pressure ration of 4.0.

6.2.3 Vapor – substrate interactions

Deposition on the substrate occurs if the heavy, refractory metal atoms have sufficient momentum to penetrate the He wall jet that develops at the substrate surface or by binary collisions between the species in a wall jet flow stream within a mean free path of the substrate surface. Since the collisions of the fast, high mass refractory metal atoms with the light He gas wall jet only weakly redirect the condensing species, most of the vapor is deposited near where it arrives at the substrate. To create a dense coating, flux shadowing (203) must be reduced. For this, the atoms on the coating surface must diffuse over the surface to vacant lattice sites where they can be absorbed to form a crystalline structure. One approach to induce this is to raise the substrate temperature and use thermal activation to overcome the energy barriers to surface atom migration (191). However, this approach typically requires the coating temperature to exceed 0.7-0.9T_M where T_M is the absolute melting temperature of the coating material (185–187). However, it becomes increasingly challenging to accomplish this with refractory metal alloys whose melting temperature exceeds 2500 K and in the case of tungsten reaches 3695 K. An alternative is to use plasma assisted deposition like that used in sputtering systems. In this case, the surface atoms acquire energies of several electron volts sufficient to briefly diffuse over a surface (191). A multi-jet hollow cathode (MJHC) system was added to the deposition approach to enable ionization of argon atoms and some of the vapor. The use of negative electrical biasing of the substrate then enables higher energy impacts with the deposition surface and promotes the formation of dense coatings (Appendix A).

The density of the film is dictated by the energy available for atoms to overcome activation barriers needed for them to diffuse once they have reached the sample surface. It is well understood in the literature that the switch from porous columnar growth to dense coatings occurs at substrate temperatures greater than $0.5T_M$, shown in Figure 37 (185). In order to get dense films with low surface roughness, the activation energy to promote the surface diffusion must be overcome (204). As the T_M of a material increases, the ability to overcome this activation barrier becomes increasingly more difficult resulting in the need for additional densification processes that increase the kinetic energy of the incoming vapor species (181,205). As a result, coatings have very rough surfaces, and often contain deep, coating penetrating pores (pinholes) between columnar grains. Though this has little effect on the measurement of the composition and x-ray diffraction determination of the phases present, if such voids are present in combinatorial libraries, they will perturb nano-indentation mechanical property measurements. It has been shown that utilization of plasma assistance during vapor deposition methods increases the atomic mobility of the vapor species and thus results in thick, dense, smooth films (206,207).

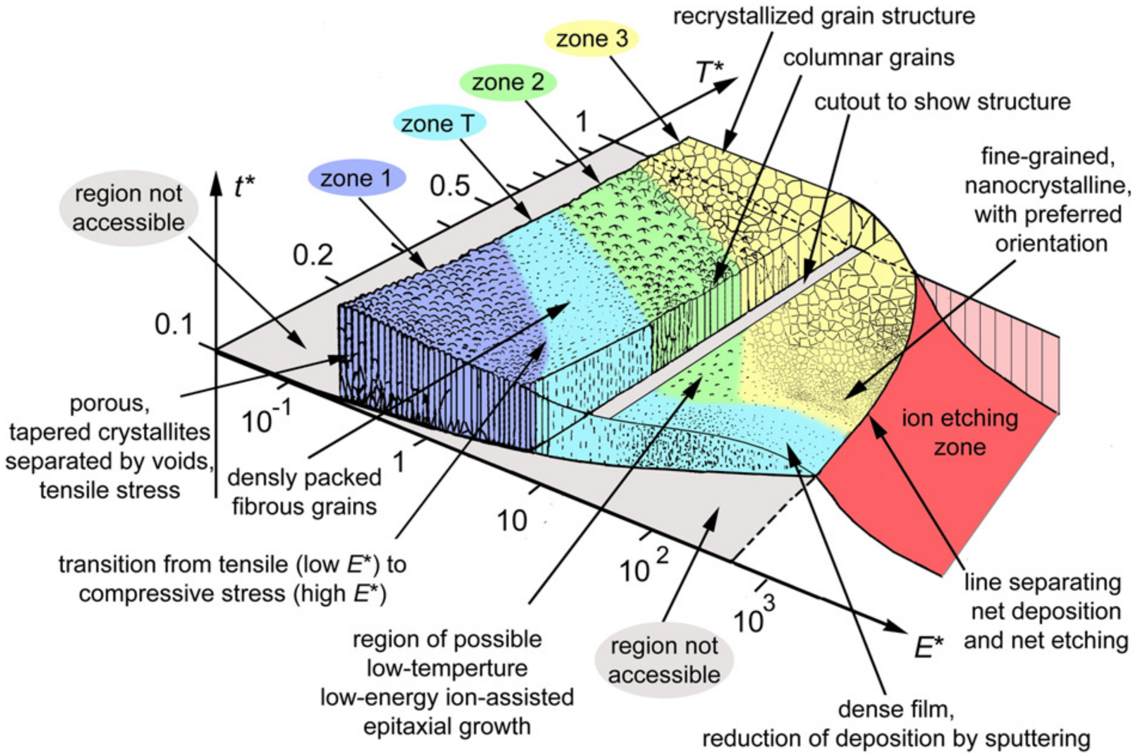

Figure 37. A structure zone diagram by Anders (Lawrence Berkeley National Laboratory) showing the temperature and vapor energy dependency on film microstructure (185).

The “hot substrate” synthesis approach is sufficient to enable dense coatings of many metal systems of interest to be studied. However, several complexities arise when coatings are required to contain elements with widely disparate melting temperatures. Consider an alloy from the $Al_2CrFeCoCuTiNi$ system. The absolute melting temperature of its elements vary from 933 K (Al) to 2133 K (Cr). If deposition were conducted at 1500 °C (70% of T/T_M for Cr) to create a dense coating, the saturation vapor pressure of aluminum at the coating surface would be 10^{-1} Pa. The resulting re-evaporation rate is then sufficient to deplete the coating of this alloy element during deposition. This might be compensated by increasing the rate of evaporation of this source material, or by reducing the substrate temperature, especially if the activation energies for surface diffusion of the refractory elements on an alloy coating surface are reduced by the presence of lighter elements. However, a better approach is to use a low substrate temperature, and rely upon a plasma assisted method for densifying the coating.

Typically, EB-DVD has been used to deposit less-refractory metals due to their lower melting temperatures and high vapor pressures. Fully dense Ni-Pt-Al combinatorial libraires have been deposited using this method (140). The use of EB-DVD to deposit combinatorial refratory metal libraires has not yet been implemented due to their high melting temperatures, susceptibility to interstitial contamination and low vapor pressures. The core motivation for this portion of the dissertation is to extend the EB-DVD combinatorial approach to refractory metal libraries to enable high-throughput materials investigation.

Monolithic refractory metal substrates can be used for high temperature RCCA alloys. These are selected to match the thermal expansion coefficient of the coatings to eliminate delamination upon cooling. For accurate assessment of properties, it is essential that the coatings are dense. There are two approaches that can be used to ensure the deposition of a dense coating. The simplest is to deposit a coating at a temperature that is high enough to allow surface diffusion of atoms to regions where the incident flux is lower than elsewhere (due to flux shadowing). This requires a temperature of approximately 0.6-0.8 T/T_M where T_M is the absolute melting temperature of the coating material. If a refractory metal substrate is used, direct current heating of the substrate can raise its temperature up to 2,000 °C if necessary.

6.3 Experimental

A comprehensive understanding of evaporation rates as a function of beam allocation, lateral gas diffusion of the vapor plume, heating and plasma effects on sample density, and He flow rate are needed to determine the necessary processing conditions for creating combinatorial libraries of refractory complex concentrated alloys. The purpose of this study was to investigate the effectiveness of the EB-DVD process on the synthesis of RCCA film libraries. Several depositions were done in order to develop an understanding of the necessary beam power allocations and He jet speed required to produce a four component RCCA library; the presented study in this chapter highlights three of the depositions.

A 0.25 mm thick molybdenum substrate with dimensions of 65 mm x 55 mm was used to deposit four 6.35 mm Mo, Nb, Ta, and V evaporation source rods (99.99% purity; Elemental Metals, NJ). The EB-DVD chamber was evacuated using a series of vacuum pumps (Rotary Vane Pump (E2M 40-275), Mechanical Booster Pump (EH1200 HC IE3 US 60HZ 230 /460V), and an additional Mechanical Booster Pump (EH4200 HC IE3 US 60HZ 230 /460V)) (Edwards Vacuum LLC, Sanborn, NY) to reduce the base pressure to 10^{-3} Pa. The system was then baked out at 120˚C for 24 hours and a copper cold trap (with liquid N_2 continuously flowing through it) further reduced the base pressure of the chamber to 10^{-4} Pa. He gas flowed through a gas purifying furnace (Oxy-Gon Model OG-120) and introduced into the chamber at 20 standard liters per minute (slm). The chamber pressure during deposition achieved an upstream to downstream pressure ratio of 1.69. The substrate was heated to and held at a temperature of 1100 °C (1373 K) (measured on the back surface of the sample using a G-type thermocouple). Three different samples were deposited with differing beam power allocations to investigate the ability to tune compositions by changing the beam power allocation from sample to sample and thus their surface temperature and evaporation rates. In the experiment four 6.35mm adjacent refractory sources (Ta, Mo, Nb and V) were melted and evaporated to produce three TaMoNbV refractory RCCA libraries: BRC103, BRC104, and BRC105. The beam power allocations are summarized in Table 4 and were less than the available 10 kW of the 70 kV EB-PVD set-up.

Table 4. Beam power allocation for Mo, Ta, Nb and V for samples BRC103, BRC104 and BRC105

	Mo allocation (kW)	**Ta allocation** (kW)	**V allocation** (kW)	**Nb Allocation** (kW)	***Total beam power*** *(kW)*
BRC103	1.16	1.96	0.28	1.58	***4.98***
BRC104	1.18	2.14	0.34	1.61	***5.27***
BRC105	1.26	2.14	0.34	1.61	***5.35***

Scanning electron microscopy (SEM) and energy dispersive X-ray spectroscopy (EDS) were used to determine the gradient in composition of the libraries. The observations were made at the five locations shown in Figure 49 and were made using a Helios NanoLab DualBeam microscope (Thermo Scientific, Hillsboro, OR) fitted with an X-MaxN 150 SDD (Oxford Instruments, Concord, MA). Surface microstructure was characterized using the SEM in secondary electron (SE) imaging mode using a high-performance ion conversion and electron (ICE) detector. The compositional variance across an array on the sample surface was determined using EDS with a high accelerating voltage of 20keV to delineate any overlapping X-ray emission peaks of the refractory metals used.

6.4 Results and Discussion

6.4.1 EB-DVD of the TaMoNbV System

Table 4 shows the beam power allocation was primarily increased for Mo to see the effect of changing the beam power allocation on the resulting library composition. EDS was then used to deduce the surface composition at five locations (directly above the center of the four sources and in the middle of the library on each library.

An EDS projection map and sample surface SEM image (center of sample) for sample BRC103 is shown in Figure 38(a) and (b), respectively. The EDS map was created by taking measured composition at each position and interpolating calculated values between each measured value. It can be seen that the film produced is rich in Ta which has a compositional variance of 10.6 at%. As you go across the sample from position (1,1) to position (5,5) on Figure 38(a), the composition of Ta falls from about 39 at% to 28.4 at% while Mo rises from approximately 29 at% to 34 at%. The sample was therefore low in Nb across all positions of the samples surface. The second largest compositional variance was seen in V going from position (1,5) to position (5,1). Sample BRC103 demonstrates the feasibility of using the EB-DVD process to produce a RCCA library in which the primary component in the alloy changes as a function of position on the surface of the deposited film. The intent of the study was to produce a library nearing equiatomic mixing at the center of the sample with a large compositional gradient (>10 at%). Although large compositional gradients were achieved, further studies conducted in Chapter 7, show the ability to finely control the evaporation rates of each source element and obtain a library with near equiatomic mixing at the center of the substrate.

The surface of the coating, in Figure 38 (b), had a textured surface across the full area of the sample. The micrograph shown is taken at the center of the sample where the Ta-Mo-V-Nb concentrations are approximately 36 at%, 30 at%, 22 at% and 12 % respectively. The sample substrate was set to 1100 °C (1373 K). The average melting temperature of the elements in an alloy of this composition (a rule of mixtures: ROM) has a melting temperature of approximately 2400°C (2673 K) giving a substrate temperature of approximately 51% of T_M. To achieve a pore free coating during the condensation of metal flux typically requires a surface temperature greater than 80% of T_M which corresponds to a temperature of ~2138 K. The effect of substrate temperature on the microstructure of RCCA libraries is assessed further in Chapter 7.

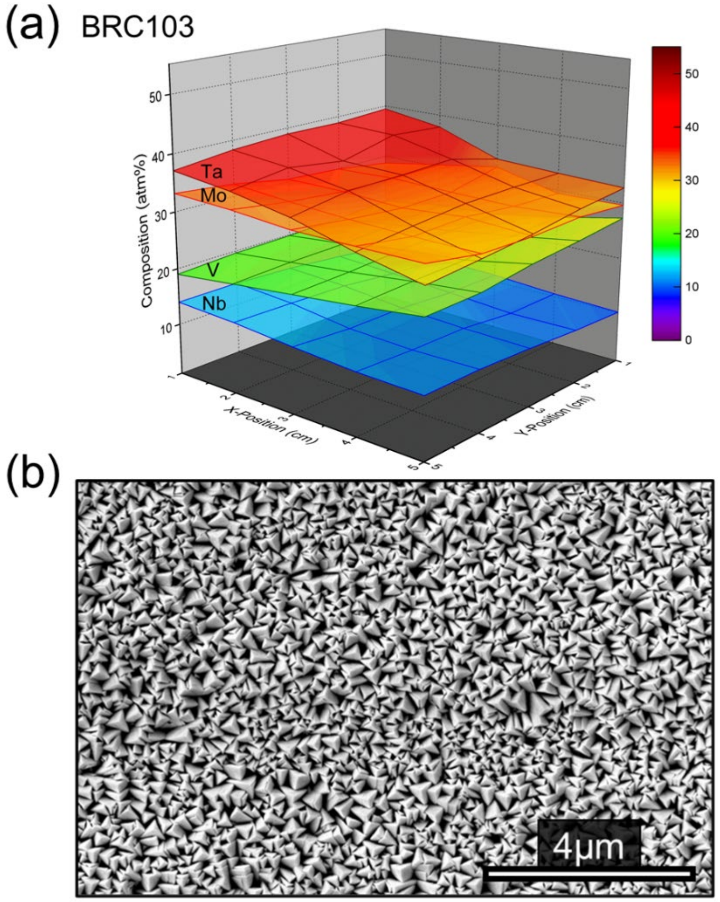

Figure 38. (a) EDS compositional map of sample BRC103 and (b) SEM plan view micrograph from center of library.

Sample BRC104 was deposited using increased beam power for all four metal sources, but with the largest relative increase in beam power allocation to the V source (from 0.28kW to 0.34kW). The EDS composition map and sample surface SEM image (center of sample) for sample BRC104 are shown in Figure 39(a) and (b), respectively. The library is enriched in V across all positions along the surface of the film. The largest compositional variance for V from (x, y) coordinate position (1,5) to (5,1) was approximately 9 at%. Mo exhibited the opposite trend in going from (5,1) to (1,5). Its compositional variance was approximately 8 at%. The film had a relatively small amount of Nb, similar to BRC103 and differed from BRC103 in that the Ta concentration was relatively low. BRC104 again had a highly faceted surface – similar to that of BRC103.

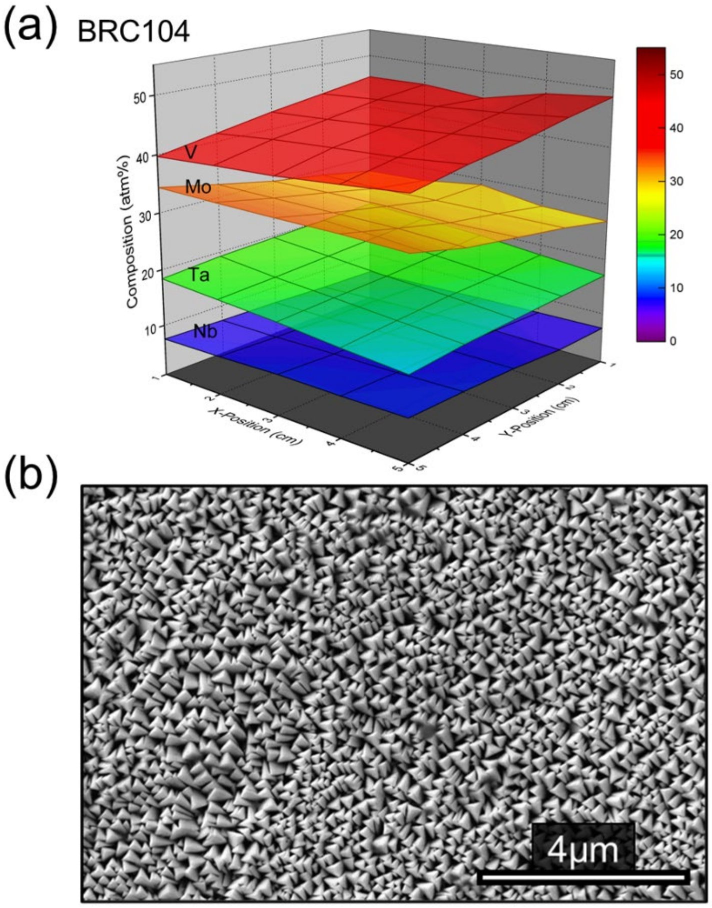

Figure 39. (a) EDS compositional map of sample BRC104 and (b) SEM plan view micrograph.

Lastly, sample BRC105 was deposited with only an increase in beam power allocation to the Mo source rod increasing it from 1.18 kW (BRC104) to 1.26kW. This increase in beam power allocation to the Mo source material resulted in a large increase in the Mo concentration across the entire film, Figure 40. The compositional variance of Mo across the sample was 11.7 at% ranging from 50.5 at% at position (1,5) to 48.8 at% at position (5,1). The film had a relatively small amount of Nb, similar to BRC103 and BRC104. Furthermore, the relative amount of Ta remained low as well, similar to that of BRC104. The surface remained faceted and similar in appearance to that of BRC103 and BRC104.

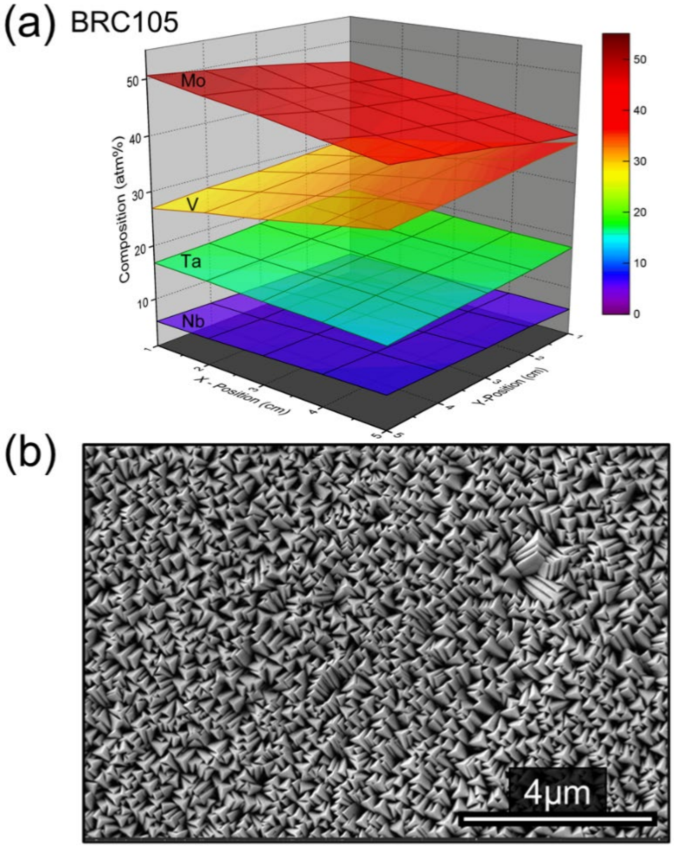

Figure 40. (a) EDS compositional map of sample BRC105 and (b) SEM plan view micrograph.

Samples BRC103 – BRC105 demonstrate the ability to control the evaporation rate as a function of beam power allocation . A summary of the atomic concentrations of Ta-Nb-V-C for each of the samples is shown in Figure 41. Chapter 7 will investigate the ability to deposit an

RCCA film with near equiatomic mixing at the center of the substrate, the crystal structures of the deposited libraries and further discuss the effect of substrate temperature.

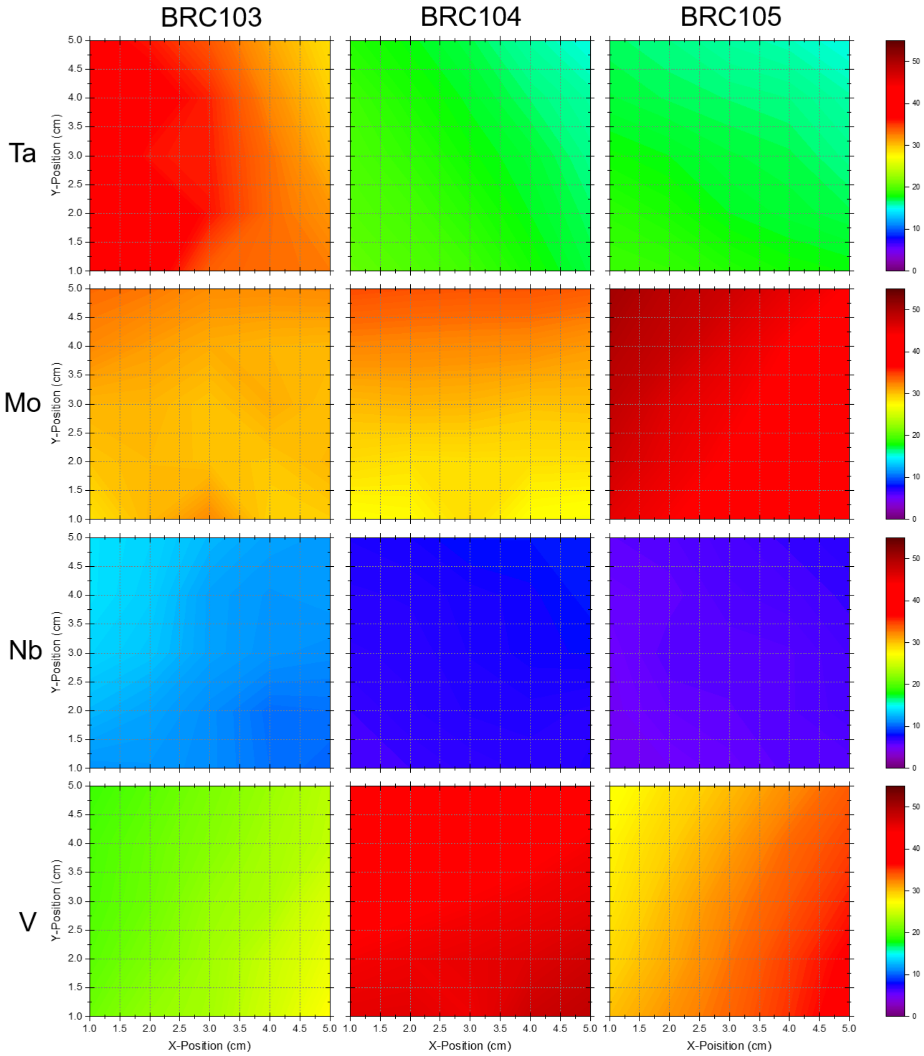

Figure 41. EDS compositional map summary of TaMoNbV samples deposited using EB-DVD upgrades.

6.4.2 Source Rod Temperatures for Evaporation

It was shown with samples BRC103, BRC104 and BRC105 that the EB-DVD method can be used with varying beam power allocation to deposit libraries with a large variability in atomic concentration. However, it is not well understood how to properly predict, and therefore implement a vapor flux for each source material in the EB-DVD process. The EB-DVD has the unique capability to rapidly carry vapor species from a molten liquid source material to a heated substrate via interactions with an inert rarified He jet that has speeds in excess of 927 m/s. The Schrage relationship, Equation 19, predicts the evaporation flux is a function of the temperature of the liquid, T_L, and the saturation vapor density $\rho_{sat}(T_L)$. The saturation vapor density can be found by using the ideal gas law:

$$PV = nRT \tag{25}$$

where P is the pressure, V is volume, n is the number of moles, R is the gas constant and T is temperature (in degrees Kelvin). In the case of the EB-DVD process, P can be approximated to be the saturation vapor pressure and T is the temperature of the liquid, T_L. Rearranging the equation for density (in moles per unit volume) yields:

$$\frac{n}{V} = \frac{P_{sat}}{RT_L} \tag{26}$$

In order to convert from units of moles per unit volume to both sides of Equation 26 can be multiplied by Avogadro's number (N_A) and the molecular weight (in kg) of the vapor species:

$$\frac{n}{V} N_A m_M = \frac{P_{sat}}{RT_L} N_A m \tag{27}$$

Substituting into Equation 19 gives the evaporated flux (with units of mass per unit area per unit time):

$$J_{evp} = \alpha \sqrt{\frac{k_B}{2\pi m}} \left(\frac{P_{sat}}{RT_L} N_A m \sqrt{T_L} \right) \tag{28}$$

The units for each parameter in Equation 28 are found in Table 5. The values for P_{sat} and T_L for the metals of interest (Ta, Mo, Nb, V, Ti, and Cr) can be taken from Figure 33. The values for the molecular weight (*m*) for each metal are found in Table 6.

Table 5. Units used in computing the evaporation flux of each metal species

Parameters	k_b	P_{sat}	R	N_A	T_L	m
Units	$\frac{m^2 kg}{s^2 K}$	$\frac{kg}{ms^2}$	$\frac{kg\, m^2}{s^2 K\, mol}$	$\frac{1}{mol}$	K	kg
$J_{evp}\left(\frac{kg}{m^2 s}\right)$						

Table 6. Mass of each element of interest

	Ta	**Mo**	**Nb**	**V**	**Ti**	**Cr**
Mass (kg)	3.00E-25	1.59E-25	1.54E-25	8.46E-26	7.95E-26	8.63E-26

The evaporation flux can then be plotted as a function of the liquid surface temperature and is shown in Figure 42. It can be seen from this plot that the EB-DVD method is capable of very high fluxes due to the rarified He jet. Furthermore, in order to have an equal vapor flux from multiple source materials, vastly different liquid surface temperatures are needed. In the case for a library consisting of TaMoNbVTiCr, in order to achieve the same J_{evp} of 0.01 kg/m^{2}s for each metal source, source temperatures would need to be approximately 3285K for Ta, 3085K for Mo, 3050K for Nb, 2050K for V, 2190K for Ti and 1810K for Cr. The ability to finely control the source temperature during EB-DVD is critical for the deposition of RCCA libraries where a near atomic mixture is near the center of the sample. Since the source evaporation in EB-DVD can be substantial in comparison to other vapor deposition methods, the need to continuously feed source materials to maintain a constant source position/ height is realized. The feed rate is therefore determined by the rate of evaporation such that the melted region can be maintained during the duration of a deposition.

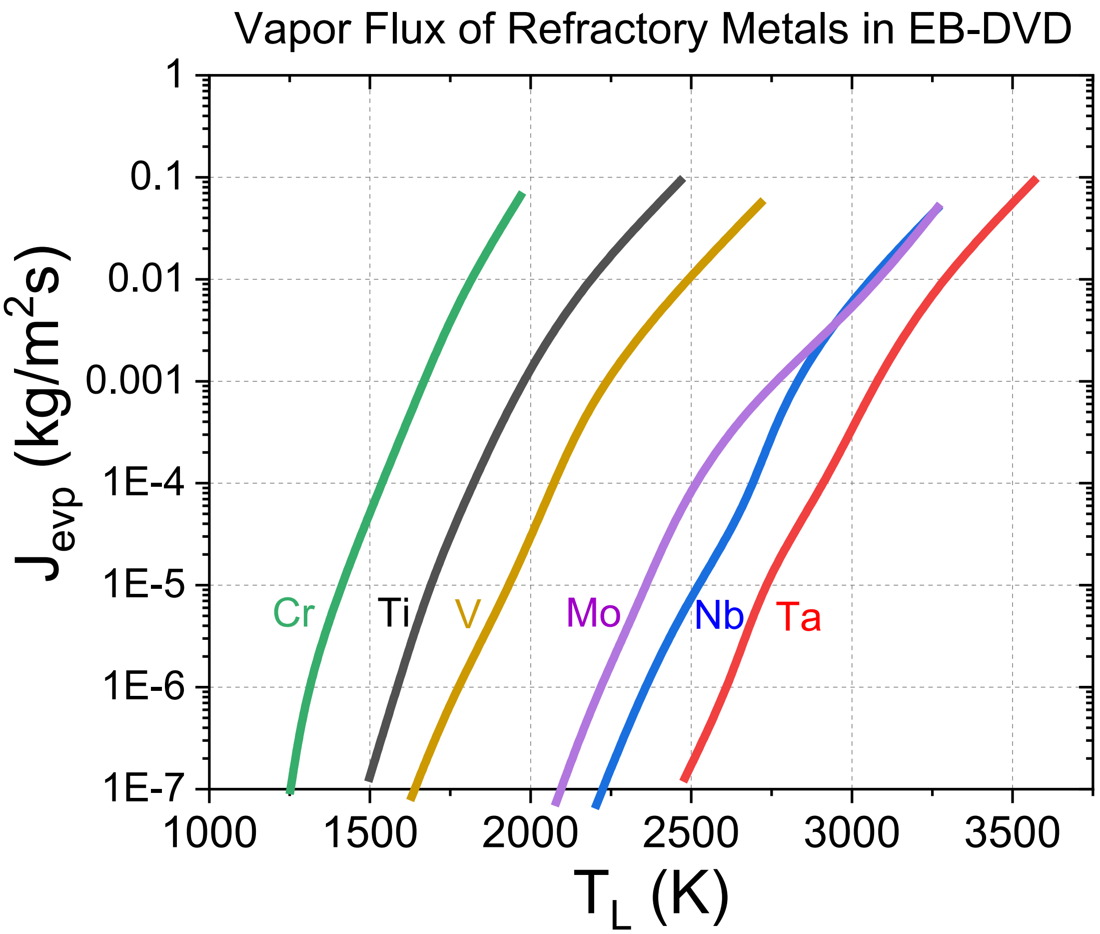

Figure 42. Vapor flux as a function of liquid surface temperature for refractory metals of interest in the EB-DVD RCCA libraries

6.5 Conclusions

The ability to synthesize and test high-throughput refractory metal libraries remains a challenge for refractory metal alloy discovery. Emerging computational methodologies and informatics tools coupled with synthesis high throughput screening methods are greatly expanding the scope for discovery of new materials for future generations of advanced engineering components (208–210). However, critical gaps in the experimental infrastructure for exploration of the extraordinarily large compositional design space have inhibited progress, especially for difficult to process refractory metal alloys. It has been demonstrated that EB-DVD of refractory metal libraries is, in principle possible. The presented study has demonstrated the following:

1. The EB-DVD method can be used to evaporate four refractory metal sources simultatneously. This is realized through the high vapor velocities induced by the inert rarified He jet that can direct the produced refractory metal vapor towards the substrate leading to rapid evaporation. This has been mathematically demonstrated with the Schrage relationship where the condensation terms go towards zero at high vapor velocities.
2. EB-DVD can be used to deposit refractory films with compositional variences greater than 10 at%. It was shown with BRC103, BRC104, and BRC105 that changing the beam power allocation, Table 4, resulted in alloys with differing concentration gradients, Figure 41.
3. Electron beam power allocation to source materials can be varied to change the composition and compositional varience in RCCA film libraries.
4. Heating of a substrate to 1,100 °C (1373 K) resulted in a faceted, rough surface morphology. Further heating or densification methods must be implemented to remove surface roughness for further material property investigation of the produced libraries.
5. The ability to control vapor source liquid temperature (T_L) allows for the ability to control J_{evp}. The Schrage relationship calculation demonstrated that for mulitple sources to have the same J_{evp}, a wide range of T_L (~1500 K – 3000 K) are needed.

Chapter 7 uses the produced knowledge from Chapter 6 to demonstrate the ability to deposit a RCCA library with near equiatomic concentrations at the center of the film and investigates the microstructure and crystal structure.

Chapter 7: Combinatorial Synthesis of RCCA Coating Libraries

7.1 Introduction

The emergence of entropy stabilization for the design of multicomponent alloys and the vast composition space available for investigation has stimulated a need for high-throughput methods for material discovery. The previous chapter indicated the promise of an EB-DVD for making combinatorial libraries in which the composition varies by several mole% per cm. However, it also identified critical gaps in in the approach that must be addressed in order to successfully implement high-throughput materials investigation. This chapter explores the use of four source evaporation with a rapidly scanned electron beam to make quaternary combinatorial libraries using an EB-DVD approach, demonstrates coatings have greater than 10 μm thickness enabling high-throughput screening measurements that are not dominated by substrate behavior, and investigates the resultant film composition and phases formed. The study focusses on the Ta-Mo/Nb-Cr-Ti-Al system which has been shown by Martin Heilmaier's group (211) to potentially offer better oxidation resistance than other RMPE alloys.

7.2 Experimental Procedure

7.2.1 Methods and Materials

The composition, crystal structure, and microstructure were investigated via four-source depositions. Four 6.35mm diameter source rods were placed in a water-cooled copper crucible with their centers situated 1cm apart in a square array. The titanium, chromium, niobium and tantalum source rods of 99.99% purity were procured from Elemental Metals (NJ). Substrate heating was implemented to heat a 0.25 mm thick molybdenum substrate (99.95% purity with mirror finish; Elemental Metals, NJ) with dimensions of 60mm x 50mm to a temperature of 1250 °C (1523 K) (measured on the back surface of the sample using a G-type thermocouple). Further details on the geometry of the heater design can be found in Appendix B. The EB-DVD chamber was evacuated using a series of vacuum pumps (Rotary Vane Pump (E2M 40-275), Mechanical Booster Pump (EH1200 HC IE3 US 60HZ 230 /460V), and an additional Mechanical Booster Pump (EH4200 HC IE3 US 60HZ 230 /460V)) (Edwards Vacuum LLC, Sanborn, NY) to reduce the base pressure to 10^{-3} Pa. The system was then baked out at 120 ˚C for 24 hours and a copper cold trap (with liquid N_2 continuously flowed through it) further reduced the base pressure of the chamber to 10^{-4} Pa. Helium (99.99%) flowed through a gas purifying furnace (Oxy-Gon Model

OG-120) and was introduced into the chamber at 20 standard liters per minute (slm). The flow rate of 20 slm of He was determined via an investigation found in Appendix C. The He flowed through a converging/diverging region of approximately 85 cm^2 between the source rod crucible and the nozzle. Additional details on the characteristics of the oxygen gettering and the inert gas nozzle geometry can be found in Appendix B. It should be noted that radiative heating from source materials and cooling from the He gas jet will affect the substrate surface temperature and should be considered in future studies.

The study investigates the synthesis of three libraries and explores the effect of varying the beam power allocation upon the composition gradient of the libraries. It includes deposition conditions that resulted in near equiatomic mixtures at the center of one of the libraries. A summary of the beam power allocation for the three samples synthesized for this study can be seen in Table 7. The beam power for Ta and Nb remained the same for all three depositions while the beam power for Cr and Ti was changed after the deposition of sample BRC523. Samples BRC523 and BRC524 were deposited for 30 minutes while BRC525 was deposited for 60 mins. The reason for the increased deposition time for BRC525 was to deposit a sample thick enough to conduct nano-indentation hardness testing that was not influenced by substrate properties. Thus, this sample was used to investigate the composition, crystal structure, and modulus/hardness of the deposited films. The beam power allocation for sample BRC525 was the same as BRC524. However, the Cr source rod for sample BRC 525 remained stationary (the feed rate was zero).

Table 7. Beam power allocation, source rod feed rate, substrate temperature, He flow rate, and deposition time for quaternary RCCA experiments

	Ta **Feed Rate** (mm/min)	**Nb** **Feed Rate** (mm/min)	**Cr** **Feed Rate** (mm/min)	**Ti** **Feed Rate** (mm/min)	**Ta** **Power** (kW)	**Nb** **Power** (kW)	**Cr** **Power** (kW)	**Ti** **Power** (kW)
BRC523	0.4	0.4	0.2	0.4	2.13	2.15	0.07	0.37
BRC524	0.4	0.4	0.1	0.4	2.13	2.15	0.19	0.35
BRC525	0.4	0.4	0	0.4	2.13	2.15	0.19	0.35

7.2.2 Characterization

Scanning electron microscopy (SEM) and energy dispersive X-ray spectroscopy (EDS) were used to determine the gradient in composition of the libraries. The observations were made at the five locations shown in Figure 43 and were made using a Helios NanoLab DualBeam microscope (Thermo Scientific, Hillsboro, OR) fitted with an X-MaxN 150 SDD (Oxford Instruments, Concord, MA). Surface microstructure was characterized using the SEM in secondary electron (SE) imaging mode using a high-performance ion conversion and electron (ICE) detector. The compositional variance across an array on the sample surface was determined using EDS with a high accelerating voltage of 20 kV to delineate any overlapping X-ray emission peaks of the refractory metals used. The film thickness was determined from SEM images of Focused Ion Beam (FIB) cross-sections on sample BRC525.

The crystal structures of BRC525 libraries were determined by X-ray diffraction using a PANalytical Empyrean (Malvern PANalytical, Westborough, MA) instrument. XRD was performed on only sample BRC525 due to its deposition time being double that of the other two samples (60 mins compared to 30 mins). The instrument was used in 2D mode using a Cu-K$_\alpha$ source and Bragg-Brentano micro-optics. The incident beam path was fitted with a 1/8° divergence slit, 2mm primary mask, ½° anti-scatter slit, with omega fixed to 15°. The area of interrogation influenced by the X-rays was approximately 5mm x 6mm due to the angle of incidence. Data were collected at diffraction angles (2θ) of 30 to 80° at a rate of 0.12°/s. An alignment camera was used to ensure the positioning of the beam optics on the samples surface. XRD data were collected at five locations shown in Figure 43.

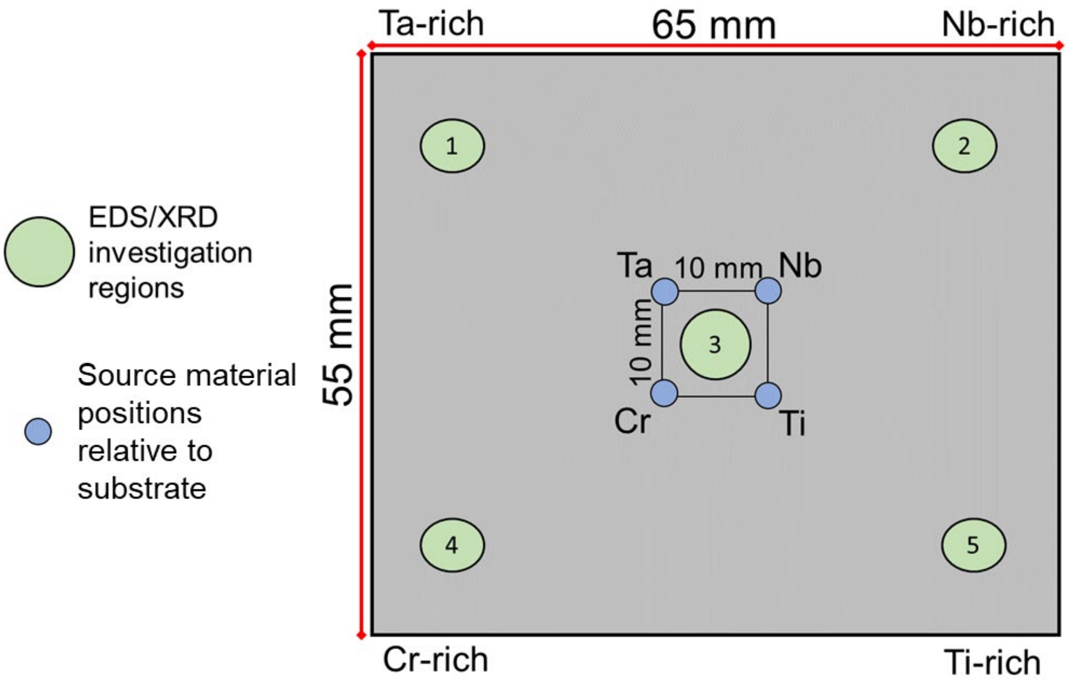

Figure 43. Locations on the combinatorial libraries where the five EDS/XRD measurements were made (green) with respect to the relative positions of the four source materials (blue).

Oxygen content of sample BRC523 was investigated using a Versaprobe XPS (Physical Electronics, Chanhassen, MN). The center of the sample was investigated using a 3 keV Ar sputtering over a 3 x 3 mm^2 area by Catherine A. Dukes (University of Virginia Laboratory for Astrophysics and Surface Physics Director). The XPS chamber reached a base pressure of $6x10^{-8}$ Pa after bakeout and cooling. The surface was pre-sputtered for 2 cycles removing approximately 3 nm to remove any contaminates. The total sputtering time was split into thirteen 10-minute cycles (130mins total) resulting in a depth analysis of 130 nm – 990 nm of the films surface.

7.3 Results

7.3.1 Compositional Variance

The composition determined by EDS analysis for samples BRC523 – BRC525 at the locations labeled 1-5 in Figure 43, are summarized in Table 8. The tabulated data show the differing atomic concentrations of Ta, Nb, Ti, and Cr as a function of substrate position for each sample. It can be seen that in the same region of interrogation, the relative amounts of each constituent element change as a function of sample, and therefore, beam power allocation, Table 7. To interpolate the values between each position, the average between two positions was taken for each constituent element to determine the value halfway between each dataset. The actual compositions at each point are likely to slightly vary from these estimates.

Table 8. EDS compositions determined at positions 1 - 5 on RCCA library samples

	Position 1 (Ta – rich)	**Position 2 (Nb – rich)**	**Position 3 (Center)**	**Position 4 (Cr – rich)**	**Position 5 (Ti-rich)**
BRC523 (at %)	Ta – 36.3 Nb – 26.4 Ti – 29.8 Cr – 7.4	Ta – 26.5 Nb – 34.2 Ti – 35.5 Cr – 3.9	Ta – 29.4 Nb – 26.1 Ti – 38.2 Cr – 6.4	Ta – 29.9 Nb – 20.6 Ti – 37.8 Cr – 11.7	Ta – 18.4 Nb – 27.2 Ti –49.5 Cr – 4.9
BRC524 (at %)	Ta –32.7 Nb – 26.7 Ti – 22.2 Cr – 18.4	Ta – 25.6 Nb – 35.7 Ti – 26.4 Cr – 12.5	Ta – 27.9 Nb – 27.7 Ti –27.8 Cr – 16.7	Ta – 24.3 Nb – 21.3 Ti – 30.4 Cr – 24.0	Ta – 18.1 Nb –28.7 Ti – 36.2 Cr – 17.0
BRC525 (at %)	Ta –37.3 Nb – 28 Ti – 34.3 Cr – 0.5	Ta – 26.3 Nb – 34.6 Ti – 38.8 Cr – 1.0	Ta – 29.6 Nb – 28.0 Ti – 42.3 Cr – 0.5	Ta – 31.9 Nb – 23.8 Ti – 44.3 Cr – 0.5	Ta – 18.1 Nb – 34.6 Ti – 52.2 Cr –0.5

Figure 44 shows maps of the elemental concentration for sample BRC523 and indicates the chromium content was of relatively low concentration. The average compositions with standard deviations were 27.96 ± 5.30 at% for Ta, 38.16 ± 5.81 at% for Ti, 26.99 ± 3.95 at% for Nb, and 6.91 ± 2.43 at% for Cr. The largest compositional variance across the library was 19.7 at% for Ti. The center composition of this library was 38.2 at% Ti, 29.4 at% Ta, 26.1 at% Nb, and 6.4 at% Cr.

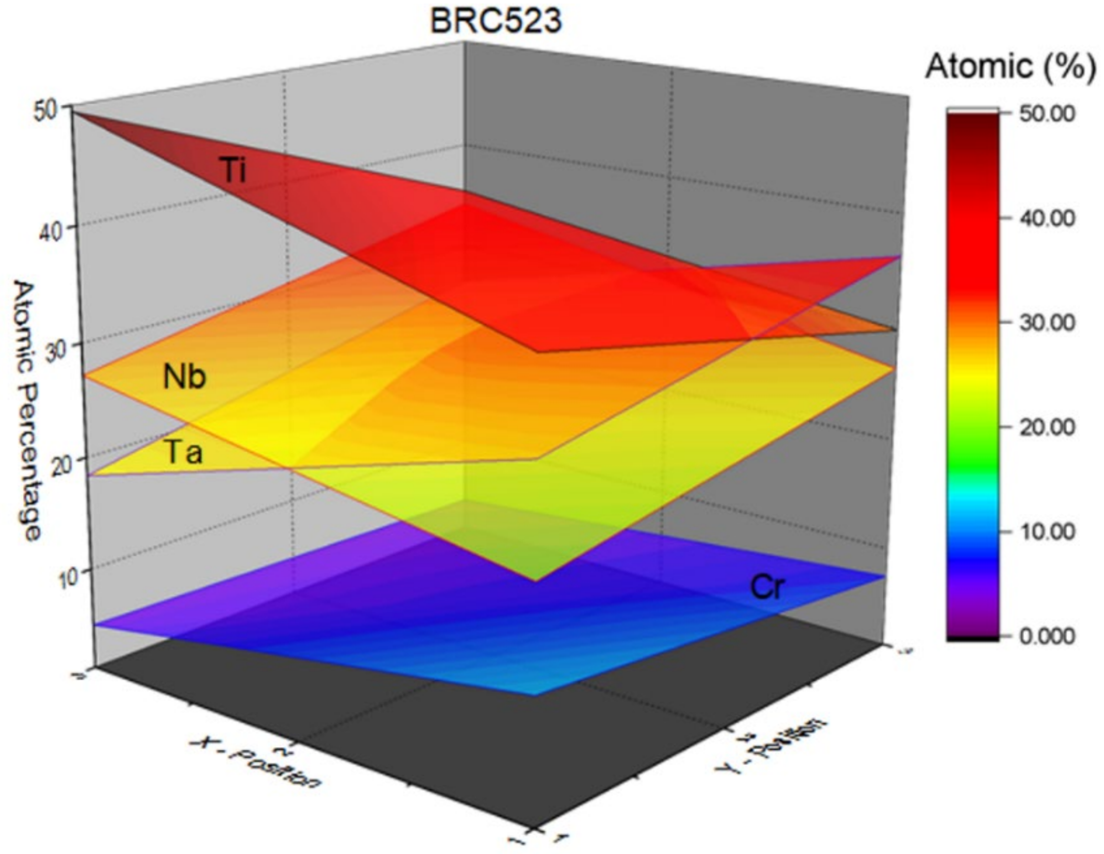

Figure 44. Sample BRC523 showing Ti-Ta-Nb-Cr coatings deposited with chromium content in relatively low concentration

Figure 45 shows compositional maps for sample BRC524 with a higher chromium content than BRC 523. The average compositions with standard deviations were 25.48 ± 4.32 at% for Ta, 28.69 ± 4.22at% for Ti, 28.10 ± 4.21 at% for Nb, and 17.83 ± 3.37 at% for Cr. The largest compositional variance observed was 14.6 at% for Ta. This sample's center composition was 27.8 at% Ti, 27.9 at% Ta, 27.7 at% Nb, and 16.7 at% Cr, and was therefore close to an equiatomic concentration which maximizes the entropy stabilization criterion.

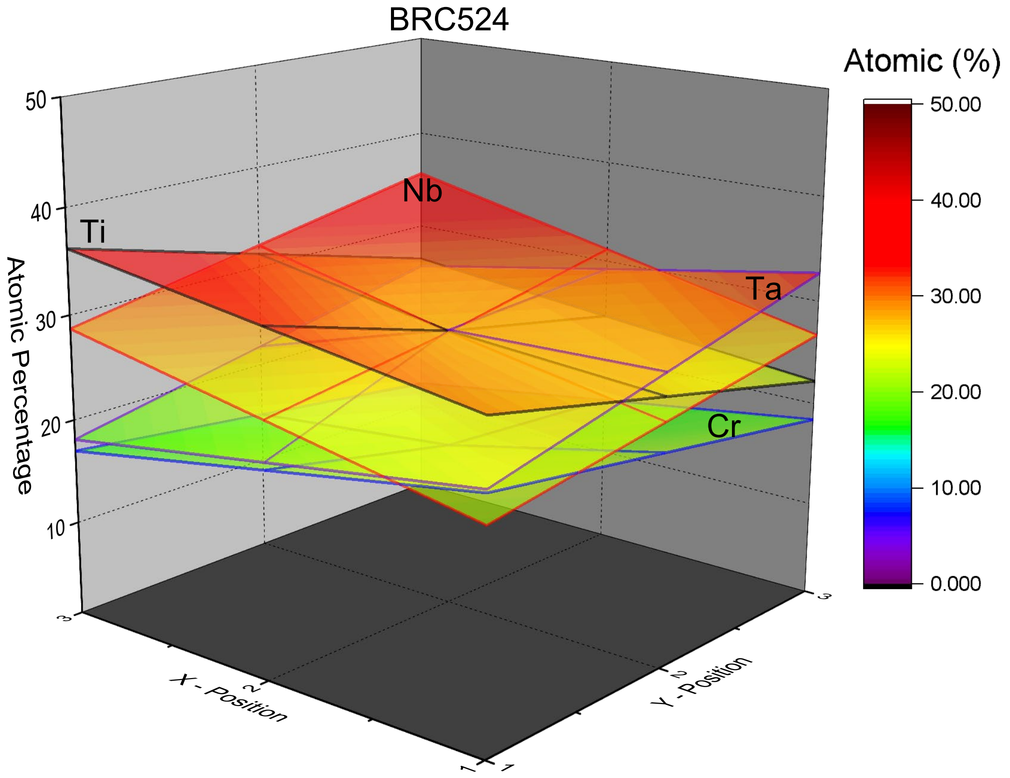

Figure 45. Sample BRC524 showing Ti-Ta-Nb-Cr coatings deposited with higher chromium content

Figure 46 shows sample BRC525 with very low chromium content with the other three constituent elements nearing equiatomic. The average compositions with standard deviations were 28.53 ± 5.80 at% for Ta, 24.39 ± 5.44at% for Ti, 28.87 ± 3.16 at% for Nb, and 0.56 ± 0.16 at% for Cr. The largest compositional variance observed was 17. 9at% for Ti. This sample's center composition was 42.3 at% Ti, 29.6 at% Ta, 28.0 at% Nb, and 0.5 at% Cr.

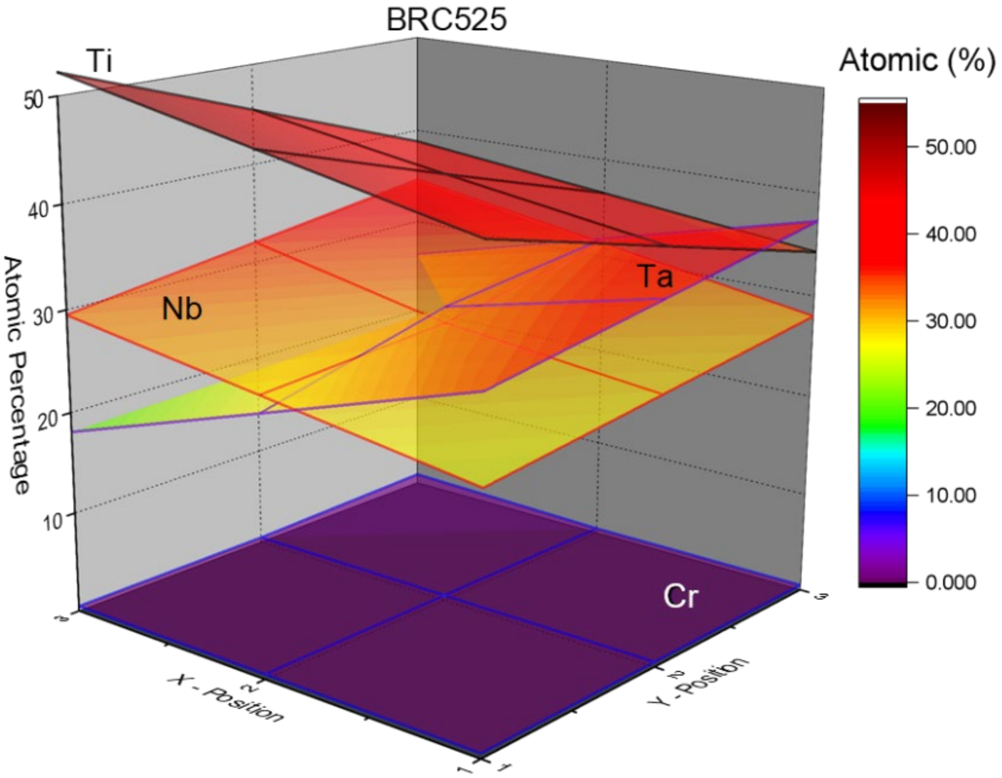

Figure 46. Sample BRC525 showing Ti-Ta-Nb-Cr coatings deposited with chromium content with almost no chromium present

7.3.2 Microstructure

SEM images of the surface of the samples taken in the data collection positions 1-5, Figure 43, can be seen in Figure 47 for BRC523, Figure 48 (BRC524), and Figure 49 (BRC525). The microstructure of the coating changes as the composition of the coating changes, where compositions with a higher concentration of elements of lower melting points (e.g., higher concentration of titanium and/or chromium) are more faceted, while compositions with a greater concentration of the higher melting point elements (e.g., higher concentration of niobium and/or tantalum) show a "cauliflower"-like microstructure. As discussed later, this observation is consistent with the zone diagram in Chapter 6, Figure 37.

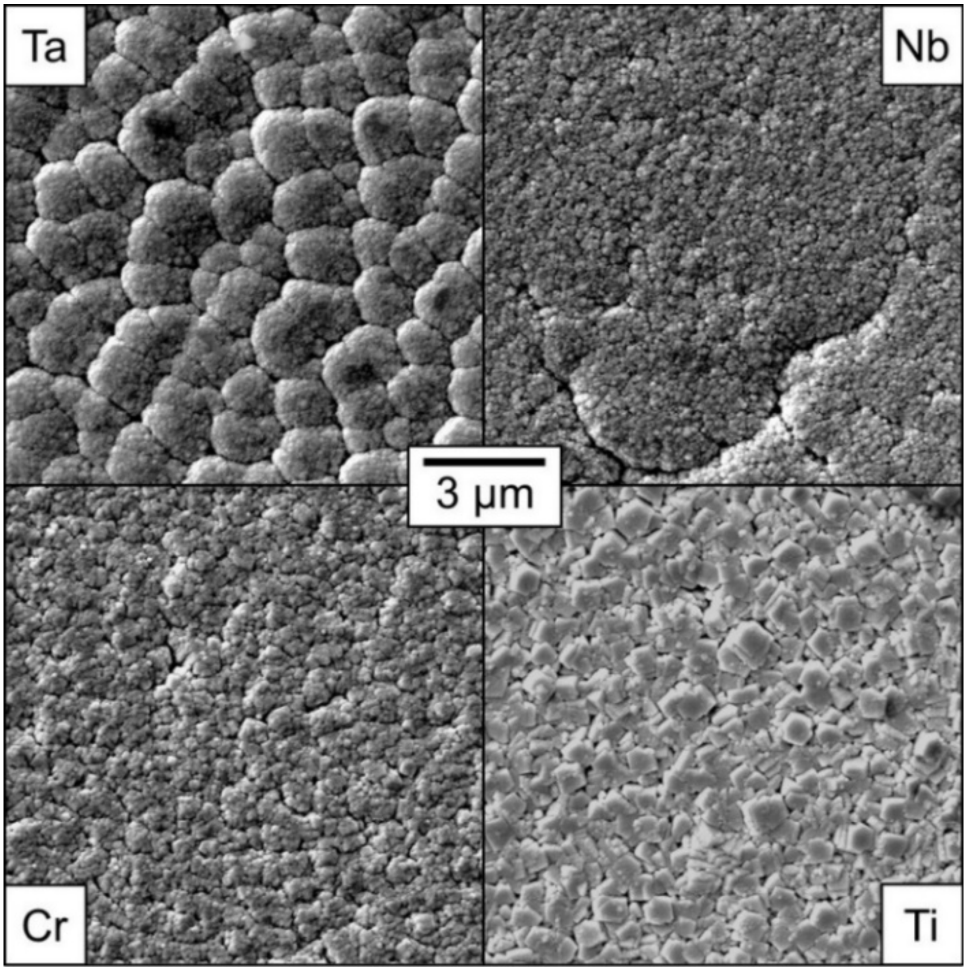

Figure 47. Microstructure of the surface of the BRC523, showing a more faceted microstructure in the Ti- and Cr-rich areas, and a "cauliflower"-like microstructure in the Nb- and Ta-rich areas

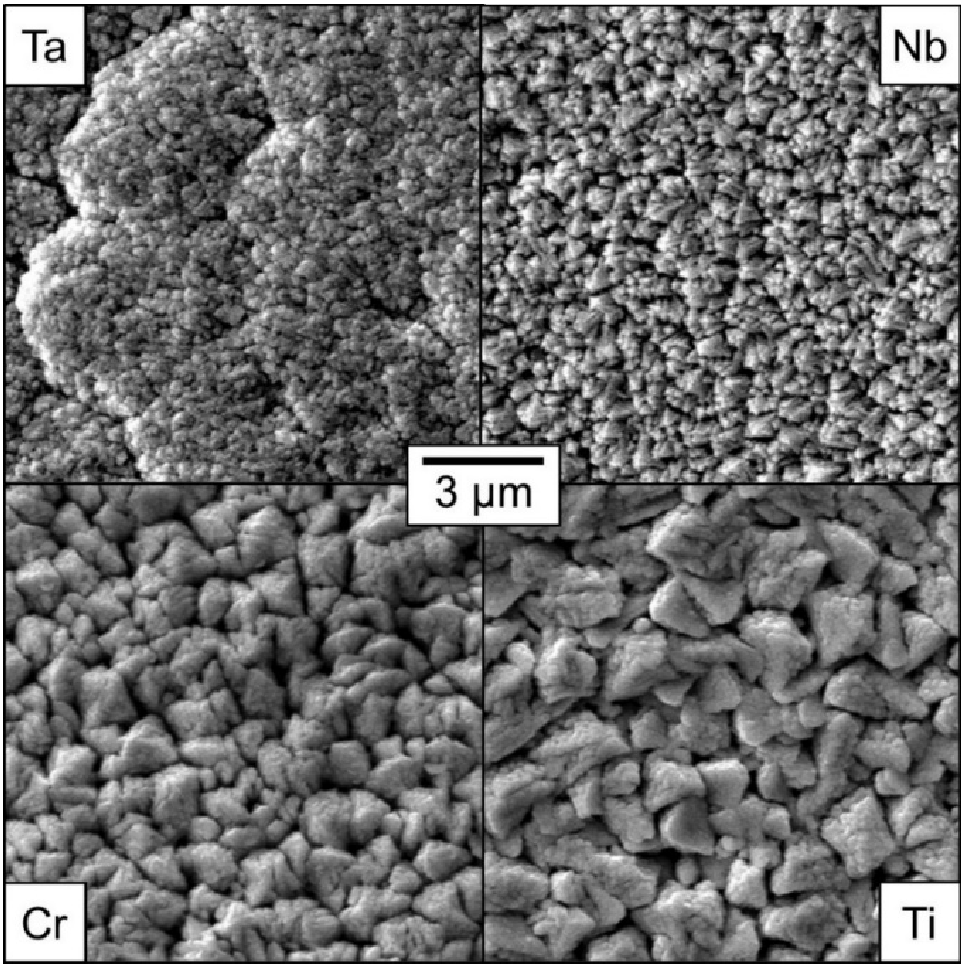

Figure 48. Microstructure of the surface of BRC524.

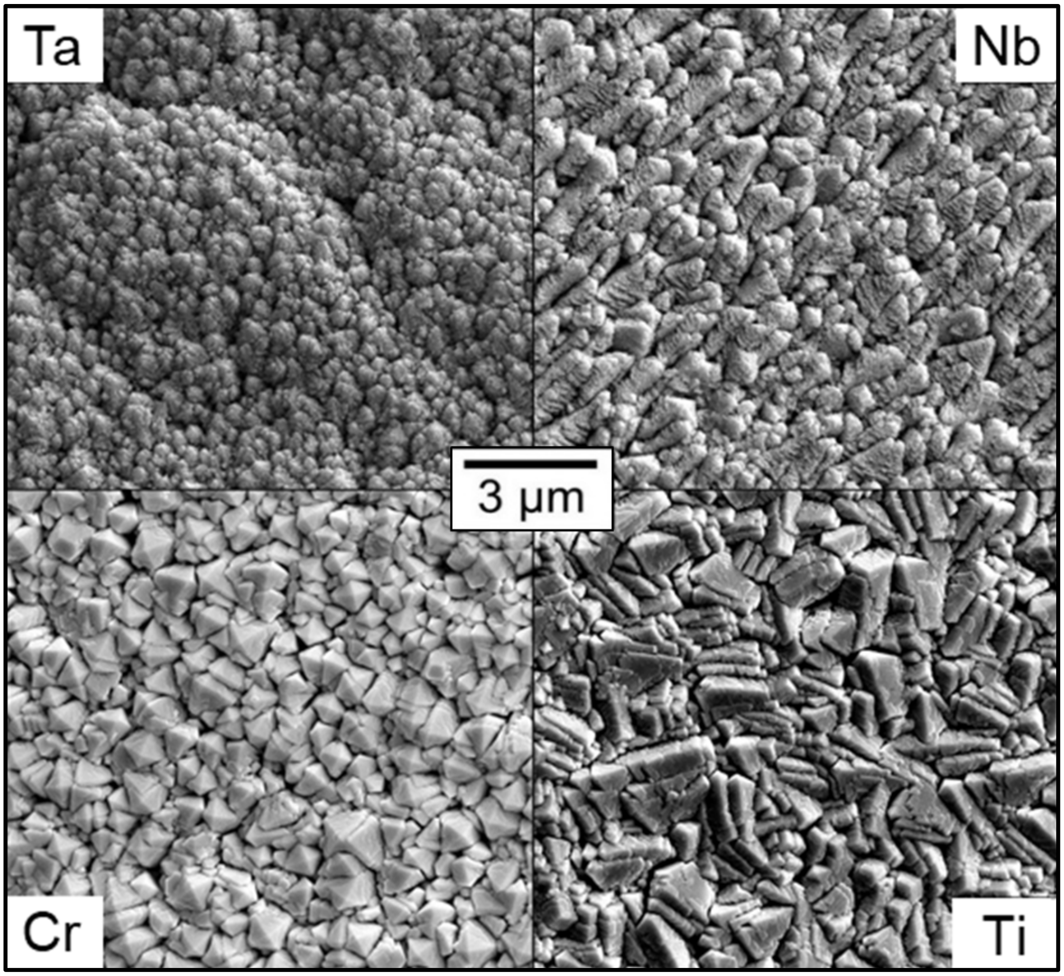

Figure 49 - Microstructure of the surface of the chromium-deficient sample (BRC525), showing a more faceted microstructure in the Ti- and Cr-rich areas, and a "cauliflower"-like microstructure in the Nb- and Ta-rich areas

In order to preserve the majority of the sample for future measurements, the thickness of BRC525 was measured by removing a small region of the sample using a SEM equipped with a focused ion beam (FIB) until the Mo substrate was reached, Figure 50, to keep the sample intact for other property measurements. The thickness of the chromium deficient coating (BRC525) was found to be ~22.5 µm at the center of the film. The substrate interface was determined by SEM image contrast as well as an EDS line scan determining the transition from a TaNbTiCr film to a Mo substrate.

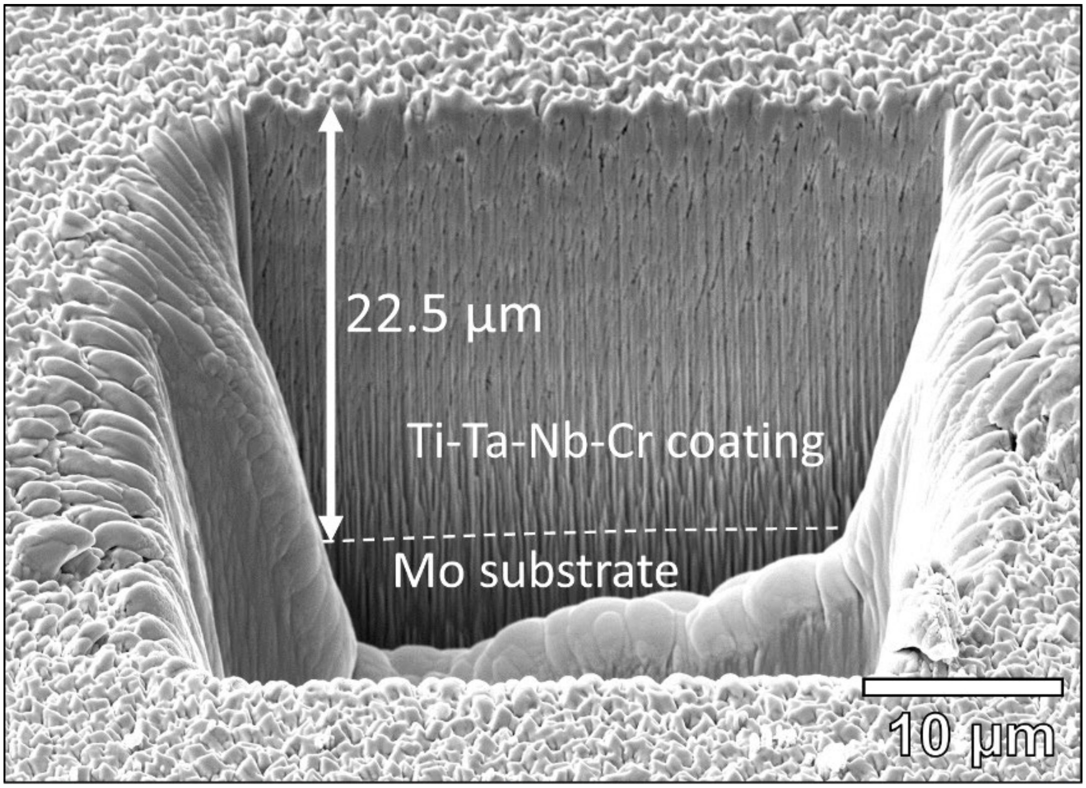

Figure 50 - Coating thickness of BRC525 measured by removing coating material at the center of the sample using FIB, finding a coating thickness of ~22.5 µm. The white dotted line was added to indicate the interface between the substrate and coating.

7.3.3 Crystal structure of BRC525

X-ray diffraction (XRD) was used to investigate the crystal structures of the deposited coating. Figure 51 shows the XRD patterns for the five regions of BRC 525 together with the deduced reflections for each peak. The data indicates that all regions of this sample had a BCC structure,

Figure 51. Investigation of the Ti, Nb and center of the sample revealed a strong <110 > reflection, a peak at <200> and a peak at <211>, indicating a preferential growth direction of <110>. The Ti and Nb corner also showed <110>, <200> and <211> peaks associated with the Mo substrate; a possible result of thinner film region in the Nb corner and higher X-ray penetration where the Ti concentration was highest. At the Ta-rich corner of the sample, the <110> peak is the largest, while a <211> was present but no discernable <200> peak could be found. In the corner of the sample situated above the Cr source material, there is only a strong <110> reflection while the <200> and <211> peaks are absent. The strong presence of <110> peaks in each scan pattern shows a strong texturing of the produced film in the <110> direction.

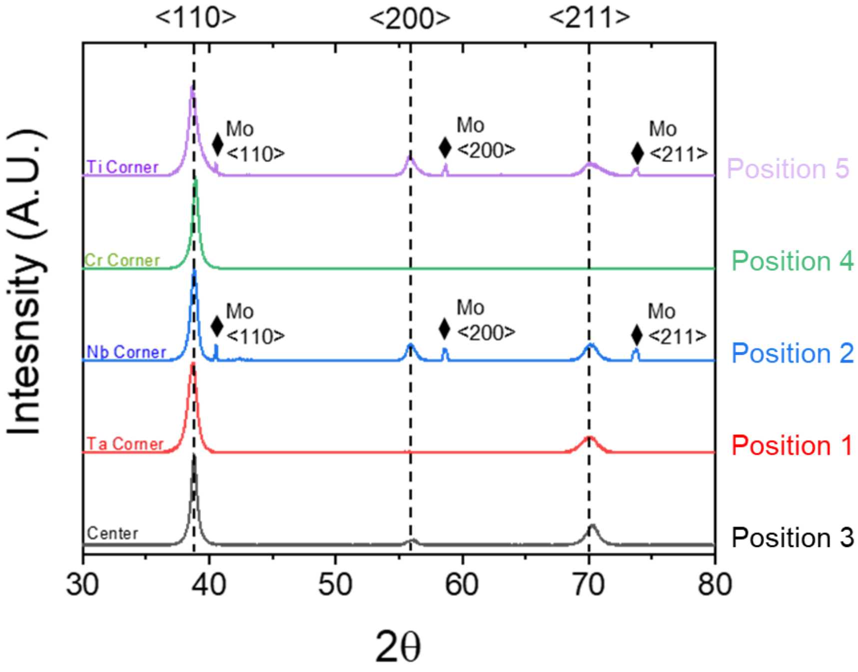

Figure 51. XRD plots of the Ti-Ta-Nb-Cr coating (BRC525) indicating a strong preferential <110> orientation.

7.3.4 XPS of BRC523

Oxygen mitigation is important to avoid forming oxides and increasing interstitial oxygen content during film growth. At temperatures above 1200 °C, metals such as Ta and Nb have roughly 5 at% oxygen interstitial solubility while titanium has almost 35 at% (212–217). On the other hand, Cr and Mo have less than 1 at% oxygen solubility (216–218). Therefore, significant oxide formation could occur in RCCAs made via the DVD process.

The introduction of some oxygen during vapor deposition is inevitable unless ultrahigh vacuum (pressure $<10^{-5}$ Pa) conditions are used and the entire interior surface of the test system had been baked out prior to deposition to desorb residual water vapor adsorbed on the interior of the system and its source materials. While significant effort was made to reduce the adsorbed water in the EB-DVD system, not all regions of the interior chamber could be heated and the lowest base pressure achievable during the bake out at 120 °C was 10^{-3} Pa. In addition, the He gas jet is also an inevitable source of oxygen. This was reduced by using 99.99% purity He (grade and supplier) and using an oxygen gettering system which lowers the amount of oxygen introduced via the carrier gas. Additional details can be found in Appendix B.

Measuring oxygen content in refractory metal coatings is not simple since the coatings are columnar and have a high surface area that when exposed to the atmosphere can adsorb water vapor and oxygen. As described in Appendix B, several mitigation techniques were developed to lower the likelihood of oxygen dissolution and oxide formation. In order to determine the oxygen content in the thin films produced, initial X-ray photoelectron spectroscopy (XPS) was performed on BRC523. BRC525 was not chosen so that other characterization methods can be explored;

however, BRC523 was used to determine the relative amounts of oxygen within the films produced under the same EB-DVD chamber conditions.

Figure 52 shows XPS spectra as a function of sputtering time and ultimately the sputtering depth (~990 nm at 130 mins). Each line represents the individual element detected. It can be seen in Figure 52 that after approximately 2 cycles, the oxygen concentration reduced from approximately 34 at% to 23 at%, where it effectively leveled out indicating likely high levels of interstitial oxygen since no oxide peaks were observed by XRD.

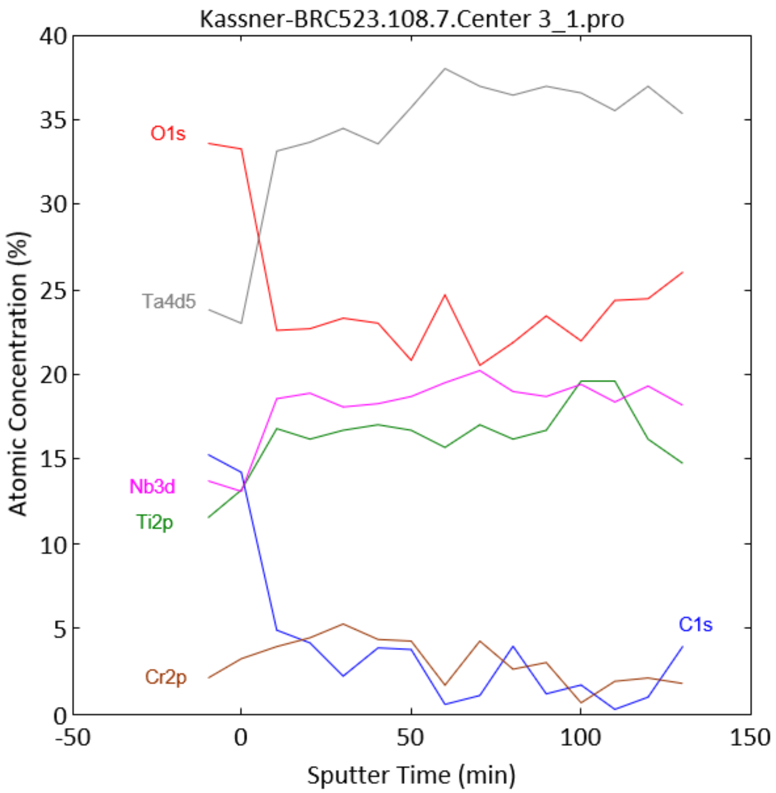

Figure 52. XPS depth profile of sample BRC523 for a depth range of 132-990nm (based on SiO$_2$)

There is potential for the oxygen that is emitted from the sample during sputtering to be back deposited back onto the film resulting in a larger oxygen count than the film actually has. Furthermore, using XPS to study a textured surface could lead to differential etching and double counting surface oxygen. To adequately determine the oxygen content within a film, a surface with low roughness/texturing would help in differentiating from surface oxygen verses interstitial oxygen content.

7.4 Discussion

7.4.1 Library compositional compositions

The compositional variance of the deposited RCCA films is dependent on the He flow conditions which determine the speed of the metal atoms during propagation from the metal evaporation surface to the substrate, the electron beam power allocation to each source rod which determines the metal atom flux from each source, and the distance the vapor must propagate to reach the substrate. Manipulating and controlling these parameters enables tuning of the composition and composition gradient within the combinatorial libraries and was shown capable of yielding samples with near equiatomic concentrations at the center of the sample, as shown in Figure 45.

Without changing the He flow conditions, electron beam power allocations (Table 7), or the distance to the substrate, the compositional variance of sample BRC524 differed from that of BRC525. The feed rate of the Cr source rod was altered from BRC524 to BRC525. The reasoning for this was that the Cr source rod does not form a melt pool (shown in Figure 53) while evaporating and, therefore, with continuously feeding, the center-to-center distance between source materials changes. Cr has a melting temperature of 1863 °C, at which it has a vapor pressure over 1 Bar. However, it can be seen in Figure 33 that at temperatures as low as 1400 °C, Cr has a saturation vapor pressure of 1 Pa. Therefore, sufficient vapor pressures for EB-DVD depositions can occur prior to the melting temperature for Cr. This phenomena has been reported in other PVD applications for Cr (219,220).

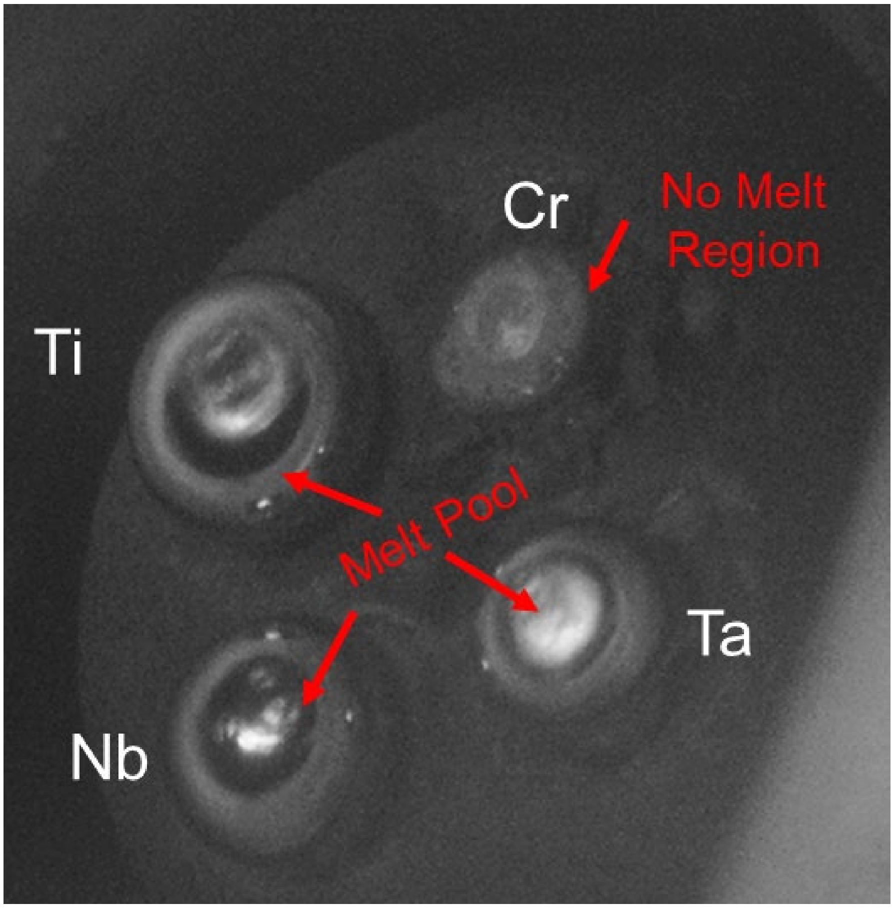

Figure 53. Image of the crucible for BRC524 post deposition showing Ti, Nb and Ta having solidified melt-pools while Cr shows just a degraded surface.

The radiative heating from source to source is a function of the center to center distance between source materials, the temperature of the source material, and the surface area exposed to the radiative heating flux from source to source. This is given by the Stefan-Boltzmann law of radiation:

$$\frac{Q}{t} = \sigma \varepsilon A [T_1^4 - T_2^4] \tag{29}$$

where Q/t is the rate of heat transfer by emitted radiation, σ is the Stefan-Boltzmann constant, ε is the emissivity, and T is the absolute temperature of the two heat sources. It can be seen that the radiated heat flux proportional to the emissivity and the temperature to the fourth power. Therefore, as the amount of a source in the field of view of an emitting surface increase, the radiative heat flux increases.

The source materials initially start with center-to-center distances equal, Figure 54 (a). At this point, the area in view surfaces of the source materials is relatively low. However, the distances can slightly change during deposition. This change in center-to-center distance, illustrated in Figure 54 (b), alters the area fraction within the view of a hot source material and therefore changing the radiative heating from source to source, thus changing the effective temperatures of the source material. For sample BRC 524, the Cr rod was continuously fed even though a sustainable melt pool was never formed while BRC525, the Cr source rod was not fed, but held at a constant position. Since the source rods are angled towards the center of the crucible, the center-to-center source rod distances changed overtime and, consequently, the surface area of the Cr source rod exposed to the Ta source rod increased as a function of time. This change in exposed surface area changed the radiative heating effects from source to source and change the effective vapor pressure at a fixed electron beam allocation. In order to effectively control the compositional variance of a sample being deposited, source rod feed rate and electron beam allocation must be held constant when an equilibrium is reached; or, direct compositional analysis of the vapor plume being produced must inform the electron beam power and material source feed rate to achieve a constant compositional variance.

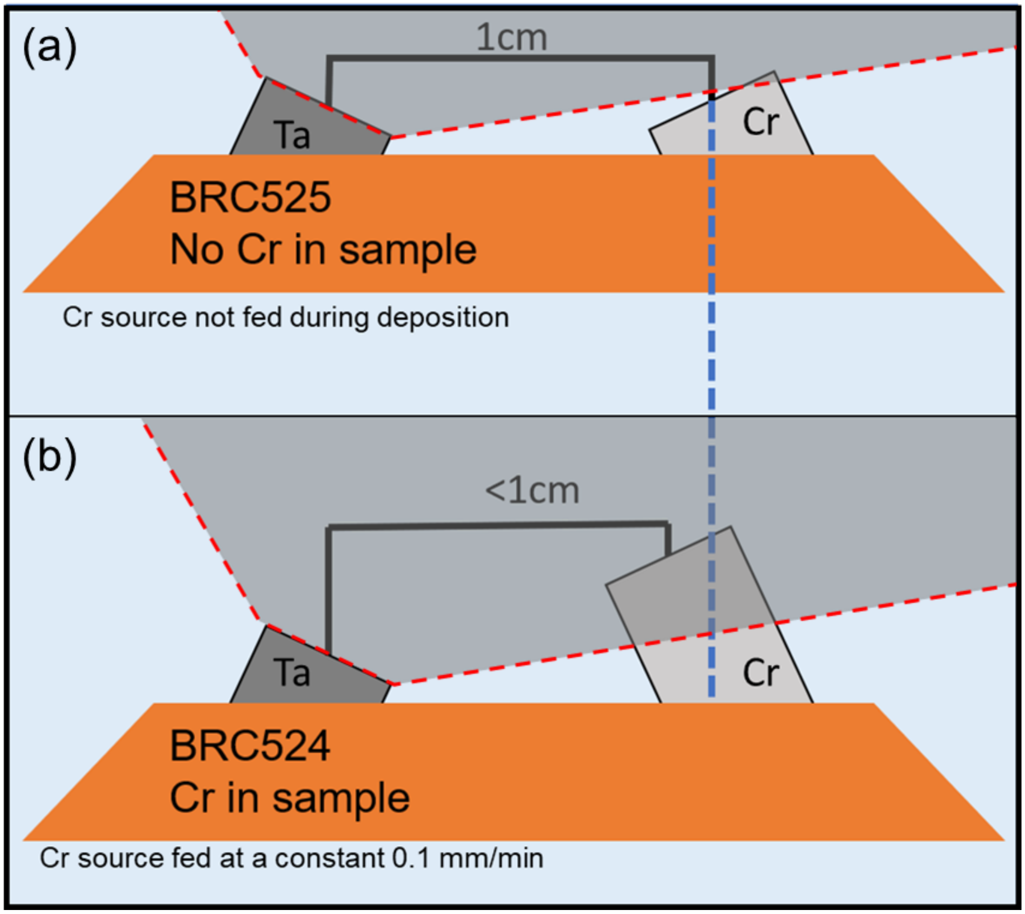

Figure 54. Change in center-to-center distance for a source rod not fed vs a source rod continuously fed.

8.4.2 Microstructural Dependency on Composition and Temperature

The microstructures of RCCA libraries deposited using the electron beam directed vapor deposition technique are highly dependent on the composition and the temperature of the substrate. The influence of the vapor is addressed below. The linkage between the melting temperature of the metals and their assembly to form a coating microstructure arises from the linear relationship between the binding energy of atoms to a metallic surface (and thus their mobility on a heated surface) and the melting temperature of a metal (221,222). The T_M for the materials used in this set of libraries were 2996 °C (3269 K) for Ta, 2468 °C (2741 K) for Nb, 1875 °C (2148 K) for Cr and 1668 °C (1941 K) for Ti. As shown in Figure 37, a high melting point and therefore high cohesive energy results in a low surface atom mobility during the assembly of a coating. Atoms that arrive at non-normal angles to the surface then accumulate at local high points on a surface and insufficient diffusion into the shadowed valleys between them results in void formation (221,222).Consequently, the porosity and microstructure of an EB-DVD coating are strongly dependent on the homologous temperature (T/T_M) at which deposition occurs, as well as the rate of arrival of atoms, their impact and potential energies and the direction of arrival of the atoms which depends upon the background pressure and other flow conditions of the DVD process (178)

Binary phase diagrams for (a) Ta-Ti (223), (b) Nb-Ta (224), (c) Cr-Ta (225), (d) Ti-Nb (226), (e) Ti-Cr (226), and (f) Cr-Nb (227) can be seen in Figure 55. It can be seen that the Nb-Ta and Ti-Nb systems have a T_M that can be approximated a ROM model while the other binary alloys of the elements used in this library have more complex binary phase diagrams with eutectics, eutectoids, and intermetallic compound formation. For example, the Ti-Ta is predicted to have both HCP and BCC phases present, Figure 56 (a), while the Ti-Nb system, Figure 56 (d) show complete solid solubility with a BCC phase above about 800K. However, Ti-Cr forms intermetallic $TiCr_2$, while the Cr-Ta system forms $TaCr_2$ and the Nb-Cr system $NbCr_2$. It is shown in Figure 51 that no intermetallic phases were present; therefore, the EB-DVD library synthesis approach suppressed the formation of intermetallic phases.

To gain further insight into the libraries assembly processes, the homologous temperature for all the compositions can be approximated by the simple ROM estimate can be used to investigate trends between the microstructure of the film and its composition. It is understood that this is only a rough approximation and real melting temperatures will likely deviate from these calculations; however, the ROM approximation is sufficient for initial understanding of the EB-DVD processing condition effects on the film's microstructure as a function of substrate temperature. Future studies should include modeling approaches to help identify optimum substrate temperatures for alloys of interest.

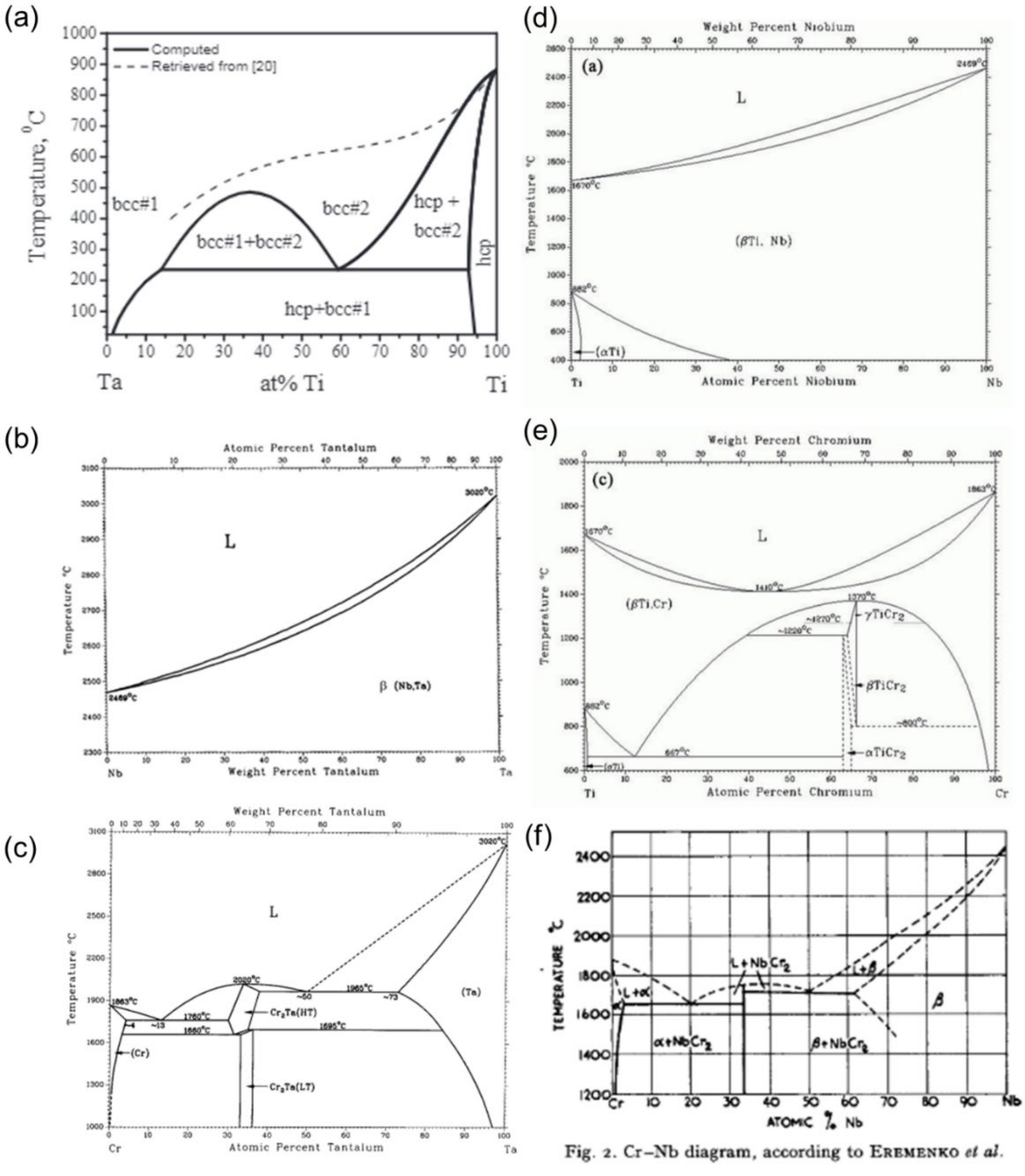

Fig. 2. Cr–Nb diagram, according to EREMENKO *et al.*

Figure 55. Binary phase diagrams of (a) Ta-Ti (223), (b) Nb-Ta (224), (c) Cr-Ta (225), (d) Ti-Nb (226), (e) Ti-Cr (226), and (f) Cr-Nb (227)

The T_M based on ROM calculations for sample BRC523 shows a range from 2140 °C (2413 K) to 2378 °C (2651 K), Figure 56. The sample substrate was set to 1250 °C (1523 K). The percentage of the samples set temperature relative to the calculated ROM T_M is shown in Figure 56. Based on the ROM calculations the microstructure for samples ranging from 57% T_M to 64% T_M should range from columnar to the beginning stages of faceted growth. Figure 47 shows the Ta-rich area of the sample resembles a 'cauliflower' like structure while the Ti-rich area of the sample exhibits faceted growth. The transition in morphology is consistent with the change in average homologous temperature of each region and the zone empirical maps of Anders and others (185–188).

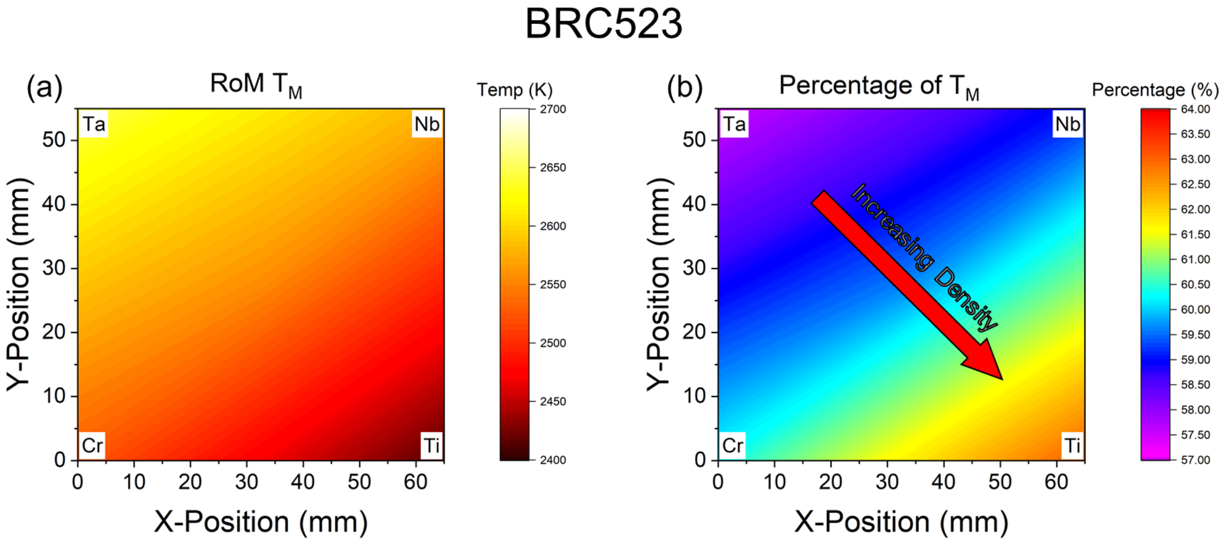

Figure 56. (a) Colored gradient showing the calculated T_M for sample BRC523 based on the composition found using EDS. (b) Percentage of T_M based on ROM calculations of T_M for BRC523 and sample substrate temperature of 1250 °C (1523 K).

Samples BRC524 and BRC525 follow a similar trend to that of BRC523 when the ROM calculations for the T_M based on the EDS data collected is used, Figure 57 and Figure 58. This is again in good agreement with the SEM images taken, Figure 48 and Figure 49, where the Ta-rich regions of the samples have a ‘cauliflower’ surface while the lower T_M regions such as Ti show more faceted growth. It is shown that the temperature at which the substrate is set as well as the T_M of the source materials greatly influence the microstructure of RCCA films deposited using the EB-DVD method. This illuminates the need for a densification process other than the hot-substrate approach. Further heating of the substrate becomes a challenge due to the increasing vapor pressure of each constituent element as T increases, Figure 33. The temperature required to densify Ta or Nb (greater than 1573 K) results in vapor pressures for Ti and Cr greater than 1 Pa. The consequence of this is the rapid evaporation of Ti and Cr from the deposited film, making the hot substrate approach infeasible for films with a large range of melting temperatures and vapor pressures.

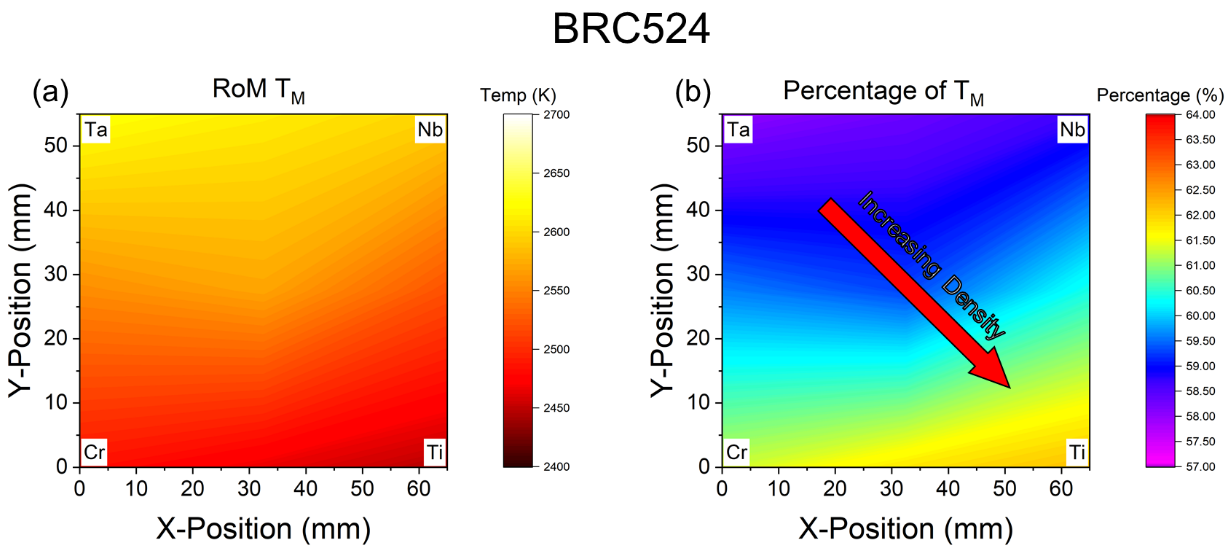

Figure 57. (a) Colored gradient showing the calculated T_M for sample BRC524 based on the composition found using EDS. (b) Percentage of T_M based on ROM calculations of T_M for BRC524 and sample substrate temperature of 1250 °C (1523 K).

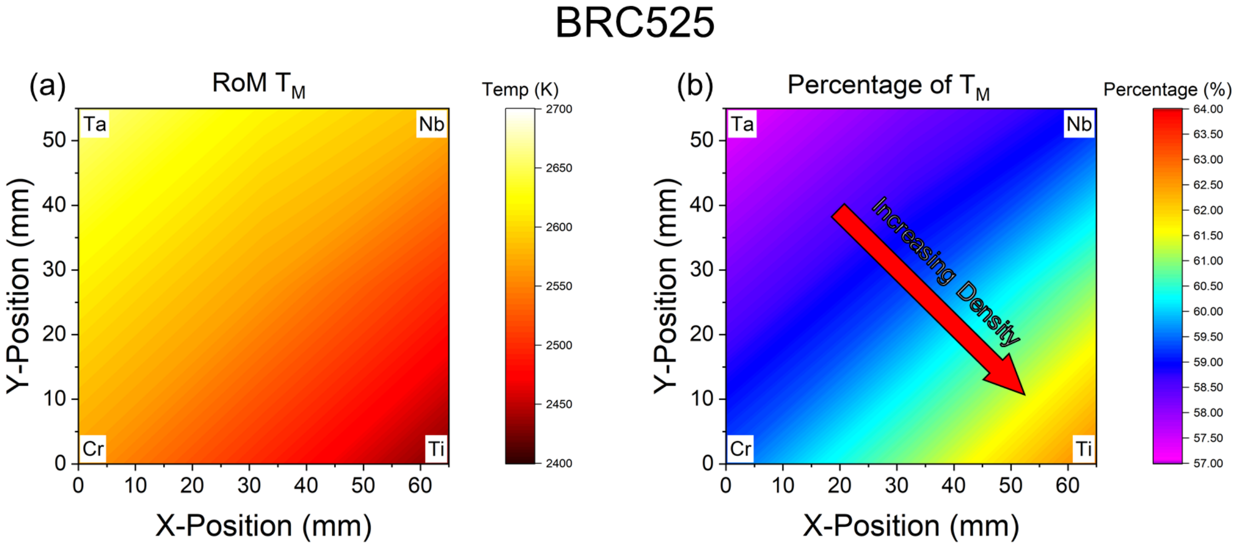

Figure 58. (a) Colored gradient showing the calculated T_M for sample BRC525 based on the composition found using EDS. (b) Percentage of T_M based on ROM calculations of T_M for BRC525 and sample substrate temperature of 1250 °C (1523 K).

8.4.3 Crystal Structure and Properties

The oxygen detected using XPS can be attributed interstitial oxygen, oxide formation, or back deposition of O_2 during the sputtering process. It should be noted that when sample BRC525 was investigated with XRD, Figure 51, there was no sign of oxide peaks and the film libraries showed metallic BCC peaks. Sample BRC525 and BRC523 were deposited under the same conditions with only a change in beam power allocation and time of deposition, Table 7. Therefore, the degree of oxygen content is expected to be similar. It was stated earlier that at temperatures around 1250 °C (the temperature of the substrate), metals such as Ta and Nb have roughly 5 at% oxygen interstitial solubility while titanium has almost 35 at% (212–217). On the other hand, Cr and Mo have less than 1 at% oxygen solubility. Sample BRC523 was a Ti-rich sample with a center concentration of 38.2 at% Ti, 29.4 at% Ta, 26.1 at% Nb, and 6.4 at% Cr. Assuming Ti has an oxygen solubility of 35%, Nb and Ta 5%, and Cr 0%, the ROM expected oxygen solubility would be approximately 16.2%. This is less than the 20-25% shown by XPS; However, it is difficult to differentiate adsorbed surface oxygen between sputtering cycles and interstitial oxygen content. At this point, the degree of interstitial oxygen has not been accurately determined; however, the lattice parameters as a function of surface position have been determined using Rietveld fitting for sample BRC525 and is compared to the mathematically determined lattice parameter to see the potential effect of oxygen interstitials on the expected lattice parameter.

Rietveld fitting was performed on the XRD spectra shown in Figure 51 using the High-Score post-processing software package to calculate the lattice parameter of the BCC phases observed across sample BRC525. The d-spacing for the Ta-rich corner was found to be 3.347 Å, Nb-rich corner was 3.327 Å, the center of the sample was 3.334 Å, the Cr-rich corner was 3.324 Å and the Ti-rich corner was 3.310 Å. As less of the larger-sized atoms (Nb, Ta) were present locally, the lattice constant was seen to decrease.

To investigate the interaction between the constituent elements and their effect on the observed lattice parameter, two methods of mathematically determining lattice parameters were implemented and their error to the measured value was assessed. The first implemented was Vegard's Law. It is noted that Vegard's Law indicates that at constant temperature, a linear relationship exists between the lattice constant of an alloy and the concentrations of its constituent elements (228). Vegard's Law is therefore a rule of mixtures (ROM) estimate for the lattice parameter. In the case of the BRC 525 library, room temperature lattice parameters of each of the pure BCC phase of the elements of interest are 3.31 Å for Ta, 3.30 Å for Nb, 2.88 Å for Cr, and 3.33 Å for Ti (229). The measured lattice parameter using XRD compared to the mathematically determined lattice parameter using Vegard's Law (ROM) is found in Table 9. It can be seen that Vegard's Law closely matches the experimentally determined lattice parameter for the Ta-Nb-Ti-Cr alloys (0.06 - 0.63% error).

Table 9. Lattice parameter of sample BRC525 determined experimentally by XRD and calculated using Vegard's Law (ROM) approach.

Conc. Of Elements	**Ta**	**Nb**	**Ti**	**Cr**	**Lattice Parameter**	**XRD (a_o)**	**ROM (a_o)**	**ROM Err (%)**
Position 1	0.319	0.238	0.443	0.005	**Position 1**	3.347	3.326	0.63
Position 2	0.373	0.280	0.343	0.005	**Position 2**	3.324	3.311	0.39
Position 3	0.296	0.280	0.423	0.005	**Position 3**	3.324	3.322	0.06
Position 4	0.181	0.295	0.522	0.005	**Position 4**	3.327	3.320	0.21
Position 5	0.263	0.346	0.388	0.010	**Position 5**	3.310	3.329	-0.57

The second method was based on an equation derived by Alonso et al. (230) based upon a mixture of solid solutions considering size factors of each element for the unit cell volume given as:

$$\begin{aligned} V = {} & Z[c_{Ta}V_{Ta} + c_{Nb}V_{Nb} + c_{Ti}V_{Ti}] + ZV_{Ta}[c_{Nb}\Omega_{Nb-Ta} + c_{Ti}\Omega_{Ti-Ta} \\ & + c_{Cr}\Omega_{Cr-Ta}] + ZV_{Nb}[c_{Ta}\Omega_{Ta-Nb} + c_{Ti}\Omega_{Ti-Nb} + c_{Cr}\Omega_{Cr-Nb}] \\ & + ZV_{Ti}[c_{Ta}\Omega_{Ta-Ti} + c_{Nb}\Omega_{Nb-Ti} + c_{Cr}\Omega_{Cr-Ti}] \\ & + ZV_{Cr}[c_{Ta}\Omega_{Ta-Cr} + c_{Nb}\Omega_{Nb-Cr} + c_{Ti}\Omega_{Ti-Cr}] \end{aligned} \tag{30}$$

where *Z* is the number of atoms in the unit cell (2 for BCC), c_i is the concentration of each element, V_i is the volume of each element, and Ω_{a-b} is the size factor interaction of atom *b* with respect to element *a*. The values for the elements of interest for *r*, *V*, and Ω_{a-b} are found in Table 10.

Table 10. Tabulated values for **r, V,** ***and*** **Ω_{a-b} with respect to Ta, Nb, Ti, and Cr.**

	Ta	**Nb**	**Ti**	**Cr**
r (Å)	1.626	1.625	1.614	1.423
V (Å^3)	18.01	17.98	17.65	12.00

Ω_{a-b}					
Ta-Nb	**Ta-Ti**	**Ta-Cr**	**Nb-Ta**	**Nb-Ti**	**Nb-Cr**
-0.0006	-0.007	-0.127	0.0006	-0.0061	-0.1260
Ti-Ta	**Ti-Nb**	**Ti-Cr**	**Cr-Ta**	**Cr-Nb**	**Cr-Ti**
0.0067	0.0062	-0.1207	0.1449	0.1443	0.1372

Since the XRD measurements showed all areas of interest on the film are a BCC phase, the lattice parameter can then be determined by taking the cube root of the unit cell volume:

$$a_o = \sqrt[3]{V_{unit\ cell}} \tag{31}$$

The size factor $\Omega_{a\text{-}b}$ and atomic volume V_i can be determined from the volume of each atom using the approach adopted by King (231):

$$V = \left({}^{\Omega_b}/{}_{\Omega_a}\right)^{\frac{1}{3}} - 1 \tag{32}$$

where $\Omega_{a\ or\ b}$ are the effective atomic volumes of element *a* and *b*. The tabulated interaction parameters, size factors, empirically determined lattice parameter and Alanso et al. calculated lattice parameters can be seen in Table 11.

Table 11. Lattice parameter of sample BRC525 determined experimentally by XRD and calculated using Alonso et al. approach.

Conc. Of Elements	**Ta**	**Nb**	**Ti**	**Cr**	**Lattice Parameter**	**XRD (a_o)**	**Alonso (a_o)**	**Alanso Err (%)**
Position 1	0.319	0.238	0.443	0.005	**Position 1**	3.347	3.207	4.18
Position 2	0.373	0.280	0.343	0.005	**Position 2**	3.324	3.202	3.67
Position 3	0.296	0.280	0.423	0.005	**Position 3**	3.324	3.202	3.67
Position 4	0.181	0.295	0.522	0.005	**Position 4**	3.327	3.205	3.67
Position 5	0.263	0.346	0.388	0.010	**Position 5**	3.310	3.209	3.05

It can be seen that the equation proposed by Alanso considering size factors determined by King shows a greater error (3.05 - 4.18%) than that of Vegard’s Law (0.06 - 0.63% error). The plotted measured XRD lattice parameter and the calculated values determined by Alonso et al. and Vegard’s Law as a function of position on substrate (Figure 43) is shown in Figure 59. It is immediately evident that Vegard’s Law more closely determines the measured lattice parameter than that proposed by Alonso et al.

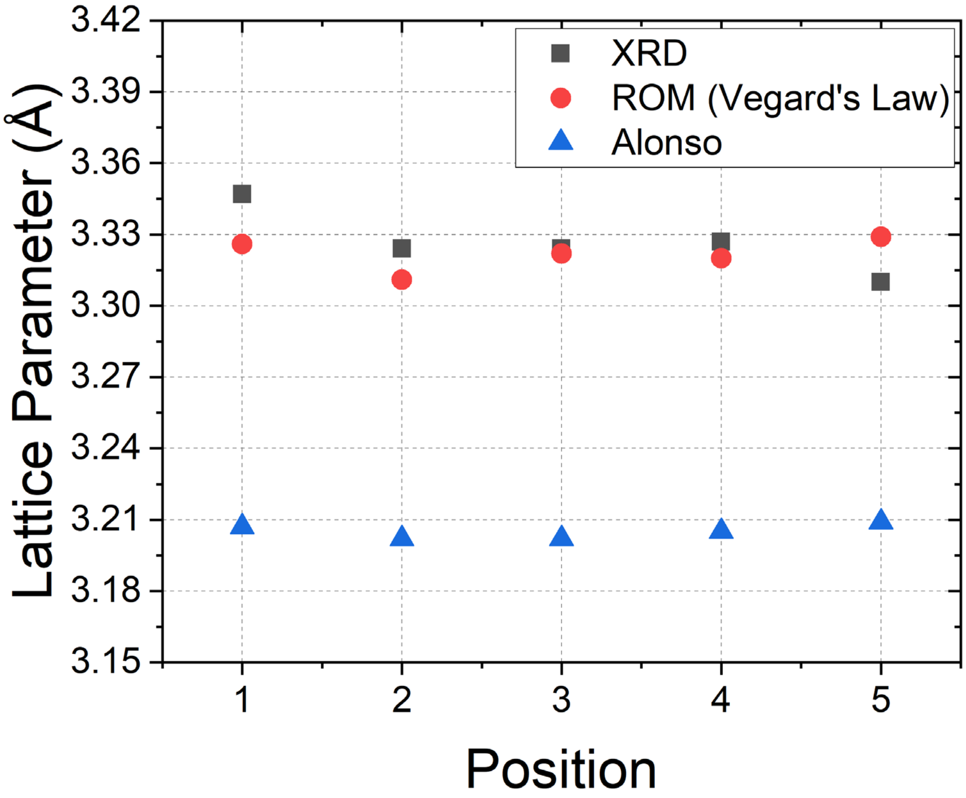

Figure 59. Lattice parameter as measured by XRD Rietveld analysis compared to calculated values determined using ROM (Vegard's Law) and Alonso et al. approach (230).

Composition was determined by EDS analysis where an average sampling over an area is made. XRD also samples an average crystal structure, and consequently, lattice parameter for the same region of interest. In a solid solution, if Ta-Nb-Ti-Cr occupy random lattice sites within their measured composition in a given area, statistically the average lattice parameter determined empirically should be closely related to the ROM calculations. It is well known that the inclusion of oxygen interstitials will increase the lattice parameter (232–234). It was shown that the films deposited could have up to approximately 20 at% oxygen concentration. The discrepancy in the calculations made are likely due to the inclusion of interstitial oxygen atoms which can change the lattice parameter up to 1% for titanium (234).

7.5 Conclusions

It has been shown that four source evaporation of combinatorial refractory metal libraries is possible using the EB-DVD method.

1. Near equiatomic films with compositions based upon Ta-Nb-Ti-Cr have been synthesized with fine control of source rod surface temperatures and helium flow conditions.
2. The center-to-center distance between source materials effects the surface temperature of each source. The drastically different melting temperatures of each source lead to changes in evaporation rate due to the radiative heating from source to source. When center to center distances change, the effect of surface temperatures changes and therefore the evaporation rate changes for each source.

3. The melting temperature of various compositions directly determines the microstructure of the film. Large variations of melting temperatures are expected in film libraries containing more refractory elements such as Ta and Nb and less refractory elements such as Ti and Cr. Because of this, the hot substrate approach is insufficient for film densification since the T/T_M is a function of composition/position on the substrate.
4. The measured lattice parameter can be closely predicted for the TaNbTiCr libraries made using Vegard's law.

The materials library approach requires high-throughput characterization to down select material candidates with optimized properties. High-throughput characterization techniques including XRD and XPS must be further developed for RCCA libraries to improve upon quick scanning of material candidates. Further investigation of this behavior is then done on selected monolithic materials synthesized by melt techniques to gain a better understanding of the underlying mechanisms. Material libraries are limited by the spatial resolution to do in-depth analysis.

It has been shown that the DVD offers a unique synthesis approach for fabricating compositionally complex refractory film libraries of sufficient thickness and compositional variance. This allows for the investigation of dozens of material candidates with a single sample. The advantages of using EB-DVD opposed to powder-based processing methods, chemical vapor deposition (CVD), or other physical vapor depositions (PVD) is the ability to finely control the compositional gradient with beam power allocation and He flow rate while depositing a film of sufficient thickness for high throughput characterization. Furthermore, oxygen mitigation techniques allow for the deposition of metallic RCCAs. However, interstitial oxygen remains a challenge. With higher deposition rates than other vapor deposition methods, the ability to fabricate many RCCA libraries quickly is realized. However, film library density remains a challenge for the EB-DVD method. Further increased heating of the substrate is not a viable option with T_M ranging from 1668°C (1941 K) for Ti to 2996°C (3269 K) for Ta. Approaching the substrate temperature needed to densify pure Ta (>1961 K $\approx 0.6T_M$) would lead to the evaporation of elements like Ti. There, a plasma assistance method is needed to densify the sample further while also maintaining a sufficient compositional gradient.

7.5.1 Novel contributions and broader impact of EB-DVD libraries

For the first time, RCCA libraries with concertation variations larger than 15 at% and film thicknesses > 25 μm have been synthesized using the EB-DVD technique. EB-DVD upgrades were implemented successfully to allow for sufficient simultaneous melting of four refractory metal sources at a controlled rate such that near equiatomic mixtures of the four refractory elements were located near the center of the sample substrate. The physics of this process has been outlined and understood which will inform future vapor deposition approaches on the necessary processing conditions for successful deposition of RCCA libraries.

It is understood that the inclusion of refractory metals with large differences in melting temperature (1,863 °C for Cr and 3,017 °C for Ta) is challenging due to the necessary temperatures (or ion energies) necessary to promote atomic diffusion being vastly different. In the case of Cr and Ta, at a temperature of 1773 K (approximately ½ T_M for Ta), Cr has a vapor pressure of 130 Pa while Ta is less than 10^{-5} Pa. This leads to rapid evaporation of Cr and making it difficult to include Cr in most processing techniques being explored (i.e., powder and vapor-based methods). The fine control of the vapor flux can account for these vapor pressures, and in the future, implement ion techniques to mitigate the hot substrate approach necessary for densification of films.

7.5.2 Future work

In order to ensure uniform libraries, an in-situ source feed-rate and electron beam power allocation feedback control must be implemented. This will ensure the vapor plume produced maintains the correct vapor concentration to produce libraries with near equiatomic mixtures at the center of the substrate. Furthermore, a plasma assistance technique must be implemented to increase the density of the produced samples. Increased heating of the substrate will result in evaporation of lower melting temperature metals such as Ti, and therefore, is not a solution for densification of the sample. A plasma technique of interest will be outlined in the concluding remarks of this dissertation.

Improvements to the EB-DVD method must be made to produce films with increased density. Further upgrades can also be made to increase the film deposition speed and therefore the efficiency of the deposition itself. The thickness of a sample deposited using the EB-DVD method varies as a function of position over the substrate. Future work will investigate the film thickness change as a function of source materials used and distance from the center of the sample. This information is critical to understanding the evaporation kinetics of the system and to further illuminate the necessary processing conditions for fine control of the film deposition.

Novel synthesis approaches paired with high throughput materials investigation and machine learning is essential for RCCA discovery. An RCCA consisting of six principal elements has over 20 million unique alloys to explore; therefore, it is critical to develop methods to quickly screen candidate alloys for specific applications. Library synthesis is a means to quickly investigate alloy candidates for promising material properties which can later be further studied using traditional metallurgy techniques. Material library investigation relies on the synthesis of material libraries as well as high throughput characterization methods. The pairing of these two concepts allows for quick investigation of thousands of alloys with minimal material preparation or analysis. Traditional characterization techniques were used in this dissertation to determine if EB-DVD RCCA library synthesis was a viable option. Further development of both the EB-DVD approach as well as high-throughput materials characterization methods is essential for the quick screening of candidate RCCAs with superior properties to conventional alloys

Appendix A: Coaxial Plasma Directed Vapor Deposition.

The objective of this study was to investigate the efficiency using coaxial plasma directed vapor deposition to achieve dens films while retaining compositional gradients. While increasing the substrate temperature activates surface atomic assembly, and reduces the formation of surface roughness and pores during deposition, it is difficult to achieve this for refractory metals since the energy barriers inhibiting surface diffusion are high. While raising the substrate temperature can improve coating density, too high of a temperature result in re-evaporation of lower T_M constituents. Additional methods for improving coating densities, other than direct heating, for refractory alloys can be implemented. Surface roughness can be greatly decreased and coating defects eliminated while maintaining stoichiometry by increasing the kinetic energy of the atomic species that condense on or impact with the coatings surface during growth. If ionized atoms are electrostatically attracted to a surface, they impact with enough energy (5-20 eV is usually enough) to cause surface bound atom re-arrangement into more tightly bound lattice sites, resulting in the growth of much lower defect content coatings (235,236).

A coaxial hollow cathode (HC) based plasma assistance approach was implemented to achieve this within the EB-DVD system, a schematic illustration of such a HC source is shown in Figure 60. The plasma is formed by the ejection of a low voltage electron beam within a 50 sccm argon gas flow from two adjacent cathodes.

Transport of an electric current is used to raise the temperature of a tungsten refractory metal tube sufficiently for thermionic electron emission to result. The emitted electrons ionize an inert gas (typically Ar) that flows through the tube forming a positively charged plasma. The, now ionized Ar+ atoms, are then attracted to the negatively biased tungsten refractory metal tube walls. These collisions further increase the temperature and thus increase the thermionic emission of electrons from the tube walls. Therefore, a plasma sheath is formed along the refractory wall, setting up an equilibrium flux of positively charged ions in and negatively charged electrons out. As the electrons are accelerated into the interior of the tube, the opposing tube wall from which the electron was emitted begins to repel the electron back to the center of the tube.

Eventually, the electrons are collimated and form a low voltage electron beam (LVEB) which propagates into the chamber by gas ejection. The electrons are electrostatically attracted to an anode resulting in an increase of the electron energy to 10-30 eV range. This energy exceeds the ionization threshold of argon, Figure 61, and the evaporant atoms in the deposition chamber. Every few milliseconds, the polarity of the potential applied to the pairs of hollow cathodes is reversed and those that served as anodes become electron emitters. By pulsing in this way, the four cathodes contribute to the formation of a dense plasma which is transported towards the substrate where a bias voltage is applied.

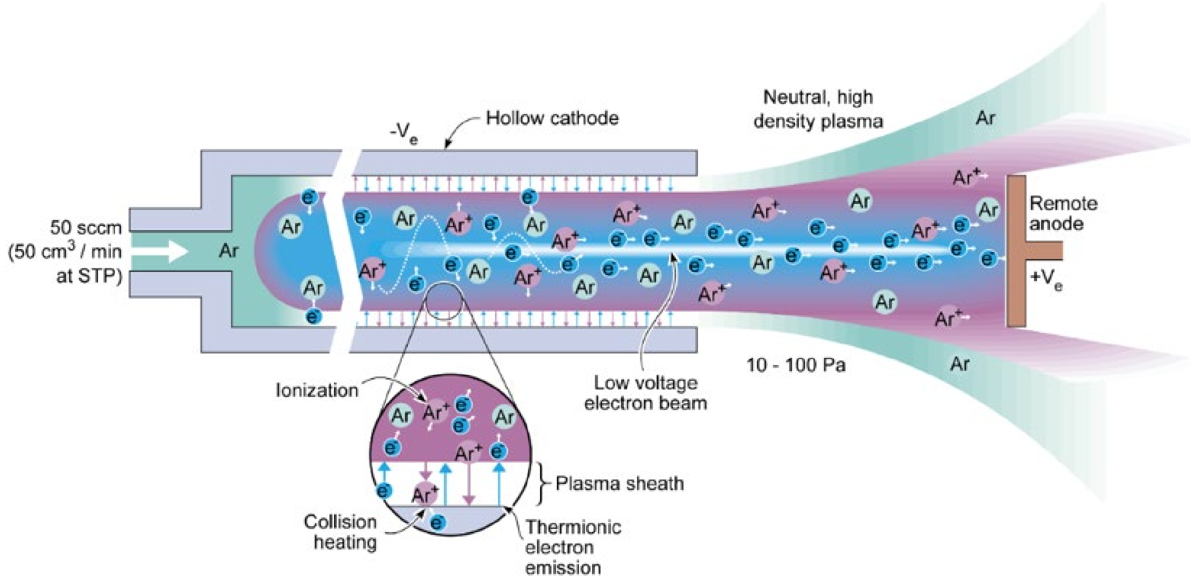

Figure 60. A schematic illustration of a hollow cathode plasma source

The hollow cathodes are ignited by a high-voltage impulse and powered by a single supply in a rotating pulse mode. A bias voltage supply system provided a DC bias voltage to accelerate ions near the substrate into the 10-50 eV range needed for metallic (conducting) coating densification.

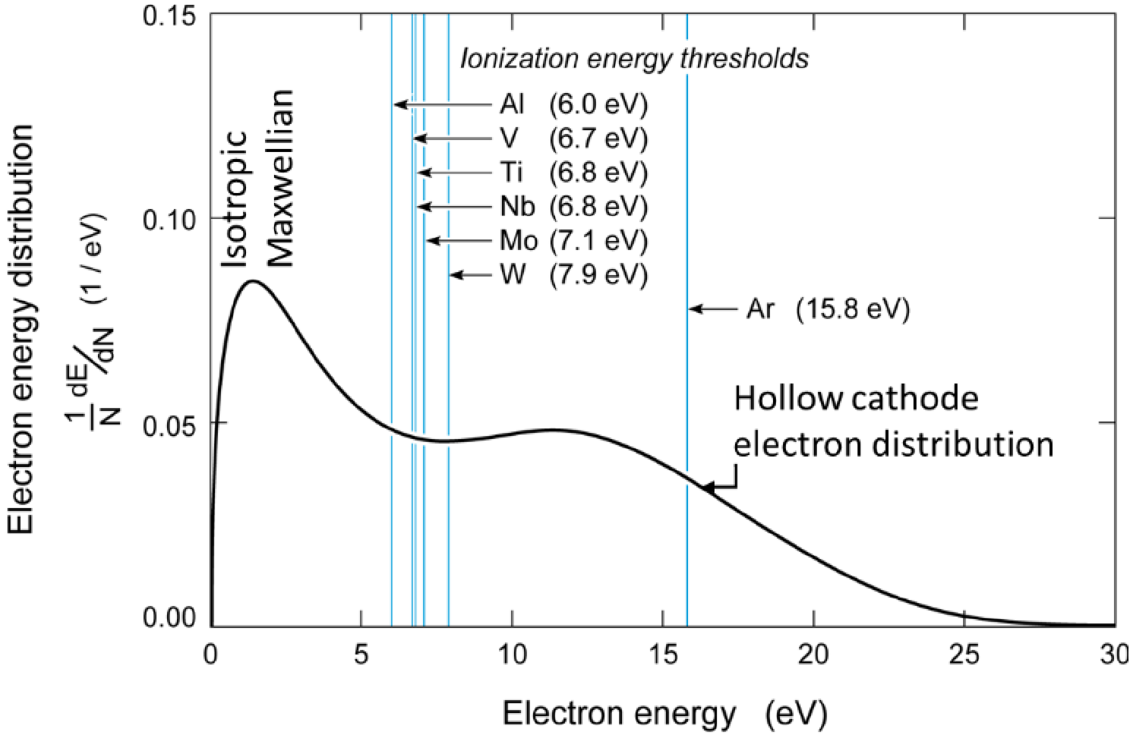

Figure 61. The electron energy distribution emitted by a hollow cathode source with the ionization thresholds of evaporants and argon superimposed

A.1 Experimental set up

The EB-DVD set up used for Mo-Nb-Ti is shown in Figure 62. A clam shell heater was used to radiatively heat the substrates. Three 12.7 mm diameter rods of Mo, Nb, and Ti were used as evaporation sources. This system includes two refractory metals as well as Ti; elements all commonly used with CCAs. The chamber was baked out at 200˚C for 36 hours at a base pressure of 8.0 x10^{-2} Pa to reduce the background H_2O vapor concentration in the chamber.

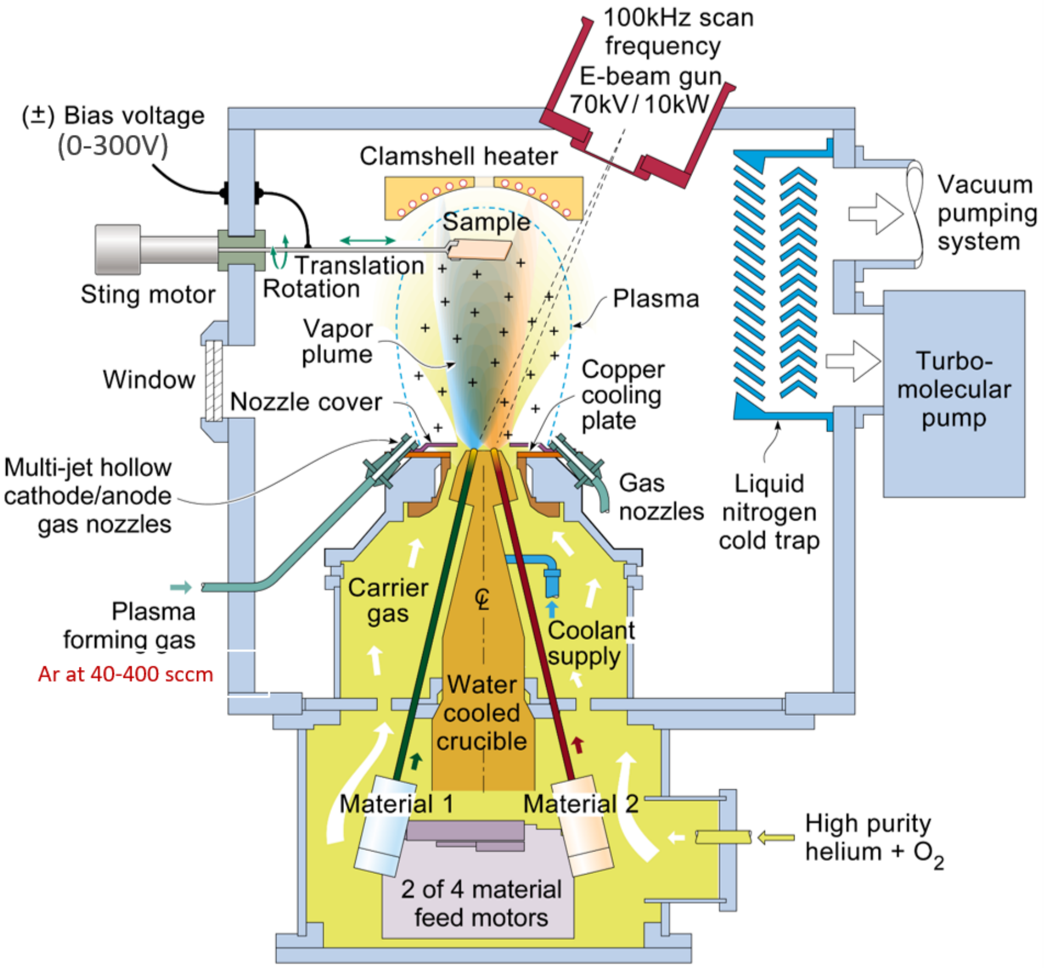

Figure 62. EB-DVD chamber schematic including a coaxial plasma assistance unit. The substrate is placed 20-25cm above the center of the crucible.

A.2 Film deposition parameters

Sample BRC021 was deposited on a molybdenum substrate (25mm x 35mm in area) which was polished on a 1200 grit polishing pad. The substrates were then heated to 900°C. The electron beam power was distributed between the three sources as follows: 2.1 kW (30mA at 70 kV) to the Mo source, 3.5 kW to Nb, and 1.75 kW Ti resulting in a total power allocation of 7.35 kW of the available 9.8 kW. The beam power allocation was determined by increasing the power allocation until all three sources were molten. The coaxial plasma and same heater system were used for sample BRC021. The beam power allocation to each source rod was distributed the same as sample BRC020. The chamber pressure during deposition was 19 Pa resulting in a pressure ratio of 2.85; ensuring a transonic He jet. The plasma was activated with an Ar flow of 50sccm per hollow cathode totaling 200sccm of Ar. The substrate was DC biased at -50V. The key difference between BRC020 and BRC021 is the use of coaxial plasma assisted DVD.

A.3 Results

A summary of BRC021 is shown in Figure 63. The surface and cross section of the deposited film, Figure 63a, reveals that the surface was less porous than BRC020. However, there was a reduction in the compositional gradient for both Mo and Ti to a maximum of approximately 8 at.%. There was still an insufficient amount of Nb in the film. This part of the study indicated that plasma assistance in combination with moderate substrate heating can produce a higher density film than with substrate heating alone. This approach must be improved to extend to a four-source evaporation since more power is clearly needed for the evaporation of Nb if its concentration is to be increased into the 25-35 at% range.

When plasma was used while keeping the beam power allocation and substrate temperature constant, as for BRC021, a few key observations were made. Although the sample showed a less faceted surface than BRC020, the cross-sectional image revealed that there was still porosity present. The porosity decreased as a result of using plasma, however, the sample is still not fully dense. In order to address this issue, a new method for heating the sample to higher temperatures must be implemented. Furthermore, the use of plasma resulted in a decrease in the atomic concentration variance from 15at.% to 8at.%; Approximately a 47% reduction in atomic concentration variance. This is a consequence of the Ar and Ar+ flux interacting with the refractory vapor plumes and increasing their interdiffusion rate.

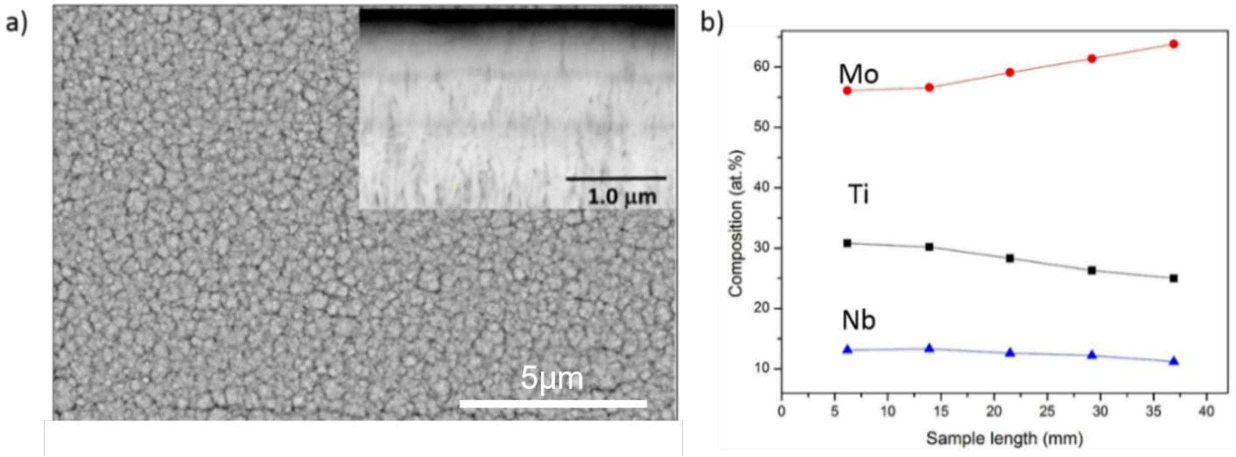

Figure 63. Sample BRC021 a) surface and cross section micrograph and b) compositional gradient diagonally across the sample surface

Appendix B: EB-DVD experimental design

The following study gives further insight into the substrate heating, oxygen mitigation techniques, and the nozzle used for the inert carrier gas.

B.1 Substrate heating

The use of a substrate heater is common in PVD processing approaches as a means to produce dense coatings. Previous studies using the DVD have utilized what is known as a clam shell heater design (168,178,181,207), shown in Figure 62. The clamshell design uses radiation to heat the substrate. However, much of the heat emitted does not reach the substrate and therefore the heating approach is inefficient. Other substrate heating techniques use a boron nitride (electrically insulating) heater block with an imbedded heating element (typically tungsten). This approach requires heat conduction from the BN block into the substrate. The heat produced from this method often results in inefficient heating due to the heat loss from the BN block.

The BN heater block approach was improved to ensure proper heating of substrate for refractory metal depositions. A BN heater block was used with a 5 mm gap to directly heat the substrates with a tungsten heating element, Figure 64. The modified substate heater allows for adequate substrate heating to temperatures exceeding 1200 °C.

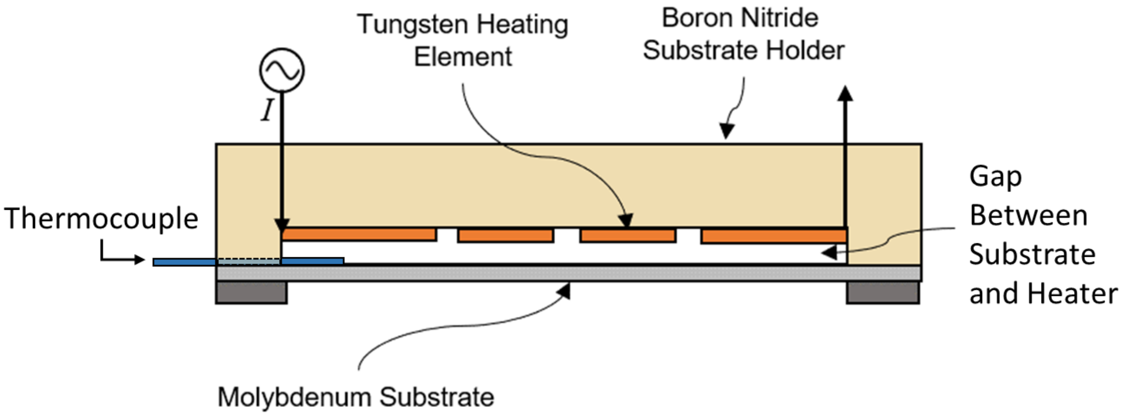

Figure 64. Substate heater design. The substrate is radiatively heated by the tungsten heating element resulting in substrate temperatures exceeding 1200°C

B.2 Lowering Background Oxygen

During EB-DVD, a rarified Ar or He gas jet is used to direct evaporant towards a substrate. Lowering the background pressure for contaminates such as C, H_2, and O_2 is vital for achieving low interstitial content films. The background oxygen partial pressure is ultimately determined by the ability to quickly pump background gasses out of the system while also controlling the amount of oxygen introduced to the system via the rarified gas jet.

A bake-out system was installed in order to raise interior chamber wall to temperatures up to 200 ˚C for 24 hours, to desorb water from the interior surfaces of the deposition system and reduce out-gassing during deposition. Furthermore, an upgraded pumping system was procured (Edwards Vacuum LLC, Sanborn, NY) and installed that resulted in 60% increase in pumping speed and 10x reduced base pressure (10^{-3} Pa). A series of three pumps including a mechanical oil-sealed rotary vane vacuum pump and two mechanical booster pumps. The specifications of each pump in the series can be seen in Table 12. Finally, working gas purifying furnaces (Oxy-Gon Model OG-120) were installed on the helium and argon gas lines used to create the rarefied gas jet and coaxial plasma deposition system.

Table 12. Pump stack series specifications

	Rotary Vane Pump E2M 40-275	Mech. Booster Pump EH1200 HC IE3 US 60HZ 230 /460V	Mech. Booster Pump EH4200 HC IE3 US 60HZ 230 /460V
Max Displacement	50.5 m^3h^{-1}	1435 m^3h^{-1}	4985 m^3h^{-1}
Pumping Speed	44 m^3h^{-1}	1020 m^3h^{-1}	3100 m^3h^{-1}

The introduction of oxygen when flowing inert gas into the system to form the carrier gas jet is inevitable; however, the oxygen gettering system implemented in the DVD process greatly lowers the amount of oxygen introduced into the system via the carrier gas and lessens the possibility of oxygen contamination to the sample. A summary of the calculated amount oxygen introduced per liter both with and without the oxygen gettering furnaces can be seen in Figure 65. It is shown that the use of oxygen gettering furnaces reduces the O_2 introduced into the system via inert gas to values on the order of 10^6 less O_2 per run.

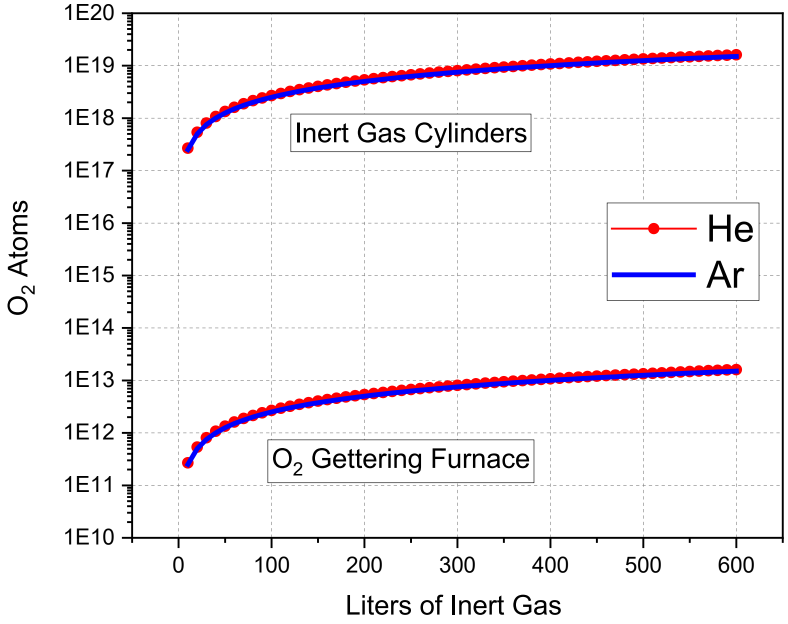

Figure 65. Oxygen introduced into the system per liter with and without the gettering furnaces.

A standard helium gas cylinder has a molecular oxygen concentration of 10^{-6} O_2 per liter. When flowed through the purifying furnace, the manufacturer's specification indicates the molecular O_2 concentration will be reduced to 10^{-12} per liter. A typical 30-minute deposition using a flow rate of 20 slm will lead to 600 L of He used during a single run. We know the mass of He is 4.0026 amu or $\sim 6.65 \times 10^{-24}$ g and its density at STP is $0.1786\ \frac{g}{L}$. We can determine from this that there are approximately 2.69×10^{22} helium atoms per liter of gas introduced to the system. During the deposition of coating over a time of 30 minutes, 600 L of gas pass through the deposition system, the total number of helium atoms introduced to the system is approximately $1.61 \times 10^{25}\,\frac{atoms}{30\,min}$. Using the O_2 concentration above, the number O_2 molecules per coating expected to be incorporated in a coating using with the as received He gas is:

$$(1.61 \times 10^{25}) \times (10^{-6}) = 1.61 \times 10^{19}\ O_2\ per\ run \text{ with He cylinder}$$

While that incorporated using the helium that had been oxygen gettered would be

$$(1.61 \times 10^{25}) \times (10^{-12}) = 1.61 \times 10^{13}\ O_2\ per\ run \text{ with oxygen getter furnace}$$

Films are deposited onto a substrate with a surface area of 50mm x 60mm. If a 20µm film is deposited over 30 minutes, the film volume would be $6e^{-8}$ m^3. The average volume of an element for a film deposited with four refractory elements of MoNbTaV would be $1.6e^{-29}$ m^3, as shown in Figure 77. For a film with a volume of $6e^{-8}$ m^3, there would be approximately $3.75e^{21}$ refractory metal atoms. Assuming 100% of the oxygen introduced from the system either dissolves or forms an oxide, dividing the number of metal atoms by the number of oxygens yields concentrations of 4000 ppm for the as received helium cylinder and $10e^{-3}$ ppm for He flown through the gettering furnaces. This system reduces ratio of oxygen molecules to refractory metal atoms to well below 10^{-8}, and is expected to greatly reduce the level of interstitial contamination.

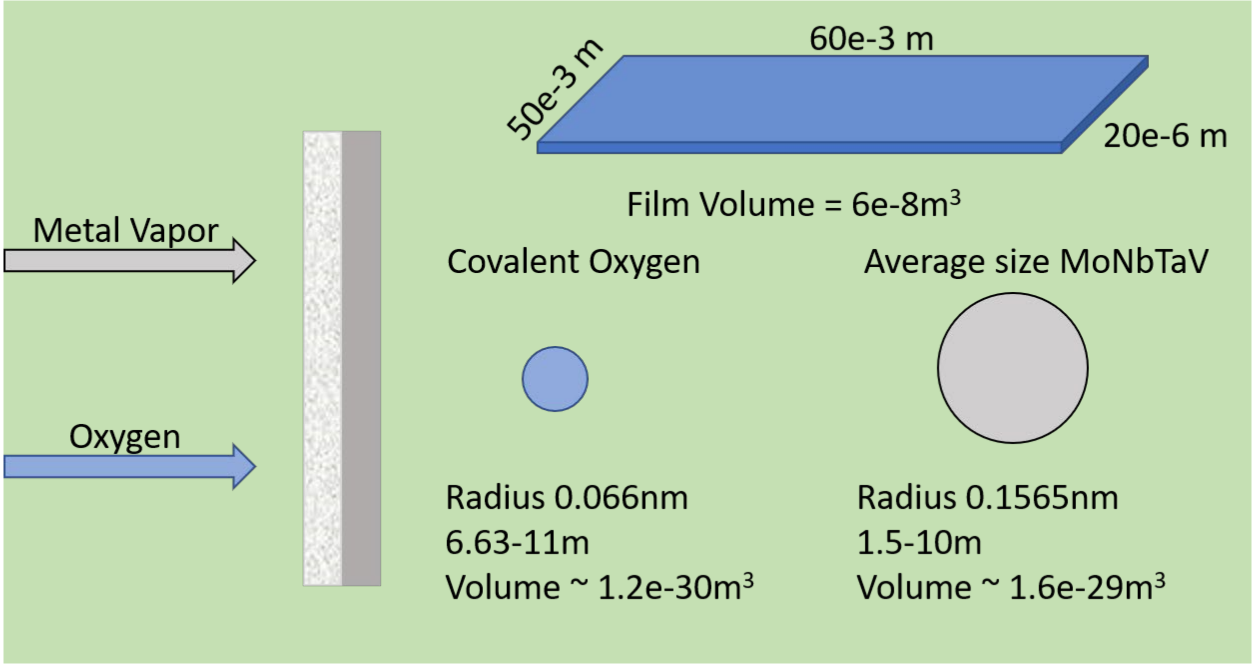

Figure 66. Refractory film volume and oxygen content

B.3 Inert Gas flow Nozzle

The EB-DVD utilizes a rarified inert gas flow coupled with a converging diverging nozzle design to focus the vapor produced from a source material. The ability to control the background pressure using an efficient vacuum system, such as the upgrade to the DVD pumping system just described, allows for a pressure differential through a nozzle resulting in a compression then rapid expansion of gas. This rapid acceleration of inert gas around the evaporating source material focuses the vapor plume by random collisions and momentum transfer resulting in a highly efficient vapor deposition.

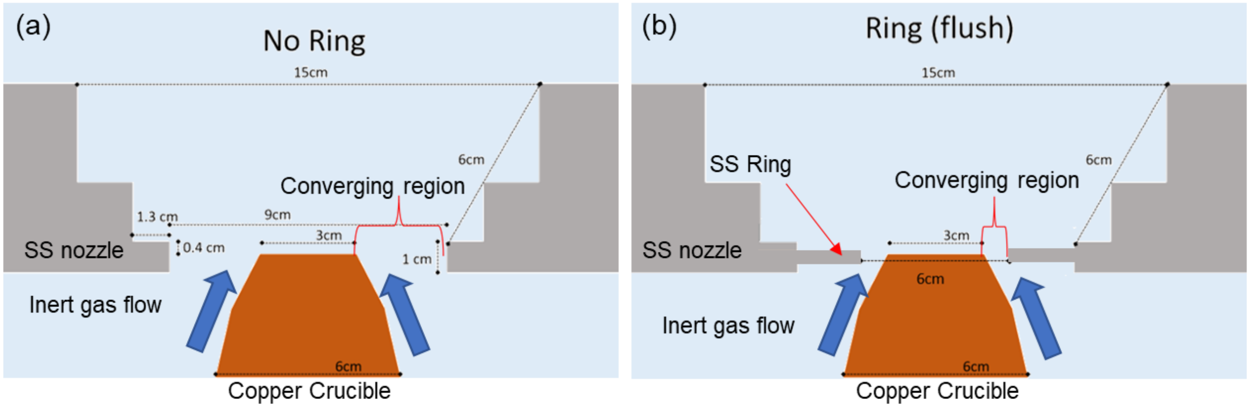

Figure 67. Inert gas jet nozzle geometries where (a) is the as is DVD system and (b) implements the reduced converging region from a 3 cm converging region to a 1.5 cm converging region.

The upstream and downstream pressures of the DVD were measured using pressure sensors situated on the chamber walls below the crucible region as well as on the interior wall of the chamber. With these pressure measurements, the ratio of the upstream to downstream pressures were determined by flowing He and Ar at increasing rates through the two nozzle geometries and measuring the pressure upstream and downstream. The resulting pressure ratios are shown in Figure 68. The ring insert geometry consistently results in a larger pressure ratio for both Ar and He with increasing inert gas flow rates.

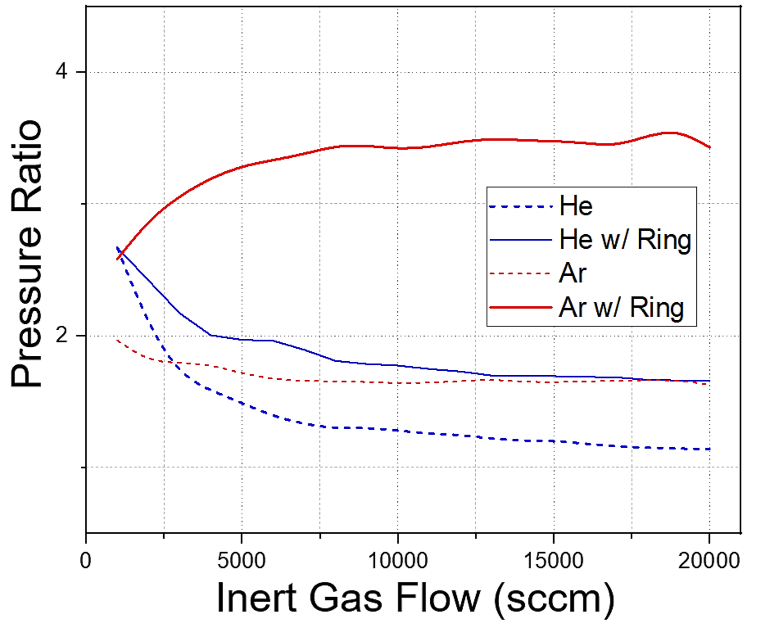

Figure 68. Pressure ratios calculated for He and Ar as a function of gas flow.

The resulting Mach numbers, calculated with Equation (19), for both He and Ar with and without the gas nozzle ring insert can be seen in Figure 69 at the nozzle opening. The ring insert consistently results in a larger Mach number for both Ar and He with increasing inert gas flow rates. Argon flown through the ring geometry exhibits the highest Mach number of approximately 3.5 at flows greater than 10slm. Helium flown though the ring geometry has the second highest Mach number of approximately 1.7 at 10slm and decreases to 1.5 at 20 slm. After a flow rate of 5slm, Ar with the ring insert is the only flow condition which exhibits a pressure ratio larger than that of 1. For both He and Ar, the nozzle geometry with the ring insert results in an increase in the Mach number.

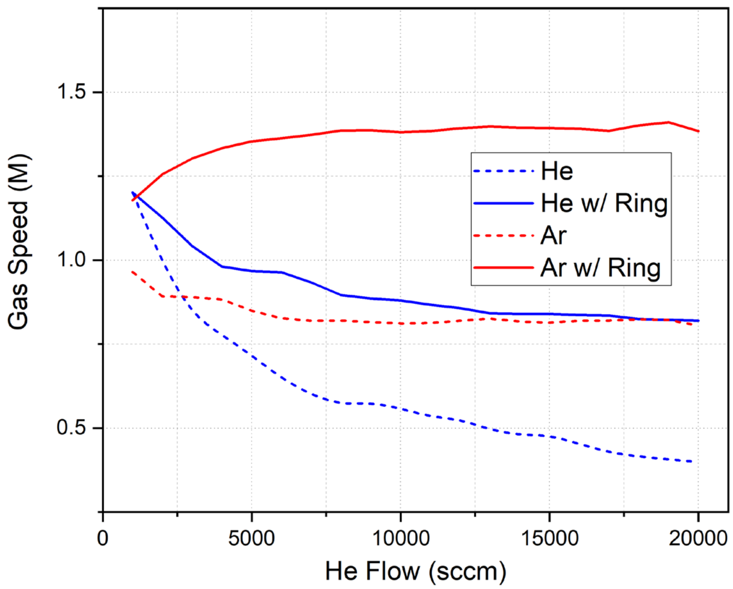

Figure 69. He and Ar Mach numbers at the nozzle opening as a function of inert gas flow with and without ring nozzle insert

Appendix C: Rarified Inert Gas Jet Effects on EB-DVD Multisource Evaporation

C.1 Introduction

The objective of this study was to optimize the inert gas selection and flow rate for both deposition rate and ability to form films with significant compositional gradients. In EB-DVD, a multi-source crucible can be used to simultaneously evaporate two or more sources to form films of binary, ternary, quaternary alloys or even HEAs containing five or more elements (140). As discussed in Chapter 6 and Chapter 7, the film chemistry can be finely controlled using the correct electron beam power allocation to evaporate metals with different melting points and vapor pressures. If done correctly, a film with an equiatomic mixture at the center of the sample can be synthesized.

A systematic investigation of the inert rarified gas jet's effects on compositional variance and deposition rate was studied using a two-source co-evaporation using the EB-DVD. In this chapter the controllability of the composition and deposition rate as well as compositional variance is investigated. Ti and Ta were chosen to be a model system to study the rarified gas jet effects on EB-DVD of refractory metals due to their large difference in melting temperatures, 1668 °C and 3017 °C, respectively. A binary phase diagram for Ta-Ti can be seen in Figure 70 showing at the deposition temperatures of interest (1250 °C) the BCC phase exists for all compositions. However, in highly rich Ti (> 80 at.%) a two-phase region exists at temperatures between 700 °C and 882 °C.

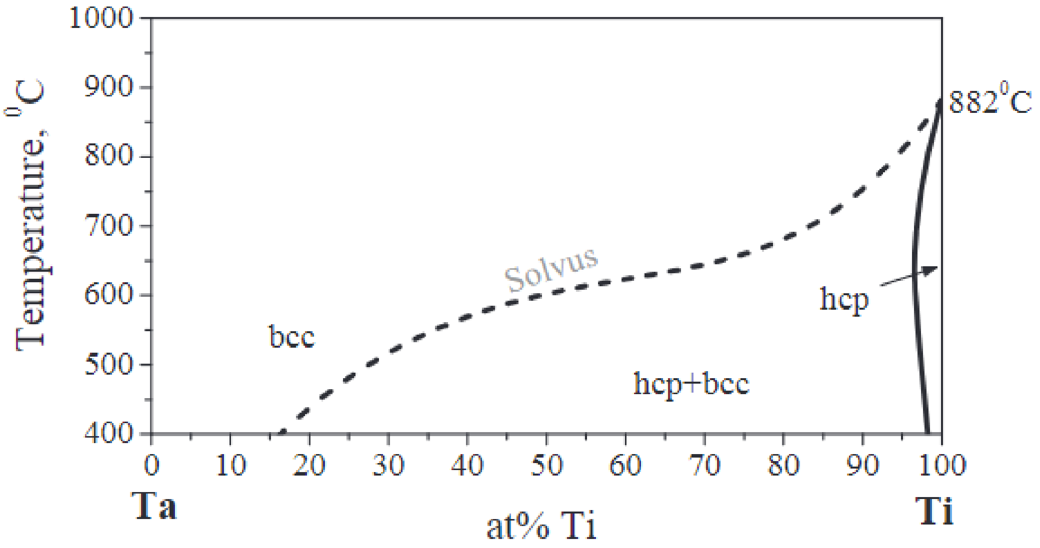

Figure 70. Binary Ta-Ti phase diagram from experimental data (223).

C.2 Materials and Methods

Ti and Ta film libraries were deposited onto a 0.25 mm thick molybdenum substrate (99.95% purity; Elemental Metals, NJ) with dimensions of 60mm x 50mm. Substrates were heated to 1200°C and held there for the duration of each deposition. A beam power allocation of 2.10 kW to Ta and 0.53 kW to Ti was used. Two 6.35 mm source rods were situated 1cm apart (center to center). The source rods used were titanium and tantalum (99.99% purity; Elemental Metals, NJ). Titanium and tantalum were selected due to their large difference in mass, melting temperature, and size, yet still having high-temperature capability.

C.2.1 Ta-Ti Multisource Evaporation: Helium and Argon Inert Gas Jet

He and Ar flow rates were systematically investigated at 5slm, 10slm, and 20slm. All samples were heated to approximately 1250°C for the duration of the depositions with the ring nozzle geometry shown in Figure 78.

C.2.2 Characterization

Scanning electron microscopy (SEM) and energy dispersive X-ray spectroscopy (EDS) were performed using a Helios NanoLab DualBeam microscope (Thermo Scientific, Hillsboro, OR) fitted with an X-MaxN 150 SDD (Oxford Instruments, Concord, MA). Surface microstructure was determined using the SEM in secondary electron (SE) imaging mode using a high-performance ion conversion and electron (ICE) detector. Compositional variance across sample surfaces was determined using EDS with a high accelerating voltage of 20 kV to delineate any overlapping X-ray emission peaks of the refractory metals used.

The film thickness was determined from SEM images of samples that were diamond wafer blade sectioned and diamond grit polishing ending with a 0.25μm diamond diameter particle suspension. An ImageJ processing package, Fiji (84) was used on cross-sectional sample images and a total of 50 measurements per sample were taken with the mean and standard deviation recorded.

C.3 Results

C.3.1 He vs Ar Flow Rate Effect on Composition and Thickness

The first series of depositions utilized an Ar rarified jet with increasing Ar flow rates. The first sample deposited, BRC500, was deposited for 30mins using an Ar flow rate of 5 slm. Figure 53(a) shows the concentration gradient resulting from a deposition using the lowest flow rate. Concentration gradients as large as 36 at% in Ti were observed, shown in Figure 65. The film, after 30 minutes of depositing, was approximately 10.15 ± 0.6 μm thick; indicating a deposition rate of 0.34 ± 0.02 μm/min. It should be noted that the cross-section thickness measurement was collected at the center of the sample, the thickest region on the sample. The cross-section of the deposited film shows a columnar structure with some pores greater than 1 μm wide. The Ti-rich corner of the sample reveals a surface with grain features approaching 1 μm while the Ta-rich corner has a finer structure.

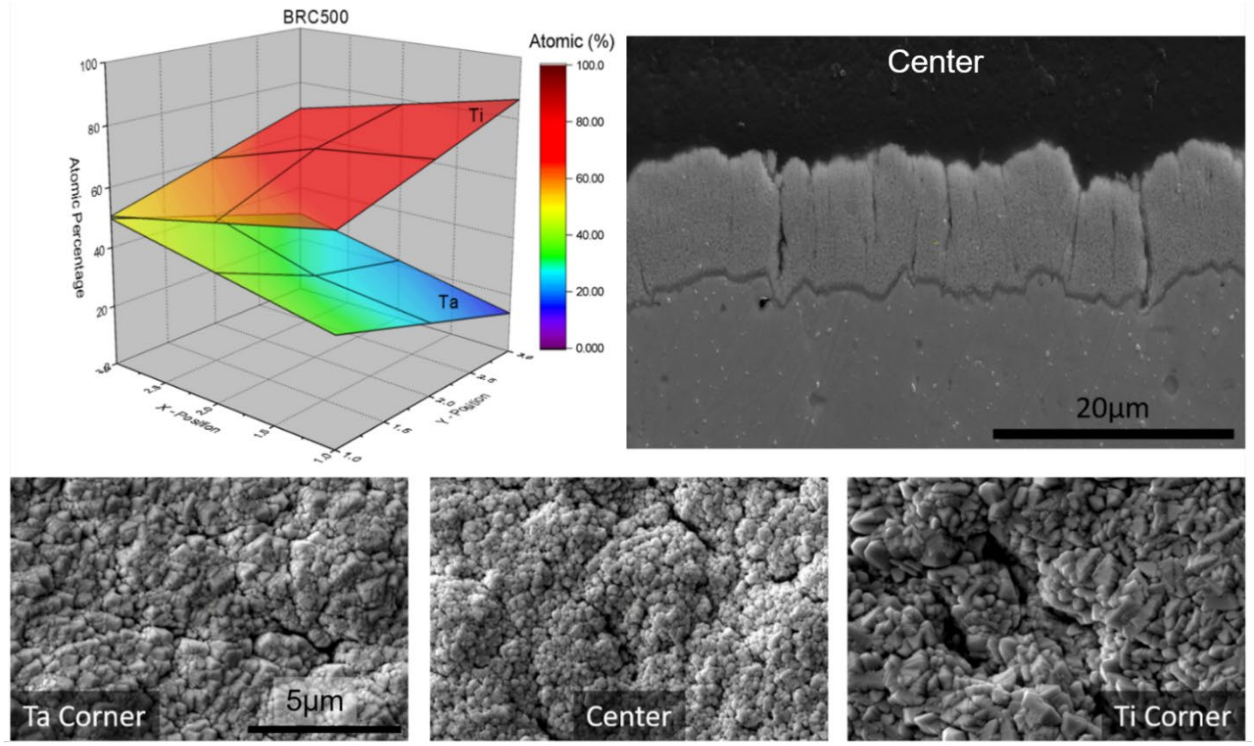

Figure 71. EDS compositional map, cross-section and surface images of sample BRC500. The scale marker of 5µm applies to the three surface micrographs shown.

BRC501 was deposited with an Ar flow rate of 10 slm. The resulting film was richer in titanium; with no tantalum in the Ti-rich corner of the sample. The compositional gradient was increased to approximately 47 at%, Figure 72. The film, after 30 minutes of depositing, was approximately 1.55 ± 0.28 µm thick; a deposition rate of 0.05 ± 0.01 µm/min. BRC501 shows a dense cross-section; however, the deposition rate for BRC501 was reduced by a factor of approximately 7 from that of BRC500. The surface micrograph of the Ti-rich corner shows a very fine textured surface. The center of the sample has a more coarsely textured surface while the corner of the sample highest in Ta appears to have a fine structure.

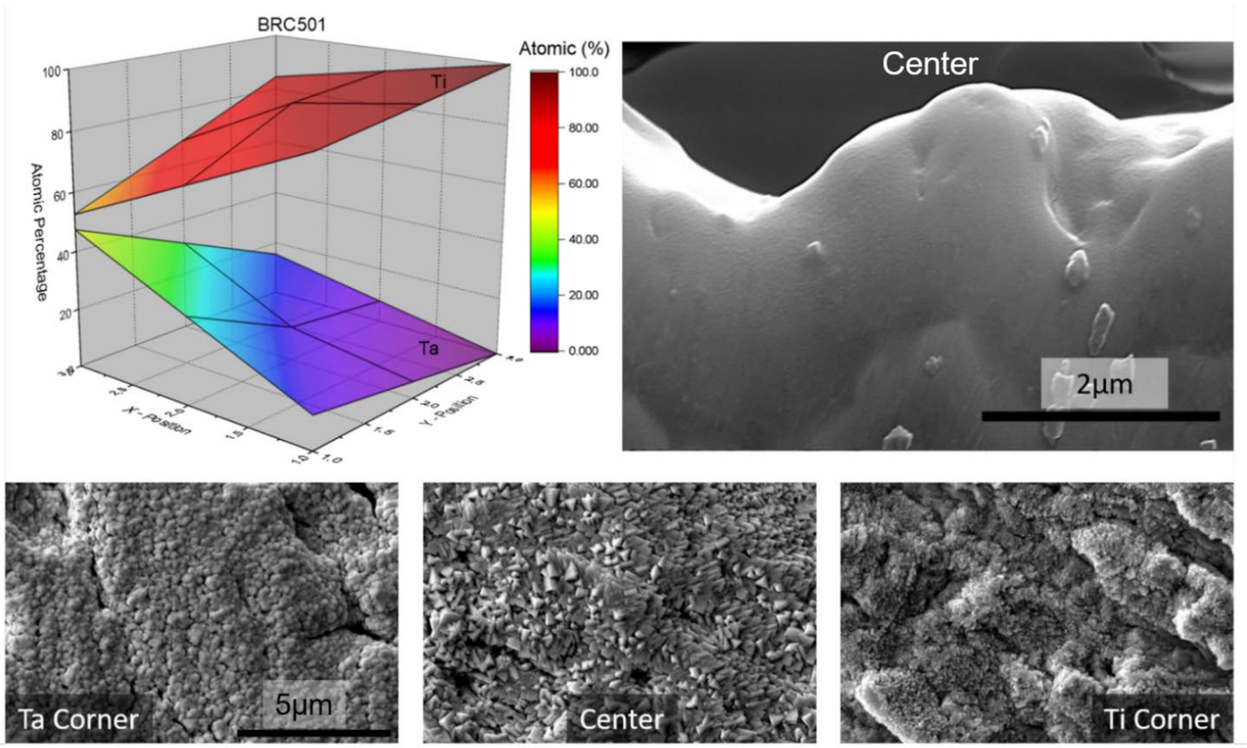

Figure 72.EDS compositional map, cross-section and surface images of sample BRC501. The scale marker of 5µm applies to the three surface micrographs shown.

The deposition of sample BRC502 was unsuccessful due to the inability to sufficiently melt the Ta source rod for deposition. A cross sectional image was not obtained, and therefore, 20 slm of Ar is deemed too high a flow rate to successfully deposit the more refractory elements.

A similar study was conducted on the effect of using He as an inert gas jet source. The first sample, BRC503, was deposited using 5 slm of He gas. A summary of the results is shown in Figure 73. The largest concentration gradient observed was 8 at%. The film, after 30 minutes of depositing, was approximately 8.2 ± 0.8 µm thick, corresponding to a deposition rate of 0.27 ±

0.03 µm/min. The cross-section reveals a porous columnar film with pores approaching 2 µm. The surface micrographs show a faceted surface across the entire surface.

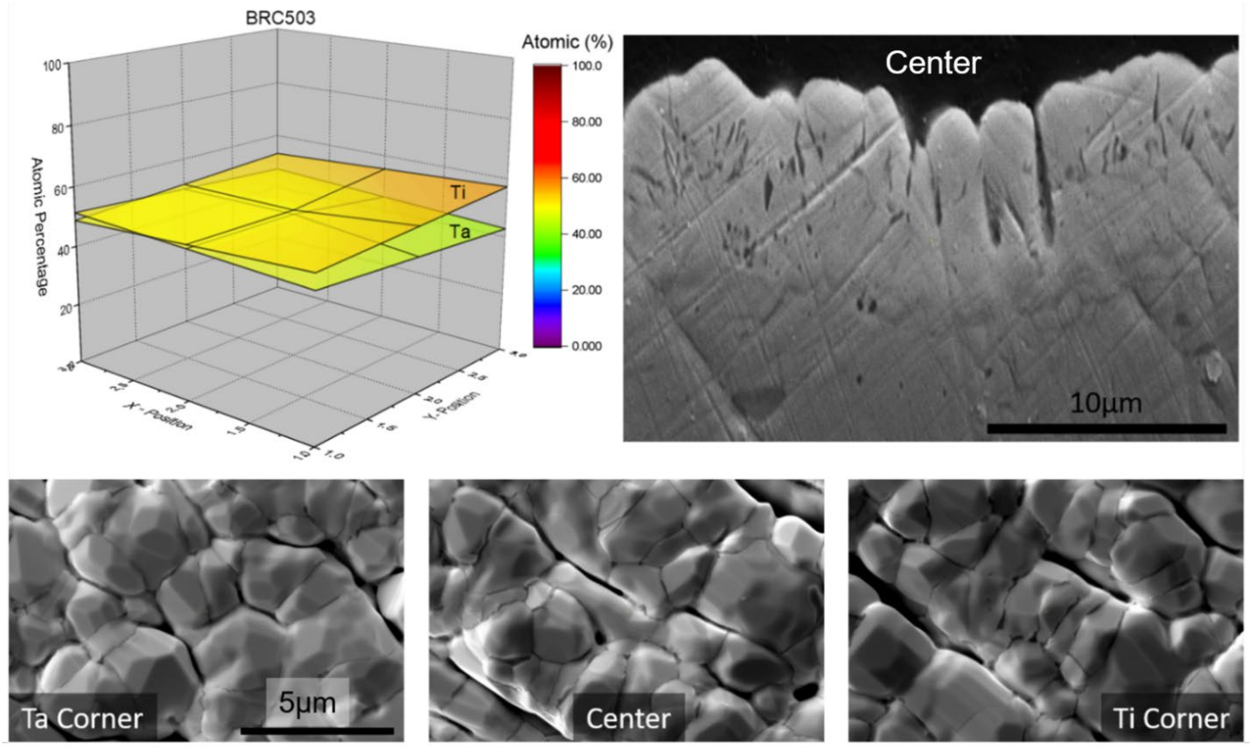

Figure 73. EDS compositional map, cross-section and surface images of sample BRC503. The scale marker of 5µm applies to the three surface micrographs shown.

Sample BRC504 was deposited using a He flow rate of 10slm. Figure 56 shows the composition map. Increasing the largest compositional gradient to approximately 16 at%, Figure 74. The film, after 30 minutes of depositing, was approximately 10.21 ± 0.65 µm thick, corresponding to a deposition rate of 0.34 ± 0.02 µm/min; an increase of 126% over the deposition rate from BRC503. The cross-section and surface features of BRC504 are comparable to that of BRC503.

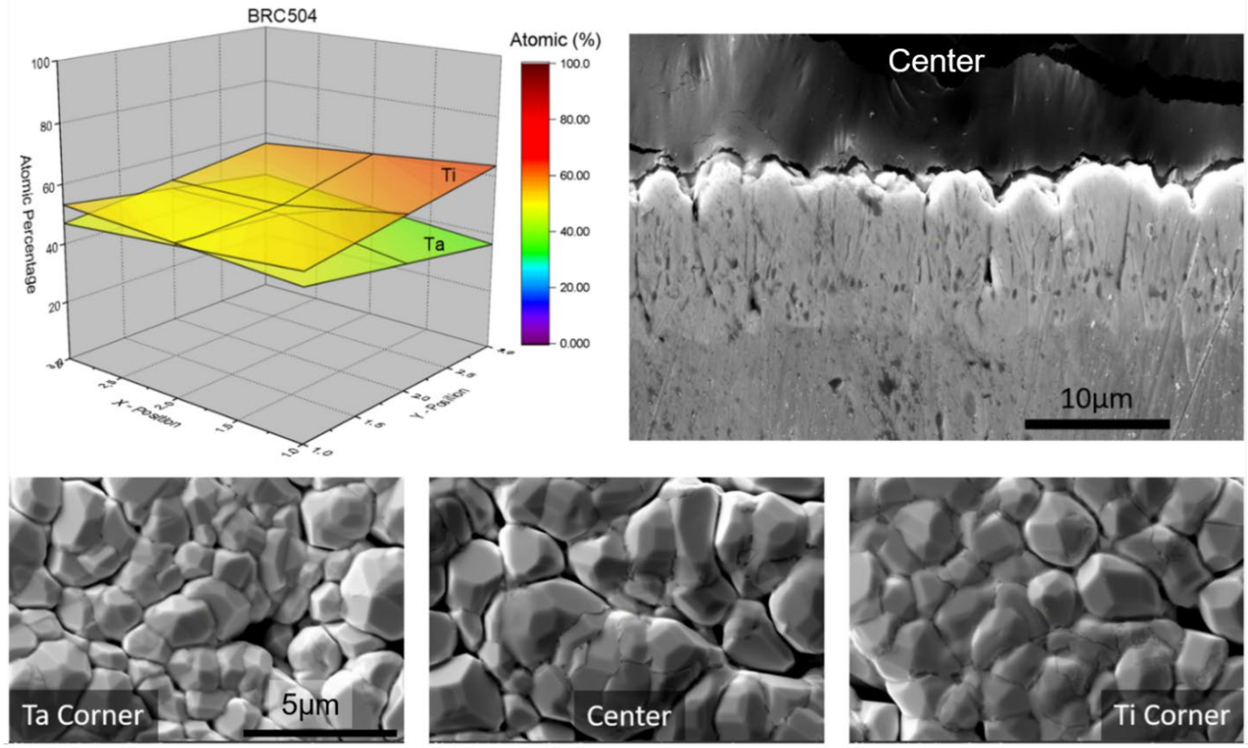

Figure 74. EDS compositional map, cross-section and surface images of sample BRC504. The scale marker of 5µm applies to the three surface micrographs shown.

The final sample deposited, BRC505, was deposited using 20slm of He, Figure 75. The largest compositional gradient was increased to 34%. The film, after 30 minutes of depositing, was approximately 13.65 ± 0.90 µm thick; showing a deposition rate of 0.455 ± 0.030 µm/min. The deposition rate for BRC505 was the largest observed for all six depositions of the inert gas flow series. The cross-section micrograph shows a columnar structure and a faceted surface.

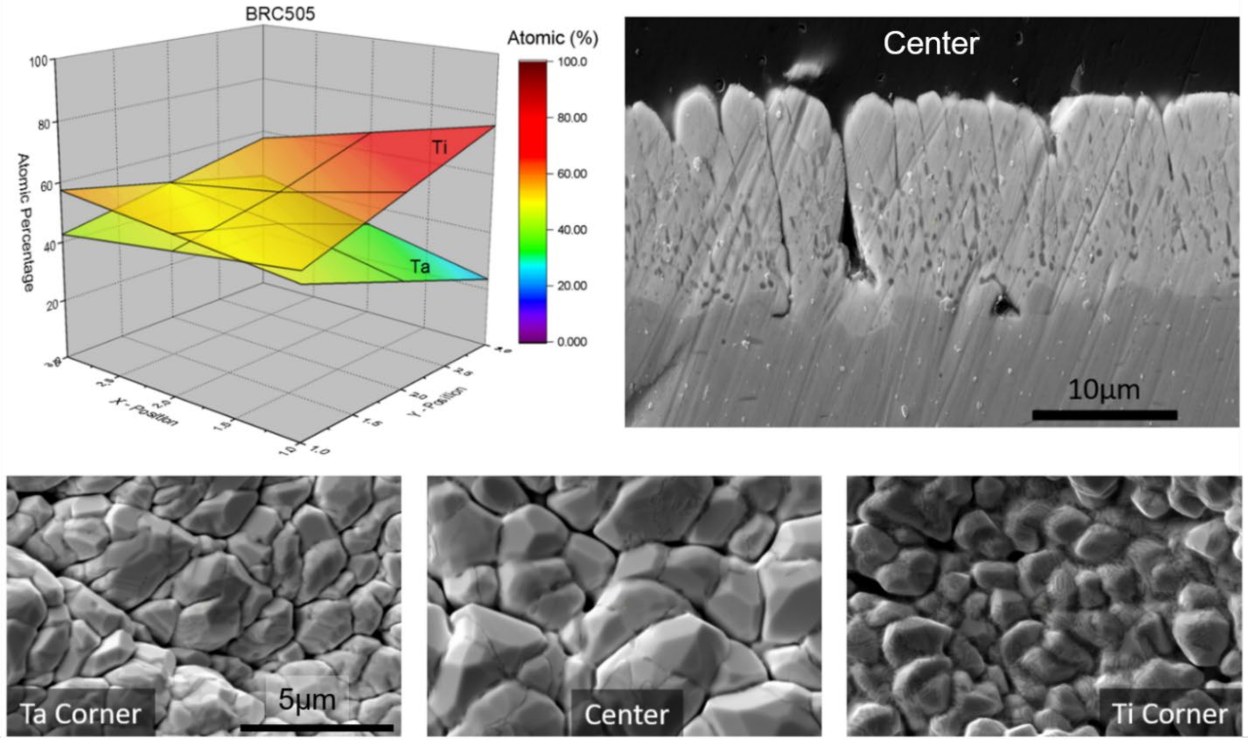

Figure 75. EDS compositional map, cross-section and surface images of sample BRC505. The scale marker of 5μm applies to the three surface micrographs shown.

A summary of the inert gas flow's effect on the compositional gradient is shown in Figure 76. The largest compositional gradient was observed with a flow rate of 10 slm of Ar gas resulting in compositional variance of 47 at%. However, the amount of Ta across the sample was lower than Ti throughout the entire sample. Conversely, when 20 slm of He was utilized, a compositional variance of 34 at% was observed while maintaining sufficient levels of both Ta and Ti.

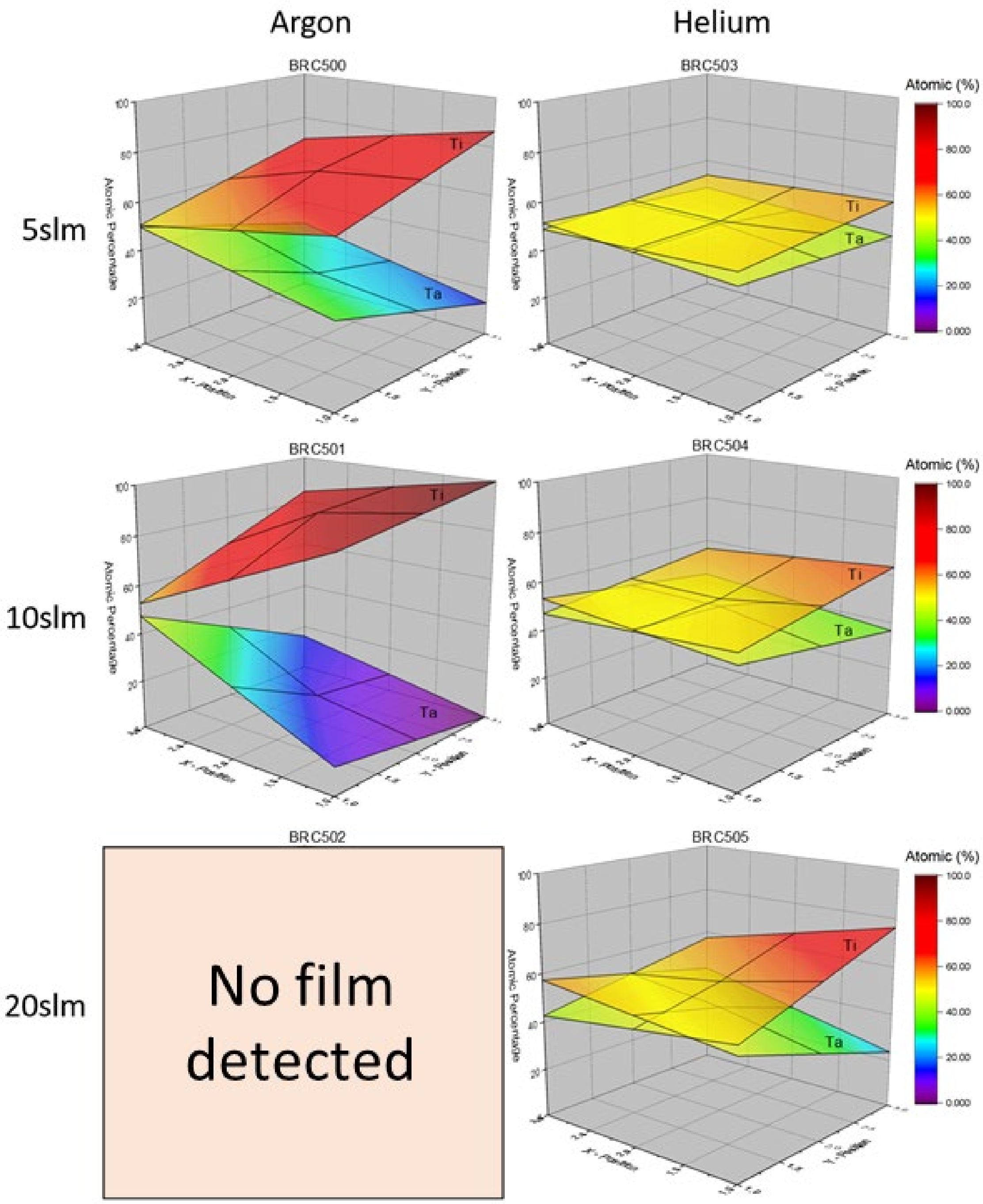

Figure 76. Summary EDS maps of Ar vs He flowrates.

C.4 Discussion

Understanding the dynamics of multisource evaporation during directed vapor deposition is critical to synthesize combinatorial libraries of two or more evaporation sources. The effect of inert gas type and flow rate must be understood to determine which processing conditions will produce the most ideal case of deposition rate while also maintaining a sufficiently large compositional gradient (>10 at%). The inert gas type and flow rate has a large effect on the lateral gas diffusion rate (compositional variance) and momentum transfer towards the substrate (deposition rate). Furthermore, the electron permeability is affected by differing chamber pressures, and therefore, the heating of the source material is directly an effect of the chamber pressure and inert gas type. The deposition efficiency and compositional variance was investigated by systematically increasing either a helium or argon gas jet flow rate during deposition of a titanium – tantalum binary alloy.

The effect of gas flow rate type and flow rate on the concentration gradient can been seen in Figure 77. At a flow rate of 10 slm of Ar, the highest concentration gradient is achieved. However, increasing the Ar flow rate from 10 slm to 20 slm results in an insufficient deposition rate. Figure 78 shows the average coating deposition rate of the titanium - tantalum alloy as a function of gas flow both helium and argon gas jets. when an argon jet was used, the deposition rate decreased with argon flow rate. The lower deposition rate is attributed to two competing mechanisms: lower wall jet penetration at the substrate and decreased heating efficiency via electron beam scattering. At 5 slm argon flow rates, the gas jet suppressed evaporation and increased the density of the wall jet at the substrate surface, making it more difficult for the metal atoms to reach the substrate (they were effectively entrained in the wall jet and lost from the system). At a 10 slm Ar jet flow, evaporation of the tantalum source rod was barely observable, while some evaporation of the titanium source rod occurred. However, when the Ar jet flow was increased to 20 slm, evaporation of tantalum and titanium was not possible.

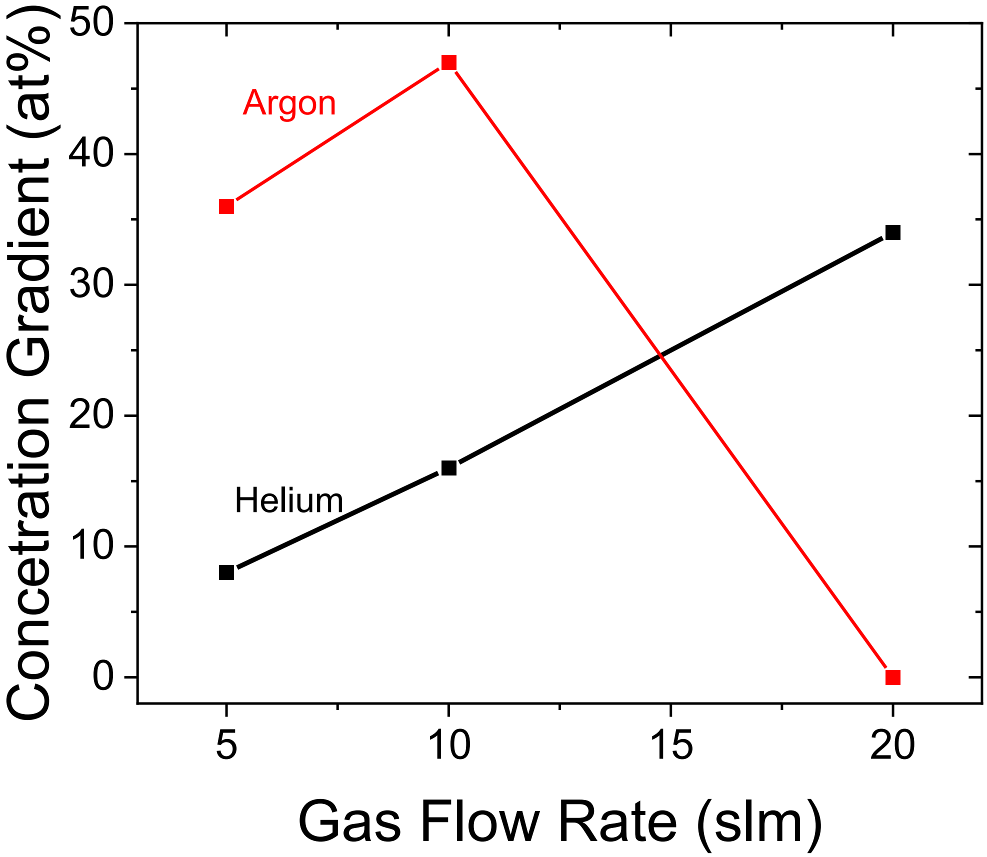

Figure 77. Concertation gradient vs gas flow rate for both He and Ar.

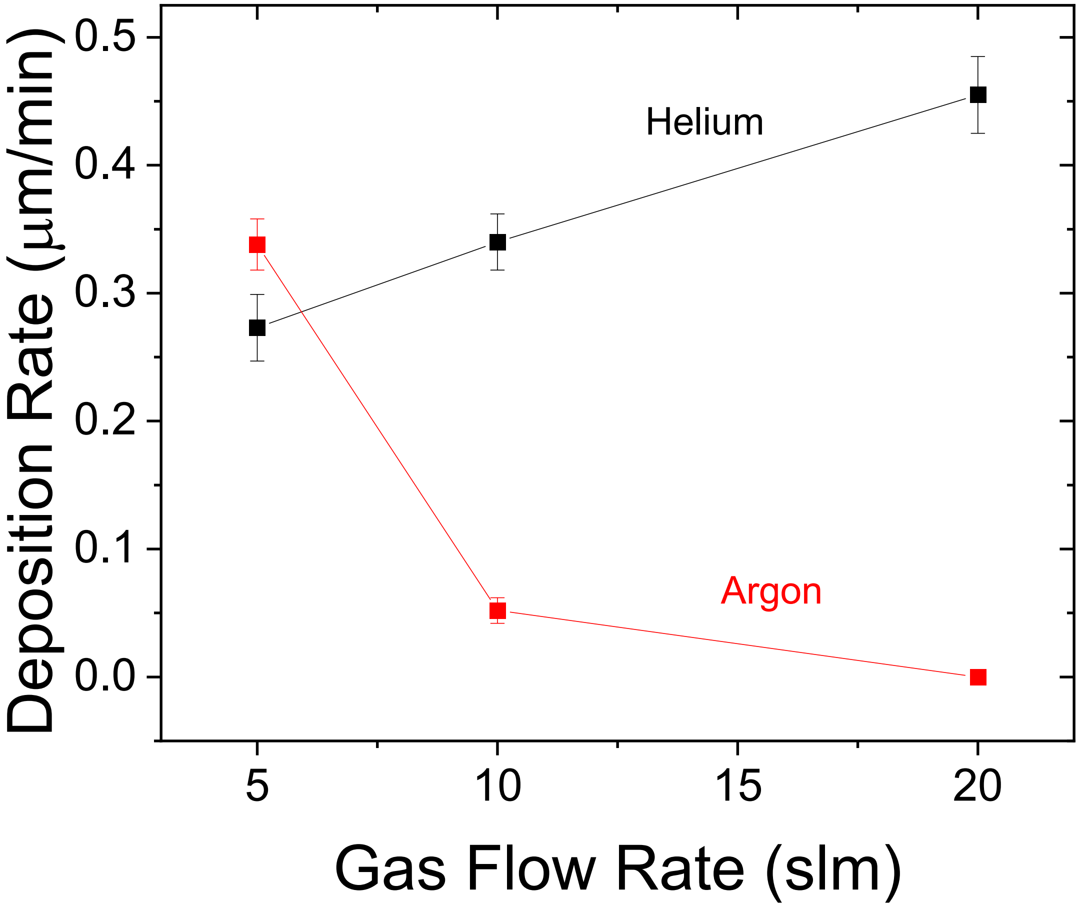

Figure 78. Average coating deposition rate as a function of the gas flow rate for helium and argon deposition

Increasing the helium flow clearly improved the concentration gradient and deposition rate, Figure 77 and Figure 78. The Increasing composition gradient as well as deposition rate achieved by more efficiently entraining the vapor atoms in the high velocity jet flow and enabling its penetration through the wall jet at the substrate surface where deposition occurred.

Argon gas is heavier with respect to helium, the momentum of the gas jet in the EB-DVD system would push heavier gas vapor species (e.g., refractory metals) inward and concentrate the flux onto the substrate. The momentum transfer, on average, for Ar and He at 20slm are shown below:

Table 13. Momentum transfer calculations for both He and Ar.

	Mass (g)	Mach 1 Velocity (m/s)	Mach #	Velocity at 20slm (m/s)	Momentum (g·m/s)
He	6.64E-24	1007	0.82	825.6	5.48E-21
Ar	6.63E-23	319	1.38	441.5	2.93E-20
$\rho = m \times v$ $\quad$ $v = Mach\# \times Mach\ velocity$					

The momentum transfer for Ar vs He for the same flow rate of 20slm reveals that Ar atoms have a moment approximately an order of magnitude higher than that for He. This would allow for heavier vapor species, such as Ta, to be more efficiently carried towards the substrate downstream from the vapor flux. However, a downside of using argon is that the electron permeation through argon gas is lower with respect to helium, and thus the efficiency of the electron beam goes down (195).

At 20 slm Ar, the deposition rate of tantalum is zero, while there is some (although negligible) titanium deposition. Although the momentum transfer for Ar at 20 slm is higher, due to the electron permeability, the 20 slm of He deposition condition results the highest deposition rate. This is understood by considering the cross-section of the He and Ar species and the interaction with the electron beam. Due to the larger cross-section of Ar atoms compared to He, the electron beam permeability is decreased with increasing Ar flow, as shown in Figure 79. As a result, the heating efficiency of the source material is decreased thus lowering the vapor pressure of each of the source materials and lowering the deposition rates.

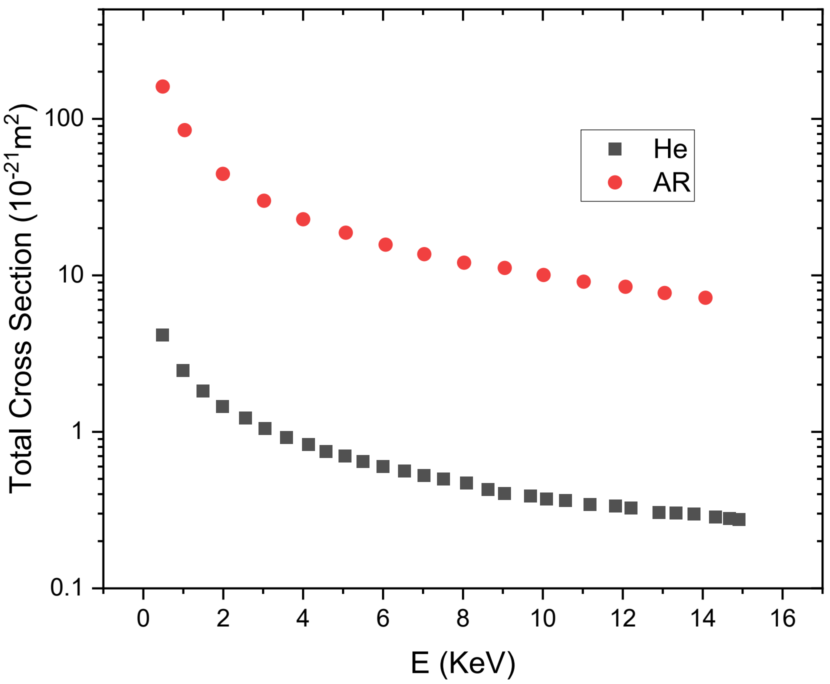

Figure 79. Atomic cross-section of gas species interacting with electron beam (237).

Figure 80 overlays Figure 77 and Figure 78 to show the most optimum conditions for both deposition rate as well as the concentration gradient. Even though Ar has the highest concentration gradient at a flow rate of 10 slm, the deposition rate is lower than all the measurements taken for deposition rate of He at all flow rates. However, at a He flow rate of 20 slm, the highest deposition rate is achieved while maintaining a large concentration gradient (34 at%). Although Ar shows a high deposition rate and concentration gradient at a flow rate of 5 slm, the concentration of Ta, the higher melting temperature metal, is substantially lower than that of Ti due to the electron beam scattering. Therefore, 20slm of He is has been chosen as the optimal gas flow condition due to the ability to sufficiently melt source material which is advantageous when increasing the number of evaporation sources within a deposition.

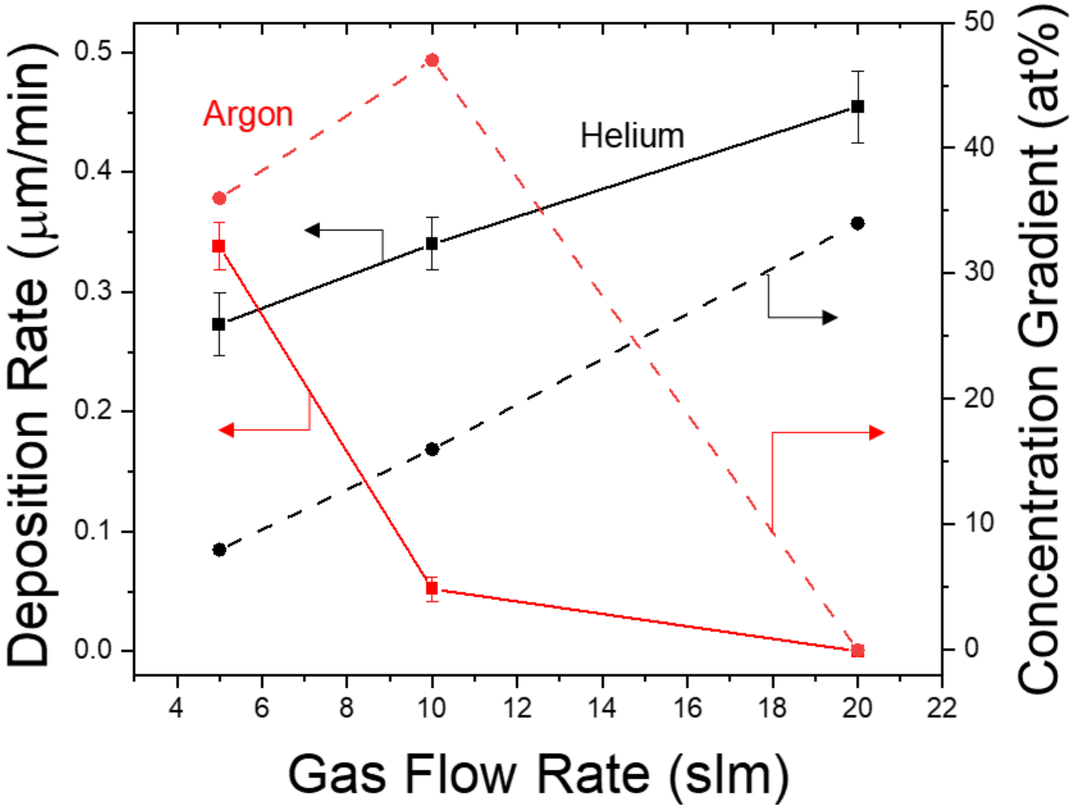

Figure 80. Deposition rate vs gas flow rate and concentration gradient vs gas flow rate for both Ar (red) and He (black).

C.5 Conclusion

The ability to deposit refractory metal libraries using EB-DVD had not been investigated previously. The inert rarified gas flow and deposition condition relationships were established leading to an understanding of the necessary parameters to ensure compositional variance while maintaining sufficient deposition speed. It was determined that an inert gas flow of 20 slm of He yields the optimal deposition efficiency while maintaining large compositional variance. The electron beam permeability through He and Ar greatly changes the heating efficiency of the electron beam due to the cross-section interaction of electrons being accelerated through increasing pressure of both He and Ar. However, increasing the He and Ar flow increases the momentum transfer of evaporated metal vapor species. The increase in moment transfer limits lateral vapor diffusion over the distance to the substrate (22.5 cm), resulting in an increase in compositional variance. The competition between momentum transfer and electron beam permeability illuminated the need for parameter optimization; resulting in 20 slm of He being the desired deposition parameter for sufficient deposition speeds as well as compositional variance. In Chapter 7, a flow rate of 20 slm of He was used, confirming the ability to sufficiently evaporate four sources including Nb and Ta with sufficient thickness and compositional variance.

Appendix D: RCCA Indentation

The objective of this work was to demonstrate suitability of the produced compositional libraries for high-throughput nano-indentation studies. It should be noted that to obtain accurate nano-indentation results, a film thickness >10 times the size of the indenter head, a polished film surface, and a low porosity is needed (153). Nano-indentation was performed with the help of Mackenzie Ridley (UVA, PhD MSE) diagonally across the sample from the Ta-rich corner to the Ti-rich corner. Eight to ten indentations were taken within a 100μm^2 area for each of the three locations of interest. As-collected data for three individual curves can be seen in Figure 81. Young's modulus measurements, less than 400nm depth, contain measurements of initial contact with the surface of the sample and are not considered for the average modulus calculations. The average Young's modulus was taken at indentation depths between 400nm and 1000nm.

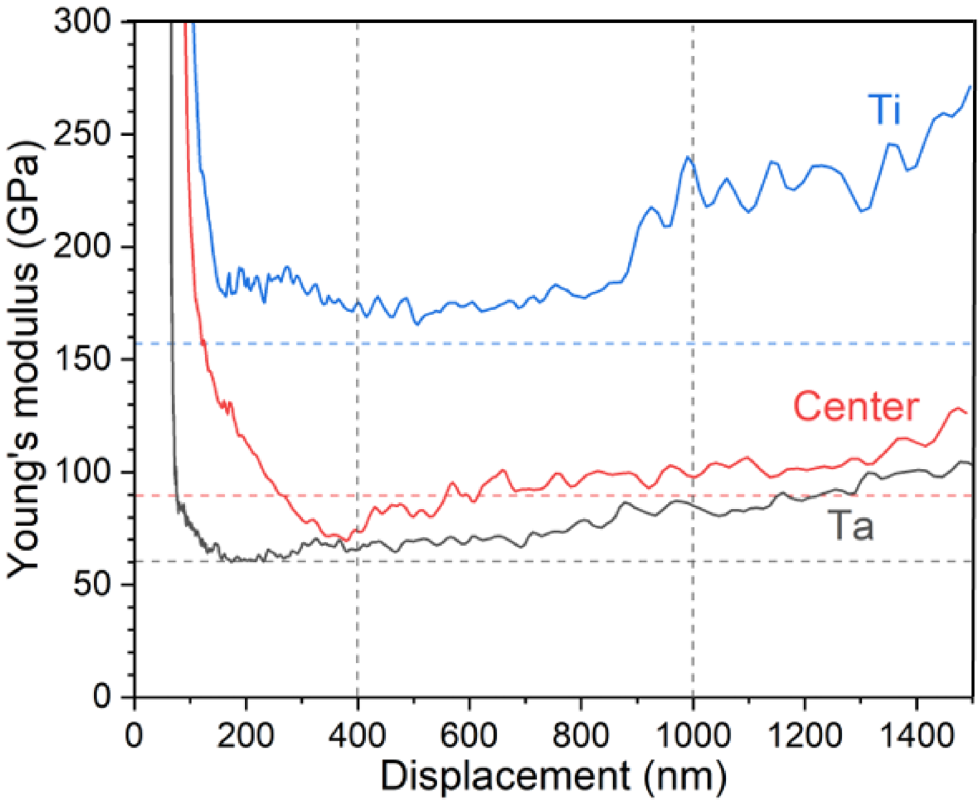

Figure 81 - Young's modulus as a function of displacement for nano-indentation done on sample BRC525

Average Young's Modulus and respective standard deviations for the three investigated positions on sample BRC525 are shown in Figure 82. The Young's modulus of the individual components are as follows: 180 GPa for Ta, 105 GPa for Nb, 245 GPa for Cr, and 120 GPa for Ti.

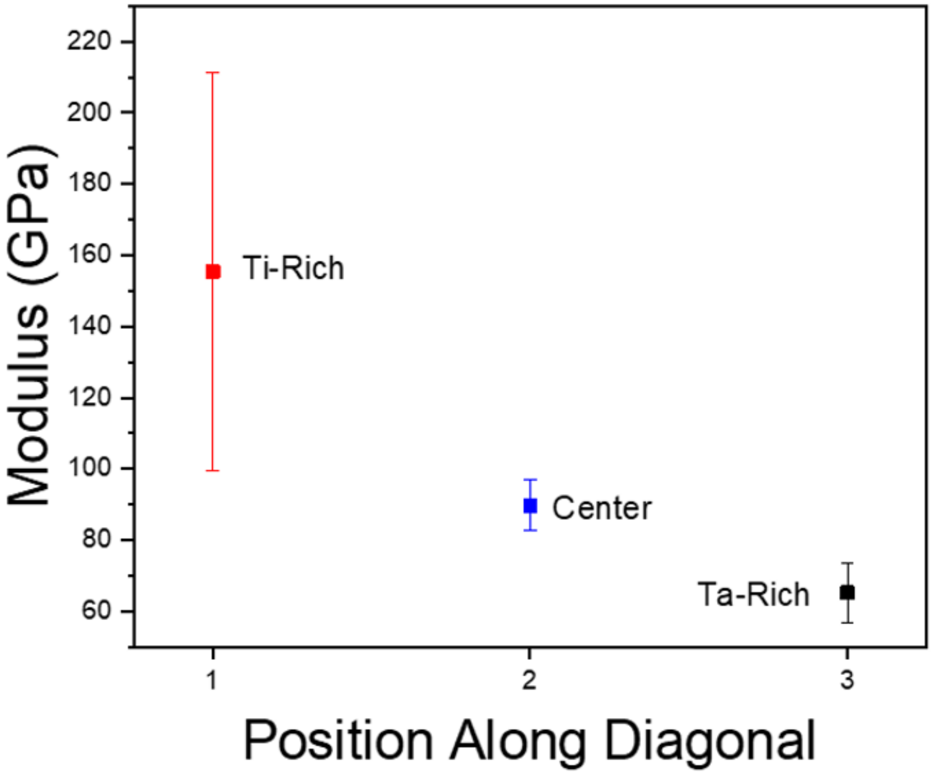

Figure 82. Summary of Modulus along the diagonal of RCCA libraries

The mechanical performance of a deposited film is dependent on the quality of the film i.e., film thickness and porosity. It was shown that the deposited films fall short of the density required to obtain accurate mechanical property information. Figure 83 shows the calculated ROM Young's modulus for sample BRC525 as well as the overlaid measured average values obtained using nanoindentation.

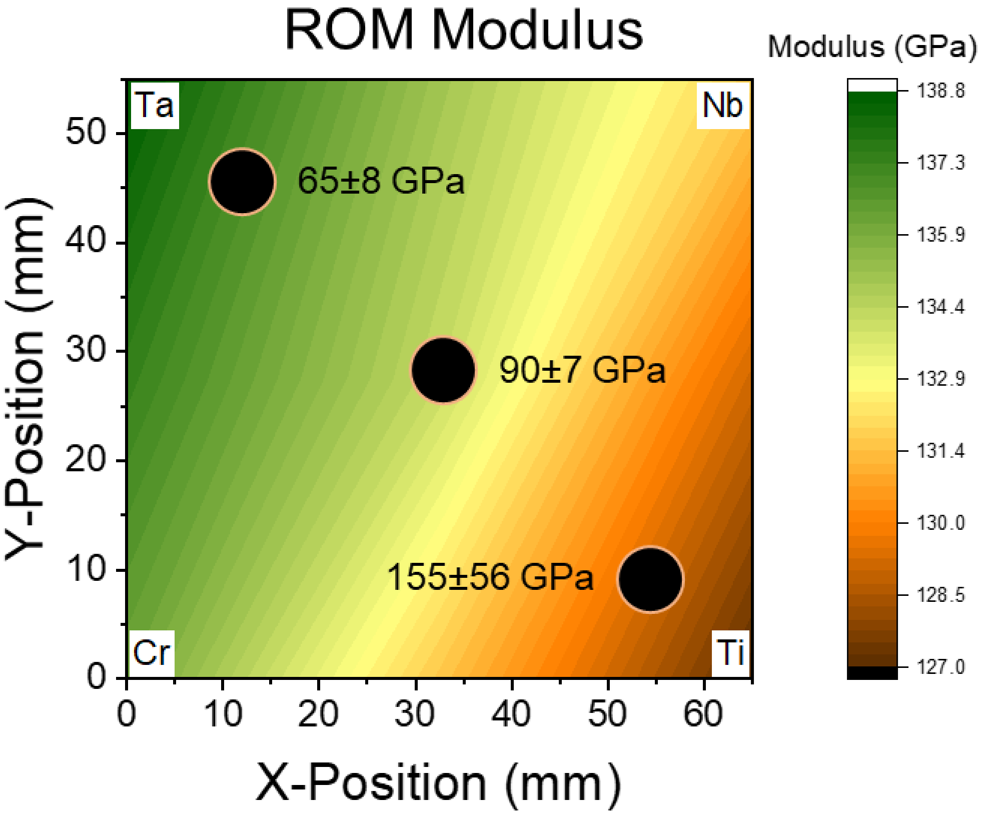

Figure 83. Colored gradient showing the calculated ROM Young's Modulus for sample BRC525 based on the composition found using EDS, overlaid with the actual Young's Modulus found using nano-indentation.

The ROM calculation predictions for modulus are not in good agreement with the measured values; measured values trend in the opposite direction compared to ROM values. It has been shown that the modulus of a thin film is dependent on the porosity of the film. Increased porosity leads to a decrease in modulus (238). The modulus of a porous film can be calculated using the Ramakrishnan-Arunachalam (239) model:

$$E_0 = \frac{E_p(1 + b_E p)}{(1 - p)^2} \tag{C1}$$

Where E_p is the modulus of the porous material, E_0 is the modulus of the fully dense material, b_E is a parameter depending on Poisson's ratio (v_0) of the fully dense material, and p is the porosity. The Poisson's ratio of the multicomponent materials of interest is not known and is needed to understand the modulus of the porous material. However, individual element Young's modulus and Poisson's ratios are known to be the following:

- E_0 =180 GPa and v_0 = 0.34 for Ta
- E_0 =105 GPa and v_0 = 0.35 for Nb
- E_0 =245 GPa and v_0 = 0.20 for Cr
- E_0 =120 GPa and v_0 = 0.35 for Ti.

Considering a value of $b_E = 2v_0$ (238), the predicted Young's modulus for a thin film as a function of porosity for the individual materials of interest is shown in Figure 84. The predicted Young's modulus using Equation (C1) shows a clear, strong dependence on the amount of porosity present in a film.

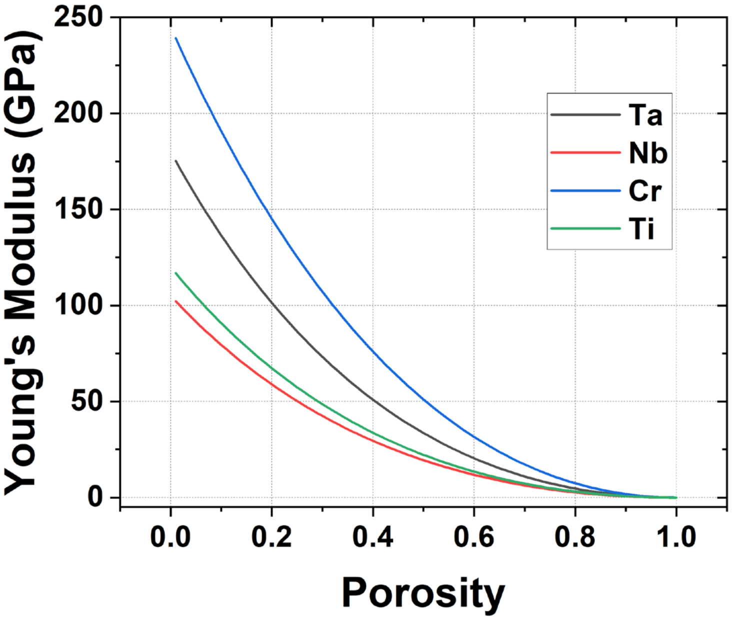

Figure 84. Calculated Young's modulus of thin films (E_p) as a function of porosity (p) for individual constituent elements.

The Ta-rich corner is predicted to have a modulus of approximately 135GPa and was measured to be 65 ± 8 GPa. The center of the sample was calculated to be approximately 129GPa and was measured to be 90 ± 7 GPa. The Ti-rich corner of the sample was measured to be higher than the ROM calculation of approximately 123GPa with a measured value of 155 ± 56 GPa. The deviation from predicted values is attributed to the microstructure of the locally investigated area. Accurate nano-indentation requires a low amount of surface roughness (i.e., polished surface) and low or uniform porosity. It was determined that the films produced in this dissertation are not adequate for Nano indentation studies and further densification methods of the samples must be explored.

Appendix E: DVD Future Upgrades

E.1 Upgraded Electron Beam Power

A key issue with the current system is insufficient EB power. This is especially critical when attempting to deposit refractory metal coatings containing four or more high melting temperature metals. Allocation of the available 10 kW of EB power to the four sources results in insufficient heating of the highest melting temperature sources, limiting the range of compositions that can be created in a combinatorial library. This issue is rapidly growing in importance as interest in engineering uses of refractory alloys has begun to resurge.

The EB gun power can be increased by use of a higher current cathode source. These are now available from FEP – the developer of the high voltage gun that we use. To maintain focus and acceleration of the higher current beam requires a modification to the existing power supply. With this upgrade to the beam power, we expect to be able to evaporate four 9 mm diameter, 300 mm long refractory metal (or metal alloy) sources at temperatures sufficient to deposit coatings at rates of 5-10 μm/min over substrates with dimensions (limited by the load lock) of up to 20 cm by 10 cm. This requires only minor modification to the gun itself (replacement of the tungsten bolt cathodes by larger diameter LaB_6 coated counterparts, and modification of the gun control software). This 50-70% increase of the electron beam power, will enable the rate of evaporation of even the most refractory (W, Ta, Re, Nb and Mo) metal sources to be increased by raising their surface temperature.

E.2 Spotless Arc Deposition

The level of porosity allows for XRD of the deposited coatings, although densification, as well as thicker coatings, would allow for higher quality data for measurements such as nano-indentation. The EB-DVD system has an upgrade planned to install a spotless arc deposition (SAD) upgrade, Figure 85. This will allow direct ionization of the refractory metal gas species without the need of an ionizing gas, resulting in high deposition rates without droplet formation, with a maximum projected deposition rate of Ti and Cr of ≤2 μm/s. This is also aided by an upgraded copper crucible that allows for evaporation of 9.5 mm (3/8”) diameter source rods, compared to the 6.3 mm (1/4”) diameter source rods used now. An increased electron beam power from 9.8 kW currently, to 15-17 kW, will allow for simultaneous evaporation of four refractory metal source rods. Finally, due to the absence of a plasma forming gas, less mixing of the vapor species will occur, and steeper concentration gradients should be possible.

While the plasma-assisted deposition of refractory metal coatings can be achieved by use of the coaxial plasma deposition approach, it suffers from three major drawbacks. The first is the release of water vapor molecules by plasma ion impacts with the interior chamber surfaces. The second issue concerns the plasma formation technique. The coaxial plasma-assisted EB-DVD system successfully combines EB source evaporation with hollow cathode plasma forming technology to allow the creation of coatings of controlled composition, structure and residual stress. However, when the working gas interacts with the metal vapor plume, lateral scattering causes the plume to homogenize resulting in a loss of concentration gradient. Furthermore, this reduces the deposition rate, prolonging the time needed to make a coating, and provides more opportunity for the incorporation of background gases in coatings.

An effective resolution to the issues identified above requires creation of a localized plasma that is aligned with the propagation direction of the vapor stream and of similar cross-sectional area. It should have applicability to widest possible range of source materials and compatibility with a broad spectrum of gases (inert gas jet gases such as helium or argon, as well as reactive gases as oxygen, nitrogen, methane, etc.). Charge carrier drag-off by the helium gas jet must not disable the plasma generating discharge, and it must provide a stable plasma for a wide range of background pressures (from below 0.01 Pa up to about 50 Pa). In addition, the plasma density and degree of ionization must be high (the latter in the 25 to 50% range) in order to raise the mean energy of rapidly condensing atoms or molecules (at high deposition rates of ~15 µm/min.

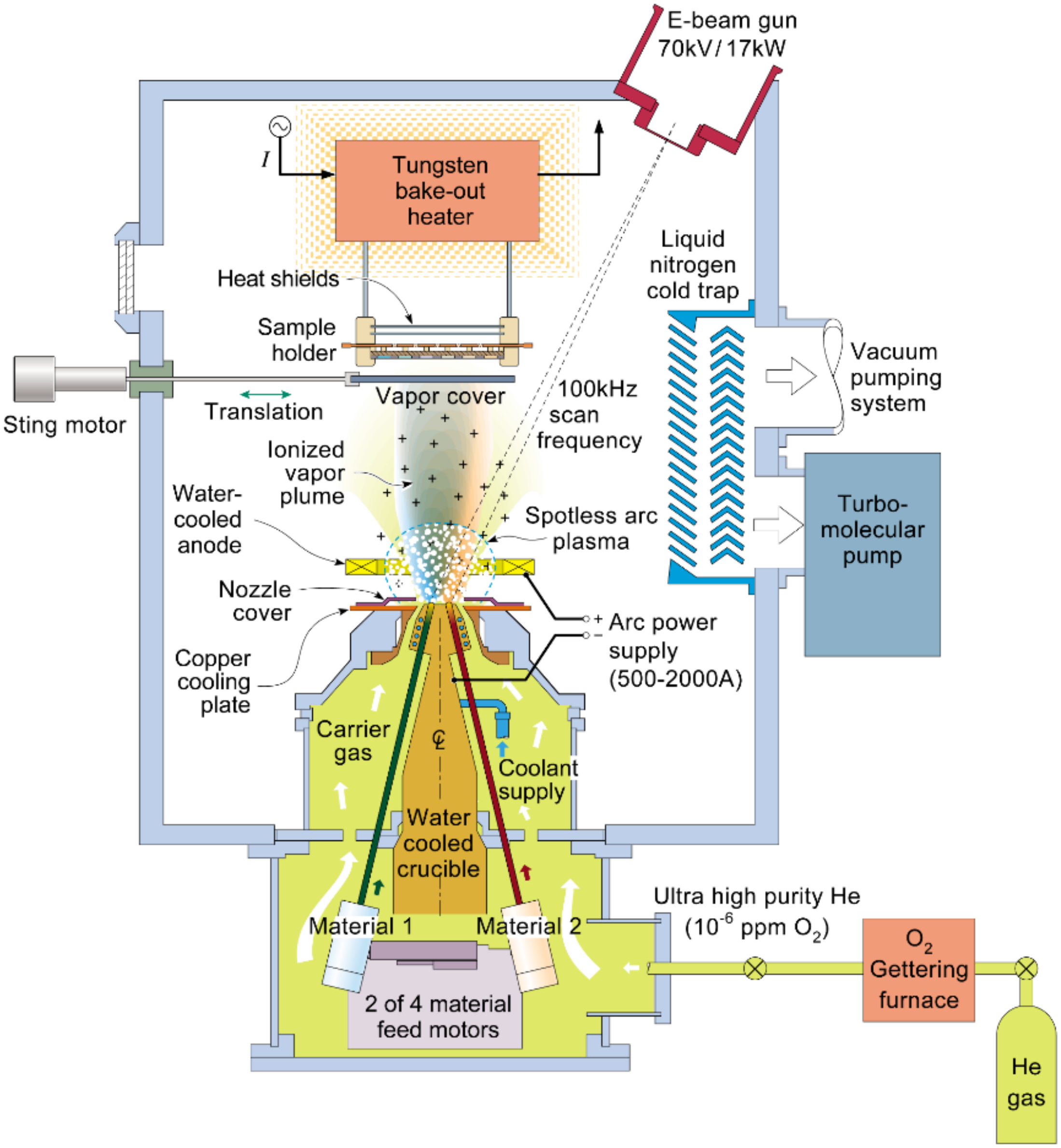

Figure 85. Schematic illustration of the spotless arc plasma assisted vapor deposition system with an upgraded 17 kW power high voltage EB gun, bake-out heater, substrate heater, and oxygen gettering furnaces.

In the plasma-assisted deposition approach proposed here, the high current density emitted from the electron beam heated evaporating pools is used to create an intense vapor plasma, as shown schematically in Figure 86. In this adaption of “cathodic arc deposition”, a circular ring, water cooled anode is positioned several centimeters from the electron beam impingement point on a vapor source, and connected to a power supply (an existing unused power supply is available for this). A positive potential of 10-80 V attracts thermionic electrons formed during the electron beam interaction with the source.

The electrostatic attraction of the thermionic electrons by the anode raises their kinetic energy into the 10-20 eV range, where their impact with vapor atoms has a high probability of causing their ionization, Figure 61. The vapor emitted from the surface is therefore both entrained in the EB-DVD helium gas jet, and ionized by collisions with the electrons in the arc during its transport to a substrate. In this elegant approach, the electron beam used for evaporation simultaneously creates and ionizes the vapor (and the jet forming gas, which can be doped with other gases including combinations of inert and reactant gases). Since the foot point of the arc is always located on the hottest region of a source material, the arc follows automatically the electron beam as it is scanned over the source(s). This means, the area that is momentarily generating the highest vapor flux coincides with the zone of maximum discharge current density, and results in very efficient ionization (of order 50%) and plasma activation of the vapor.

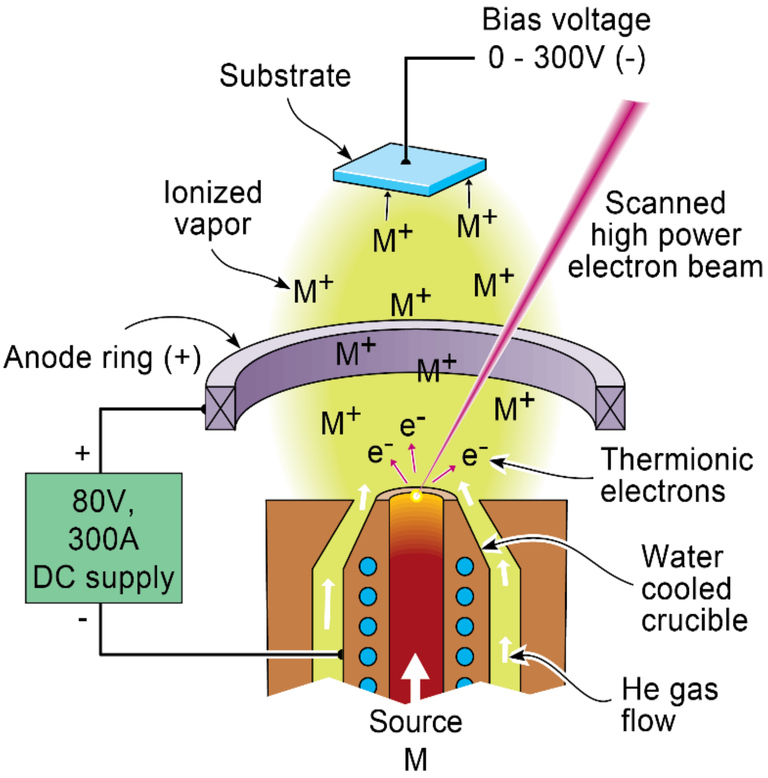

Figure 86. Schematic illustration the formation of a plasma by collisions of thermionic emission of electrons from a refractory material source with vapor from a source material

The arc discharge plasma is at first transported towards the substrate by the vapor entraining gas jet through an ion-drag mechanism. However, when the substrate is sufficiently charged (electrically biased), the plasma ions are also electrostatically accelerated towards the substrate across a plasma sheath, and this extra momentum aids in densification and defect removal during coating deposition on a component surface. Since no plasma forming gas need be injected into the deposition system, this aspect of the upgrade overcomes many of the issues associated with the use of coaxial hollow cathodes for plasma activation in EB-DVD processes, and results in a low-cost plasma assistance concept.

This plasma assisted deposition approach is (synergistically) complimented by the proposed modification of the EB gun power supply enabling the existing 10 kW EB gun power to be increased to 15-17 kW. Importantly, the thermionic current flow through the source materials contributes substantial additional heating of the source, increasing its surface temperature and evaporation rate. The voltage of the positively polarized anode ring controls the power of the arc discharge that forms the plasma. This ring anode draws a significant thermionic current from heated refractory metal source(s). From Richardson's law, the thermionic component of the current from a 12.5 mm diameter refractory metal source with a work function of about 4 eV, when heated to 3,000 K is ~200 Amps. The D.C. power can easily support a 50V bias, resulting in a 10 kW plasma power (about double that of the existing coaxial plasma). About a half of this power is dissipated in the source material where thermionic electron emission occurs (the remainder is dissipated in the anode, requiring its water-cooling). However, the 5 kW spotless arc power deposited in the source adds to that applied by the electron beam, and increases the evaporate rate of the highest melting temperature source materials during multi-source evaporation. Since the flux of water vapor incident upon a substrate is fixed (by the desorption rate from interior chamber surfaces), this increase in deposition rate also results in an additional decrease in the oxygen impurity level in the coatings. It also enables sharper composition gradients in combinatorial library samples intended for our BRC collaborators, because argon-ion assistance need not be used.

The proposed EB-DVD upgrades will overcome many of the issues associated with the use of low film density and lowering of concentration gradients due coaxial hollow cathodes for plasma activation in the DVD process. Future work will implement the increased electron beam power and the SAD technique to deposit films with high densities, low oxygen concentration, large compositional gradients (>15at%), and sufficient thickness (>100μm) for high throughput investigation such as micro-mechanical testing and XRD.

References

1. Deijkers JA, Wadley HNG. Hafnium silicate formation during oxidation of a permeable silicon + HfO2 powder composite system. Acta Mater. 2020 Dec 1;201:448–61.

2. Marshall DB, Cox BN. Integral Textile Ceramic Structures. Annu Rev Mater Res. 2008 Aug 1;38(1):425–43.

3. Kolagar AM, Tabrizi N, Cheraghzadeh M, Shahriari MS. Failure analysis of gas turbine first stage blade made of nickel-based superalloy. Case Stud Eng Fail Anal. 2017 Apr 1;8:61–8.

4. Lee WE, Gilbert M, Murphy ST, Grimes RW. Opportunities for Advanced Ceramics and Composites in the Nuclear Sector. J Am Ceram Soc. 2013 Jul 1;96(7):2005–30.

5. Parthasarathy TA, Petry MD, Cinibulk MK, Mathur T, Gruber MR. Thermal and Oxidation Response of UHTC Leading Edge Samples Exposed to Simulated Hypersonic Flight Conditions. J Am Ceram Soc. 2013 Mar 1;96(3):907–15.

6. Senkov ON, Miracle DB, Chaput K, Couzinie J. Development and exploration of refractory high entropy alloys—A review. J Mater Res. 2018 Oct 14;33(19):3092–128.

7. Perepezko JH. The Hotter the Engine, the Better. Science. 2009 Nov 20;326(5956):1068–9.

8. Grady JE. CMC Technology Advancements for Gas Turbine Engine Applications. :19.

9. Epstein AH. Aeropropulsion for Commercial Aviation in the Twenty-First Century and Research Directions Needed. AIAA J. 2014 May;52(5):901–11.

10. Lee KN. Protective Coatings for Gas Turbines. In: The Gas Turbine Handbook. 2006. p. 419–37.

11. Padova C, Dunn MG, Barton J, Turner K, Turner A, DiTommaso D. Casing Treatment and Blade-Tip Configuration Effects on Controlled Gas Turbine Blade Tip/Shroud Rubs at Engine Conditions. J Turbomach [Internet]. 2010 Sep 22 [cited 2021 Dec 10];133(1). Available from: https://doi.org/10.1115/1.4000539

12. Kumar R, Kumar VS, Butt MM, Sheikh NA, Khan SA, Afzal A. Thermo-mechanical analysis and estimation of turbine blade tip clearance of a small gas turbine engine under transient operating conditions. Appl Therm Eng. 2020 Oct 1;179:115700.

13. Steibel J. Ceramic Matrix Composites Taking Flight at GE Aviation. ACerS Bullitin. 98:30–3.

14. Refractory Metals (Definition, Examples, and Applications) [Internet]. Available from: https://msestudent.com/refractory-metals-definition-examples-and-applications/

15. Miracle DB, Senkov ON. A critical review of high entropy alloys and related concepts. Acta Mater. 2017 Jan 1;122:448–511.

16. Senkov ON, Jensen JK, Pilchak AL, Miracle DB, Fraser HL. Compositional variation effects on the microstructure and properties of a refractory high-entropy superalloy AlMo0.5NbTa0.5TiZr. Mater Des. 2018 Feb 5;139:498–511.

17. Couzinié JP, Senkov ON, Miracle DB, Dirras G. Comprehensive data compilation on the mechanical properties of refractory high-entropy alloys. Data Brief. 2018 Dec;21:1622–41.

18. Senkov ON, Wilks GB, Miracle DB, Chuang CP, Liaw PK. Refractory high-entropy alloys. Intermetallics. 2010 Sep 1;18(9):1758–65.

19. Senkov ON, Wilks GB, Scott JM, Miracle DB. Mechanical properties of Nb25Mo25Ta25W25 and V20Nb20Mo20Ta20W20 refractory high entropy alloys. Intermetallics. 2011 May 1;19(5):698–706.

20. Furrer D. Oral Presentation presented at: Conference of Metallurgists; 2015; Canada.

21. Gibson LJ, Ashby MF. Cellular Solids, Structure and properties. 2nd ed. Univesrity of Cambridge; 1997. (Cambridge Solid State Science).

22. Banhart J, Seeliger HW. Aluminium Foam Sandwich Panels: Manufacture, Metallurgy and Applications. Adv Eng Mater. 2008 Sep 1;10(9):793–802.

23. Sun G, Wang E, Zhang J, Li S, Zhang Y, Li Q. Experimental study on the dynamic responses of foam sandwich panels with different facesheets and core gradients subjected to blast impulse. Int J Impact Eng. 2020 Jan 1;135:103327.

24. Wadley HNG. Multifunctional periodic cellular metals. Philos Trans R Soc Math Phys Eng Sci. 2006 Jan 15;364(1838):31.

25. Dong L, Deshpande V, Wadley H. Mechanical response of Ti–6Al–4V octet-truss lattice structures. Int J Solids Struct. 2015 May;60–61:107–24.

26. Hertz A, Bruce IJ. Inorganic materials for bone repair or replacement applications. Nanomed. 2007 Dec 1;2(6):899–918.

27. Mahjoob S, Vafai K. A synthesis of fluid and thermal transport models for metal foam heat exchangers. Int J Heat Mass Transf. 2008 Jul 15;51(15):3701–11.

28. Boomsma K, Poulikakos D, Zwick F. Metal foams as compact high performance heat exchangers. Mech Mater. 2003 Dec;35(12):1161–76.

29. Giani L, Groppi G, Tronconi E. Mass-Transfer Characterization of Metallic Foams as Supports for Structured Catalysts. Ind Eng Chem Res. 2005 Jul 1;44(14):4993–5002.

30. Vásquez L, Campagnolo L, Athanassiou A, Fragouli D. Expanded Graphite-Polyurethane Foams for Water–Oil Filtration. ACS Appl Mater Interfaces. 2019 Aug 21;11(33):30207–17.

31. Kennedy MW, Zhang K, Fritzsch R, Akhtar S, Bakken JA, Aune RE. Characterization of Ceramic Foam Filters Used for Liquid Metal Filtration. Metall Mater Trans B. 2013 Jun;44(3):671–90.

32. Liang X, Li Y, Yan W, Wang Q, Tan F, He Z, et al. Preparation of SiC reticulated porous ceramics with high strength and increased efficient filtration via fly ash addition. J Eur Ceram Soc. 2020 Nov;S0955221920309389.

33. Salvini VR, Luchini B, Aneziris CG, Pandolfelli VC. Innovation in ceramic foam filters manufacturing process. Int J Appl Ceram Technol. 2019 Jan;16(1):378–88.

34. Mohan M, Sharma VK, Kumar EA, Gayathri V. Hydrogen storage in carbon materials—A review. Energy Storage. 2019 Apr;1(2):e35.

35. Esser B, Barcena J, Kuhn M, Okan A, Haynes L, Gianella S, et al. Innovative Thermal Management Concepts and Material Solutions for Future Space Vehicles. J Spacecr Rockets. 2016 Nov 1;53(6):1051–60.

36. Ortona A, Pusterla S, Gianella S. An integrated assembly method of sandwich structured ceramic matrix composites. J Eur Ceram Soc. 2011 Aug 1;31(9):1821–6.

37. Deshpande VS, Ashby MF, Fleck NA. Foam topology: bending versus stretching dominated architectures. Acta Mater. 2001 Apr 2;49(6):1035–40.

38. Shin C, Jin HH, Kim WJ, Park JY. Mechanical Properties and Deformation of Cubic Silicon Carbide Micropillars in Compression at Room Temperature. J Am Ceram Soc. 2012 Sep 1;95(9):2944–50.

39. Ashby MF, Medalist RFM. The mechanical properties of cellular solids. Metall Trans A. 1983 Sep 1;14(9):1755–69.

40. Scheffler M, Colombo P, editors. Cellular ceramics: structure, manufacturing, properties and applications. Weinheim: Wiley-VCH; 2005. 645 p.

41. Gibson LJ. Biomechanics of cellular solids. J Biomech. 2005 Mar;38(3):377–99.

42. Colombo P, Modesti M. Silicon Oxycarbide Ceramic Foams from a Preceramic Polymer. J Am Ceram Soc. 2004 Dec 22;82(3):573–8.

43. Zhang L, Ferreira JMF, Olhero S, Courtois L, Zhang T, Maire E, et al. Modeling the mechanical properties of optimally processed cordierite–mullite–alumina ceramic foams by X-ray computed tomography and finite element analysis. Acta Mater. 2012 Jun;60(10):4235–46.

44. Knackstedt MA, Arns CH, Saadatfar M, Senden TJ, Sakellariou A, Sheppard AP, et al. Virtual Materials Design: Properties of Cellular Solids Derived from 3D Tomographic Images. Adv Eng Mater. 2005 Apr;7(4):238–43.

45. Roberts AP, Garboczi EJ. Computation of the linear elastic properties of random porous materials with a wide variety of microstructure. In: Proceedings of the Royal Society A: Mathematical, Physical and Engineering Sciences. 2002.

46. Chen Z, Li Z, Li J, Liu C, Lao C, Fu Y, et al. 3D printing of ceramics: A review. J Eur Ceram Soc. 2019 Apr;39(4):661–87.

47. Schaedler TA, Carter WB. Architected Cellular Materials. Annu Rev Mater Res. 2016 Jul;46(1):187–210.

48. Bauer J, Hengsbach S, Tesari I, Schwaiger R, Kraft O. High-strength cellular ceramic composites with 3D microarchitecture. :6.

49. Bauer J, Meza LR, Schaedler TA, Schwaiger R, Zheng X, Valdevit L. Nanolattices: An Emerging Class of Mechanical Metamaterials. Adv Mater. 2017 Oct;29(40):1701850.

50. Meza LR, Das S, Greer JR. Strong, lightweight, and recoverable three-dimensional ceramic nanolattices. Science. 2014 Sep 12;345(6202):1322–6.

51. Meza LR, Zelhofer AJ, Clarke N, Mateos AJ, Kochmann DM, Greer JR. Resilient 3D hierarchical architected metamaterials. Proc Natl Acad Sci. 2015 Sep 15;112(37):11502–7.

52. Zheng X, Lee H, Weisgraber TH, Shusteff M, DeOtte J, Duoss EB, et al. Ultralight, ultrastiff mechanical metamaterials. Science. 2014 Jun 19;344(6190):1373.

53. Ge Q, Li Z, Wang Z, Kowsari K, Zhang W, He X, et al. Projection micro stereolithography based 3D printing and its applications. Int J Extreme Manuf. 2020 Jun 7;2(2):022004.

54. Ashby MF, Evans T, Fleck N, Hutchinson JW, Wadley HNG, Gibson LJ. Metal Foams: A Design Guide [Internet]. Elsevier Science; 2000. Available from: https://books.google.com/books?id=C0daIBo6LjgC

55. KOTANI M, NISHIYABU K, MATSUZAKI S, TANAKA S. Processing of polymer-derived porous SiC body using allylhydridopolycarbosilane (AHPCS) and PMMA microbeads. J Ceram Soc Jpn. 2011;119(1391):563–9.

56. Lefebvre LP, Banhart J, Dunand DC. Porous Metals and Metallic Foams: Current Status and Recent Developments. Adv Eng Mater. 2008 Sep;10(9):775–87.

57. Vakifahmetoglu C, Zeydanli D, Colombo P. Porous polymer derived ceramics. Mater Sci Eng R Rep. 2016 Aug 1;106:1–30.

58. Saha SK, Wang D, Nguyen VH, Chang Y, Oakdale JS, Chen SC. Scalable submicrometer additive manufacturing. Science. 2019 Oct 4;366(6461):105–9.

59. Colombo P, Mera G, Riedel R, Sorarù GD. Polymer-Derived Ceramics: 40 Years of Research and Innovation in Advanced Ceramics: Polymer-Derived Ceramics. J Am Ceram Soc. 2010 Jun 7;no-no.

60. RIEDEL R, MERA G, HAUSER R, KLONCZYNSKI A. Silicon-Based Polymer-Derived Ceramics: Synthesis Properties and Application- A Review. J Ceram Soc Jpn. 2006;114(1330):425–44.

61. Eckel ZC, Zhou C, Martin JH, Jacobsen AJ, Carter WB, Schaedler TA. Additive manufacturing of polymer-derived ceramics. Science. 2016 Jan 1;351(6268):58–62.

62. Greil P. Polymer Derived Engineering Ceramics. Adv Eng Mater. 2000;(6):10.

63. Greil P. Active-Filler-Controlled Pyrolysis of Preceramic Polymers. J American Ceramic Society. 1995;78(4):835–48.

64. Colombo P, Perini K, Bernardo E, Capelletti T, Maccagnan G. Ceramic Microtubes from Preceramic Polymers. J Am Ceram Soc. 2003 Jun;86(6):1025–7.

65. Yajima S, Hasegawa Y, Hayashi J, Iimura M. Synthesis of continuous silicon carbide fibre with high tensile strength and high Young's modulus. J Mater Sci. 1978 Dec 1;13(12):2569–76.

66. Guo A, Roso M, Modesti M, Liu J, Colombo P. Preceramic polymer-derived SiOC fibers by electrospinning. J Appl Polym Sci. 2014 Feb 5;131(3):n/a-n/a.

67. Laine RM, Babonneau F. Preceramic polymer routes to silicon carbide. Chem Mater. 1993 Mar;5(3):260–79.

68. Mehr M, Moore DT, Esquivel-Elizondo JR, Nino JC. Mechanical and thermal properties of low temperature sintered silicon carbide using a preceramic polymer as binder. J Mater Sci. 2015 Nov 1;50(21):7000–9.

69. King D, Apostolov Z, Key T, Carney C, Cinibulk M. Novel processing approach to polymer-derived ceramic matrix composites. Int J Appl Ceram Technol. 15(2):399–408.

70. Kotani M, Inoue T, Kohyama A, Okamura K, Katoh Y. Consolidation of polymer-derived SiC matrix composites: processing and microstructure. Compos Sci Technol. 2002;62(16):2179–88.

71. Poerschke DL, Braithwaite A, Park D, Lauten F. Crystallization behavior of polymer-derived Si-O-C for ceramic matrix composite processing. Acta Mater. 2018;147:329–41.

72. Ly HQ, Taylor R, Day RJ, Heatley F. Conversion of polycarbosilane (PCS) to SiC-based ceramic Part 1. Characterisation of PCS and curing products. J Mater Sci. 2001 Aug 1;36(16):4037–43.

73. Yu Z, Min H, Yang L, Feng Y, Zhang P, Riedel R. Influence of the architecture of dendritic-like polycarbosilanes on the ceramic yield. J Eur Ceram Soc. 2015 Apr;35(4):1161–71.

74. Li H, Zhang L, Cheng L, Wang Y, Yu Z, Huang M, et al. Effect of the polycarbosilane structure on its final ceramic yield. J Eur Ceram Soc. 2008 Jan;28(4):887–91.

75. Zunjarrao SC, Rahman A, Singh RP. Characterization of the Evolution and Properties of Silicon Carbide Derived From a Preceramic Polymer Precursor. J Am Ceram Soc. 96(6):1869–76.

76. Moraes KV, Interrante LV. Processing, Fracture Toughness, and Vickers Hardness of Allylhydridopolycarbosilane-Derived Silicon Carbide. J Am Ceram Soc. 2003 Feb 1;86(2):342–6.

77. Hensleigh RM, Cui H, Oakdale JS, Ye JC, Campbell PG, Duoss EB, et al. Additive manufacturing of complex micro-architected graphene aerogels. Mater Horiz. 2018;5(6):1035–41.

78. Hundley JM, Eckel ZC, Schueller E, Cante K, Biesboer SM, Yahata BD, et al. Geometric characterization of additively manufactured polymer derived ceramics. Addit Manuf. 2017 Dec;18:95–102.

79. Wen Q, Xu Y, Xu B, Fasel C, Guillon O, Buntkowsky G, et al. Single-source-precursor synthesis of dense SiC/HfCxN1−x-based ultrahigh-temperature ceramic nanocomposites. Nanoscale. 2014;6(22):13678–89.

80. Hurwitz FI, Field L. Suspension of sic powders in allylhydridopolycarbosilane (ahpcs): Control of rheology. In John Wiley & Sons, Inc.; 2009. p. 45–52.

81. Starfire Systems. StarPCS SMP-10 Technical Data Sheet. Schenectady, NY;

82. König K, Boffa V, Buchbjerg B, Farsi A, Christensen ML, Magnacca G, et al. One-step deposition of ultrafiltration SiC membranes on macroporous SiC supports. J Membr Sci. 2014 Dec;472:232–40.

83. Key TS, Wilks GB, Parthasarathy TA, King DS, Apostolov ZD, Cinibulk MK. Process modeling of the low-temperature evolution and yield of polycarbosilanes for ceramic matrix composites. J Am Ceram Soc. 101(7):2809–18.

84. Schindelin J, Arganda-Carreras I, Frise E, Kaynig V, Longair M, Pietzsch T, et al. Fiji: an open-source platform for biological-image analysis. Nat Methods. 2012 Jul;9(7):676–82.

85. Rueschhoff L. TEM images of SiC particles provided by the Air Force Research Laboratory.

86. Sreeja R, Swaminathan B, Painuly A, Sebastian TV, Packirisamy S. Allylhydridopolycarbosilane (AHPCS) as matrix resin for C/SiC ceramic matrix composites. Mater Sci Eng B. 2010 Apr;168(1–3):204–7.

87. Apostolov ZD, Heckman EP, Key TS, Cinibulk MK. Effects of low-temperature treatment on the properties of commercial preceramic polymers. J Eur Ceram Soc. 2020 Jul;40(8):2887–95.

88. Kaur S, Riedel R, Ionescu E. Pressureless fabrication of dense monolithic SiC ceramics from a polycarbosilane. J Eur Ceram Soc. 2014 Dec;34(15):3571–8.

89. Larson NM, Zok FW. In-situ 3D visualization of composite microstructure during polymer-to-ceramic conversion. Acta Mater. 2018 Feb;144:579–89.

90. Key TS, Patel DK, Wilks GB, Cinibulk MK. Modeling the pyrolysis of preceramic polymers: A kinetic study of the polycarbosilane SMP-10. J Eur Ceram Soc. 2021 Jun;S0955221921004234.

91. Li H, Zhang L, Cheng L, Wang Y, Yu Z, Huang M, et al. Polymer–ceramic conversion of a highly branched liquid polycarbosilane for SiC-based ceramics. J Mater Sci. 2008 Apr;43(8):2806–11.

92. Korobeinichev OP. Kinetics of thermal decomposition of PMMA at different heating rates and in a wide temperature range. Thermochim Acta. 2019;9.

93. Lomakin SM, Brown JE, Breese RS, Nyden MR. An investigation of the thermal stability and char-forming tendency of cross-linked poly(methyl methacrylate). Polym Degrad Stab. 1993 Jan;41(2):229–43.

94. Novozhilov V, Joseph P, Ishiko K, Shimada T, Wang H, Liu J. Polymer Combustion as a Basis for Hybrid Propulsion: A Comprehensive Review and New Numerical Approaches. Energies. 2011 Oct 24;4(10):1779–839.

95. Hirata T, Kashiwagi T, Brown JE. Thermal and oxidative degradation of poly(methyl methacrylate): weight loss. Macromolecules. 1985 Jul;18(7):1410–8.

96. Rahaman MN, Boiteux Y, Jonghe LCD. Surface Characterization of Silicon Nitride and Silicon Carbide Powders. Am Ceram Soc. 1985;33.

97. Weimer AW, Nilsen KJ, Cochran GA, Roach RP. Kinetics of carbothermal reduction synthesis of beta silicon carbide. AIChE J. 1993 Mar;39(3):493–503.

98. Hettler S, Dries M, Hermann P, Obermair M, Gerthsen D, Malac M. Carbon contamination in scanning transmission electron microscopy and its impact on phase-plate applications. Micron. 2017 May;96:38–47.

99. Farr NTH, Hughes GM, Rodenburg C. Monitoring Carbon in Electron and Ion Beam Deposition within FIB-SEM. Materials. 2021 Jun 2;14(11):3034.

100. Wang Z, Schmalbach KM, Penn RL, Poerschke D, Antoniou A, Mara NA, et al. 3D Periodic and Interpenetrating Tungsten–Silicon Oxycarbide Nanocomposites Designed for Mechanical Robustness. ACS Appl Mater Interfaces. 2021 Jul 14;13(27):32126–35.

101. Gao Y, Mera G, Nguyen H, Morita K, Kleebe HJ, Riedel R. Processing route dramatically influencing the nanostructure of carbon-rich SiCN and SiBCN polymer-derived ceramics. Part I: Low temperature thermal transformation. Eng Ceram 2011 - Mater Compon. 2012 Jul 1;32(9):1857–66.

102. Naviroj M, Miller SM, Colombo P, Faber KT. Directionally aligned macroporous SiOC via freeze casting of preceramic polymers. J Eur Ceram Soc. 2015 Aug 1;35(8):2225–32.

103. Renlund GM, Prochazka S, Doremus RH. Silicon oxycarbide glasses: Part I. Preparation and chemistry. J Mater Res. 1991 Dec;6(12):2716–22.

104. Jacobson NS, Lee KN, Fox DS. Reactions of Silicon Carbide and Silicon(IV) Oxide at Elevated Temperatures. J Am Ceram Soc. 1992 Jun;75(6):1603–11.

105. Barick P, Chakravarty D, Saha BP, Mitra R, Joshi SV. Effect of pressure and temperature on densification, microstructure and mechanical properties of spark plasma sintered silicon carbide processed with β-silicon carbide nanopowder and sintering additives. Ceram Int. 2016 Feb;42(3):3836–48.

106. Sanders WS, Gibson LJ. Mechanics of hollow sphere foams. Mater Sci Eng A. 2003 Apr;347(1–2):70–85.

107. Hasegawa Y, Iimura M, Yajima S. Synthesis of continuous silicon carbide fibre. J Mater Sci. 1980 Mar 1;15(3):720–8.

108. L.J. G, M.F. A. The mechanics of three-dimensional cellualr materials. Proc R Coc Lond. 1982;A 382:43–59.

109. Ansys Granta Selector software, ANSYS, Inc., Cambridge, UK, 2021.

110. Jana DC, Sundararajan G, Chattopadhyay K. Effect of Porosity on Structure, Young's Modulus, and Thermal Conductivity of SiC Foams by Direct Foaming and Gelcasting. Colombo P, editor. J Am Ceram Soc. 2017 Jan;100(1):312–22.

111. Kuo T, Rueschhoff LM, Dickerson MB, Patel TA, Faber KT. Hierarchical porous SiOC via freeze casting and self-assembly of block copolymers. Scr Mater. 2021 Jan;191:204–9.

112. Colombo P. Macro- and micro-cellular porous ceramics from preceramic polymers. Compos Sci Technol. 2003 Dec;63(16):2353–9.

113. Durif C, Wynn M, Balestrat M, Franchin G, Kim YW, Leriche A, et al. Open-celled silicon carbide foams with high porosity from boron-modified polycarbosilanes. J Eur Ceram Soc. 2019 Dec;39(16):5114–22.

114. Yuan X, Jin H, Yan X, Cheng L, Hu L, Xue Q. Synthesis of ordered mesoporous silicon oxycarbide monoliths via preceramic polymer nanocasting. Microporous Mesoporous Mater. 2012 Jan;147(1):252–8.

115. Wang Z, Feng P, Wang X, Geng P, Akhtar F, Zhang H. Fabrication and properties of freeze-cast mullite foams derived from coal-series kaolin. Ceram Int. 2016 Aug;42(10):12414–21.

116. Licitra L, Luong DD, Strbik OM, Gupta N. Dynamic properties of alumina hollow particle filled aluminum alloy A356 matrix syntactic foams. Mater Des. 2015 Feb;66:504–15.

117. Bauer J, Hengsbach S, Tesari I, Schwaiger R, Kraft O. High-strength cellular ceramic composites with 3D microarchitecture. Proc Natl Acad Sci. 2014 Feb 18;111(7):2453.

118. Bauer J, Schroer A, Schwaiger R, Kraft O. Approaching theoretical strength in glassy carbon nanolattices. Nat Mater. 2016 Apr;15(4):438–43.

119. do Rosário JJ, Lilleodden ET, Waleczek M, Kubrin R, Petrov AYu, Dyachenko PN, et al. Self-Assembled Ultra High Strength, Ultra Stiff Mechanical Metamaterials Based on Inverse Opals: Self-Assembled Ultra High Strength, Ultra Stiff Mechanical Metamaterials…. Adv Eng Mater. 2015 Oct;17(10):1420–4.

120. Cantor B, Chang ITH, Knight P, Vincent AJB. Microstructural development in equiatomic multicomponent alloys. Mater Sci Eng A. 2004 Jul 1;375–377:213–8.

121. Yeh JW, Chen SK, Lin SJ, Gan JY, Chin TS, Shun TT, et al. Nanostructured High-Entropy Alloys with Multiple Principal Elements: Novel Alloy Design Concepts and Outcomes. Adv Eng Mater. 2004;6(5):299–303.

122. Oses C, Toher C, Curtarolo S. High-entropy ceramics. Nat Rev Mater. 2020 Apr 1;5(4):295–309.

123. Toher C, Oses C, Esters M, Hicks D, Kotsonis GN, Rost CM, et al. High-entropy ceramics: propelling applications through disorder. ArXiv211111519 Cond-Mat [Internet]. 2021 Nov 22 [cited 2022 Apr 15]; Available from: http://arxiv.org/abs/2111.11519

124. Senkov ON, Gorsse S, Miracle DB. High temperature strength of refractory complex concentrated alloys. Acta Mater [Internet]. 2019 Jun 20; Available from: http://www.sciencedirect.com/science/article/pii/S1359645419304033

125. Yeh JW. Recent Progress in High-entropy Alloys. Ann Chim – Sci Mater. 2006;31:633–48.

126. Cuesta-Lopez S. Report on refractory metal increase potential-substitutes non-refractory metals. 2016 Dec p. 63. Report No.: MSP-REFRAM D5.2.

127. Hume-Rothery W. Researches on the nature, properties, and conditions of formation of intermetallic compounds, with special reference to certain compounds of tin. 1926;

128. Feng XB, Zhang JY, Wang YQ, Hou ZQ, Wu K, Liu G, et al. Size effects on the mechanical properties of nanocrystalline NbMoTaW refractory high entropy alloy thin films. Int J Plast. 2017 Aug;95:264–77.

129. Feng X, Zhang J, Xia Z, Fu W, Wu K, Liu G, et al. Stable nanocrystalline NbMoTaW high entropy alloy thin films with excellent mechanical and electrical properties. Mater Lett. 2018 Jan;210:84–7.

130. Zou Y, Maiti S, Steurer W, Spolenak R. Size-dependent plasticity in an Nb25Mo25Ta25W25 refractory high-entropy alloy. Acta Mater. 2014 Feb 15;65:85–97.

131. Lilensten L, Couzinié JP, Perrière L, Bourgon J, Emery N, Guillot I. New structure in refractory high-entropy alloys. Mater Lett. 2014 Oct 1;132:123–5.

132. Popov VV, Katz-Demyanetz A, Koptyug A, Bamberger M. Selective electron beam melting of Al0.5CrMoNbTa0.5 high entropy alloys using elemental powder blend. Heliyon. 2019 Feb 1;5(2):e01188.

133. Knoll H, Ocylok S, Weisheit A, Springer H, Jägle E, Raabe D. Combinatorial Alloy Design by Laser Additive Manufacturing. Steel Res Int. 2017 Aug;88(8):1600416.

134. Moorehead M, Bertsch K, Niezgoda M, Parkin C, Elbakhshwan M, Sridharan K, et al. High-throughput synthesis of Mo-Nb-Ta-W high-entropy alloys via additive manufacturing. Mater Des. 2020 Feb;187:108358.

135. Melia MA, Whetten SR, Puckett R, Jones M, Heiden MJ, Argibay N, et al. High-throughput additive manufacturing and characterization of refractory high entropy alloys. Appl Mater Today. 2020 Jun;19:100560.

136. Kang B, Lee J, Ryu HJ, Hong SH. Ultra-high strength WNbMoTaV high-entropy alloys with fine grain structure fabricated by powder metallurgical process. Mater Sci Eng A. 2018 Jan;712:616–24.

137. Waseem OA, Lee J, Lee HM, Ryu HJ. The effect of Ti on the sintering and mechanical properties of refractory high-entropy alloy TixWTaVCr fabricated via spark plasma sintering for fusion plasma-facing materials. Mater Chem Phys. 2018 May;210:87–94.

138. Sriharitha R, Murty BS, Kottada RS. Alloying, thermal stability and strengthening in spark plasma sintered AlxCoCrCuFeNi high entropy alloys. J Alloys Compd. 2014 Jan 15;583:419–26.

139. Murty BS, Yeh JW, Ranganathan S, Bhattacharjee PP. High-Entropy Alloys [Internet]. Elsevier Science; 2019. Available from: https://books.google.com/books?id=VU2NDwAAQBAJ

140. Hass DD, Dharmasena K, Wadley HNG. An Electron Beam Method for Creating Combinatorial Libraries: Application to Next Generation Thermal Barrier Coatings Systems. 2002;E Beam(International Conference on High-Power Electron Beam Technology).

141. Talapatra A, Duong T, Son W, Gao H, Radovic M, Arróyave R. High-throughput combinatorial study of the effect of M site alloying on the solid solution behavior of M 2 AlC MAX phases. Phys Rev B. 2016 Sep 9;94(10):104106.

142. Liu Y, Padmanabhan J, Cheung B, Liu J, Chen Z, Scanley BE, et al. Combinatorial development of antibacterial Zr-Cu-Al-Ag thin film metallic glasses. Sci Rep. 2016 Jul;6(1):26950.

143. Barata D, van Blitterswijk C, Habibovic P. High-throughput screening approaches and combinatorial development of biomaterials using microfluidics. Acta Biomater. 2016 Apr;34:1–20.

144. Potyrailo R, Rajan K, Stoewe K, Takeuchi I, Chisholm B, Lam H. Combinatorial and High-Throughput Screening of Materials Libraries: Review of State of the Art. ACS Comb Sci. 2011 Nov 14;13(6):579–633.

145. Chan EM. Combinatorial approaches for developing upconverting nanomaterials: high-throughput screening, modeling, and applications. Chem Soc Rev. 2015;44(6):1653–79.

146. Siol S, Dhakal TP, Gudavalli GS, Rajbhandari PP, DeHart C, Baranowski LL, et al. Combinatorial Reactive Sputtering of In $_2$ S $_3$ as an Alternative Contact Layer for Thin Film Solar Cells. ACS Appl Mater Interfaces. 2016 Jun 8;8(22):14004–11.

147. Liu P, Guo B, An T, Fang H, Zhu G, Jiang C, et al. High throughput materials research and development for lithium ion batteries. High-Throughput Exp Model Res Adv Batter. 2017 Sep 1;3(3):202–8.

148. Feng X, Tang G, Sun M, Ma X, Wang L, Yukimura K. Structure and properties of multi-targets magnetron sputtered ZrNbTaTiW multi-elements alloy thin films. Surf Coat Technol. 2013 Aug;228:S424–7.

149. Kube SA, Sohn S, Uhl D, Datye A, Mehta A, Schroers J. Phase selection motifs in High Entropy Alloys revealed through combinatorial methods: Large atomic size difference favors BCC over FCC. Acta Mater. 2019 Mar;166:677–86.

150. Xue D, Balachandran PV, Hogden J, Theiler J, Xue D, Lookman T. Accelerated search for materials with targeted properties by adaptive design. Nat Commun. 2016 Sep;7(1):11241.

151. Koinuma H, Takeuchi I. Combinatorial solid-state chemistry of inorganic materials. Nat Mater. 2004 Jul;3(7):429–38.

152. Waseem OA, Ryu HJ. Combinatorial synthesis and analysis of AlxTayVz-Cr20Mo20Nb20Ti20Zr10 and Al10CrMoxNbTiZr10 refractory high-entropy alloys: Oxidation behavior. J Alloys Compd. 2020 Jul;828:154427.

153. Saha R, William N. Effects of the substrate on the determination of thin film mechanical properties by nanoindentation. 2002 Jan;50(1):23–38.

154. Alvi S, Jarzabek DM, Kohan MG, Hedman D, Jenczyk P, Natile MM, et al. Synthesis and Mechanical Characterization of a CuMoTaWV High-Entropy Film by Magnetron Sputtering. ACS Appl Mater Interfaces. 2020 May 6;12(18):21070–9.

155. Couet A. Integrated high-throughput research in extreme environments targeted toward nuclear structural materials discovery. J Nucl Mater. 2022 Feb;559:153425.

156. Yu Z, Dharmasena KP, Hass DD, Wadley HNG. Vapor deposition of platinum alloyed nickel aluminide coatings. Surf Coat Technol. 2006 Dec 4;201(6):2326–34.

157. Ohring M, Zarrabian S, Grogan A. The materials science of thin films. \ao. 1992 Dec;31(34):7162.

158. Maissel LI, Glang R. Handbook of Thin Film Technology. New York: McGraw- Hill Book Company; 1970.

159. Holland L. Vacuum Deposition of Thin Films. New York: John Wiley & Sons; 1956.

160. Baumgartner H. Spraying virtual iron on real engines. Mechanical Engineering. 1996;84.

161. Wolf S, Tauber RN. Silicon Processing for the VLSI Era. 1st ed. Sunset Beach, CA: Lattice Press; 1986. (Processing Technology; vol. 1).

162. Anthony TC, Brug JA, Zhang S. Magnetoresistance of symmetric spin valve structures. IEEE Trans Magn. 1994;30(6):3819–21.

163. Meier SM, Gupta DK. The Evolution of Thermal Barrier Coatings in Gas Turbine Engine Applications. J Eng Gas Turbines Power. 1994 Jan 1;116(1):250–7.

164. Choy K. Chemical vapour deposition of coatings. Prog Mater Sci. 2003;48(2):57–170.

165. Lampert CM. Heat mirror coatings for energy conserving windows. Sol Energy Mater. 1981;6(1):1–41.

166. Pindera MJ, Williams TO, Arnold SM. Thermoplstic response of metal-matrix composites with homogenized and functionally graded interfaces. Use Compos Funct Graded Mater. 1994 Jan 1;4(1):129–45.

167. Groves JF, Wadley HNG. Functionally graded materials synthesis via low vacuum directed vapor deposition. Use Compos Multi-Phased Funct Graded Mater. 1997 Jan 1;28(1):57–69.

168. Wadley HNG, Hsiung LM, Lankey RL. Artificially layered nanocomposites fabricated by jet vapor deposition. Use Compos Multi-Phased Funct Graded Mater. 1995 Jan 1;5(7):935–50.

169. Bunshah RF. Handbook of Deposition Technologies for Films and Coatings: Science, Technology, and Applications [Internet]. Noyes Publications; 1994. (Materials science and process technology series). Available from: https://books.google.com/books?id=IfCBIv3HdhMC

170. Schiller S, Heisig U, Panzer Siegfried. Electron beam technology. New York: Wiley; 1982.

171. Bunshah RF, Raghuram AC. Activated Reactive Evaporation Process for High Rate Deposition of Compounds. J Vac Sci Technol. 1972 Nov;9(6):1385–8.

172. Ritter E. Deposition of Oxide Films by Reactive Evaporation. J Vac Sci Technol. 1966 Jul;3(4):225.

173. Coburn J, Kay E. Positive-ion bombardment of substrates in rf diode glow discharge sputtering. J Appl Phys. 1972;43(12):4965–71.

174. Mattox DM. Fundamentals of Ion Plating. :7.

175. Sanders DM, Anders A. Review of cathodic arc deposition technology at the start of the new millennium. Surf Coat Technol. 2000;133:78–90.

176. Glocker DA, Shah SI. Handbook of Thin Film Process Technology. Philadelphia, PA: Institute of Physics Publishing; 1997.

177. Wadley HNG, Kim Y, Jin S. Thin Film Battery Synthesis by Directed Vapor Deposition. US 8,784,512 B2, 2014.

178. Hass DD, Zhao H, Dobbins T, Allen AJ, Slifka AJ, Wadley HNG. Multi-scale pore morphology in directed vapor deposited yttria-stabilized zirconia coatings. Mater Sci Eng A. 2010 Sep 15;527(23):6270–82.

179. Rodgers TM, Zhao H, Wadley HNG. Vapor deposition on doublet airfoil substrates: Coating thickness control. J Vac Sci Technol Vac Surf Films. 2015 Nov;33(6):061509.

180. Queheillalt DT, Hass DD, Sypeck DJ, Wadley HNG. Synthesis of open-cell metal foams by templated directed vapor deposition. J Mater Res. 2001 Apr;16(4):1028–36.

181. Hass DD, Parrish PA, Wadley HNG. Electron beam directed vapor deposition of thermal barrier coatings. J Vac Sci Technol Vac Surf Films. 1998 Nov;16(6):3396–401.

182. Yu Z, Zhao H, Wadley HNG. The Vapor Deposition and Oxidation of Platinum- and Yttria-Stabilized Zirconia Multilayers: Vapor Deposition and Oxidation of Pt/YSZ Multilayers. J Am Ceram Soc. 2011 Aug;94(8):2671–9.

183. Wadley HNG, Mattausch G, Morgner H. (54) COAXIAL, HOLLOW CATHODE PLASMA. :19.

184. Hass DD. Thermal Barrier Coatings Via Directed Vapor Deposition. University of Virginia; 2001.

185. Anders A. A structure zone diagram including plasma-based deposition and ion etching. Thin Solid Films. 2010 May;518(15):4087–90.

186. Thornton JA. Influence of substrate temperature and deposition rate on structure of thick sputtered Cu coatings. J Vac Sci Technol. 1975 Jul;12(4):830–5.

187. Grovenor CRM, Hentzell HTG, Smith DA. The development of grain structure during growth of metallic films. Acta Metall. 1984 May;32(5):773–81.

188. Mirica E, Kowach G, Du H. Modified Structure Zone Model to Describe the Morphological Evolution of ZnO Thin Films Deposited by Reactive Sputtering. Cryst Growth Des. 2004 Jan 1;4(1):157–9.

189. Liang Z, Biben T, Keblinski P. Molecular simulation of steady-state evaporation and condensation: Validity of the Schrage relationships. Int J Heat Mass Transf. 2017 Nov;114:105–14.

190. Chen W, Koplik J, Kretzschmar I. Molecular dynamics simulations of the evaporation of particle-laden droplets. Phys Rev E. 2013 May 23;87(5):052404.

191. Zhou XW, Murdick DA, Gillespie B, Wadley HNG. Atomic assembly during GaN film growth: Molecular dynamics simulations. Phys Rev B. 2006 Jan 31;73(4):045337.

192. Chandra A, Keblinski P. Investigating the validity of Schrage relationships for water using molecular dynamics simulations. J Chem Phys. 2020 Sep 28;153(12):124505.

193. Langmuir I. The Vapor Pressure of Metallic Tungsten. Phys Rev. 1913 Nov 1;2(5):329–42.

194. Schrage RW. A Theoretical Study of Interphase Mass Transfer [Internet]. Columbia University Press; 1953. Available from: https://doi.org/10.7312/schr90162

195. Groves J. Directed Vapor Deposition [Doctor of Philosophy]. University of Virginia; 1998.

196. Fedorovich ED, Rohsenow WM. The effect of vapor subcooling on film condensation of metals. Cambridge, Mass.: MIT Engineering Projects Laboratory,[1968]; 1968.

197. Hogge JW, Giles NF, Rowley RL, Knotts TA, Wilding WV. New Vapor-Pressure Prediction with Improved Thermodynamic Consistency using the Riedel Equation. Ind Eng Chem Res. 2017 Dec 13;56(49):14678–85.

198. Honig R. Vapor pressure data for the solid and liquid elements. RCA Rev. 1969;30:285–305.

199. Scoles G. Atomic and Molecular Beam Methods [Internet]. Oxford University Press; 1988. (Atomic and Molecular Beam Methods). Available from: https://books.google.com/books?id=zPHPngEACAAJ

200. Harnett LN. Experimental Investigation of Normal Shock Wave Velocity Distribution Functions in Mixtures of Argon and Helium. Phys Fluids. 1972;15(4):565.

201. Poling BE, Prausnitz JM, O'Connell JP. The properties of gases and liquids. McGraw-Hill. 2000;5th ed.

202. Chapman S, Cowling TG. The Mathematical Theory of Non-Uniform Gases: An account of the kinetic viscocity, thermal conduction, and diffusion in gases. 3rd ed. Cambridge U; 1970.

203. Yu Z, Hass DD, Wadley HNG. NiAl bond coats made by a directed vapor deposition approach. Mater Sci Eng A. 2005 Mar 15;394(1):43–52.

204. Zou W, Wadley HNG, Zhou XW, Johnson RA, Brownell D. Composition-Morphology-Property Relations For Giant Magnetoresistance Multilayers Grown By RF Diode Sputtering. MRS Proc. 2001;674:T1.5.

205. Rodgers TM, Zhao H, Wadley HNG. Microstructure of vapor deposited coatings on curved substrates. J Vac Sci Technol Vac Surf Films. 2015 Sep;33(5):05E118.

206. Kim YG, Wadley HNG. Lithium phosphorous oxynitride films synthesized by a plasma-assisted directed vapor deposition approach. J Vac Sci Technol Vac Surf Films. 2008 Jan;26(1):174–83.

207. Kim YG, Wadley HNG. Plasma-assisted deposition of lithium phosphorus oxynitride films: Substrate bias effects. J Power Sources. 2009 Feb;187(2):591–8.

208. Kalinin SV, Lupini AR, Dyck O, Jesse S, Ziatdinov M, Vasudevan RK. Lab on a beam—Big data and artificial intelligence in scanning transmission electron microscopy. MRS Bull. 2019 Jul;44(7):565–75.

209. Reyes KG, Maruyama B. The machine learning revolution in materials? MRS Bull. 2019 Jul;44(7):530–7.

210. Rubinstein RY, Kroese DP. The Cross-Entropy Method: A Unified Approach to Combinatorial Optimization, Monte-Carlo Simulation and Machine Learning [Internet]. Springer New York; 2013. (Information Science and Statistics). Available from: https://books.google.com/books?id=8KgACAAAQBAJ

211. Gorr B, Müller F, Azim M, Christ HJ, Müller T, Chen H, et al. High-Temperature Oxidation Behavior of Refractory High-Entropy Alloys: Effect of Alloy Composition. Oxid Met. 2017 Oct;88(3–4):339–49.

212. Nico C, Monteiro T, Graça MPF. Niobium oxides and niobates physical properties: Review and prospects. Prog Mater Sci. 2016 Jul 1;80:1–37.

213. Wriedt HA, Murray JL. The N-Ti (Nitrogen-Titanium) system. Bull Alloy Phase Diagr. 1987 Aug 1;8(4):378–88.

214. Garg SP, Krishnamurthy N, Awasthi A, Venkatraman M. The O-Ta (Oxygen-Tantalum) system. J Phase Equilibria. 1996 Jan 1;17(1):63–77.

215. Wriedt HA. The O-V (Oxygen-Vanadium) system. Bull Alloy Phase Diagr. 1989 Jun 1;10(3):271–7.

216. ASM International, editor. ASM handbook. 10th editon. Materials Park, Ohio: ASM International; 1990.

217. Bryant RT. The solubility of oxygen in transition metal alloys. J Common Met. 1962 Feb;4(1):62–8.

218. Okamoto H. Cr-O (chromium-oxygen). J Phase Equilibria. 1997 Aug 1;18(4):402.

219. Mazurkiewicz A, Smolik J, Zbrowski A, Kacprzyńska J. Innovative technical solutions for evaporation of multilayer coatings by EB-PVD method. Arch Civ Mech Eng. 2014 Feb 1;14(2):250–4.

220. Mazurkiewicz A, Smolik J. The Innovative Directions In Development And Implementations Of Hybrid Technologies In Surface Engineering. Arch Metall Mater. 2015 Sep 1;60(3):2161–72.

221. Yang YG, Zhou XW, Johnson RA, Wadley HNG. Monte Carlo simulation of hyperthermal physical vapor deposition. Acta Mater. 2001 Sep;49(16):3321–32.

222. Yang YG, Johnson RA, Wadley HNG. A Monte Carlo simulation of the physical vapor deposition of nickel. Acta Mater. 1997 Apr;45(4):1455–68.

223. Barzilai S, Toher C, Curtarolo S, Levy O. Evaluation of the tantalum-titanium phase diagram from ab-initio calculations. Acta Mater. 2016 Nov 1;120:255–63.

224. Isomorphous Binary Phase Diagram Of Nb (Niobium) - Ta (Tantalum) System Drawn At 1 Atm Ambient Pressure [Internet]. Available from: Chegg.com

225. Venkatraman M, Neumann JP. The Cr−Ta (Chromium-Tantalum) system. J Phase Equilibria. 1987 Apr 1;8(2):112–6.

226. Kolli R, Devaraj A. A Review of Metastable Beta Titanium Alloys. Metals. 2018 Jun 30;8(7):506.

227. Goldschmidt HJ, Brand JA. The constitution of the chromium-niobium-molybdenum system. J Common Met. 1961 Feb 1;3(1):44–61.

228. Denton AR, Ashcroft NW. Vegard's law. Phys Rev A. 1991 Mar;43(6):3161–4.

229. Appendix E: Parameter Tables of Crystals. In: Crystallography and Surface Structure [Internet]. Weinheim, Germany: Wiley-VCH Verlag GmbH & Co. KGaA; 2011 [cited 2021 Sep 26]. p. 265–6. Available from: https://onlinelibrary.wiley.com/doi/10.1002/9783527633296.app5

230. Alonso JC, Coreño Alonso O. Derivation of unit cell volume, and lattice parameter of cubic high entropy alloys from volume size factors. Intermetallics. 2021 Oct;137:107299.

231. King HW. Quantitative size-factors for metallic solid solutions. J Mater Sci. 1966 Feb;1(1):79–90.

232. Kwasniak P, Muzyk M, Garbacz H, Kurzydlowski KJ. Influence of oxygen content on the mechanical properties of hexagonal Ti—First principles calculations. Mater Sci Eng A. 2014 Jan;590:74–9.

233. Murray JL, Wriedt HA. The O−Ti (Oxygen-Titanium) system. J Phase Equilibria. 1987 Apr 1;8(2):148–65.

234. Kværndrup FB, Kücükyildiz ÖC, Winther G, Somers MAJ, Christiansen TL. Extreme hardening of titanium with colossal interstitial contents of nitrogen and oxygen. Mater Sci Eng A. 2021 May;813:141033.

235. Fietzke F, Morgner H, Günther S. "Magnetically enhanced hollow cathode-a new plasma source for high-rate deposition processes." Plasma Process Polym. 2009 Jun;6(S1):S242–6.

236. Zimmermann B, Mattausch G, Scheffel B, Heinß JP, Rögner FH. The potential of plasma activation for EB-PVD of EBC systems on CMC components. :3.

237. Mansour O, Aidaoui K, Kadoun AED, Khouchaf L, Mathieu C. Monte Carlo simulation of the electron beam scattering under gas mixtures environment in an HPSEM at low energy. Vacuum. 2009 Dec 8;84(4):458–63.

238. Chen Z, Wang X, Bhakhri V, Giuliani F, Atkinson A. Nanoindentation of porous bulk and thin films of La0.6Sr0.4Co0.2Fe0.8O3−δ. Acta Mater. 2013 Sep;61(15):5720–34.

239. Ramakrishnan N, Arunachalam VS. Effective elastic moduli of porous solids. J Mater Sci. 1990 Sep 1;25(9):3930–7.